

**STRESS CORROSION CRACKING OF X65 PIPELINE STEEL IN  
FUEL GRADE ETHANOL ENVIRONMENTS**

A Dissertation  
Presented to  
The Academic Faculty

by

Lindsey R. Goodman

In Partial Fulfillment  
of the Requirements for the Degree  
Doctor of Philosophy in the  
School of Materials Science and Engineering

Georgia Institute of Technology  
December 2012

# **STRESS CORROSION CRACKING OF X65 PIPELINE STEEL IN FUEL GRADE ETHANOL ENVIRONMENTS**

Approved by:

Dr. Preet M. Singh, Advisor  
School of Materials Science and  
Engineering  
*Georgia Institute of Technology*

Dr. Arthur Ragauskas  
School of Chemistry  
*Georgia Institute of Technology*

Dr. Faisal Alamgir  
School of School of Materials Science and  
Engineering  
*Georgia Institute of Technology*

Dr. Naresh N. Thadhani  
School of Materials Science and  
Engineering  
*Georgia Institute of Technology*

Dr. Hamid Garmestani  
School of Materials Science and  
Engineering  
*Georgia Institute of Technology*

Date Approved: July 25, 2012

## ACKNOWLEDGEMENTS

There are many individuals who, without their help and support, I would not have been able to complete my doctoral studies. First and foremost, I would like to extend the deepest of thanks and appreciation for my wonderful advisor, Dr. Preet M. Singh. His exceptionally supportive and patient manner and technical expertise in the corrosion field have given me the encouragement and direction I needed with both technical and non-technical aspects of my doctoral work. I would also like to thank Dr. Naresh Thadhani for his support and discussions of my research, as well as his encouragement and guidance during my participation on the GT Materials Society executive board. Many thanks to Dr. Faisal Alamgir for his help in deciphering the data from my XPS studies and for meaningful discussions on grad school in the beginning of my stay at GT. Thanks also to Dr. Art Ragauskas for his candid and very practical advice on the subjects of research, writing, and life. I am grateful to Dr. Hamid Garmestani for taking the time to serve on my committee with fairly late notice, and also for his help during my role as the graduate student liaison for the Atlanta ASM chapter. I would also like to acknowledge Jake Haase (Colonial Pipeline Company), Chuck Corr (ADM), and Dr. Xiaoyuan Lou (GE Global Research) for asking and answering my technical questions and providing interesting views on my dissertation topic. Many thanks to Walter Henderson for his excellent training and advice on the operation of analytical equipment, notably the XPS, and for always having a good answer to my questions.

I would like to express my gratitude to Jamshad Mahmood, who was instrumental in my success in the lab. He was always willing to both answer my questions and provide a helping hand, which were vital to my research progress. Special thanks also to Sam Raji for his help in the lab, and for continuously asking me very good questions. Many thanks also to the other members of Dr. Singh's group who have helped keep me grounded during my PhD studies.

Lastly, but most importantly, I would like to express my deep appreciation for the loving support of my friends and family during this often-stressful portion of my career. Thanks to my mom, dad, and sister for their love and encouragement and endless support. Thank you to Kyle Anderson, my fiancé and love of my life for his moral support. Thanks to Dr. Jon Vernon for being an amazing researcher and role model PhD student for me, and for teaching me how to properly use an SEM. Many thanks to my other friends and peers, as you have all influenced me in PhD and in life.

Sponsors of this work include Colonial Pipeline Company (project no. 3306F49), US DOT PHMSA (contract no. DTPH56-08-T-000013 and DTPH56-09-T-000004). Many thanks to the IPST PSE foundation for providing stipend support.

## TABLE OF CONTENTS

LIST OF TABLES	ix
LIST OF FIGURES	xi
LIST OF ABBREVIATIONS	xviii
SUMMARY	xix
1 INTRODUCTION	1
1.1 Objectives	4
1.2 Organization of Upcoming Chapters	5
2 BACKGROUND	6
2.1 Stress Corrosion Cracking	6
2.2 Corrosion Theory	10
2.3 SCC Mechanisms: Interaction of Corrosion and Stress	15
2.3.1 Anodic SCC mechanisms	16
2.3.2 Cathodic SCC mechanisms	18
2.3.3 Role of corrosion and surface film formation in anodic SCC	19
2.3.4 Role of crack tip chemistry	21
2.4 Testing for SCC Susceptibility	22
2.5 SCC of Pipeline Steel in FGE	26
2.5.1 Fuel grade ethanol environment	26
2.5.2 Pipeline steel	30
2.5.3 Corrosion and electrochemistry in organic solvents	31
2.5.4 SCC of pipeline steel	35
3 MATERIALS AND METHODS	40
3.1 Pipeline-grade Carbon Steel	40
3.2 Test Environments	41

3.2.1	Fuel grade ethanol	41
3.2.2	Simulated fuel grade ethanol	44
3.2.3	Ethanol chemical analysis	45
3.3	Slow Strain Rate Tests (SSRT)	46
3.3.1	Test specimen design	46
3.3.2	SSRT procedures	48
3.3.3	Metallography, Fractography, and visual characterization	49
3.4	Electrochemical Measurements	51
3.4.1	A note on challenges with electrochemistry in ethanol	53
3.5	Scratched Electrode Tests	56
3.6	Characterization of Surface Film Composition and Morphology	59
3.6.1	Static coupon exposures for film growth	59
3.6.2	XPS analysis	61
3.6.3	Atomic force microscopy	63
4	EFFECTS OF FGE FEEDSTOCK AND SOURCE ON SCC OF X65	65
4.1	Introduction	65
4.2	Chemical Characterization of all FGE Samples	67
4.3	Electrochemical Polarization of X65 in FGE	71
4.4	SCC in FGE in Notched SSRT	75
4.5	SSRT <i>In-situ</i> Electrochemistry	80
4.6	Discussion of Results and Comparison to Similar Studies	87
4.7	Chapter Summary and Conclusions	88
5	EFFECTS OF COMMON CONSTITUENTS AND CONTAMINANTS ON SCC AND CORROSION OF X65 IN FGE AND SFGE	89
5.1	Introduction	89
5.2	Denaturant and Inhibitor Effects	90

5.3	Chloride Thresholds for SCC in FGE	95
5.3.1	Electrochemical measurements	100
5.4	Water Effects on SCC and Corrosion Behavior	101
5.5	Effects of Strain on SCC Initiation and Propagation	109
5.5	Effects of pHe and Oxygen	114
5.6	Chapter Summary and Conclusions	118
6 INVESTIGATION OF THE REPASSIVATION KINETICS OF X65 STEEL IN FGE AND SFGE ENVIRONMENTS		120
6.1	Introduction	120
6.2	Repassivation Time Scale	122
6.3	Electrochemical Challenges When Measuring High Currents	123
6.4	Effects of Environment on Current Decay and Localized Corrosion Within the Scratch	128
6.5	Comparison of repassivation kinetics in commercial FGE and SFGE	135
6.6	Current transient analysis and modeling	136
6.7	Summary and Relationship of Current Decay to SCC Behavior	142
6.8	Conclusions	145
7 EFFECTS OF SFGE AND FGE ENVIRONMENT ON THE COMPOSITION AND MORPHOLOGY OF THE X65 SURFACE FILM		146
7.1	Introduction	146
7.2	Effects of SFGE and FGE on X65 Surface Film Composition and Morphology	147
7.2.1	Film behavior in baseline SFGE and comparison to commercial FGE	160
7.2.2	Effects of pHe variations on film composition	162
7.2.3	Water effects	165
7.2.4	Effects of chloride and deaeration	168
7.3	Chapter Summary and Conclusions	175

8 OVERALL CONCLUSIONS AND RECOMMENDATIONS FOR FUTURE WORK	177
8.1 Introduction	177
8.2 Summary of Constituent Effects on SCC behavior	177
8.3 Evidence of Film Rupture-Anodic Dissolution Mechanism	178
8.4 Film Formation of X65 Surface in FGE and SFGE	179
8.5 Proposed Mechanism of SCC of X65 Steel in FGE and SFGE: Role of Chloride, Oxygen, and Water	181
8.6 Mechanisms of SCC Mitigation in De-oxygenated and Alkaline SFGE and FGE	186
8.7 Implications for Safe Transport of FGE in X65 Steel Pipelines	187
8.8 Recommendations for Future Work	188
APPENDIX	190
REFERENCES	194
VITA	208

## LIST OF TABLES

Table 2-1 Select properties of ethanol and ultrapure water .....	27
Table 2-2 ASTM Specifications for Chemical Content of FGE [55] .....	29
Table 2-3 Specifications for Alloying Content of Pipeline Steels [56] .....	30
Table 3-1 Composition of pipeline steel test materials (*Nominal, **Analyzed).....	40
Table 3-2 List of commercial ethanol samples received with feedstock, production process, and producer/user classification information .....	43
Table 3-3 Composition of baseline simulated fuel grade ethanol used in this study.....	44
Table 3-4 Calculation of constants $C_1$ , $C_2$ , $C_3$ , and $C_4$ for calculation of $K_t$ (from [82]) .	48
Table 4-1 Sulfate, chloride, and water content, and pHe of all commercial FGE samples .....	68
Table 4-2 Summary of impurity content of commercial FGE samples.....	70
Table 4-3 Electrochemical parameters for each of the commercial FGE samples.....	71
Table 4-4 Results of post-SSRT FGE chloride content analysis .....	84
Table 5-1 Water content, pHe, and conductivity of FGE samples .....	90
Table 5-2 Summary table of SSRT for inhibitor/denaturant effects on SCC .....	91
Table 5-3 Post-test solution color change indicating increase in dissolved Fe at 5 vol% water content .....	107
Table 5-4 Composition of anhydrous SFGE.....	108
Table 5-5 Changes in SCC severity when SSRT is potentiostatically held at its original OCP, based on crack density and percent reduction in area of failed specimen. .....	109
Table 5-6 Environment compositions used in interrupted SSRT .....	110
Table 5-7 Solution compositions for pHe and oxygen variations.....	115
Table 5-8 Summary of results of tests with pHe variations and deaeration .....	115
Table 5-9 Dissolved Fe and solution color of deaerated SFGE after potentiostatic SSRT at X65 OCP (-0.111V vs. Ag/AgCl/EtOH).....	117

Table 6-1 Calculated scratch resistances ( $R_s$ ) and corresponding IR drops, assuming typical scratch lengths $l_s = 5\text{mm}$ and widths $w_s = 40\mu\text{m}$ . .....	125
Table 6-2 Characteristic data from SFGE environments with varied chloride content. Two of the environments were also under deaeration via nitrogen purge (highlighted in gray). .....	128
Table 6-3 Characteristic scratch test data from aerated SFGE environments with varied water content .....	129
Table 6-4 Scratch data for SFGE environments with varying pHe, altered by additions of acetic acid or sodium hydroxide.....	129
Table 6-5 Baseline current, OCP, $i_{bare}$ , current density and total charge density 120s after introduction of a scratch in commercial FGE with and without inhibitor .....	135
Table 7-1 Coupons of X65 were exposed to the environments listed, prior to XPS analysis .....	149
Table 7-2 Fe2p peak binding energies found from powder standards.....	153
Table 7-3 Average peak binding energies and assignments for the peaks found in the Fe2p spectra of X65 sample surfaces after environmental exposures.....	155
Table 7-4 Sampling depth of XPS data from steel surface, $h\nu = 1486.7\text{eV}$ , $\phi_s = 4.2\text{eV}$ , $\theta = 0^\circ$ . .....	156
Table 7-5 Average peak B.E. for O1s and C1s XPS spectral data of X65 surfaces after peak fitting.....	159
Table 7-6 Oxide thickness in each environment, calculated using equation (7-4) .....	160

## LIST OF FIGURES

Figure 1-1 Stress corrosion cracks and leaks in carbon steel equipment in the ethanol industry [6] a) ethanol tank b) welds in air-eliminator vessel c) pipes .....	3
Figure 2-1 Three factors must be simultaneously present for stress corrosion cracking to occur: A susceptible material must undergo stress in the presence of a specific environment.....	7
Figure 2-2 micrographs of a) an intergranular crack path [25]. b) a transgranular crack path [26]. .....	9
Figure 2-3 Schematic of mixed potential and polarization resulting from changes in mixed potential on current density. $i_{1a}$ and $i_{2a}$ are the anodic portions of half reactions 1 and 2, respectively. $i_{1c}$ and $i_{2c}$ are the cathodic portions of the designated half reaction. The metal in solution containing reactant 1 will equilibrate at potential $E_{mix,1}$ , with corrosion current $i_1$ . When reactant 1 becomes depleted and reaction $i_{2c}$ becomes the dominant cathodic reaction, the metal becomes polarized to potential $E_2$ and reacts at a higher corrosion rate, with a current density, $i_2$ .....	12
Figure 2-4 Schematic of an idealized potentiodynamic polarization curve displaying several important values that can be obtained using the potentiodynamic scan technique. ....	14
Figure 2-5 Pourbaix diagram for iron showing regions of stable passivity, active dissolution, or corrosion immunity based on electrode and electrolyte pH [29] .....	15
Figure 2-6 In the film rupture model, SCC propagation occurs because of active dissolution from the crack tip, which can (a) remain un-protected due to plasticity ahead of the crack tip, or (b) intermittently repassivate leading to discontinuous crack propagation [21] .....	17
Figure 2-7 Schematic of SCC caused by a hydrogen embrittlement mechanism. The image depicts atomic hydrogen migrating into the region of high stress concentration ahead of a crack tip where it will pin dislocations, increasing triaxial stress and facilitating crack propagation [34] .....	19
Figure 2-8 A schematic depicting the relationship between current flowing after film rupture and SCC susceptibility. (I) depicts rapid repassivation. (II) intermediate repassivation resulting in SCC, and (III)lateral dissolution which blunts the crack [35].....	20
Figure 2-9 Schematic of polarization behavior of an active passive alloy. Ranges of SCC susceptibility are shaded in gray. [35].....	21

Figure 2-10 Failed U-bend specimen [43] .....	23
Figure 2-11 C-ring test specimens for a) constant strain, and b) constant load testing [21] .....	24
Figure 2-12 Slow strain rate testing apparatus [45] .....	25
Figure 2-13 GC-MS Spectrum of Brazilian FGE [54].....	29
Figure 2-14 Anodic polarization curves for iron in MeOH-0.1M H <sub>2</sub> SO <sub>4</sub> solution with varying water content. Increasing water content decreased E <sub>p</sub> and increased stable passivity [63].....	32
Figure 2-15 Schematic illustrating the structure of alcohol-water solutions based on the mole fraction of alcohol (X <sub>alc</sub> ) present. Clustering decreases as carbon chain length increases [66].....	33
Figure 2-16 Pourbaix diagram for iron in pure ethanol [19] .....	38
Figure 3-1 Microstructure of as-received X65 pipeline steel. a) Lighter-colored grains are ferrite; dark areas are pearlite. b) High magnification image of a pearlite grain. Lighter-colored lamella are cementite, darker are ferrite.....	41
Figure 3-2 Smooth slow strain rate test specimen (scale bar in inches) .....	46
Figure 3-3 Close-up of the notched portion of the notched SSRT samples. The sample diameter (D), sample radius at the notch (h), and notch root radius (r) were measured using Clemex image analysis software. These parameters were used to compute initial stress concentration factor at the notch. ....	47
Figure 3-4 Environmental cell for slow strain rate testing in FGE.....	49
Figure 3-5 Elliptical fracture surface of a smooth SSRT specimen. Widest and narrowest dimensions were used to calculate area of the fracture surface for comparisons of % area reduction of samples strained in varied SFGE and FGE environments. .....	50
Figure 3-6 a) Front view of the environment cell with in-situ electrochemistry in place. The sample is threaded into steel grips for straining. b) side view of the three- electrode geometry within the cell .....	53
Figure 3-7 The electrochemical cell and its equivalent circuit approximation. Impedance within the reference electrode is often negligible and can be ignored. The potential of interest is E <sub>DL</sub> , thus corrections must be made if E <sub>IRu</sub> is high.....	54
Figure 3-8 Configuration of the working electrode (WE), counter electrode (CE) and reference electrode (RE) within the electrochemical cell used in ethanolic environments .....	56

Figure 3-9 Schematic of the test cell used for performing mechanical scratch tests .....	58
Figure 3-10 Schematic of coupon exposure test setup.....	60
Figure 4-1 GC-MS spectrum of Lot 7 FGE. The numbers correspond to the following constituents: 1. Internal standard, 2. Fatty acids, 3. C16:COOH ethyl ester, 4. 2,2 bis[(4-hydroxy)phenyl]propane, 5. Pimaric acid derivatives, 6. Pimaric acid, 7. Isopimaric acid, 8. Dehydroabietic acid, 9. Abietic acid.....	68
Figure 4-2 OCP of an X65 coupon in aerated FGE measured for 12 hours. The rate of OCP increase decreased after approximately 10 hours, exhibiting only small changes after this duration.....	72
Figure 4-3 (a) Potentiodynamic polarization of FGE lot 3 through 5, (b) Cyclic polarization of FGE lots 6 through 8.....	73
Figure 4-4 a) SSRT fracture surface exhibiting thumbnail-shaped area of brittle fracture. b) Notched SSRT specimen exhibiting a circumferential ring of brittle fracture [19]. .....	76
Figure 4-5 SEM images of fracture surfaces of notched samples strained in Lot 2 FGE which exhibit ductile failure characterized by microvoid coalescence. No brittle failure was detected; typical dimpled morphology of ductile failure surface is seen all the way to the outer edge of the sample. ....	77
Figure 4-6 Fracture surface of notched samples strained in a) Lot 6 FGE and b) Lot 9 FGE. No evidence of brittle fracture was observed around the circumference of either of the fracture areas. ....	78
Figure 4-7 Thumbnail region of mixed-mode SCC of notched sample strained in Lot 8 FGE .....	79
Figure 4-8 Fracture surface of a sample strained in Lot 2 FGE while OCP was measured. Transgranular SCC was exhibited, identifiable by the brittle fracture morphology near the outer edge of the sample. ....	81
Figure 4-9 Simultaneous loading and OCP measurement. (a) shows the OCP trend for the entire test duration. (b) depicts the rise and subsequent decrease in OCP corresponding to a stress relaxation event.....	82
Figure 4-10 Fracture surface of a sample from a repeated test, strained in Lot 2 FGE while OCP was measured. SCC results were nearly identical to the sample in Figure 4-8 Fracture surface of a sample strained in Lot 2 FGE while OCP was measured. Transgranular SCC was exhibited, identifiable by the brittle fracture morphology near the outer edge of the sample. Figure 4-8 above, with a ring of brittle transgranular SCC morphology. ....	83

Figure 4-11 Top: A thumbnail-shaped crack in a notched sample strained in Lot 2 FGE containing 6ppm Cl <sup>-</sup> . Bottom: The brittle area showed a transgranular crack morphology. ....	85
Figure 4-12 Optical stereo micrographs of samples strained in lot 2 FGE. OCP was measured (salt bridge was present) during straining of the sample in a). This sample exhibited a continuous ring of transgranular SCC. No electrochemistry was performed during straining of the sample in b).....	86
Figure 5-1 Cyclic polarization scans in commercial virgin FGE (no added inhibitor or denaturant), FGE containing denaturant only (FGE WOI), inhibitor only (FGE WOD) and both inhibitor and denaturant (FGE-S).....	91
Figure 5-2 Percent reduction in area of specimens before and after cracking.....	93
Figure 5-3 Number of cracks per millimeter on specimens strained in FGE in presence and absence of denaturant and inhibitor. Data for SFGE has been added for comparison. ....	93
Figure 5-4 Maximum stress ( $\sigma_{max}$ ) sustained by SSRT specimens in the FGE environments was not affected in a predictable manner by presence of SCC. .	94
Figure 5-5 Surface of tensile samples statically strained in a) FGE-WOI and b) FGE-S. The sample strained in FGE-WOI exhibits localized dissolution at Lüder's bands, areas of high strain accumulation at the surface. ....	95
Figure 5-6 Transgranular SCC seen on polished cross sections of SSRT specimens strained in FGE WOI with (a) 5ppm Cl <sup>-</sup> and (b) 150ppm Cl <sup>-</sup> . Light-colored grains are ferrite, and darker areas are pearlite. ....	97
Figure 5-7 Maximum stress vs. Cl <sup>-</sup> content for SSRT done in FGE WOI with varied levels of dissolved Cl <sup>-</sup> . ....	98
Figure 5-8 A comparison of SCC severity based on %RA and crack densities vs Cl <sup>-</sup> in FGE, FGE WOI, and SFGE .....	99
Figure 5-9 Cyclic polarization in FGE WOI with varied Cl <sup>-</sup> levels .....	100
Figure 5-10 Changes in open circuit potential (OCP) of X65 carbon steel with SFGE water content variations .....	102
Figure 5-11 smooth tensile samples strained to failure in SFGE with a) no added water, b) 1 vol % water, c) 2 vol % water, d) 5 vol% water .....	103
Figure 5-12 %RA and crack density versus water content. At 2% water content, SCC was markedly less severe than in lower water content SFGE, and thus necked to a greater extent before failure .....	104

Figure 5-13 Current measurement during straining in SFGE containing (a) 0.05 vol%, (b) 1 vol%, and (c) 5 vol% water .....	106
Figure 5-14 Enlarged stress vs time plot showing stress at the onset of anodic current for a) anhydrous SFGE, and b) baseline SFGE .....	107
Figure 5-15 Schematic of loading schedule for interrupted SSRT. Samples were loaded to point 1, then unloaded and examined in SEM. The process was repeated on the same sample for points 2, 3, and 4. ....	111
Figure 5-16 SEM images of the I-SSRT sample strained in air. The straining direction was parallel to polishing lines. The numbering corresponds to the specific stress values shown in Figure 5-15. See text for description of images. ....	112
Figure 5-17 SEM images of the I-SSRT sample strained in FGE-WOI (100ppm Cl <sup>-</sup> and 56ppm acetic acid). The straining direction was perpendicular to polishing lines. The numbering corresponds to the specific stress values shown in Figure 5-15. See text for description of images.....	113
Figure 5-18 SEM images of the I-SSRT sample strained in FGE-S (100ppm Cl <sup>-</sup> and 56ppm acetic acid). The straining direction was parallel to polishing lines. The numbering corresponds to the specific stress values shown in Figure 5-15. See text for description of images.....	114
Figure 5-19 Reduction in area vs. chloride content for SSRT in aerated and deaerated SFGE .....	116
Figure 6-1 Current transients measured at two different sampling rates to investigate decay on short and long time scales .....	123
Figure 6-2 Simultaneous potential and current measurements showing a potential drift during introduction of the scratch .....	127
Figure 6-3 Graph of current density vs. time for mechanically scratched X65 steel in SFGE containing 32ppm Cl <sup>-</sup> .....	130
Figure 6-4 Pitting and surrounding corrosion product within scratched region in SFGE containing 32ppm Cl <sup>-</sup> .....	131
Figure 6-5 Pitting within the scratch in deaerated SFGE, 10ppm Cl <sup>-</sup> .....	132
Figure 6-6 Pitting within the scratch in deaerated SFGE, no chloride .....	132
Figure 6-7 Localized corrosion within the scratched region in SFGE containing 5 vol% water .....	134
Figure 6-8 Current transients in alkaline (pHe = 13), neutral (pHe = 5.4), and highly acidic SFGE (pHe = 4.3) .....	134

Figure 6-9 (a) Log-log plots of current transients in selected environments. Linear fitting was performed on the curve in alkaline SFGE (b) Plots of $\text{Log}(i)$ vs $q^{-1}$ .....	138
Figure 6-10 Current transients fitted with equation ( 6-5).....	141
Figure 6-11 Fitted scratch transient data, deconvoluted into dissolution current and film current components. Fraction of surface coverage, $\theta$ , is also displayed. ....	142
Figure 7-1 Topographical AFM scans of the air-exposed coupon surface. The color gradients on the right side of each image correspond to topographical differences in nm. ....	151
Figure 7-2 XPS Fe2p data on surface and after removal of surface layers by $\text{Ar}^+$ sputtering.....	152
Figure 7-3 XPS data of Fe2p on the surface of an X65 "control" sample, polished and exposed only to dry air. Eight peaks are present, representing iron in its un-oxidized state, 2+ and 3+ oxidized states, and oxide satellite peaks.....	154
Figure 7-4 Average binding energy values and assignments as determined from standard reference compounds in literature and the NIST database [88, 93, 144, 146] B.E. values that were very close together were grouped as "mixed iron oxides" in the analysis of X65 surfaces.....	155
Figure 7-5 High-resolution (a) carbon and (b) oxygen spectra from air-exposed X65 surface .....	158
Figure 7-6 C1s signal from air-exposed X65 coupon after brief sputtering time showed rapid attenuation of C1s signal just below surface.....	158
Figure 7-7 Fe2p, C1s, and O1s XPS data from X65 surface after 5-day exposure in baseline SFGE .....	161
Figure 7-8 Fe2p, C1s, and O1s XPS data from X65 surface after 5-day exposure in standard commercial FGE.....	162
Figure 7-9 High resolution iron, carbon, and oxygen spectra from the surface of X65 exposed to acidic SFGE, $\text{pHe} = 4.2$ (left column) and alkaline SFGE, $\text{pHe} = 13$ (right column).....	164
Figure 7-10 AFM images of the X65 coupon surface after exposure in alkaline SFGE.	165
Figure 7-11 High resolution Fe2p, O1s, and C1s spectra from the anhydrous sample (left) and the high water-content sample (right).....	167
Figure 7-12 O1s spectrum of iron ethoxide powder .....	168

Figure 7-13 High resolution Fe2p, O1s, and C1s spectra from the samples exposed to SFGE containing 10ppm Cl <sup>-</sup> (left) and deaerated SFGE (right) .....	170
Figure 7-14 XPS Cl2p depth profile from X65 coupon surface after 5-day static exposure in SFGE containing 10ppm Cl <sup>-</sup> .....	171
Figure 7-15 SEM of X65 sample after exposure to SFGE containing Cl <sup>-</sup> . The top EDS spectrum, taken in the area on a white particle, shows peaks for Cl <sup>-</sup> . The bottom EDS spectrum, taken on the base metal away from the particle, does not show Na or Cl peaks. ....	171
Figure 7-16 Top: SEM image of an X65 coupon after removal from SFGE containing 150ppm Cl <sup>-</sup> . Patches of dried crystalline-looking residue are present on the coupon. Bottom: EDS of the boxed area, indicating presence of Na and Cl in the dried residue. ....	172
Figure 7-17 AFM images of X65 surfaces a) as-polished, b) after 5-day exposure to deaerated SFGE, c) after 5-day exposure to alkaline SFGE, d) after 5-day exposure to SFGE containing 10ppm Cl <sup>-</sup> . Bounded regions are 5μm x 5μm areas selected for surface roughness analysis. ....	174
Figure 7-18 Calculated RMS surface roughness for X65 surfaces after exposure to the given SFGE environment. ....	175
Figure 8-1 Schematic of proposed SCC mechanism. a) straining of the steel leads to b) multiple film rupture events as stress ( $\sigma$ ) exceeds yield. c) Chloride increases anodic dissolution current from film-ruptured sites. Crack extends, which increase stress concentration locally. d) further straining causes exposure of bare steel, which dissolves anodically. Crack walls are able to passivate, maintaining crack geometry. e) Process repeats. ....	185

## LIST OF ABBREVIATIONS

SCC	Stress corrosion cracking
FGE	Fuel grade ethanol
SFGE	Simulated fuel grade ethanol
SEM	Scanning electron microscope
AFM	Atomic force microscopy
XPS	X-ray photoelectron spectroscopy
SSRT	Slow strain rate test
%RA	Percent reduction in area

## SUMMARY

In recent years, the demand for alternatives to fossil fuels has risen dramatically, and ethanol fuel has become an important liquid fuel alternative globally. The most efficient mode of transportation of petroleum-based fuel is via pipelines, and due to the 300% increase in ethanol use in the U.S. in the past decade, a similar method of conveyance must be adopted for ethanol. Low-carbon, low-alloy pipeline steels like X52, X60, and X65 comprise the existing fuel transmission pipeline infrastructure. However, similar carbon steels, used in the ethanol processing and production industry, were found to exhibit stress corrosion cracking (SCC) in ethanol service. Prior work has shown that contaminants absorbed by the ethanol during distillation, processing or transport could be the possible determinants of SCC susceptibility; 200 proof ethanol alone was shown not to cause SCC in laboratory studies. To ensure the safety and integrity of the pipeline system, it was necessary to perform a mechanistic study of SCC of pipeline steel in fuel grade ethanol (FGE).

The objective of this work was to determine the environmental factors relating to SCC of X65 steel in fuel grade ethanol (FGE) environments. To accomplish this, a systematic study was done to test effects of FGE feedstock and common contaminants and constituents such as water, chloride, dissolved oxygen, and organic acids on SCC behavior of an X65 pipeline steel. Slow strain rate tests (SSRT) were employed to evaluate and compare specific constituents' effects on crack density, morphology, and severity of SCC of X65 in FGE. SCC did not occur in commercial FGE environments,

regardless of the ethanol feedstock. In both FGE and simulated fuel grade ethanol (SFGE), SCC of carbon steel was found to occur at low water contents (below 5 vol%) when chloride was present above a specific threshold quantity. Cl<sup>-</sup> threshold for SCC varied from 10ppm in FGE to approximately 1 ppm in SFGE. SCC of carbon steel was inhibited when oxygen was removed from solution via N<sub>2</sub> purge or pHe was increased by addition of NaOH. During SSRT, *in-situ* electrochemical measurements showed a significant role of film rupture in the SCC mechanism. Analysis of repassivation kinetics in mechanical scratch tests revealed a large initial anodic dissolution current spike in SCC-causing environments, followed by repassivation indicated by current transient decay. In the deaerated environments, repassivation did not occur, while in alkaline SFGE repassivation was significantly more rapid than in SCC-inducing SFGE. Composition and morphology of the passive film on X65 during static exposure tests was studied using X-ray photoelectron spectroscopy (XPS) and atomic force microscopy (AFM). Results showed stability of an air-formed native oxide under static immersion in neutral (pHe = 5.4) SFGE, and dissolution of the film when pHe was decreased to 4.3. XPS spectra indicated changes in film composition at high pHe (near 13) and in environments lacking sufficient water. In light of all results, a film-rupture anodic-dissolution mechanism is proposed in which local plastic strains facilitates local breakdown of the air-formed oxide film, causing iron to dissolve anodically. During crack propagation anodic dissolution occurs at the crack tip while crack walls repassivate preserving crack geometry and local stress concentration at the tip. It is also proposed that SCC can be mitigated by use of alkaline inhibitors that speed repassivation and promotes formation of a more protective Fe(OH)<sub>3</sub> film.

## INTRODUCTION

Due to society's rising energy needs, depletion of natural resources, national security concerns and increasing cost of petroleum based fuel, there is an increasing demand for fossil fuel alternatives, especially renewable bio-fuels. Ethanol fuel, specifically, has become a very important renewable fuel source globally; ethanol from corn feedstocks already comprises 3.5% of motor vehicle gasoline in the United States [1], and sugar cane ethanol is the source of more than 45% of automotive fuel in Brazil [2]. Moreover, United States energy bill H.R. 6 [3] mandates that the nation increase its consumption of renewable fuels to 31 billion gallons per year by 2017, with a maximum ethanol capacity of 15 billion gallons of corn-derived ethanol. The remaining quantity must thus be comprised of ethanol from non-corn feedstocks and other renewable fuels; development of ethanol production from cellulosic sources is already occurring [4, 5]. These projected increases in U.S. ethanol production and consumption necessitate the development of an efficient mode of transportation for these fuels. In the U.S., pipelines are the main method used to move fossil fuels and natural gas throughout the country; however, because of material compatibility concerns, ethanol fuels are still transported via energy-intensive tanker trucks and trains. Specifically, stress corrosion cracking (SCC) of low carbon pipeline-grade steels has become a noticeable issue in the U.S. ethanol industry. Several cases of SCC and leaks in carbon steel tanks and piping used in storage and handling of

ethanol fuel (Figure 1-1) were compiled in a 2007 industry survey [6]. Ethanol fuel could potentially have similar damaging effects on carbon steel pipelines. Investigation of SCC mechanisms of pipeline steels is imperative to the implementation of a safe, effective, and economical renewable fuel transportation system.

Corrosion has long been an issue plaguing our nation's infrastructure. Specifically, environmentally assisted corrosion of transportation systems such as pipelines, bridges, and railroads, is costly and can be hazardous if improperly mitigated, causing accidents and even fatalities. According to a 2002 study, corrosion and degradation of transportation infrastructure costs the U.S. \$29.7 billion each year. In 2000, a pipeline failure attributed to corrosion fatigue cracking in Greenville, TX [8] caused approximately 564,000 gallons of gasoline to be released into a nearby river, endangering wildlife and residents of the surrounding area, and wasting valuable fuel. The subsequent cleanup and repairs cost \$18 million. In 1999, environmentally induced cracking caused \$7 million worth of damage from a pipeline rupture in Knoxville, TN [9]. However, if corrosion phenomena are properly detected and controlled, pipelines are the safest and most efficient medium for widespread fuel transport.

In Brazil, one of the leading producers of ethanol fuel from sugarcane since the 1970s, over 500 miles of pipeline infrastructure exists solely for transportation of fuel grade ethanol (FGE) [10]. Stress corrosion cracking (SCC) has not been an issue in these ethanol pipelines, but general corrosion is an issue, and is mitigated by the use of inhibitors. In the U.S., corrosion in petroleum and natural gas-carrying carbon steel pipelines is also well regulated due to the previous research and subsequent development and application of corrosion protection and detection methods in this system. However,

prior to the study detailed in this dissertation, knowledge and understanding of corrosive and cracking effects of fuel grade ethanol on these steels was limited. In general, corrosion and SCC mechanisms in non-aqueous environments is not well-understood, and little research on steel SCC in organic solvents has been reported [10, 11]. The number of research groups investigating the SCC phenomenon in ethanol fuels is small, and much research is necessary before understanding of the mechanisms operating in SCC and corrosion of carbon steels in fuel grade ethanol is achieved. Before the existing American pipeline system can safely and effectively transport ethanol-based bio fuels, much research is needed to identify the effects of FGE on the corrosion and SCC of materials that compose the pipeline system.

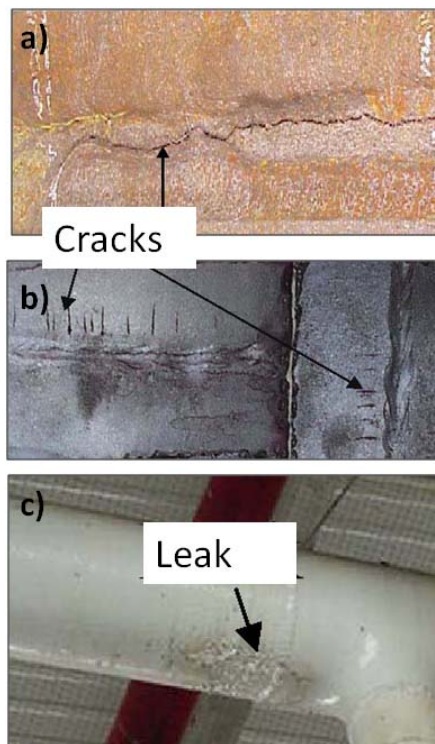


**Figure 1-1 Stress corrosion cracks and leaks in carbon steel equipment in the ethanol industry [6] a) ethanol tank b) welds in air-eliminator vessel c) pipes**

## 1.1 Objectives

The main objective of this research is to further the understanding of the mechanism of stress corrosion cracking of pipeline steel in fuel grade ethanol. The proposed research will help to understand the SCC mechanism in this system and clearly define the environment-related parameters that are important in SCC susceptibility in pipeline steels in fuel grade ethanol solutions, thus enabling the development of strategies for mitigation of this issue. The key technical objectives are to:

1. Investigate the role of fuel grade ethanol composition on the SCC susceptibility of carbon steel, specifically focusing on effects of
  - Variations in ethanol feedstock
  - Common non feedstock-based constituents or contaminants
2. Compare and contrast SCC of commercial fuel grade ethanol with that in simulated fuel grade ethanol solutions
3. Investigate changes in repassivation kinetics and passive film composition of carbon steel with variations in FGE chemistry to further the understanding of the film's role in the SCC mechanism

To achieve these objectives, various techniques were used to test, analyze, and characterize the corrosion and SCC of carbon steel in fuel grade ethanol environments. Slow strain rate tests (SSRT) were employed to evaluate degree of SCC susceptibility in FGE environments.

## 1.2 Organization of Upcoming Chapters

In Chapter 2, an overview of corrosion theory, SCC mechanisms, and prior studies on SCC susceptibility of steels in both aqueous environments and organic solvents will be presented to introduce the reader to the subject and recent research progress on SCC in non-aqueous environments. In Chapter 3, details are given about the material (pipeline steel) and environment (FGE) of study, and all of the experimental techniques and procedures utilized throughout this study. Chapters 4 and 5 detail the findings on effects of feedstock, and contaminants and additives, respectively, on the SCC susceptibility of X65 pipeline steel in FGE and SFGE. Chapter 6 explains effects of specific environmental constituents on corrosion and repassivation behavior of plastically deformed steel, and characterization of the effects of variations in FGE chemistry on X65 passive film composition and morphology is given in chapter 7. In chapter 8, a summary of results and discussion of the relationship of repassivation kinetics and film composition to SCC susceptibility of X65 in FGE environments is presented. Implications of the experimental results for the fuel pipeline industry, as well as potential areas for future study to further advance the knowledge and understanding of FGE SCC of carbon steels are also discussed in chapter 8.

## BACKGROUND

Prediction and proper mitigation of stress corrosion cracking (SCC) of carbon steel pipelines in fuel grade ethanol (FGE) requires an in-depth understanding of the environmental parameters that influence crack initiation and growth in this system. External SCC of buried petroleum pipelines in aqueous groundwater environments is well-characterized [12-17], as is SCC of pipelines used in petroleum production. In FGE and simulated FGE (SFGE) environments, studies have been conducted to evaluate specific environmental constituents on the degree of carbon steel SCC susceptibility [18-20]. There is, however, a need to also determine the existence and nature of feedstock or processing-related compositional variations in commercial FGE and their effect on SCC susceptibility of pipeline steels. Moreover, there is a need for a more in-depth understanding of how specific FGE chemical composition affects the mechanism of pipeline steel SCC.

In this chapter, the SCC phenomenon is described, and details on the material (pipeline steel) and environment (fuel grade ethanol) of interest are explained. Pertinent prior work on SCC of pipeline steel in FGE and non-FGE environments is reviewed.

### 2.1 Stress Corrosion Cracking

SCC is a synergistic failure process that occurs when a specific material is subject to a tensile stress ( $\sigma$ ) while exposed to a specific environment. SCC is characterized by

crack initiation and propagation due to the simultaneous action of chemical (corrosive) and mechanical factors (stresses) where neither factor would lead to cracking independently [21]. This phenomenon is depicted graphically in Figure 2-1, where the environment/material combination of interest is FGE/pipeline steel. Not all materials undergo SCC, but materials that do so are generally only susceptible in a very specific combination of stress and environment conditions. Conditions necessary for SCC are unique for every material/environment combination, and alloys that are susceptible to SCC in one environment may not be susceptible in others [21]. For instance, austenitic stainless steels will undergo SCC when subjected to tensile stresses in chloride-containing aqueous environments above 80°C, but are immune to SCC in the same solution at room temperature [22]. High strength steels are highly susceptible to cracking in H<sub>2</sub>S-containing environments, whereas titanium alloys are most susceptible in chloride-containing media [23].

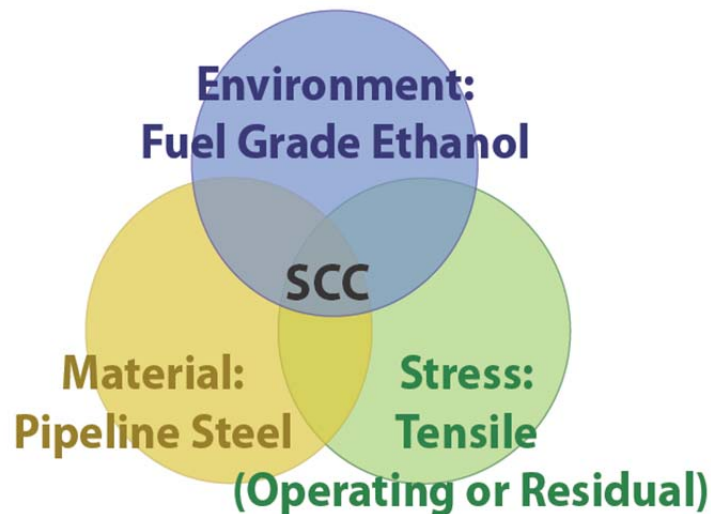


**Figure 2-1 Three factors must be simultaneously present for stress corrosion cracking to occur: A susceptible material must undergo stress in the presence of a specific environment.**

SCC is a delayed-failure process in which cracks initiate and then propagate until stresses in the intact ligaments of the material exceed fracture strength thereby causing

material failure. Once a crack initiates, applied tensile stress becomes intensified locally at the crack tip. The magnitude of stress intensity ( $K$ ) depends on crack geometry and loading conditions. For the crack to propagate, the material must experience a certain level of stress intensity, called threshold stress intensity. Cracks propagate only when local stress intensity meets or exceeds threshold stress intensity ( $K_{ISCC}$ ), which is typically much smaller than the fracture toughness of materials ( $K_{IC}$ ) [21]. This stress level is thought to correspond to the minimum stress required to enable a synergistic material-environment interaction [21]. Stress required for SCC propagation is usually below, but can be above macroscopic yield stress. Often, internal residual stresses from welding or cold work can be sufficient to provide the necessary stress intensity to initiate SCC. Moreover, stress raisers like intermetallic particles or localized areas of corrosion can also cause sufficient stress concentrations for crack initiation. Stress-induced events that can enable such material-environment interaction include, dependent upon the SCC mechanism, the following:

- rupture of a passive film
- sufficient dilation of the grain boundaries to allow solution to enter or hydrogen to become absorbed
- dislocation motion leading to the emergence of a non-passivated slip step

SCC occurs in two stages: Initiation and propagation. SCC initiation most commonly occurs at the material surface exposed to the environment, at sites of local passive film rupture or areas of high stress concentration like pits and metallurgical discontinuities [24]. Stress can become concentrated at the bottom of a corrosion pit to the point where  $K_{ISCC}$  is reached, thus initiating a crack. Strain accumulation at the surface can cause

highly localized film rupture which can also lead to selective dissolution around intermetallic particles, at grain boundaries, or of a specific phase, which is also commonly seen as a mechanism for crack initiation.

Cracks can propagate via tortuous intergranular paths (Figure 2-2 a), or transgranularly through grains (Figure 2-2 b), depending on which metallurgical factors and corrosive processes govern the SCC mechanism. No single mechanism exists which can explain the interaction of stress, microstructure, and environment for all alloy-environment combinations; thus multiple mechanisms have been proposed by researchers for different systems. However, no matter the proposed mechanism, cracks characteristically propagate perpendicularly to the direction of the tensile component of stress.

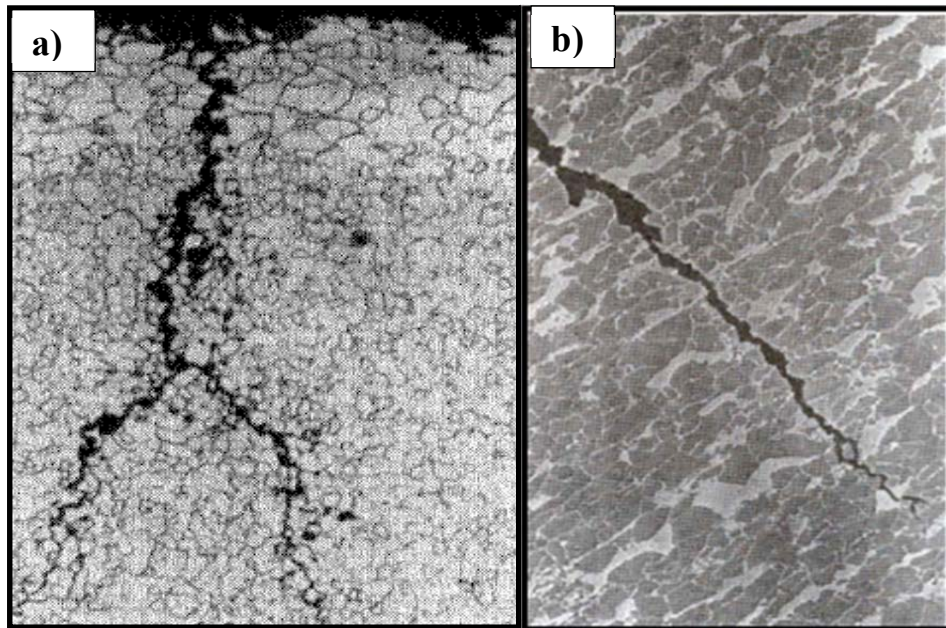


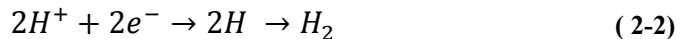
**Figure 2-2 micrographs of a) an intergranular crack path [25]. b) a transgranular crack path [26].**

## 2.2 Corrosion Theory

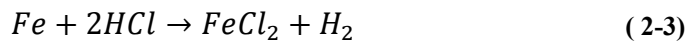
All corrosion processes in metallic materials involve electrochemical reactions. A corrosion cell is a system in which oxidation or reduction reactions occur at the surface of electrodes when immersed in an electrolyte. The change in free energy ( $\Delta G$ ) associated with each reaction determines the direction in which each reaction spontaneously proceeds. Each corrosion reaction can be broken into two half-cell reactions: at least one each of an *anodic* (oxidation) and a *cathodic* (reduction) reaction. These half-cell reactions can take place on two separate surfaces, or on separate areas of the same surface. A metal will often become the *anode*, undergoing an oxidation (anodic) reaction to produce metallic ions and electrons that will flow to the *cathode* and participate in a reduction (cathodic) reaction. For example, if a carbon steel electrode (predominantly iron) were immersed in an aqueous solution of hydrochloric acid (HCl), the anodic half reaction might be:



while the cathodic half reaction would be:



and the resulting full electrochemical reaction:



In this case, iron dissolves anodically, forming iron ions which combine with chloride ions to form a corrosion product ( $FeCl_2$ ). Cathodic reduction of protons in the electrolyte consumes the electrons liberated by iron oxidation and produces hydrogen atoms, which can be absorbed into the iron matrix and lead to its embrittlement, or combine to form hydrogen gas. Half-cell reactions are kinetically coupled because the

rates of combined anodic and cathodic reactions must be equal in order to maintain electric neutrality.

The corrosion cell essentially forms an electrical circuit, and  $\Delta G$  is associated with an electrochemical potential ( $\Delta E$ ).  $\Delta G$  for an electrochemical reaction is inversely proportional to  $\Delta E$ , so this potential difference becomes the thermodynamic driving force for continued anodic and cathodic reactions. Potential of a half-reaction is determined by the activities of reactants participating in the reaction. The most common cathodic reactions in aqueous environments [27], hydrogen evolution,  $O_2$  reduction to form water,  $O_2$  reduction to form hydroxide, metal ion reduction (if multiple valence states, i.e.  $Fe^{3+} + e^- \rightarrow Fe^{2+}$ ), and metal deposition, occur at different potentials depending on reactant availability. For example, potential  $E_{H_2/H^+}$  of the hydrogen reduction half reaction in ( 2-2) is determined by the *Nernst Equation*:

$$E_{H_2/H^+} = E_{H_2/H^+}^0 + \frac{RT}{2F} \ln \frac{[H^+]^2}{p_{H_2}} \quad (2-4)$$

where R is the gas constant, T is temperature in °K, and F is the Faraday's constant,  $E^0$  is the standard potential for the reaction at unit concentration of ions,  $p_{H_2}$  is the partial pressure of hydrogen gas, and  $[H^+]$  is the activity of protons in the electrolyte. At fixed partial pressure of  $p_{H_2}=1\text{atm}$ , potential of the reaction is solely dependent on the pH of the electrolyte. The potential of the anodic reaction in ( 2-1) varies in a similar manner, dependent on the concentration of  $Fe^{2+}$  ions in the environment. Actual cell potential ( $E_{\text{corr}}$ ) will be determined by the *mixed potential*, or sum of the coupled anodic and cathodic reaction potentials. This potential corresponds to a value where the sum of all anodic currents in the cell is equal to the sum of cathodic currents involved. If changes occur in the electrolyte, or if electric current is supplied to an electrode, the electrode

potential is altered and the reaction is said to become *polarized*. Polarization affects the value of potential, and thus  $\Delta G$ , and can alter the direction and kinetics of the spontaneous reaction. For this reason, composition of the environment plays a very large role in corrosion processes. A schematic of the mixed potential concept is given in Figure 2-3. In this schematic, a metal M is in an electrolyte containing Reactant 1 and Reactant 2. If it is assumed that cathodic reaction for reactant 1 dominates, the mixed potential of the metal/electrolyte system will fall at  $E_{\text{mix},1}$  with current density  $i_1$ . If, however, reactant 1 is removed and reaction 2 dominates, the metal becomes polarized to  $E_{\text{mix},2}$ , and current density rises to  $i_2$ .

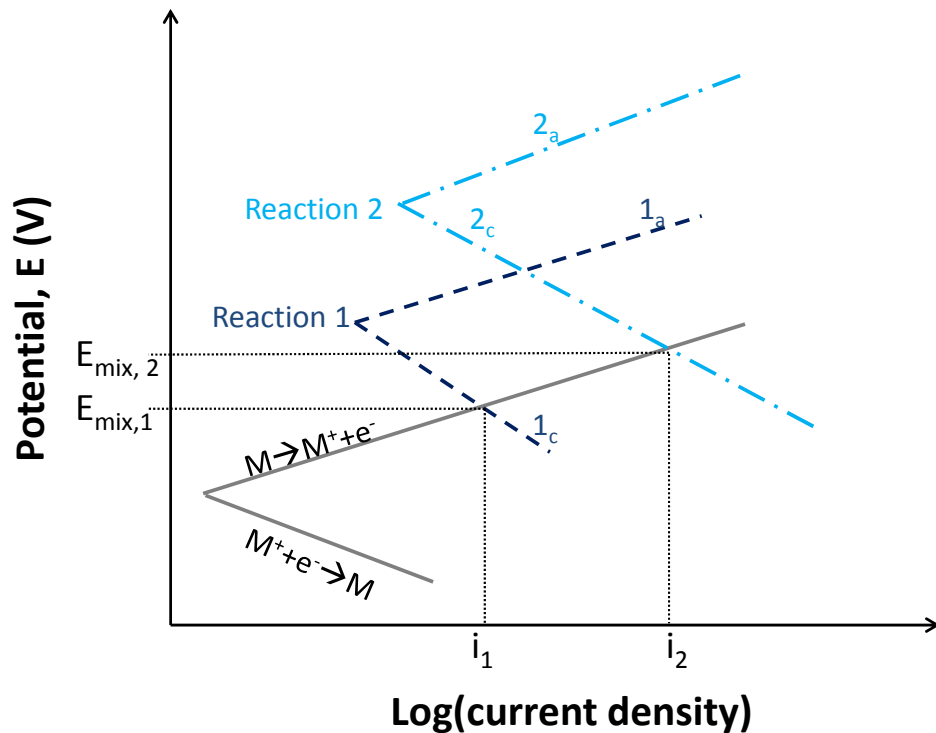


**Figure 2-3 Schematic of mixed potential and polarization resulting from changes in mixed potential on current density.  $1_a$  and  $2_a$  are the anodic portions of half reactions 1 and 2, respectively.  $1_c$  and  $2_c$  are the cathodic portions of the designated half reaction. The metal in solution containing reactant 1 will equilibrate at potential  $E_{\text{mix},1}$ , with corrosion current  $i_1$ . When reactant 1 becomes depleted and reaction  $2_c$  becomes the dominant cathodic reaction, the metal becomes polarized to potential  $E_2$  and reacts at a higher corrosion rate, with a current density,  $i_2$ .**

Corrosion rate is measured by the amount of charge flowing from anode to cathode per unit area of anode (anodic current density,  $i$ ) within the corrosion cell, and it is often desirable to stifle the anodic or cathodic reaction to slow the corrosion process. Often, as a metal becomes polarized,  $i$  rises exponentially as shown in Figure 2-3. However, for some engineering materials in specific environments, the material surface can react to form a protective (passive) film when electrode potential reaches a certain value ( $E_{\text{pass}}$ ). Passive films significantly reduce the corrosion current.

The potentiodynamic polarization test technique can be used to gain information about passive film formation, dissolution rate-limiting steps, localized corrosion, and cathodic and anodic surface reactions. Potentiodynamic polarizations are performed using a potentiostat to vary the potential applied to the working electrode at a specified rate (i.e. 1mV/s) while measuring the resulting current flowing through an external circuit between working electrode and counter electrode. By plotting the electrode potential versus current density ( $i$ ) for an alloy, one can easily see when passive behavior is exhibited. Equilibrium corrosion current density ( $i_{\text{corr}}$ ) of the working electrode can be determined by performing Tafel analysis of a potentiodynamic curve near open circuit potential (OCP). A schematic of an idealized potentiodynamic curve is depicted in Figure 2-4. The data shows a negative slope below OCP ( $E_{\text{OCP}}$ ), indicating cathodic behavior at potentials below OCP. Above  $E_{\text{OCP}}$ , a positive slope indicates increasing anodic behavior until  $E_{\text{pass}}$  is reached. Above  $E_{\text{pass}}$ , the material exhibits a passive property, indicated by a resistance to anodic dissolution as current remains constant while potential is raised. At significantly higher anodic potentials, a transpassivity occurs wherein a new reaction is activated or passivity otherwise becomes unstable, and active anodic reactions occur. As

potential is decreased from the transpassive region, in some cases the current density does not decrease and the curve exhibits hysteresis indicating that pitting or localized corrosion is occurring in that particular alloy/environment system. These areas of local passivity breakdown can, however, repassivate if potential is lowered to the protection potential ( $E_{\text{prot}}$ ).

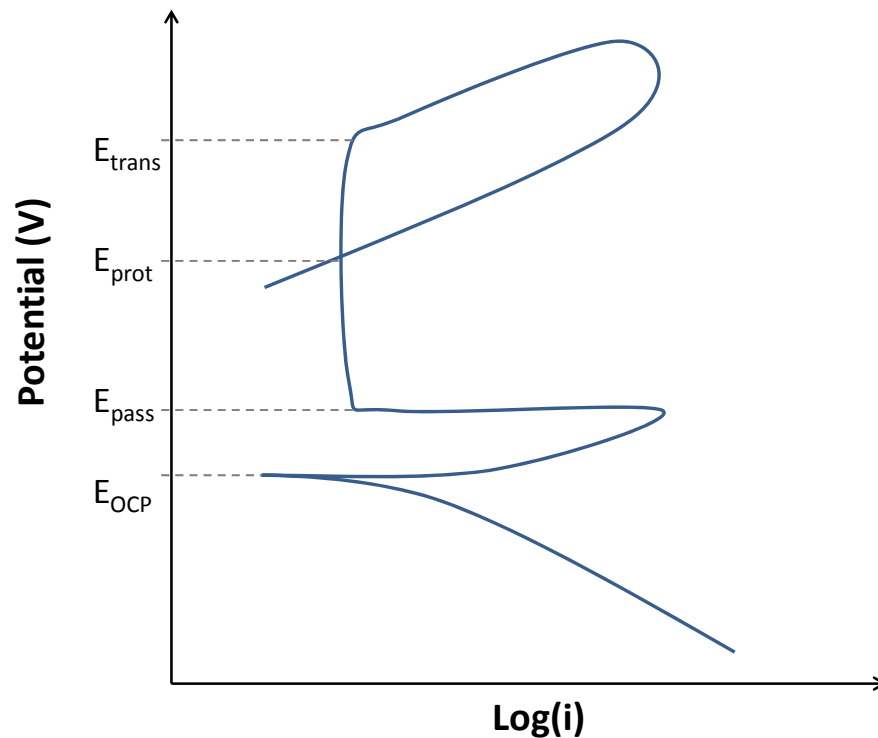


**Figure 2-4 Schematic of an idealized potentiodynamic polarization curve displaying several important values that can be obtained using the potentiodynamic scan technique.**

Potential-pH (Pourbaix) diagrams can be utilized to predict the thermodynamic stability of chemical species that can form at a specific potential and pH for a given metal/environment system [28]. The diagrams define regions of immunity, active dissolution, or passivation of an alloy under specific conditions. The Pourbaix diagram

for iron (Figure 2-5) shows regions of environment pH and electrode potential that will lead to formation of a stable passive film ( $\text{Fe}(\text{OH})_2$  or  $\text{Fe}(\text{OH})_3$ ), active dissolution ( $\text{Fe}^{2+}$  or  $\text{Fe}^{3+}$ ), or immunity to corrosion ( $\text{Fe}$ ).

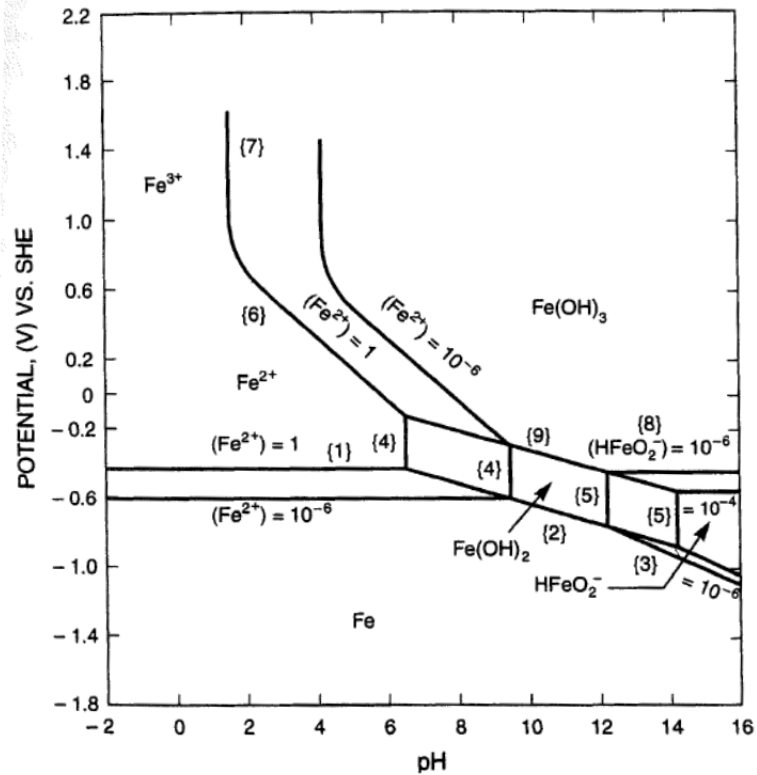


Figure 2-5 Pourbaix diagram for iron showing regions of stable passivity, active dissolution, or corrosion immunity based on electrode and electrolyte pH [29]

### 2.3 SCC Mechanisms: Interaction of Corrosion and Stress

Because corrosion or electrochemical processes play a large role in SCC, common SCC mechanisms are broken into two categories: 1) anodic and 2) cathodic. There are two main commonly theorized anodic mechanisms, and one main cathodic mechanism. The two anodic mechanisms involve crack propagation by dissolution from bare metal

exposed when a protective film is ruptured by applied stress. For instance, in austenitic stainless steels, sensitization leading to growth of chromium carbide precipitates and thus chromium-depleted zones at grain boundaries, can facilitate intergranular SCC (IGSCC) [21] because stable passivity is highly difficult to achieve where Cr is not present, thus continuous anodic dissolution occurs at grain boundaries as applied stresses facilitate entry of solution between grains. Segregation of phosphorous to grain boundaries in low-alloy steels leads to IGSCC in nitrate solutions for a similar passivity-related reason [30]. The most prevalently accepted cathodic mechanism is hydrogen embrittlement, wherein production of hydrogen inside a crack leads to adsorption and diffusion and trapping of H atoms into the material matrix leading to embrittlement ahead of the crack tip. In the case of mild steels in simulated groundwater environments, a transition from IGSCC mode to transgranular, or cleavage-like SCC (TGSCC) mode is observed when pH shifts from alkaline to near-neutral and the steel is polarized toward cathodic values [31]. In this case, TGSCC is attributed to a cathodic mechanism where ingress of hydrogen into the steel leads to embrittlement ahead of the crack path. Not all transgranular SCC occurs by cathodic mechanism, nor does IGSCC by anodic mechanism. Commonly proposed SCC mechanisms are explained in more detail below.

### **2.3.1 Anodic SCC mechanisms**

The two anodic mechanisms are: 1) Film rupture-anodic dissolution, and 2) slip-step dissolution. In the film rupture/anodic dissolution model of SCC, crack initiation occurs because of anodic dissolution of the metal upon exposure to the environment due to rupture of the material's passive film. A schematic of this mechanism is shown in Figure 2-6 (a). The crack tip generally remains active under the influence of stress while

the crack walls passivate, because the rate of generation of bare metal surfaces at the crack tip where stress is concentrated is greater than the repassivation rate. This continuous anodic dissolution from the crack tip results in crack extension. In the slip dissolution model, which differs from the film rupture model in that a passive film is able to form on the crack tip, dissolution occurs as a result of repeated re-rupture of the film as slip steps emerge due to continuous application of stress. Discontinuous crack growth is observed in this mechanism, and is depicted in Figure 2-6 (b). In this mechanism, film rupture contributes to the propagation of a crack solely as a rate-limiting step in the anodic dissolution process.

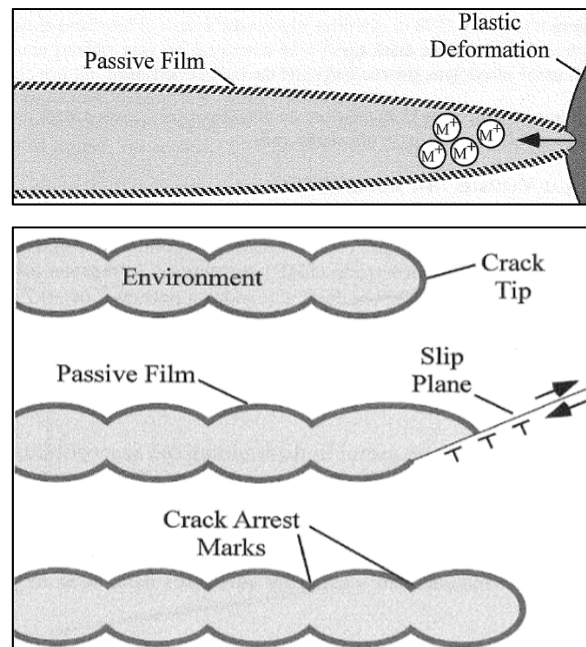


**Figure 2-6 In the film rupture model, SCC propagation occurs because of active dissolution from the crack tip, which can (a) remain un-protected due to plasticity ahead of the crack tip, or (b) intermittently re-passivate leading to discontinuous crack propagation [21]**

### 2.3.2 Cathodic SCC mechanisms

Cathodic SCC mechanisms generally involve the cathodic reduction of water or protons to form atomic hydrogen or hydrogen gas. These types of SCC often occur in systems that are under external cathodic protection, thus facilitating the cathodic reaction and quickening the production of hydrogen as in ( 2-2). Tensile stresses on the metal dilate the metal matrix, allowing the hydrogen to diffuse into interstitial sites and other defects within the bulk, where atomic hydrogen creates internal stresses by pinning dislocations or combining to form hydrogen gas and expanding. These internal stresses contribute to strain hardening, causing the alloy to become more brittle, and thus increasing susceptibility to cracking. Typically, if a hydrogen embrittlement mechanism is active, microcracks will appear in the bulk material just ahead of the main crack tip, as shown in Figure 2-7.

Another hydrogen-related SCC mechanism occurs when hydride formation is possible. In the case of Ni coatings deposited under cathodic polarization in an  $H_2SO_4$  environment, it was demonstrated that unstable Ni hydrides could form at grain boundaries [32]. Formation and decomposition of these hydrides caused expansion and contraction of the Ni matrix, resulting in extremely high residual internal stresses and leading to cracking of the coatings. A similar phenomenon was observed in high-nitrogen containing austenitic stainless steels [33]. This hydride-related cracking phenomenon is associated with long-duration cathodic charging in which hydrogen evolution is the prominent cathodic reaction.

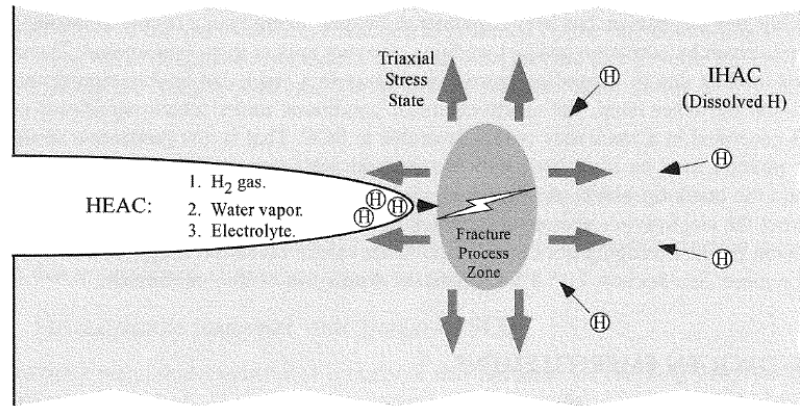


**Figure 2-7 Schematic of SCC caused by a hydrogen embrittlement mechanism. The image depicts atomic hydrogen migrating into the region of high stress concentration ahead of a crack tip where it will pin dislocations, increasing triaxial stress and facilitating crack propagation [34]**

### **2.3.3 Role of corrosion and surface film formation in anodic SCC**

For SCC to occur, thermodynamic and kinetic conditions must be met, and environment plays a large role in both thermodynamic and kinetic aspects of SCC. For this reason, electrolyte composition can be a very significant factor controlling SCC for a given alloy. In anodically-controlled SCC mechanisms, dissolution or oxidation of the metal and its dissolution into the electrolyte must be thermodynamically feasible [21]. Additionally, a dissolution-inhibiting film must be thermodynamically stable for crack geometry to be maintained. In most proposed anodic SCC mechanisms, a stress concentration acts to repeatedly rupture this film at the crack tip, or prevent the tip from fully repassivating, resulting in crack growth due to intermittent or continuous dissolution of the exposed metal at the tip. If the passive film is stable and quick-forming, dissolution will be prevented or insufficient and no cracking will occur (Figure 2-8 (I)). To maintain a high stress concentration at the crack tip, a high aspect ratio must be maintained, thus dissolution activity from crack walls must become limited while that at the tip remains

rapid (Figure 2-8 (II)). If the environment is such that a passive film does not form or repassivation is very slow, the crack walls undergo dissolution at higher rates than the crack tip causing cracks to blunt, as there will no longer be a sharp tip where stresses can concentrate (Figure 2-8 (III)). For this reason, the potential ranges in which anodic SCC would likely occur, shown in gray in Figure 2-9, are usually within a transition region between active and passive behavior [21, 35]. However, the polarization behavior of the bulk alloy in the bulk electrolyte may not fully describe corrosive processes within the crack.

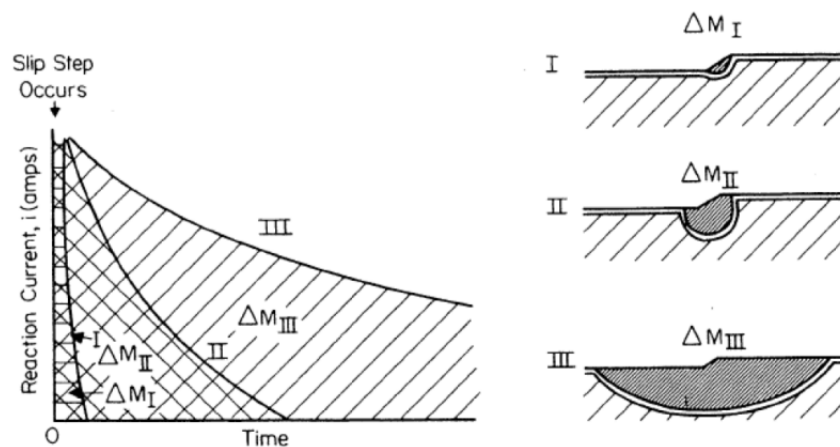


**Figure 2-8** A schematic depicting the relationship between current flowing after film rupture and SCC susceptibility. (I) depicts rapid repassivation. (II) intermediate repassivation resulting in SCC, and (III) lateral dissolution which blunts the crack [35]

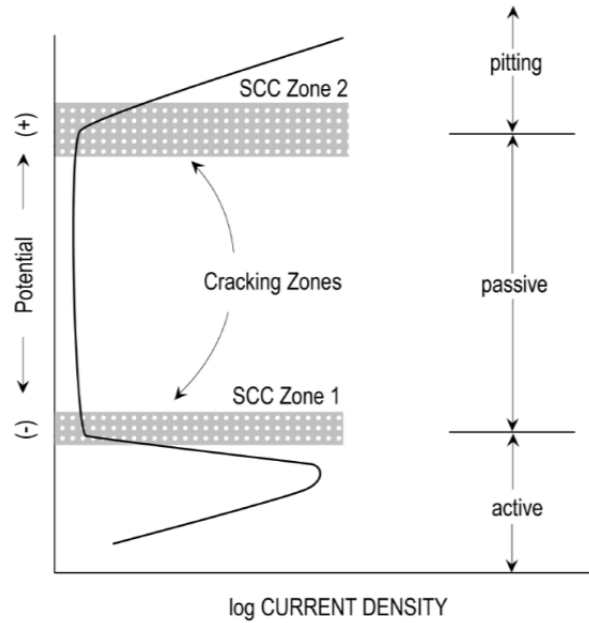


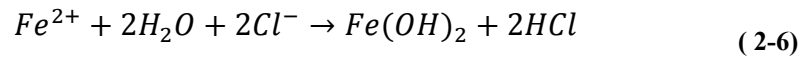
Figure 2-9 Schematic of polarization behavior of an active passive alloy. Ranges of SCC susceptibility are shaded in gray. [35]

### 2.3.4 Role of crack tip chemistry

Many researchers propose that because the occluded geometry of a crack restricts mass transport between the bulk environment and the solution within the crack, impurities and dissolution-enhancing species become concentrated within the occluded crack area, making the electrolyte within the crack differ significantly from the bulk electrolyte [36-39]. It is commonly thought that the crack tip becomes deaerated as oxygen near the tip is rapidly reduced, providing the cathodic reaction that supports anodic dissolution. For a surface crack in carbon steel in aerated neutral seawater, iron dissolution according to eq. ( 2-1) will provide the anodic reaction and reduction of oxygen to produce hydroxide ions will provide the cathodic reaction:



As the crack advances, electrons produced by iron oxidation are immediately consumed in reduction of oxygen, which eventually becomes depleted due to the occluded confines of the crack. An excess of positive iron ions attracts negatively charged  $Cl^-$  ions into the crack, which react together with water:



significantly lowering pH and accelerating dissolution [26, 34] which propagates the crack. Acidification and hydrolysis within a crack can also lead to cathodic reduction of protons ( $H^+$ ) on crack walls, which can embrittle the alloy if absorbed into the matrix near the crack tip, facilitating crack propagation by brittle cleavage. Experimental evidence exists indicating that the concentration of  $Cl^-$  ions within a pit differs from that in the bulk solution, and that potential gradients may exist between the mouth of a crevice and the innermost crevice area [37]. During in-situ microscopic observation of active pits and crevices researchers noticed the evolution of gas bubbles ( $H_2$ ) even when potentials applied to the bulk metal were out of the range of  $H_2$  evolution [40], indicating that potential conditions within the pit differed significantly from the bulk.

## 2.4 Testing for SCC Susceptibility

Several varieties of tests exist to evaluate alloys' stress corrosion cracking susceptibility. Statically-stressed specimens in constant-strain (fixed displacement) or constant load configurations can be good for comparing resistance to SCC of multiple alloys or a single alloy in multiple environments. Tests involving slow dynamic loading, on the other hand, allow consistent quantitative comparison of SCC susceptibility in less time than the static test methods. One such dynamic test is a slow strain rate test (SSRT).

Static, constant-strain tests like U-bend, bent beam or C-ring tests are inexpensive and require simple setups to execute. A failed U-bend specimen is depicted in Figure 2-10. Standardized testing methods have been developed for both of these specimen configurations [41, 42] to facilitate repetition and comparison of test results among laboratories. U-bend specimens are plastically strained and held in the deformed configuration while exposed to the environment of interest. Because the U-bend test is a very severe test, it is generally most useful for qualitatively determining obvious differences in SCC resistance of 1) multiple alloys in a single environment, 2) one alloy in several environments, or 3) different metallurgical configurations of one alloy in a specific environment [21]. Stress conditions in U-bend specimens are difficult to replicate accurately, thus results of U-bend tests are not generally used for quantitative assessment of SCC.

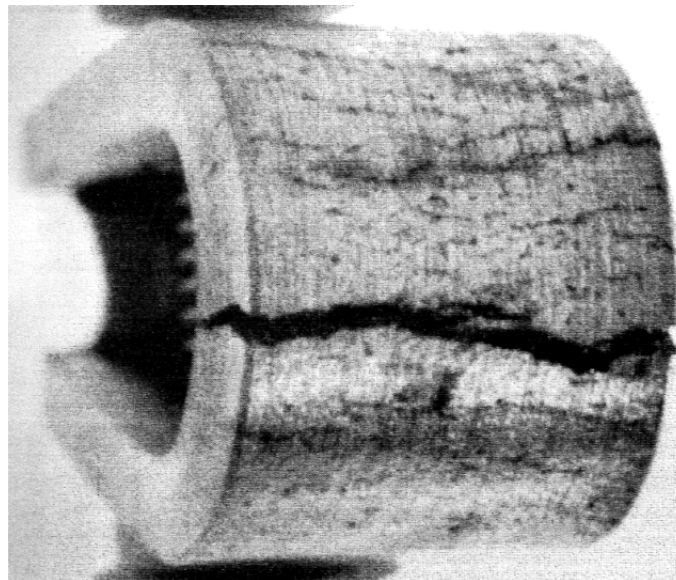


**Figure 2-10 Failed U-bend specimen [43]**

C-ring and other bent-beam specimens can be used in cases where cracking behavior under elastic strain conditions is of interest. The C-ring configuration, shown schematically Figure 2-11, can be stressed in a constant strain or a constant load condition, depending on the configuration of the test. C-ring testing is an efficient way to determine the SCC susceptibility of tubing where circumferential stresses are of interest. However, C-ring specimens can require long exposure times, sometimes multiple weeks, before SCC evaluation is possible.

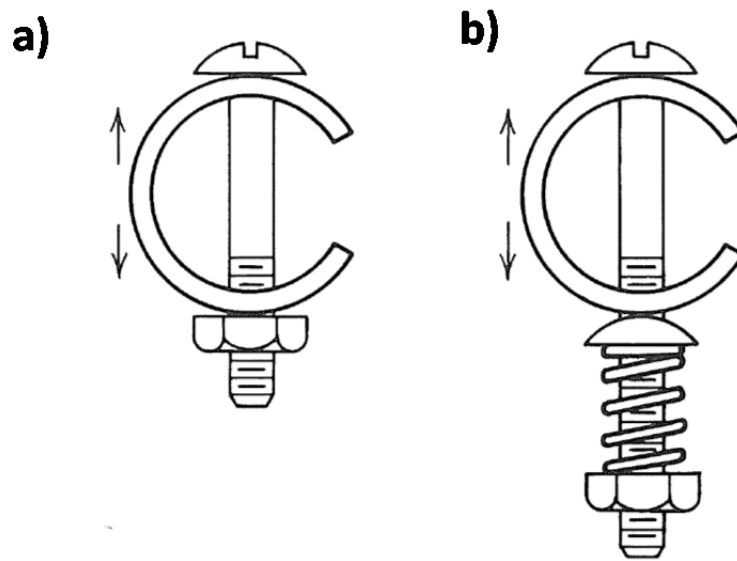


**Figure 2-11 C-ring test specimens for a) constant strain, and b) constant load testing [21]**

The dynamic SSRT method has been established as an efficient, effective method of obtaining data on crack initiation and propagation processes and evaluating material susceptibility to environmentally assisted cracking in specific environments [21, 44] . These dynamic tests provide quantitative comparison of SCC and require far less time than static test methods. In a SSRT, a tensile sample of the material is placed in a cell

containing the environment of study, and placed in a loading rig where the bottom of the sample is clamped in a fixed position, and the top of the sample attached to a crosshead controlled by a tunable velocity motor. The dimensions of the tensile sample follow guidelines laid out by the ASTM standard for tension testing of metallic materials [44]. The crosshead speed is set at a desired value depending on the initial strain rate required for tests. Although the extension rate is constant, the strain rate experienced by the sample does decrease with extension of the gauge. Load on the sample is continuously measured by a load cell. An example of a SSRT apparatus can be seen in Figure 2-12.

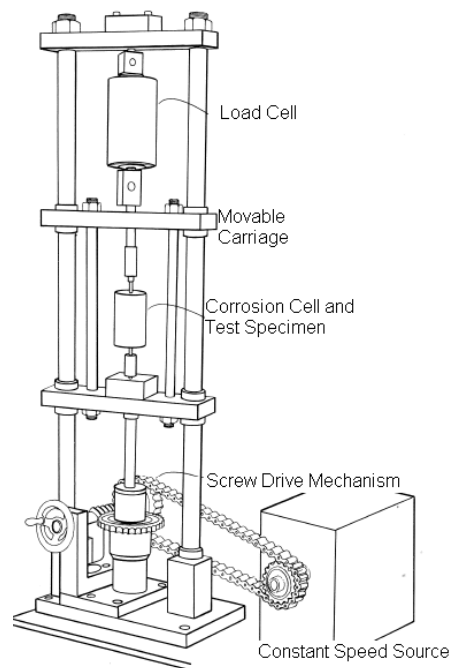


**Figure 2-12 Slow strain rate testing apparatus [45]**

In the anodic dissolution mechanism of SCC, it has been shown that film rupture on the crack tip can be a rate-limiting step in crack propagation [46]. Since strain is the controlling factor between film rupture events, strain rate determines whether cracks will

achieve a high aspect ratio and continue to propagate as a stress corrosion crack. If strain rate is too high, creep ahead of crack tip material can cause crack blunting, and the material will likely fail in a ductile manner, not allowing time for environmental interaction to cause SCC. However, if the strain rate is too low, the crack tip will re-passivate faster than the film breakdown rate, which will lead to insufficient dissolution to extend a crack. Straining at the correct rate, however, will provide valuable data on SCC initiation and propagation modes. Dynamic testing using continual application of strain, as in SSRT, helps maintain optimum creep rates at the crack tip so crack propagation mechanism can be accurately assessed.

## **2.5 SCC of Pipeline Steel in FGE**

The mechanisms and reactions proposed above were developed in aqueous environments. The environment of interest in this study is a non-aqueous organic solvent. Properties of the environment are described below, and existing literature on corrosion and SCC mechanisms in organic solvents is reviewed in this section.

### **2.5.1 Fuel grade ethanol environment**

The ethanol molecule,  $C_2H_5OH$ , is a polar molecule. Ethanol is protic, i.e. capable of proton dissociation, and easily dissolves acids, as well as organic and inorganic species by dipole-dipole and ion-dipole forces [47]. Ethanol is also hygroscopic. If left in an open container at room temperature in a humid environment, the water content of ethanol will increase rapidly over time [19]. Properties of ethanol are compared with those of DI water in Table 2-1.

**Table 2-1 Select properties of ethanol and ultrapure water**

<b>Solvent</b>	<b>Polar</b>	<b>Dielectric Constant</b>	<b>Protic</b>	<b>Resistivity (kΩ-cm)</b>	<b>NaCl solubility (mass fraction)</b>	<b>O<sub>2</sub> solubility (mM fraction, 298K, 1atm) [48]</b>
<b>Ethanol</b>	Y	24.3	Y	12.9	0.055 [49]	0.56
<b>Water (DI)</b>	Y	80	Y	1.2	26.5 [50]	0.0228

Pure 200-proof (anhydrous) ethanol alone does not lead to SCC of carbon steel in SSRT [6, 11]. Fuel ethanol, however, is a multi-component system that may include acids, water, denaturant, and dissolved oxygen, and thus may contain the oxidizing, or corrosive, species as a solute [47]. FGE composition can vary due to different production processes and ethanol feedstocks, or impurities in ethanol can be produced by degradation reactions [47], possibly caused by a reaction with a metallic material [51]. Furthermore, ethanol is an excellent solvent, and because of this, FGE may absorb contaminants during production, processing, and transportation. It is thought by many [47, 52, 53] that these trace impurities and organic constituents are the major causal factors of SCC.

Preliminary studies on FGE SCC [19, 20] demonstrated that corn-based “producer” ethanol (un-denatured ethanol from an ethanol production plant before transport), caused less severe stress corrosion cracking than “user” ethanol (fuel-ready ethanol from a holding tank or blending station) from the same corn feedstock, indicating that during transportation and processing, the ethanol might have undergone compositional changes affecting its corrosiveness. However, these effects could also be due to impurity pickup during transportation. The specific alterations to the FGE environment that led to SCC in the presence of user ethanol but not in producer ethanol

have not been determined. Possible impurities include a range of organic and inorganic compounds, such as water, carboxylic acids, ketones, sulfates, chlorides, and others, and it is difficult to pinpoint which, of these many possible combinations of species present in FGE, may affect SCC in pipeline steels in FGE solutions.

Fuel grade ethanol is produced by distillation and fermentation of sugars from various sources such as corn, sugarcane, algae and switchgrass. Researchers in Brazil identified and characterized organic impurities in a Brazilian FGE from sugarcane [54] using a gas chromatography-mass spectrometry (GC-MS) technique. Compounds such as saturated linear hydrocarbons, ketones, aldehydes, and alcohols were detected. A GC-MS spectrum from this experiment is shown in Figure 2-13. However, many of the detected compounds are oxidation products of ethanol, implying that they may not have been present from distillation, but might have formed during production. Additionally, presence of these compounds varies qualitatively as well as quantitatively, depending on ethanol batch. The effects of these trace organic species on carbon steel SCC are not known and thus must be investigated.

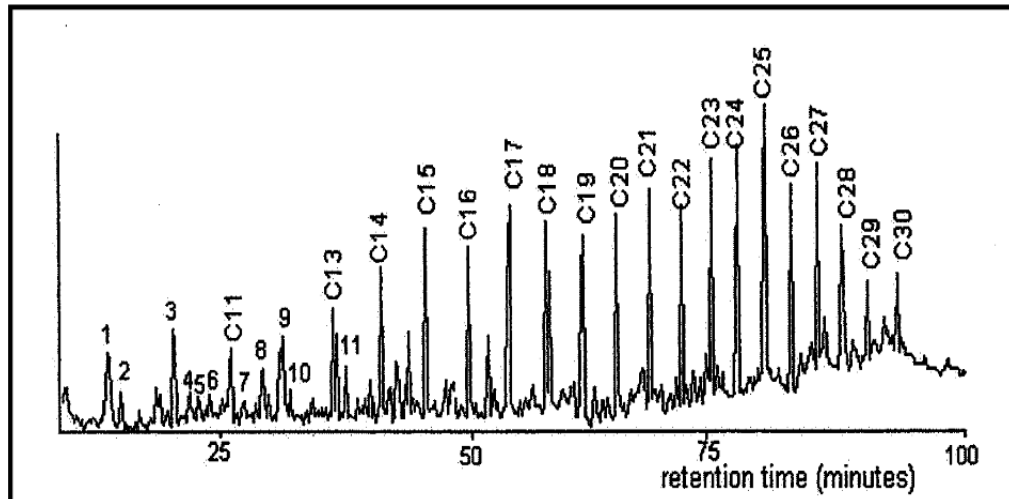


Figure 2-13 GC-MS Spectrum of Brazilian FGE [54]

ASTM international published a standard regulating allowable levels of certain common FGE constituents, which are displayed in Table 2-2. This regulatory standard only takes into consideration the chemicals which may interfere upon combustion of the fuel, and does not account for all compounds present in FGE in liquid form. However, it is liquid FGE that contacts carbon steel pipeline surfaces, and is thus the substance of interest in SCC studies.

Table 2-2 ASTM Specifications for Chemical Content of FGE [55]

Contaminant	Minimum	Maximum
Ethanol, volume %	92.1	
Methanol, volume%		0.5
Solvent-washed gum, mg/100L		5.0
Water, volume%		1.0
Acidity (as acetic acid) mg/L		0.007
pHe	6.5	9.0
Inorganic chloride mg/L		10
Sulfur, mg/L		30
Sulfate, mg/L		4
Copper, mg/kg		0.1
Denaturant	1.96	5.0

## 2.5.2 Pipeline steel

Pipelines are typically constructed from grades of low carbon steel, ranging from X42 to a recently developed X100, in compliance with specifications imposed by The American Petroleum Institute in Table 2-3 [56]. Most existing pipelines for liquid petroleum fuels are made out of X52, X65, or X70. Desirable properties of pipeline steels include high strength and toughness to withstand high operating pressures, good corrosion resistance, and field weldability [57]. These properties can be achieved by varying composition and microstructure. Alloying elements like manganese, sulfur, and phosphorous contribute to the weldability and formability of the steel [56].

**Table 2-3 Specifications for Alloying Content of Pipeline Steels [56]**

Steel	Maximum wt %					Minimum Yield Stress		Minimum UTS	
	C	Mn	S	Ti	P	Ksi	MPa	Ksi	MPa
<b>X52</b>	0.28	1.40	0.03	0.04	0.03	52	358	66	455
<b>X65</b>	0.26	1.40	0.03	0.04	0.03	65	448	77	530
<b>X70</b>	0.22	1.65	0.03	0.06	0.03	70	482	82	565
<b>X80</b>	0.22	1.85	0.03	0.06	0.03	80	551	90	620

The microstructures of pipeline steel vary with grade. Older steels such as X46 and X52 were manufactured under fewer regulations on alloying content, and tend to contain higher percentages of solutes like C, S and Mn. X60 and X65 steels produced by conventional hot rolling have coarse-grained banded ferrite and pearlite microstructures [57]. Grade X80 steels are subject to thermomechanical rolling and accelerated cooling, producing microstructures of fine-grained ferrite and bainite. Cooling low carbon steels at an accelerated rate produces an uncontrollable amount of martensite [57] which is

undesirable in pipeline steel because it decreases weldability, increases brittleness, and induces internal stresses within the steel.

### **2.5.3 Corrosion and electrochemistry in organic solvents**

Corrosion behavior of metals and alloys in ethanol and other organic solvents differs from that of aqueous solutions and is not as well understood. Minor additions (on the order of  $10^{-4}$ M) of acids, water, or chloride to organic solvents produces significant variation in pitting and corrosion rate whereas such small concentrations of such solutes generally do not significantly affect aqueous corrosion. Some studies have been performed on general corrosion of iron steels in ethanol [19, 47, 52, 58, 59], and organic solvents similar to ethanol, such as methanol [47, 52, Banas, 1987, 60], dimethylformamide (DMF) [47, 53], propylene carbonate [61, 62] and isopropyl alcohol [52].

Electrochemical studies on effects of added water and chloride ions on the corrosion behavior of pure iron in a methanol-0.5M  $H_2SO_4$ -0.1M  $H_2O$  solution remained in a state of active dissolution, but when more water was added to the solution, electrochemical data showed that the iron surface formed a stable passive film [63] (Figure 2-14). Similar studies on iron in neutral methyl, ethyl, isopropyl, n-butyl and 2-chloroethyl alcohols [52] revealed that in completely anhydrous methanol, iron does not undergo an active/passive transition.

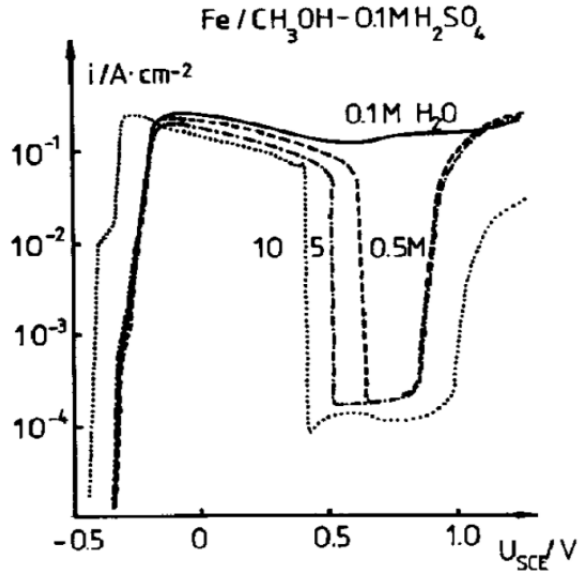


**Figure 2-14 Anodic polarization curves for iron in MeOH-0.1M H<sub>2</sub>SO<sub>4</sub> solution with varying water content. Increasing water content decreased  $E_p$  and increased stable passivity [63]**

In two-, three-, and four-carbon chain alcohols, corrosion current density increased with water concentration [52]. It was proposed that water forms a chemisorbed monolayer on the electrode surface, producing a difference between concentration of water at the metal/solution interface and that in the bulk solution. Thus, chemical content of a bulk ethanol solution can differ greatly than that at the metal surface. This phenomenon of inhomogeneous distribution of water in ethanol was reported in a letter to Nature in 2002 [64]. Researchers commented on their observations of incomplete mixing in water/alcohol solutions, stating that neutron diffraction experiments interpreted by the empirical potential structure refinement model showed that local ordering of methanol molecules was modified by small additions of water. In a 70% methanol- 30% water mixture, it was expected that most water would exist as isolated water molecules, but radial distribution function data showed three-molecule clusters or strings of two to twenty molecules. Results of a low-frequency Raman spectroscopy study on clustering

behavior in ethanol-water binary solutions by Egashira et al. [65] supported the Nature article findings that, on a molecular level, ethanol-water binary solutions are not ideally mixed but are in a state of microscopic phase separation. This clustering effect is expected to influence the ethanol/steel interface and the corrosion behavior of carbon steel when water is present in FGE even in minute amounts.

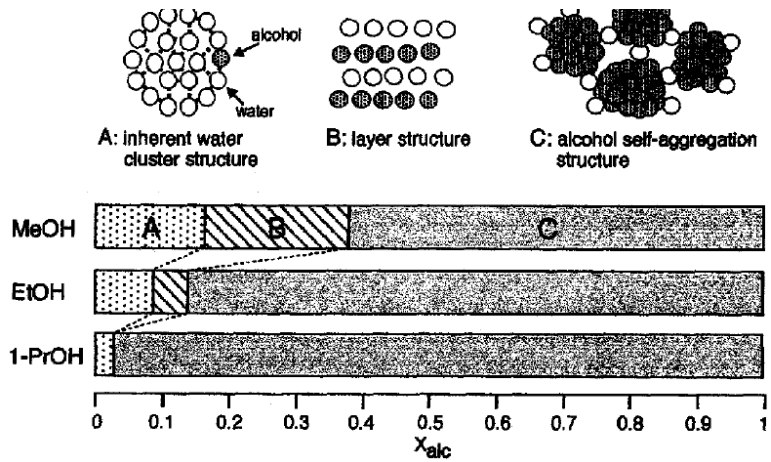


Figure 2-15 Schematic illustrating the structure of alcohol-water solutions based on the mole fraction of alcohol ( $X_{alc}$ ) present. Clustering decreases as carbon chain length increases [66]

Brossia and Kelly performed a systematic investigation of the role of chloride, acidity, sulfate, water, and combinations of these factors on corrosion behavior of iron in methanol. These particular species were chosen because of their presence in commercially available methanol fuels [60], and are very similar to constituents found in other alcohol-based biofuels, particularly ethanol [55]. Species added to the solution had effects on corrosion individually as well as synergistically. The most dramatic effects resulted from additions of 1mM acid, shifting corrosion rate by an order of magnitude and corrosion potential anodically by 200mV. This increase in corrosion rate was not

seen when 0.5% water was added to the acidic methanol, demonstrating the ability of water to inhibit acid attack on the iron surface. The researchers concluded that water decreased the mobility of  $H^+$  ions due to preferential protonation of water over methanol. Data from these studies confirmed evidence found in other studies of the inhibiting effects of water in organic solvents containing acid.

The recent findings of SCC in steel ethanol fuel holding tanks and equipment has prompted research on the corrosive effects of FGE. Sridhar et al. performed electrochemical polarization tests in SFGE to evaluate the effects of additions of water, acetic acid, corrosion inhibitor, chloride, methanol, oxygen, denaturant, and galvanic coupling on X65 pipeline steel corrosion, keeping levels of all contaminants within those deemed acceptable by the ASTM standard [19]. The presence of dissolved oxygen and water in the solution led to dramatic changes in polarization behavior of the steel [19, 20]. Maximum anodic current density, which can be linked to corrosion rate, increased with increasing water content up to 2000ppm, then decreased with subsequent water addition.

In other recent studies in SFGE it was demonstrated that pitting corrosion occurred on pipeline steel surfaces in aerated SFGE solutions containing 5 vol% water [59]. When oxygen was completely removed from solutions by deaeration, pit density and pit size were drastically reduced but overall dissolution of the ferrite phase was observed. This illustrates the effects of the presence of both oxygen and water on the severity and morphology of corrosion of pipeline steel in SFGE solutions. Data on corrosion of steels in organic solvents indicates that small amounts of water and acid greatly affect steel corrosion rate and passivation behavior. Water can inhibit

corrosion in the presence of an acid, and intensify corrosion when acid is absent [67]. Additionally, presence of chloride ions can increase corrosion rate and decrease stability of passive films formed. The composition of FGE differs from that of SFGE due to the presence of organic and inorganic species from distillation and processing. Characterization of the effects of these impurities and trace additives in FGE on passivation and general corrosion behavior of pipeline steel has not been performed; hence effects of the constituents of FGE on steel corrosion and passivation must be examined. Investigation on corrosion of pipeline steel corrosion behavior in actual FGE solutions done in the present study has provided clues pertaining to film formation and pitting that will prove invaluable in determination of the mechanism of SCC in an FGE environment.

## **2.5.4 SCC of pipeline steel**

### **2.5.4.1 SCC in aqueous environments**

Fuel transmission pipelines comprised of carbon steel are often buried underground where the groundwater environment can create a corrosive environment for the steel. As a result, external SCC of pipeline steels in aqueous environments has frequently been a research topic of interest. As pipelines are generally buried underground, the outer surface of the pipeline can be exposed to near-neutral pH (NNpH) groundwater environments or high pH aqueous environments. NNpH SCC occurs in groundwater containing a dilute solution of bicarbonate ions and carbon dioxide [15], and the cracking mode has been characterized by many researchers [24, 68, 69] as transgranular. High-pH SCC is linked to the formation of highly concentrated carbonate/bicarbonate solution with pH 9.5 to 12.5 [24] and generally propagates

intergranularly. Chu et al mentioned that X65 pipeline steel in NNpH environments is prone to general corrosion and formation of tiny surface pits, and that these pits are likely to be SCC initiation sites [24]. Cyclic loading tests were done on X65 pipeline steel in an NNpH environment, which were accelerated versions of actual pressure fluctuations seen in a pipeline over a 20-year service life. Results showed crack initiation primarily at corrosion pits, at grain boundaries, and in areas of the steel where there were residual stresses (banded microstructures). Preferential crack initiation and propagation was also found in pearlitic colonies. Crack propagation was transgranular. Parkins and Zhou did systematic studies looking at the effects of pH and environmental chemistry on the nature of SCC in carbon-manganese steel and found that the type and severity of cracking was dependent on pH and concentration of ions in solution [31]. Asher and Singh looked at the possibility of effects of hydrogen production in the NNpH groundwater environment on cracking of X65 pipeline steel [15], and indeed found evidence of hydrogen ingress into the steel at open circuit potential, indicating contributions of hydrogen embrittlement to NNpH SCC.

In summary, these findings in aqueous solutions imply a general trend in SCC of low carbon steels: SCC initiation, propagation mode, and severity are dependent on environment pH and chemistry as well as residual stresses in the steel, localized corrosion on the steel surface, and microstructural phases.

#### 2.5.4.2 SCC in fuel grade ethanol

Failures caused by internal SCC in certain carbon steel tanks and piping used in storage, transportation, and distribution of corn-based ethanol fuel, have become an issue for the ethanol industry. Studies aimed at determining what types of environmental

conditions lead to SCC in FGE have been published [6, 19, 70, 71-75], yet there remains a large gap in knowledge of the SCC mechanism of pipeline steels in ethanolic biofuels. The API survey [6] noted that there were no reported cases of SCC in equipment at ethanol manufacturing plants, nor in facilities handling 10% and 85% ethanol/gasoline blends. Results of the research by Sridhar et al. [19] supported the survey's findings, further stating that the carbon steel tested exhibited a notably higher corrosion potential in corn-derived “producer” ethanol, i.e. ethanol obtained directly from the manufacturer with no denaturants added, than in denatured fuel-ready “user” ethanol procured from a holding tank, indicating that SCC would happen more readily in user ethanol, or moreover that the SCC was caused by a change in the composition of the FGE environment from user condition to producer condition.

Research on simulated fuel grade ethanol (SFGE) solutions, comprised of pure reagent-grade ethanol and varied additives based on compounds regulated by the ASTM standard for ethanol fuel (Table 2-2) on pipeline grade carbon steels has been systematically evaluated [18, 19]. Specifically, effects of water, oxygen, and pH variations on SCC of pipeline steels were studied. However, effects of organic constituents in commercial FGE, possibly due to feedstock- or processing-based differences, have not yet been considered in depth. It was concluded that oxygen content was one of the factors that most affect corrosion rate; however, the role of oxygen in the SCC mechanism of carbon steel in FGE was not described. There are several possibilities to explain why oxygen may be detrimental to steel in FGE solution; one theory is that the ethanol will oxidize into organic byproducts such as acetaldehyde or ethyl esters of organic acids; organic solvents tend to chemically degrade or change when in the

presence of an oxidant or proton donor [47]. These intermediate oxidation products of ethanol can then turn into organic acids, lowering the pH of the solution and enhancing corrosion. It is also hypothesized that the oxygen plays a role in formation of a brittle oxide on the steel surface that ruptures when stress is introduced into the material in a FGE environment. When the film ruptures, fresh metal is exposed to solution where it anodically dissolves until another oxide film forms, propagating a crack in the steel.

Pourbaix diagrams of iron in acid-containing and pure ethanol (Figure 2-16) were developed using a previously developed mixed solution electrolyte model to establish stability fields of iron compounds in ethanol containing different impurities [19]. These diagrams are often useful for predicting thermodynamics of corrosion in a particular system [28]. However, the theoretical film compositions were not experimentally verified.

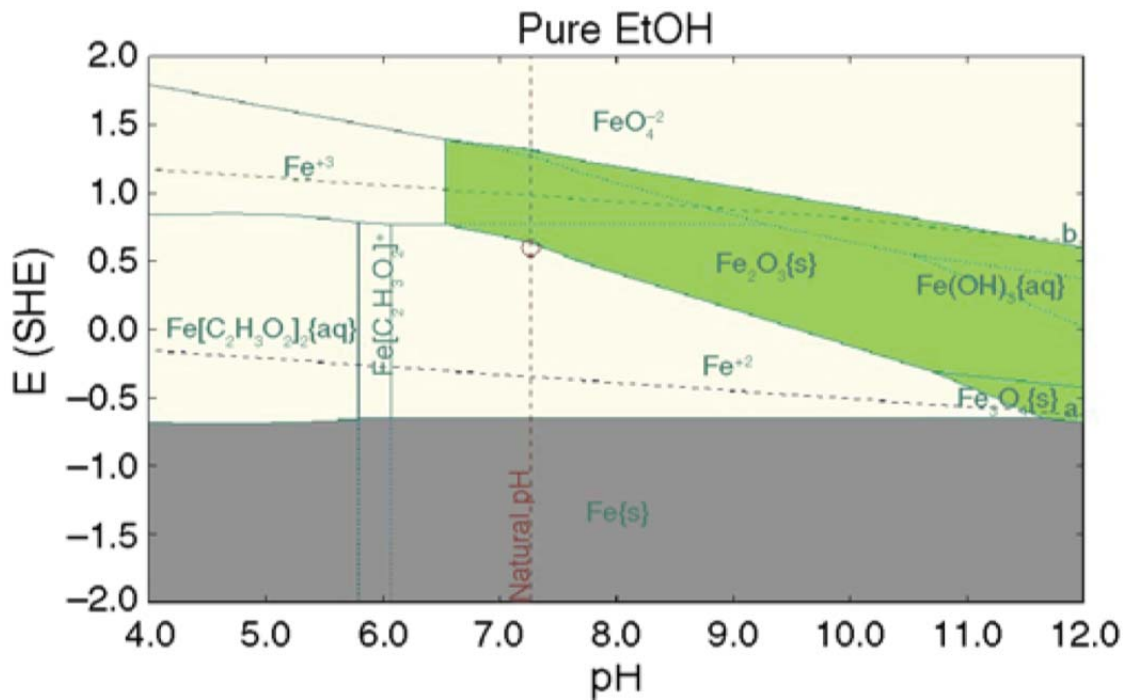


Figure 2-16 Pourbaix diagram for iron in pure ethanol [19]

Oxide formation in ethanol is very different from that in water, as can be seen in this diagram. The researchers determined that adding water to ethanol will shift the stability fields and make iron oxide stable over a larger range. According to their results, the presence of other selected impurities did not alter the thermodynamics of passivation, but did shift the pH of ethanol to more acidic values [76].

In the very recent past, several studies have surfaced geared toward finding a more in-depth mechanistic explanation of FGE SCC [18, 51, 59, 77-79]. Based on findings from these studies, the SCC mechanism is unlikely to be a cathodic one [51], therefore finding evidence in support of the anodic dissolution/film rupture mechanism and creating a more detailed mechanistic picture will be the main focus of the research reported in this dissertation.

## MATERIALS AND METHODS

### 3.1 Pipeline-grade Carbon Steel

The materials studied in this project are low carbon, pipeline-grade steels. X60 and an X65 steel were obtained from out of service pipelines. Compositions of the two steels are listed in Table 3-1. Both steels have a ferrite-pearlite microstructure, shown in Figure 3-1. The X60 steel was only utilized in fabrication of notched tensile specimens for slow strain rate tests, described below in section 3.3. For all other tests, X65 steel was the material of study.

**Table 3-1 Composition of pipeline steel test materials (\*Nominal, \*\*Analyzed)**

Steel	C wt%	Mn wt%	P wt%	Al wt%	S wt%	Si wt%	Other wt %	Fe wt %	Yield Stress		UTS	
									Ksi	MPa	Ksi	MPa
<b>X60*</b>	0.28	1.40	0.03	-	0.03	-	Ti, 0.04	Bal	60	414	75	517
<b>X65**</b>	0.08	1.26	0.01	0.041	0.002	0.24	--	Bal	69	478	81	561

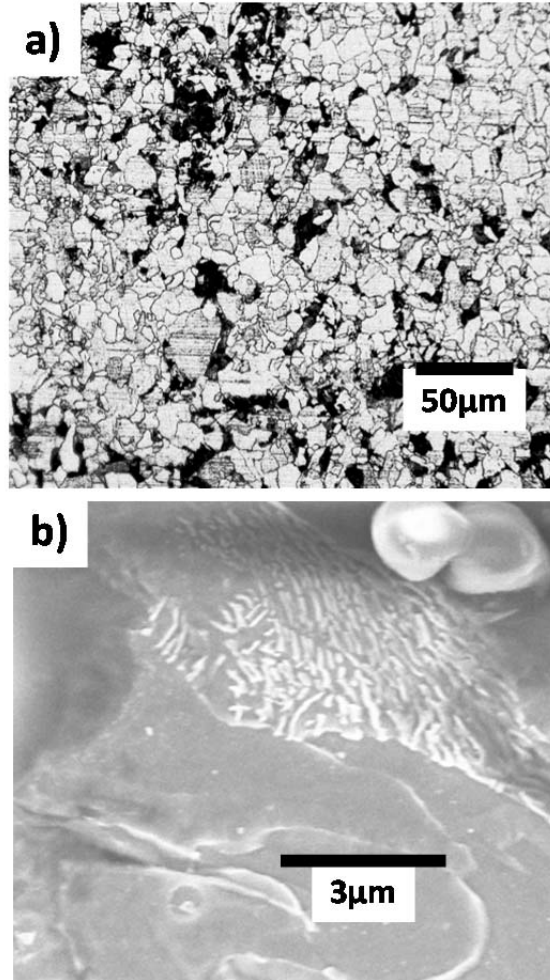


Figure 3-1 Microstructure of as-received X65 pipeline steel. a) Lighter-colored grains are ferrite; dark areas are pearlite. b) High magnification image of a pearlite grain. Lighter-colored lamella are cementite, darker are ferrite.

## 3.2 Test Environments

### 3.2.1 Fuel grade ethanol

In order to investigate effects of variations in ethanol feedstock and production conditions, eight different samples of commercial fuel grade ethanol (FGE) were obtained. Samples were given names of Lot 2 through 9. In experiments described within this dissertation, the different FGE will be referred to by lot number, e.g. Lot 2 or Lot 7.

These commercial FGE samples were obtained from commercial suppliers located in the U.S., Brazil, and Canada, and were produced from various feedstocks including:

- Wet milled corn
- Dry milled corn
- Sugarcane
- Cellulose

In preliminary studies done on SCC susceptibility of carbon steels in FGE [6, 19], a specific trend was noticed: SCC issues were prevalent in what are commonly called “user” facilities, and not in so-called “producer” facilities [6]. The latter are facilities in which ethanol is distilled from the desired feedstock and has not yet been altered by transport or additions of inhibitors or denaturants, while the former are those that process and handle ethanol that is fuel-ready and generally contains inhibitors, denaturants, and contaminants absorbed during transport from the producer facilities. User ethanol may also remain in holding vessels for long periods of time. For this reason, among the obtained commercial FGE samples there were corn-based ethanol samples from producers before being shipped, or from user terminals where they are ready to be blended into gasoline for automotive use.

A total of eight commercial ethanol samples were received and used in SCC susceptibility testing. Table 3-2 lists the nomenclatures given to the FGE samples, feedstock, distillation process, along with producer/user classification if known. These samples were utilized for investigating the dependence of inherent organic constituents or trace contamination due to feedstock, processing, and transport on SCC and corrosion behavior.

Samples were shipped and stored at 4°C. The ethanol was brought to room temperature before use in tests. Ethanol samples were stored in identical 5-gallon containers to control any variations in storage conditions that might alter the ethanol composition. Ethanol is hygroscopic, thus water content can rise if the ethanol is not properly stored. Similarly, decomposition of ethanol into ethyl aldehyde or ketones is possible in small amounts in the presence of oxygen; therefore, it was necessary to store all samples in identical conditions.

**Table 3-2 List of commercial ethanol samples received with feedstock, production process, and producer/user classification information**

<b>Sample name</b>	<b>Feedstock</b>	<b>Process</b>	<b>Ethanol received from</b>
Lot 2	Corn	Dry milled	Producer
Lot 3	Corn	Wet and dry milled (mix)	User terminal where SCC was previously reported
Lot 4	Corn	Wet and dry milled (mix)	User terminal where SCC was previously reported
Lot 5	Corn	Wet mill	Producer
Lot 6	Corn	Dry mill	Producer
Lot 7	Sugarcane	Unknown	Unknown- imported from Brazil
Lot 8	Corn	Dry mill	Producer
Lot 9	Cellulosic	unknown	Producer

To enable comparison of effects of FGE common additives like inhibitor and denaturant on SCC of pipeline steel without varying feedstock, three additional samples of ethanol were obtained, all from the same producer as Lot 5. These were identical to

Lot 5 except that one was FGE with no added inhibitor or denaturant (Virgin FGE), one contained denaturant only (FGE-WOI), and one contained inhibitor only (FGE WOD).

Ethanol that is blended with gasoline in the United States is regulated by the ASTM Standard Specification for Denatured FGE [55], which lists allowable constituents and their respective allowable quantities (see Table 2-2). It is important to note, however, that this standard regulates FGE composition for purposes of blending and minimization of combustion products, and was not meant to govern corrosion or material compatibility with FGE.

### 3.2.2 Simulated fuel grade ethanol

There are potentially many factors affecting the composition, and thus the corrosiveness, of commercial FGE, including feedstock, processing, transportation, storage, additives, etc. To control for these factors in some experiments a simulated fuel grade ethanol (SFGE) was utilized to create a more standardized environment, based on ASTM D 4806 [55], containing maximum levels of methanol, water, and acetic acid as dictated within the standard. SFGE solutions were synthesized using reagent-grade chemicals, including an undenatured 200-proof ethanol, ACS grade anhydrous methanol (EMD chemicals), glacial acetic acid (J.T. Baker), ultrapure deionized water, and pure NaCl and NaOH (>99% pure).

**Table 3-3 Composition of baseline simulated fuel grade ethanol used in this study**

<b>Ethanol (vol%)</b>	<b>Methanol (vol%)</b>	<b>Water (vol%)</b>	<b>NaCl (mg/L)</b>	<b>Acetic Acid (mg/L)</b>
98.5	0.5	1.0	10	56

In experiments where SFGE was used, the term “baseline SFGE” refers to SFGE with the composition in Table 3-3. In many cases, the SFGE composition was altered by addition of one or more of the following: water, chlorides, acid or alkaline, or removal of air.

### **3.2.3 Ethanol chemical analysis**

Several analytical techniques were utilized throughout these studies to determine and verify the chemical composition of test solutions. Water content was determined by Karl Fischer titration method using an Aquastar V1B KF Titrator. The reagent used was EMD chemicals Comp Star 5. pHe was measured according to ASTM 6423 standard for determination of pHe of ethanol [80]. Capillary ion electrophoresis (CIE) was used to quantify  $\text{Cl}^-$  and  $\text{SO}_4^{2-}$  ion content. Concentrations of metallic cations, such as iron and sodium, were determined by inductively coupled plasma spectroscopy (ICP).

A gas-chromatography mass-spectroscopy (GC-MS) technique was used to detect trace organic constituents. GC-MS was performed using a HP5890 gas chromatograph equipped with a HP5971A mass detector. A J&W (Agilent) 60 meter DB5 column was used for analyte separations. FGE samples were prepared for GC-MS by mixing 1mL of FGE with 5 $\mu\text{L}$  of an internal standard containing 3.9mg/mL myristic acid methyl ester. The mixture was evaporated under  $\text{N}_2$  at 50°C, and then 25 $\mu\text{L}$  N-methyl-n(trimethylsilyl)trifluoroacetamide (MSTFA) was applied to the residue. This mixture was capped and heated at 50°C for 30 minutes for derivatization. GC-MS was performed both on the derivatized mixture and directly on the FGE sample. The GC-MS program commenced at 50°C and was ramped to 75°C at 1°C/min. It was held at 75°C for two minutes, then ramped to 300°C at 10°C/min and held for 20 min. Analysis of the first

two samples revealed that no significant impurities could be found upon direct analysis of the sample, so only the derivatized samples were analyzed for the remaining lots of FGE.

### 3.3 Slow Strain Rate Tests (SSRT)

#### 3.3.1 Test specimen design

Two types of SSRT specimens were used in this research: notched and smooth. Samples were designed according to the guidelines in ASTM E8 and G129 [44, 81]. Samples were cylindrical, with a 1" (25.4mm) gauge section in which the diameter was reduced from ¼" (6.3mm) to 1/8" (3.2mm). Smooth specimens (Figure 3-2) were identical to the notched specimens except that the notched specimen contained a u-shaped groove in the center of the gauge region (Figure 3-3).



Figure 3-2 Smooth slow strain rate test specimen (scale bar in inches)

Stress concentration factor for the notched tensile samples,  $K_t$ , was calculated according to the following formula [82]:

$$K_t = C_1 + C_2 \left( \frac{2h}{D} \right) + C_3 \left( \frac{2h}{D} \right)^2 + C_4 \left( \frac{2h}{D} \right)^3 \quad (3-1)$$

where  $h$  is the notch depth, and  $D$  is the diameter of the sample gauge, shown in Figure 3-3.  $C_1$  through  $C_4$  are calculated based on  $h/r$  ratio, according to the formulas given in Figure 3-4. Measurements of these parameters were made via optical microscope

and Clemex image analysis software prior to testing. The value of  $K_t$  fell between 2.9 and 3.1 for all samples tested.

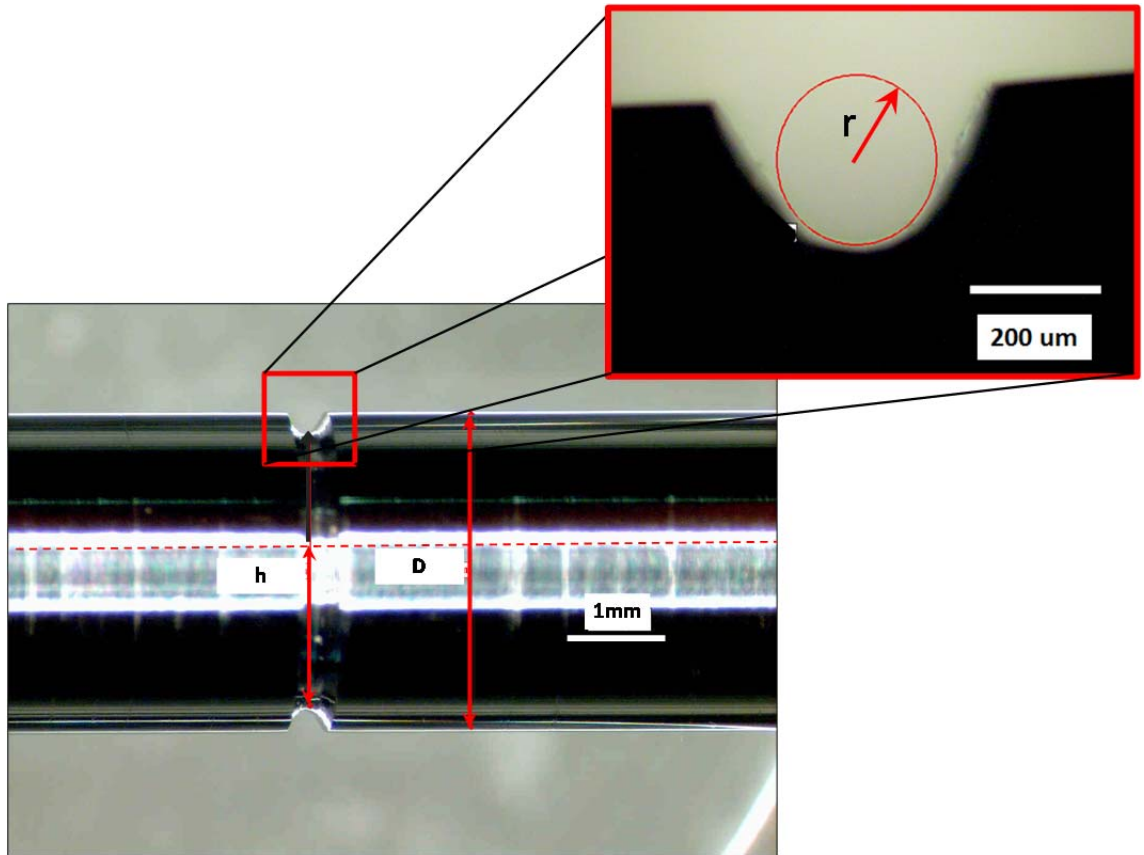


**Figure 3-3** Close-up of the notched portion of the notched SSRT samples. The sample diameter ( $D$ ), sample radius at the notch ( $h$ ), and notch root radius ( $r$ ) were measured using Clemex image analysis software. These parameters were used to compute initial stress concentration factor at the notch.

**Table 3-4 Calculation of constants C<sub>1</sub>, C<sub>2</sub>, C<sub>3</sub>, and C<sub>4</sub> for calculation of K<sub>t</sub> (from [82])**

	$0.25 \leq h/r \leq 2.0$	$2.0 \leq h/r \leq 50.0$
C <sub>1</sub>	$0.455 + 3.354\sqrt{h/r} - 0.769(h/r)$	$0.935 + 1.922\sqrt{h/r} + 0.004(h/r)$
C <sub>2</sub>	$3.129 - 15.955\sqrt{h/r} + 7.404(h/r)$	$0.537 - 3.708\sqrt{h/r} + .040(h/r)$
C <sub>3</sub>	$-6.909 + 29.286\sqrt{h/r} - 16.104(h/r)$	$-2.538 + 3.438\sqrt{h/r} - 0.012(h/r)$
C <sub>4</sub>	$4.325 - 16.685\sqrt{h/r} + 9.469(h/r)$	$2.066 - 1.652\sqrt{h/r} - 0.031(h/r)$

### 3.3.2 SSRT procedures

The procedures for notched and smooth-sided SSRT specimens were identical. The tensile specimens were placed into an environmental cell, consisting of glass tubing sealed on top and bottom by grooved PTFE flanges (Figure 3-4). The upper flange contained ports for gas inlet and outlet, sample, and counter and reference electrodes for the option of performing in-situ electrochemistry. The SSRT cell with electrochemistry set-up is shown in Figure 3-6. Details on electrochemical measurements are given in the next section.

The sample/cell assembly was threaded into grips and connected to the mechanical testing rig. The test solution was funneled into the cell and gas purge commenced. All gases were purged through a dessicant trap and a flask containing the test solution to trap any impurities and moisture in the gases before they bubbled into the test cell. The outlet gas was sent into a final test-solution trap to prevent evaporation during testing. Samples were elongated at a constant extension rate until failure. Extension rates varied from 5E-7 in/s to 1E-6in/s.

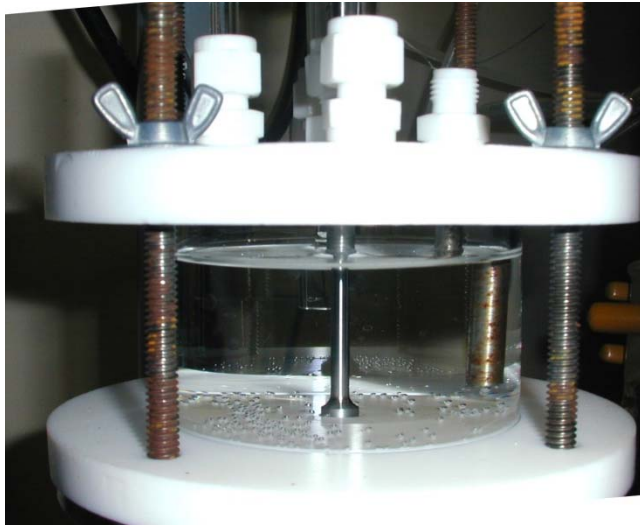


Figure 3-4 Environmental cell for slow strain rate testing in FGE

### 3.3.3 Metallography, Fractography, and visual characterization

Visual analysis of failed SSRT specimens was performed using a Nikon Optiphot-2 optical microscope. Higher magnification observation was performed using a Leo 1530 field emission scanning electron microscope (SEM) or a Hitachi S-3700N VP SEM. Both SEMs were equipped with energy dispersive spectroscopy (EDS) detectors, which were utilized for compositional analysis of microstructural features or corrosion products.

For examination of crack path, crack length and density, failed SSRT specimens were hot-mounted in Bakelite and polished down to a 0.05 $\mu$ m finish with an Al<sub>2</sub>O<sub>3</sub> suspension, then etched with a 2% Nital solution. Crack length was measured using Clemex image analysis software that had been calibrated with optical standards. Fracture surfaces of failed specimens were examined in SEM to characterize failure mode (brittle, ductile) and crack morphology (intergranular, transgranular).

Percentage reduction in cross sectional area (%RA) from initial SSRT specimen to failed specimen is a criterion commonly used to evaluate and compare SCC severity of SSRT specimens [44]. %RA was calculated for all smooth-gauge SSRT specimens by dividing the area of the fracture surface by the pre-test cross-sectional area of the specimen. Fracture surfaces were consistently elliptical in shape, so fracture surface area was determined as specified in ASTM E8 [81] by measuring the widest and narrowest dimension of the surface at 10X magnification, then using the formula for ellipse area:

$$A_{ellipse} = \pi ab \quad (3-2)$$

where 2a and 2b were the measured lengths of the widest and narrowest dimensions of the fracture surface, respectively (Figure 3-5). Reduction in area ratio (RRA) was also calculated as the ratio of %RA of a sample strained in an FGE environment to %RA of a control sample strained in air.

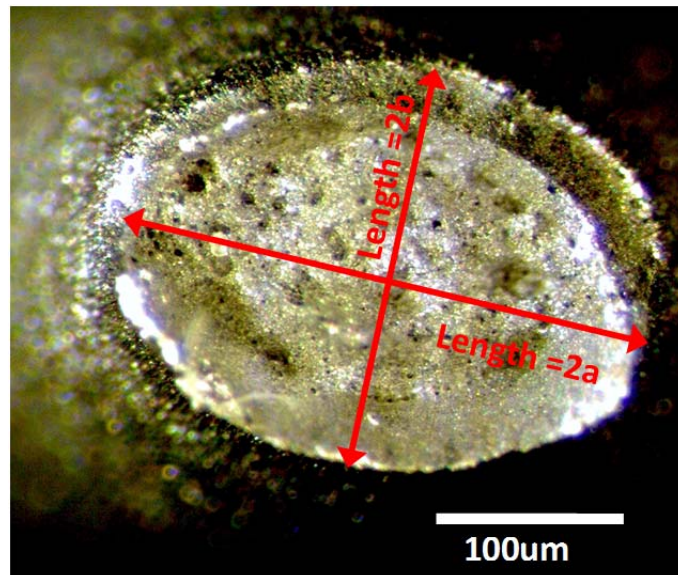


**Figure 3-5 Elliptical fracture surface of a smooth SSRT specimen. Widest and narrowest dimensions were used to calculate area of the fracture surface for comparisons of % area reduction of samples strained in varied SFGE and FGE environments.**

Crack density (number of cracks per unit length of a failed specimen) was evaluated by counting the cracks present on the polished cross section of the failed SSRT sample over a length of 1cm from the fracture surface.

### **3.4 Electrochemical Measurements**

Potentiostatic current monitoring, potentiodynamic polarization, and open circuit potential monitoring were the electrochemical techniques most commonly employed in this study to characterize electrochemical corrosion behavior of pipeline steel. Electrochemical measurements were carried out using a three-electrode assembly commonly employed in corrosion testing. X65 steel samples served as the working electrode, while a small piece of platinum foil or platinum mesh was used as a counter electrode. The reference electrode was a silver-silver chloride electrode with a 1M LiCl-ethanol solution as the electrode buffer. This type of reference electrode configuration was first used by Brossia and Kelly and filled with a methanol-LiCl solution for use in a methanol electrolyte [60], and has become common for electrochemical measurements in non-aqueous alcohol-based solutions [18, 19, 74, 78, 83]. The electrode was fabricated by forming silver chloride on the pure silver wire surface by galvanostatically polarizing the wire with a current of  $0.4\text{mA}/\text{cm}^2$  in 1M HCl aqueous solution for two hours. A porous Vycor frit was fitted onto the end of a glass body to serve as a salt bridge between reference solution and test solution. The AgCl-coated silver wire was placed into the glass electrode body, which was then filled with 1M LiCl-ethanol solution (Mettler Toledo) and sealed with a rubber septum (Ace Glass). A gamry reference 600 potentiostat was used for all electrochemical testing over the course of this study.

Electrochemical experiments were performed in either a round-bottomed glass flask with five ports or in the sealed glass and PTFE SSRT cell (Figure 3-6). X65 samples were ground with wet SiC paper to 1000 grit, then subject to a final dry polishing step with 2000 grit paper. Samples were measured for accurate calculation of surface area and current density, then rinsed and ultrasonically cleaned in acetone prior to insertion into the electrochemical cell.

Conductivity of the ethanol solutions was measured using a Cole Parmer 19100-20 conductivity meter. Conductivity measurements were verified using electrochemical impedance spectroscopy measurements with the Gamry potentiostat.

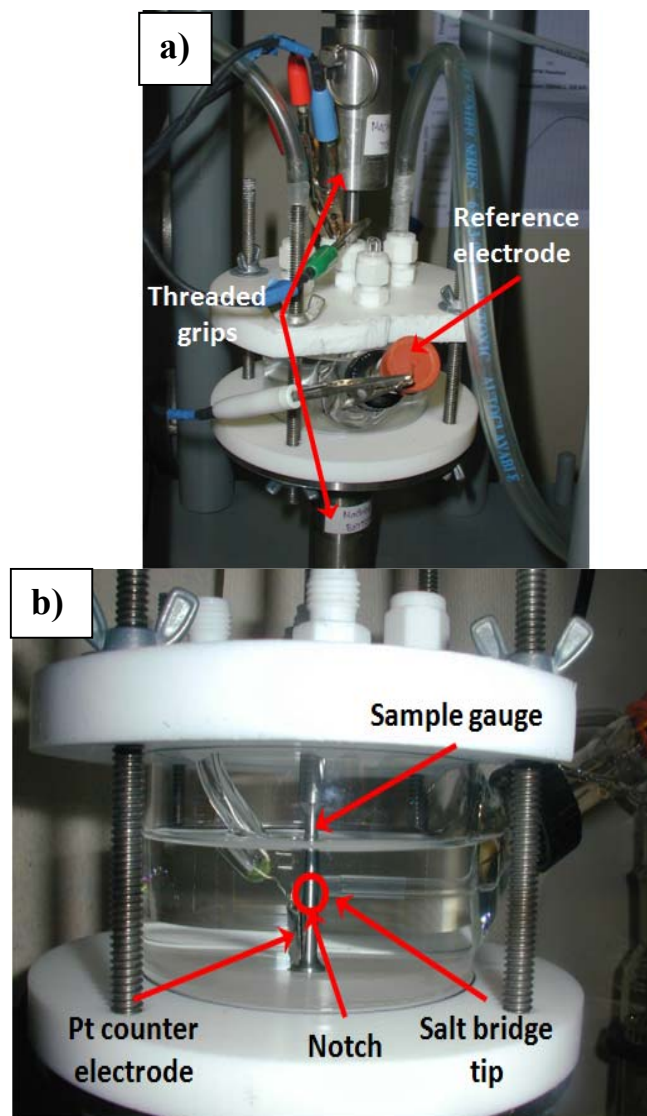


**Figure 3-6 a) Front view of the environment cell with in-situ electrochemistry in place. The sample is threaded into steel grips for straining. b) side view of the three-electrode geometry within the cell**

### **3.4.1 A note on challenges with electrochemistry in ethanol**

Obtaining accurate electrochemical data in highly resistive solutions, such as ethanol, can be challenging. A potentiostat must be able to accurately measure and control the  $\Delta E$  near the electrode surface, between the surface and the bulk solution. However, measurements of electrode potential are actually measurements of the total potential

difference between the electrode surface and the reference electrode, which includes the potential drop due to solution resistance ( $IR_u$ ) (Figure 3-7). When solution resistance is high, it is necessary to compensate for  $IR_u$  to accurately control potential at the electrode surface so electrochemical activity can be studied.

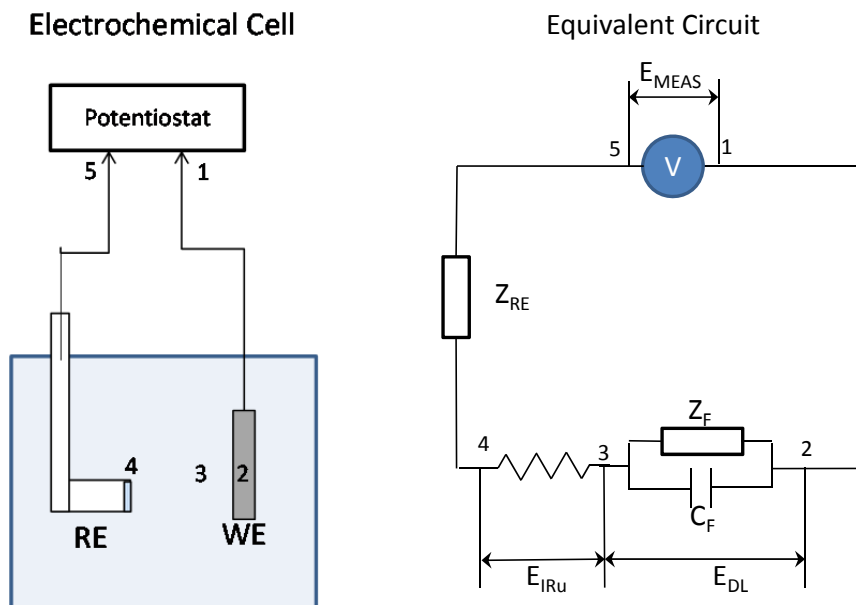


**Figure 3-7 The electrochemical cell and its equivalent circuit approximation. Impedance within the reference electrode is often negligible and can be ignored. The potential of interest is  $E_{DL}$ , thus corrections must be made if  $E_{IRu}$  is high**

One method of decreasing solution resistance is to dissolve a conductive salt (supporting electrolyte) into the resistive solution. An ideal supporting electrolyte will increase the conductivity of the test solution without interfering with anodic or cathodic reactions at the electrode surface of interest.  $LiClO_4$  is a supporting electrolyte that has been frequently utilized in past electrochemical studies of iron and steel in organic solvents [84, 85]. However, it has been shown that  $LiClO_4$  is not completely inert in these

solutions and may alter the surface reactions [86, 87]. Tetrabutylammonium tetrafluoroborate (TBA-TFB), LiCl, and LiNO<sub>3</sub> were investigated for their utility as supporting electrolytes in SFGE [87], but none was found to consistently raise the electrolyte conductivity without interfering with electrochemical potential or causing localized corrosion. To eliminate the risk of supporting electrolyte interference in electrochemical activity of pipeline steel in FGE and SFGE, no supporting electrolyte was used in this study.

During electrochemical measurements, solution resistance was instead compensated for by applying an automatic IR<sub>u</sub> compensation function which used a current interrupt method during data acquisition to measure and correct for solution resistance. IR<sub>u</sub> compensation was used in all electrochemical measurements unless otherwise specified. Lou et al demonstrated that when applying potentials in a range close to E<sub>corr</sub>, the automatic IR<sub>u</sub> compensation function is as accurate as retroactively applying a value calculated from impedance measurements at the beginning of a test [83].

Optimization of the electrochemical cell geometry also aids in reducing the errors imparted by the large IR<sub>u</sub> value, so each three-electrode setup was built to keep the distances between reference, counter, and working electrodes constant and at a minimum (Figure 3-8). The reference electrode was fixed at a distance of 1cm from the working electrode, which was slightly more than twice the diameter of the Vycor frit (4mm). In SSRT or potentiodynamic tests, the Pt mesh or foil counter electrode encircled the working electrode at a constant distance of 3mm.

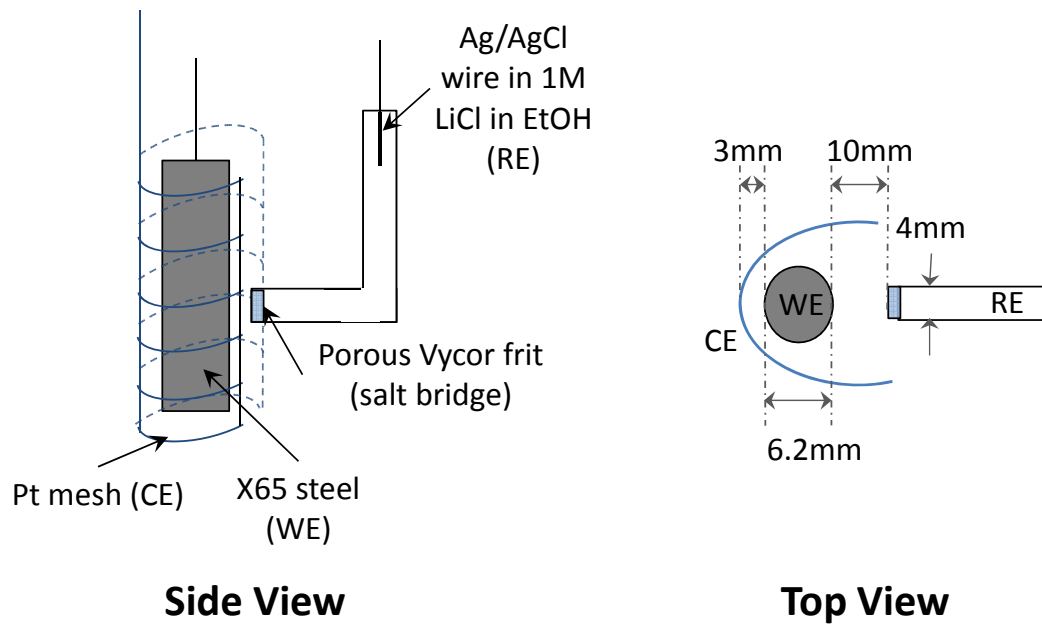


**Figure 3-8 Configuration of the working electrode (WE), counter electrode (CE) and reference electrode (RE) within the electrochemical cell used in ethanolic environments**

### 3.5 Scratched Electrode Tests

For scratched electrode tests, rectangular cubic coupons with dimensions 2.5cm x 0.5cm x 0.5cm and threaded on one end were machined out of the X65 pipeline steel. All four faces were ground with wet SiC paper up to 1000 grit, rinsed in deionized water and ultrasonically degreased in acetone. A final grinding was done with dry 2000 grit paper, followed by acetone rinse and ultrasonic cleaning.

The test cell (Figure 3-9) was similar to that used for SSRT, comprised of a glass tube sealed at the ends by two PTFE end caps. The top end cap contained airtight ports for insertion of the steel coupons, gas inlet and outlet, reference electrode, and a scratcher. The scratcher was a diamond-tipped scribe mounted perpendicularly to a vertical

stainless steel rod assembly that allowed for horizontal rotation and rapid upward motion of the scribe tip.

The desired SFGE or commercial FGE solution was funneled into the cell, and a gas purge was started. All test solutions were pre-purged with compressed air unless indicated as deaerated. For the deaerated tests, dissolved oxygen was removed from the test solution by an N<sub>2</sub> gas purge. The desired purge gas was sent through a liquid trap containing the test solution before entering the test cell in order to trap any moisture or trace impurities. Test solutions were gas sparged for 30 minutes prior to inserting the X65 test coupons. X65 coupons were threaded onto a carbon steel rod to maintain an electrical connection to the exterior of the cell. The rod was insulated from the FGE environment by a Teflon tube, sealed to the sample with a Teflon washer and Viton O-ring. The samples were allowed to reach stable open circuit potential (OCP) in the test solutions for three to five hours. OCP was not measured during this time in order to minimize the risk of Cl<sup>-</sup> ion leakage into the cell from the salt bridge. Instead, the sample was allowed to reach a stable OCP value for an initial time period which was longer than the previously measured average times for X65 samples to reach semi-stable OCP in the same or similar solutions [83].

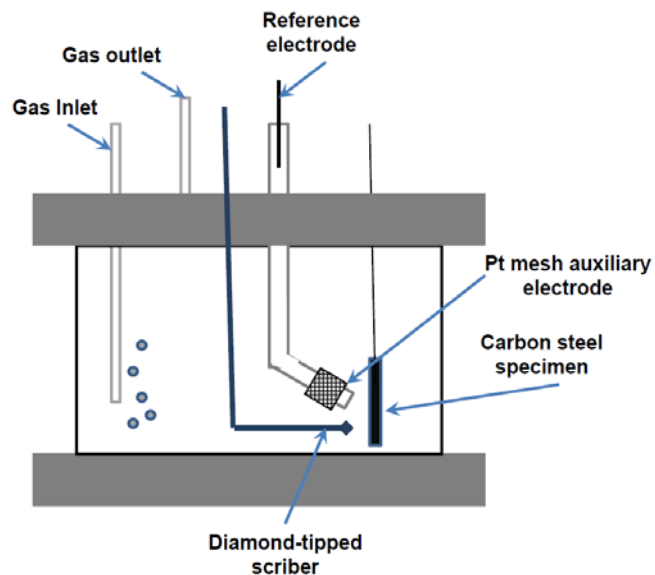


**Figure 3-9 Schematic of the test cell used for performing mechanical scratch tests**

After allowing sufficient time for passive layer formation and OCP stabilization, the counter and reference electrodes were inserted into the cell. To minimize  $IR_u$  drop and maintain identical three-electrode geometry for all tests, the  $1\text{cm}^2$  platinum mesh counter electrode was attached to the exterior of the reference electrode body just behind the salt bridge tip, and the assembly was situated within  $1.5\text{cm}$  of the test sample. A Gamry reference 600 potentiostat was connected to the cell, and OCP was measured for 120s. The sample was then polarized potentiostatically while surface current was measured. Unless specified, the applied potential was equal to the measured OCP value. Automatic  $IR_u$  compensation was applied during all electrochemical measurements unless otherwise specified.

Approximately 60 seconds after starting the polarization, the sample surface was rapidly scratched with the diamond-tipped scribe. For repeatability, four scratches (one on each side of the coupon) were performed in each solution, with a 20-minute waiting

period between events to ensure full decay of any current transients from the previous scratch. Current was initially sampled at a rate of 100 samples/s to examine the current decay on the millisecond time scale. This high sampling rate limited the total measurement time to 60s and eliminated the ability to apply automatic IR compensation. However, because long current transient times were observed in the ethanolic environments, subsequent tests were conducted for 600 seconds at a sampling rate of 5 samples/s.

After completion of 4 scratches in a given environment, samples were examined with an optical microscope. To compute scratch area, length and width of each scratch were measured using Clemex image analysis software. SEM was used for higher magnification observation within scratches, and EDS was employed to identify any corrosion products or anomalous features.

### **3.6 Characterization of Surface Film Composition and Morphology**

For purposes of analyzing effects of FGE and SFGE chemistry on X65 surface film composition, samples were exposed to various FGE and SFGE environments for several days, then analyzed using X-ray photoelectron spectroscopy (XPS).

#### **3.6.1 Static coupon exposures for film growth**

Coupons were cut from the X65 steel pipe in the dimensions of 1cm x 1cm x 0.2-0.3 cm. Coupon faces were ground to 2000 grit SiC paper, then polished to 1 $\mu$ m using a series of diamond suspensions, then to a 0.05 $\mu$ m finish using an Al<sub>2</sub>O<sub>3</sub> suspension. Polished coupons were ultrasonically cleaned in acetone, dried, and immediately immersed into the solution of interest.

Each test environment was funneled into a 250mL glass flask 2 hours prior to inserting the samples and sealed, with the exception two glass tubes which served as the inlet and outlet gas ports. Gas was purged continuously to allow the air content of the solution in the test cell to stabilize before insertion of the samples. Prior to entering the test cell, purge gas was sent through a separate cell containing the test solution to trap any moisture or impurities from the gas purge. Similarly, outlet gas was purged through another flask containing test solution to prevent evaporation of ingress of air or moisture during the test. A schematic of the test setup is depicted in Figure 3-10.

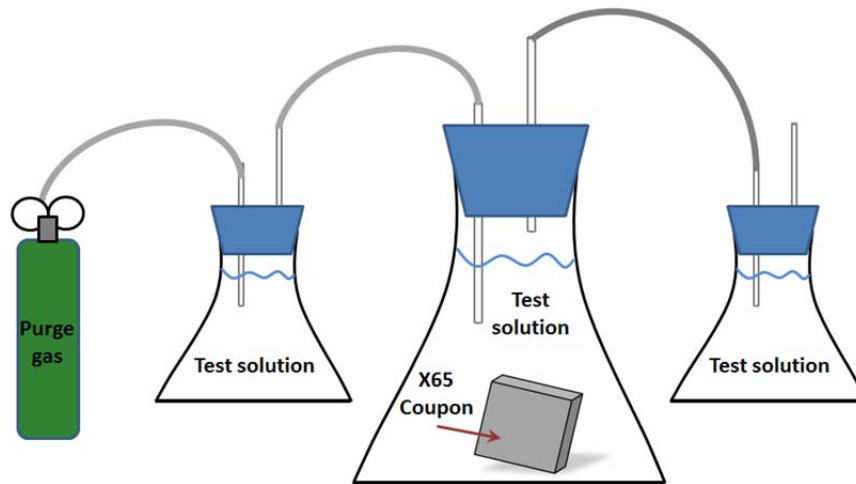


**Figure 3-10 Schematic of coupon exposure test setup**

Coupons were exposed to their respective environments for five days, then rinsed within the test solution by holding with tongs and vigorously moving them back and forth within the test solution. Samples were then immediately transferred to a  $N_2$  atmosphere and dried under  $N_2$ . Samples were stored in airtight

N<sub>2</sub>-filled vials under vacuum until XPS analysis could be performed. All samples were analyzed within 48 hours of removal from the cell, and were exposed to atmosphere for as short a time as possible to minimize atmospheric contamination of the surface.

### **3.6.2 XPS analysis**

In order to investigate the composition of films formed on X65 steel in FGE and SFGE environments, X-ray photoelectron spectroscopy was utilized. XPS spectra were obtained using a Thermo k-alpha XPS spectrometer. X-rays were generated by a monochromated Al k- $\alpha$  source, operated at 12kV with incident characteristic X-ray photon energy ( $h\nu$ ) of 1486.7 eV. Pass energy of the concentric hemispherical analyzer was set to 50eV. Takeoff angle was 90° with respect to the sample surface. Pressure inside the chamber was in the 10<sup>-9</sup> Torr range. A flood gun was used to eliminate any sample charging. High resolution spectra were obtained for three single elements: iron, carbon, and oxygen. Three to five scans were performed and averaged to obtain a final spectrum for each element.

In some cases, the surface was sputtered with Ar<sup>+</sup> ions to etch away successive layers of oxidized steel. A medium current and beam energy of 1000eV were used, with a sputter area of 2mm diameter. This low beam energy and current were used to prevent reduction of the surface products by Ar<sup>+</sup> ions. Estimated sputter depth, as calibrated for these parameters on a Ta<sub>2</sub>O<sub>5</sub> substrate, was 0.2nm/s.

Spectra were analyzed using the Thermo Advantage software. For all spectra, background subtraction was performed using a “Smart” background algorithm. The Smart background subtraction bases the calculation of background on the more

commonly used Shirley algorithm, and then iteratively adjusts the background position so that the corrected background does not rise above the data curve. The Shirley method gives a curved S-shaped background for each peak, calculated based on the assumption that the background intensity is proportional to the peak area on the high binding energy (B.E.) side of the peak. This can create errors when a spectral background continues to rise even though no peak is present, which commonly occurs in transition element spectra because the high density of states at the Fermi level creates an asymmetric peak shape. For this reason, the Smart technique led to a higher level of accuracy, particularly when fitting doublet peaks in the iron spectra.

A nonlinear least squares method was used to fit and deconvolute overlapping peaks for a single element. Common peak B.E.s and full width-half maximum (FWHM) values for fitted peaks were obtained from literature and used as initial constraints for the fitting algorithm. Peak FWHM for a specific species can often vary based on the resolution of XPS instrumentation, but should not vary more than several tenths of an eV. The FWHM values chosen from literature were those which were obtained using standard reference compounds and had been fitted using a similar number of peaks. For instance, in this dissertation, Fe2p spectra were deconvoluted into four pairs of peaks, so similarly-fitted literature FWHM values were averaged and used as initial constraints for the Avantage software's non-linear least-squares (NLLS) fitting method. Typically, before performing a fit using the software, peaks were identified and constrained based on the information from literature. First, peak B.E.s were fixed to within  $\pm 0.3$  eV of average literature values, and FWHM constraints were also set based on literature values. Then, an initial fit was performed, allowing FWHM and B.E. to vary together. Next, FWHM

values were fixed based on the initial fit, and another fit was performed. Peak values were then fixed, and FWHM were allowed to shift close to the values obtained from the initial fit. This procedure was iterated until a good fit was achieved, similarly to the peak fitting routine performed by Lin et al. [88]. Goodness of fit was evaluated based on the normalized Chi-Square ( $X^2$ ) value calculated by the software using the following general formula:

$$X^2 = \sum \frac{(data - fit)^2}{fit} \quad (3-3)$$

where *data* is the value obtained experimentally, and *fit* is the value calculated from summation of the spectral intensities of the fitted peaks at each B.E. Normalized  $X^2$  values typically fell between 1 and 5 for O1s and C1s spectra, and between 5 and 9 for Fe2p spectra.

For all experiments, the C1s spectra were fitted first, to verify that the main hydrocarbon peak near 285.0eV had not shifted due to sample charging. This peak was used as a relative reference value for calibration of the rest of the spectra from a sample, as is common in many other XPS studies on iron and steels and their oxides [89-93, 94]. If the peak was shifted more than 0.3eV from 285.0eV, all spectra from that sample were shifted so that the peak B.E. of the main hydrocarbon peak was 285.0eV. In this way, a basis for comparison between all spectra was achieved.

### 3.6.3 Atomic force microscopy

Atomic force microscopy (AFM) imaging was performed on X65 coupons before and after exposure tests in SFGE. Topographical information and surface morphologies were easily obtained and compared using the AFM technique. An Asylum MFP-3D AFM was used with Olympus Si cantilevers with a nominal spring constant of 42N/m and 300kHz

drive frequency. Imaging was done in AC (tapping) mode. Images were processed using Gwyddion image analysis software. Scan sizes ranged from 20x20  $\mu\text{m}^2$  to 1x1  $\mu\text{m}^2$ .

## EFFECTS OF FGE FEEDSTOCK AND SOURCE ON SCC OF X65

### 4.1 Introduction

Early FGE SCC discoveries were in “user” and not “producer” facilities [56], so contaminants or ethanol degradation products arose as possible SCC causal factors. Moreover, pure 200-proof ethanol (water content < 500ppm) did not lead to SCC in preliminary studies, and this prompted the exploration of the effect of non-ethanol FGE constituents’ and contaminants’ on SCC susceptibility in carbon steel handling equipment.

In this chapter, experiments to determine effects of ethanol feedstock or source on SCC of pipeline steel are described. Complete chemical analysis of all FGE samples was performed to identify any constituents that could potentially lead to changes in SCC or corrosion susceptibility among the environments. Electrochemical polarization and slow strain rate tests were performed to evaluate the corrosion and SCC behavior of the steel in FGE. X60 pipeline steel, composition and microstructure described in Chapter 3 was chosen for the specimens to facilitate direct comparison with similar tests performed at other laboratories in identical environments [19, 95]. It was noted in prior published studies [19] that SCC could not be statistically evaluated in smooth samples due to secondary cracking in the plastically deformed region of the samples, so to control for secondary cracking and facilitate accurate comparison of the effects of FGE feedstock on SCC propagation, notched samples were used in the experiments in this chapter. SCC behavior was evaluated and compared by visual analysis of the fracture surfaces,

maximum load in stress-strain curves, and time to failure for the specimens tested in different environments.

The objective of the research presented in this chapter was to determine the differences in SCC susceptibility of pipeline grade carbon steel based on:

- Feedstock and distillation process of FGE
- User or producer status

Prior to this research, feedstock-dependent variations in SCC susceptibility had not been systematically studied. There is existing literature on limited studies of effects of ethanol/gasoline blend ratio [71] and producer/user ethanol [19], however no in-depth work on SCC variations caused by potential feedstock-based chemical differences was previously undertaken.

## 4.2 Chemical Characterization of all FGE Samples

Semi-quantitative analysis was done on the GC-mass spectra to find the amounts of individual impurities within the FGE samples. Feedstock and source information for all FGE samples used, as well as detailed information about the GC-MS equipment and procedure can be found in Chapter 3. Identification of constituent peaks was based on the Palisade Complete Mass Spectra Library, 600K edition. An example spectrum with several peaks labeled with identified constituents is shown in Figure 4-1. Quantitative content ( $C$ ) of an identified constituent was calculated by using the ratio of the constituent's peak area ( $A_x$ ) to the peak area of the internal standard ( $A_{STD}$ ) that was added to the sample before injection using the following formula:

$$C = \frac{A_x}{A_{std}} \times \frac{C_{std}}{RF_{GC}} \quad (4-1)$$

where  $C_{STD}$  is the concentration of internal standard within the injected mixture and  $RF_{GC}$  is the instrument response factor, assumed in this case to be 1 for all analyzed solutions. It was ensured that the internal standard peak did not overlap with any compound in the spectrum. From this analysis, it was feasible to compare relative concentrations of constituents between FGE samples.

Results of water content analysis, pHe measurement, chloride and sulfate content are shown below in Table 4-1. Based on analysis, all tested commercial FGE samples had compositions in compliance with the ASTM regulation. Chloride and sulfate content of all samples was less than 1 ppm, and, with the exception of lot 6, all contained less than 1 vol% water. The cellulosic ethanol had the lowest water content.

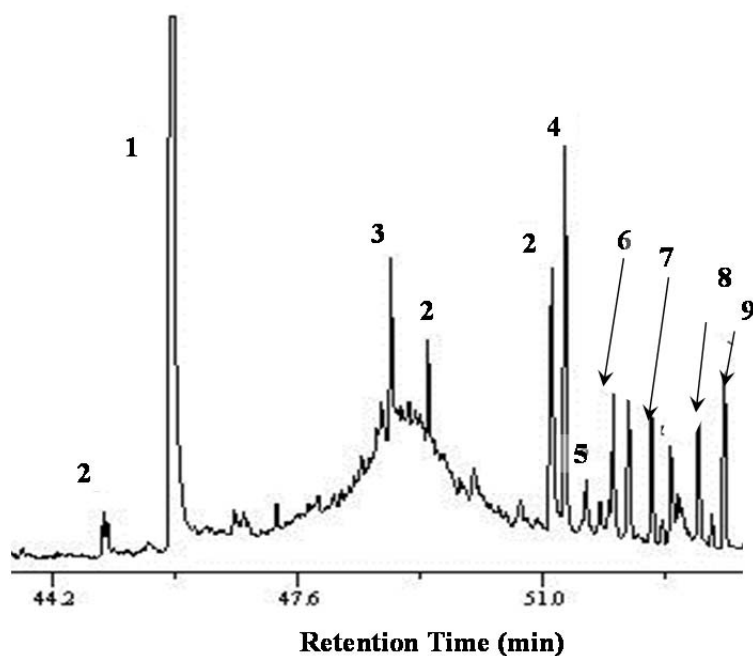


Figure 4-1 GC-MS spectrum of Lot 7 FGE. The numbers correspond to the following constituents: 1. Internal standard, 2. Fatty acids, 3. C16:COOH ethyl ester, 4. 2,2 bis[(4-hydroxy)phenyl]propane, 5. Pimaric acid derivatives, 6. Pimaric acid, 7. Isopimaric acid, 8. Dehydroabietic acid, 9. Abietic acid

Table 4-1 Sulfate, chloride, and water content, and pH<sub>e</sub> of all commercial FGE samples

	Lot 2	Lot 3	Lot 4	Lot 5	Lot 6	Lot 7	Lot 8	Lot 9
Cl <sup>-</sup> (ppb)	88.5	< 60	< 60	48	16	60	<60	100
SO <sub>4</sub> <sup>2-</sup> (ppb)	148	102	225	123	298	93	33	30
pH <sub>e</sub>	7.8	7.7	7.9	7.1	7.6	7.8	7.9	8
Water (vol %)	0.92	0.55	0.64	0.88	1.01	0.65	0.67	0.12

Though the ASTM regulation [55] does not account for trace organics that FGE may contain as a result of variations in ethanol feedstock and processing conditions (other than methyl alcohol as a denaturant), GC-MS analysis of all as-received commercial fuel grade ethanol did not reveal significant differences in organic

composition. A summary of GC-MS findings is given in Table 4-2. Full data tables of GC-MS results can be found in the

APPENDIX. All FGE contained trace amounts of 2-butenal or 3-methyl butenol, and very small traces of rosin acid compounds. Analysis of a commercial denaturant revealed that it was the likely source of butenal and butenol constituents. Analysis of a pure, 200-proof reagent grade ethanol containing no denaturant or inhibitors confirmed this, as no other alcohol or alcohol intermediates were found within this undenatured reagent ethanol. The assumed source of the rosin acids was the shipping containers, as these compounds were also not present in the reagent ethanol. Lots 2, 4, 5, 7 and 9 all contained compounds attributed as fatty acid ethyl esters in quantities less than 200µg/ml. For proprietary reasons, inhibitor samples could not be obtained for direct chemical analysis, but comparison of GC-MS analyses of a FGE known to contain inhibitor and a virgin (no inhibitor, no denaturant) FGE indicated that the inhibitor was comprised of large fatty-acid molecules, which explained the presence of fatty acid ethyl esters found in some FGE lots.

**Table 4-2 Summary of impurity content of commercial FGE samples.**

<b>FGE Lot</b>	<b>Non-ethanol alcohols (µg/L)</b>	<b>Fatty acid esters (µg/L)</b>	<b>Hydrocarbons (µg/L)</b>	<b>Rosin acids (µg/L)</b>
Lot 2	433.66	6.18	0	5.66
Lot 3	372.73	10.79	0	29.31
Lot 4	617.55	1.33	0	0.54
Lot 5	0.00	1.94	0	0.39
Lot 6	0.00	2.29	0	3.38
Lot 7	0.00	5.39	0	6.07
Lot 8	389.35	1.21	0	2.91
Lot 9	0.00	177.52	65.9x10 <sup>3</sup>	336.26

### 4.3 Electrochemical Polarization of X65 in FGE

Cyclic polarization tests were performed on X65 in each of the commercial fuel grade ethanol samples to characterize and compare values of corrosion potential ( $E_{\text{corr}}$ ) and corrosion current density ( $i_{\text{corr}}$ ) and evaluate the nature of the electrochemical reactions on the pipeline steel surface at various potentials in each FGE solution.

Polarizations were carried out at a scan rate of 2mV/s.

**Table 4-3 Electrochemical parameters for each of the commercial FGE samples**

	<b>Lot 2</b>	<b>Lot 3</b>	<b>Lot 4</b>	<b>Lot 5</b>	<b>Lot 6</b>	<b>Lot 7</b>	<b>Lot 8</b>	<b>Lot 9</b>
<b>Resistivity (kΩ-cm)</b>	50	50	90	40	40	20	80	32
<b><math>E_{\text{corr}}</math> (V vs Ag/AgCl/EtOH)</b>	No data	0.011	0.063	0.000	0.123	0.180	0.080	0.153
<b><math>i_{\text{corr}}</math> (nA/cm<sup>2</sup>)</b>	73	70	73	71	82	40	49	27

To obtain a steady value of  $E_{\text{corr}}$ , it was necessary to expose the sample to FGE for more than 10 hours prior to scanning. This slow OCP stabilization is a stark contrast to the behavior of pipeline steel in aqueous environments, where stable potential can be reached within seconds or minutes. Based on changes in polarization resistance and electrochemical impedance behavior over time [83, 96], these continuous changes in OCP are attributed to slow kinetics of passivation. In FGE, OCP typically increased at a rate of approximately 40-60mV/h during the first 45 minutes of OCP measurement, slowing to a rate of 4-6mV/h after nine hours (Figure 4-2).

Representative polarization curves in FGE are shown in Figure 4-3. The Tafel extrapolation method was used to calculate  $i_{\text{corr}}$  from all curves. For lot 6,  $i_{\text{corr}}$  was found to be approximately  $0.05\mu\text{A}/\text{cm}^2$ , corresponding to a general corrosion penetration rate ( $r$ ) of  $0.58\mu\text{m}/\text{year}$ , based on the following [26, p.76]:

$$r = 3.27 \frac{N_{\text{EQ}} i_{\text{corr}}}{\rho} \quad (4-2)$$

where  $N_{\text{EQ}}$ , the equivalent weight of the material, was taken to be 27.92, and steel density  $\rho$  was approximated as  $7.87\text{g}/\text{cm}^3$ . This is considered a very low corrosion rate, as corrosion rates for carbon steel in seawater have been determined to be as high as  $100\mu\text{m}/\text{year}$  [97].

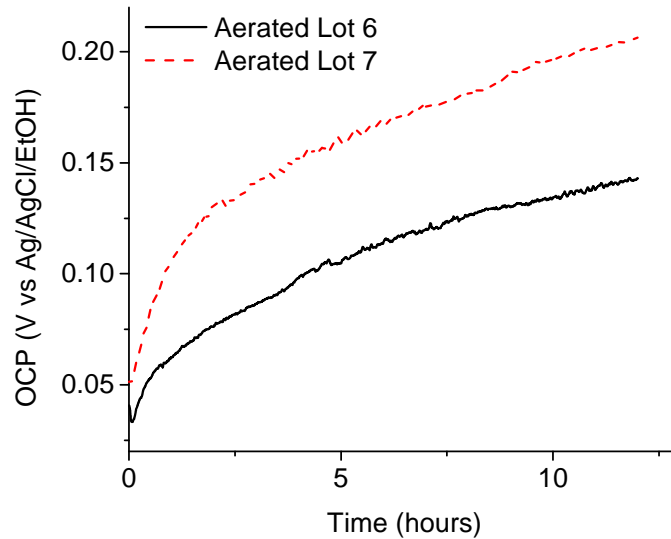


**Figure 4-2 OCP of an X65 coupon in aerated FGE measured for 12 hours. The rate of OCP increase decreased after approximately 10 hours, exhibiting only small changes after this duration**

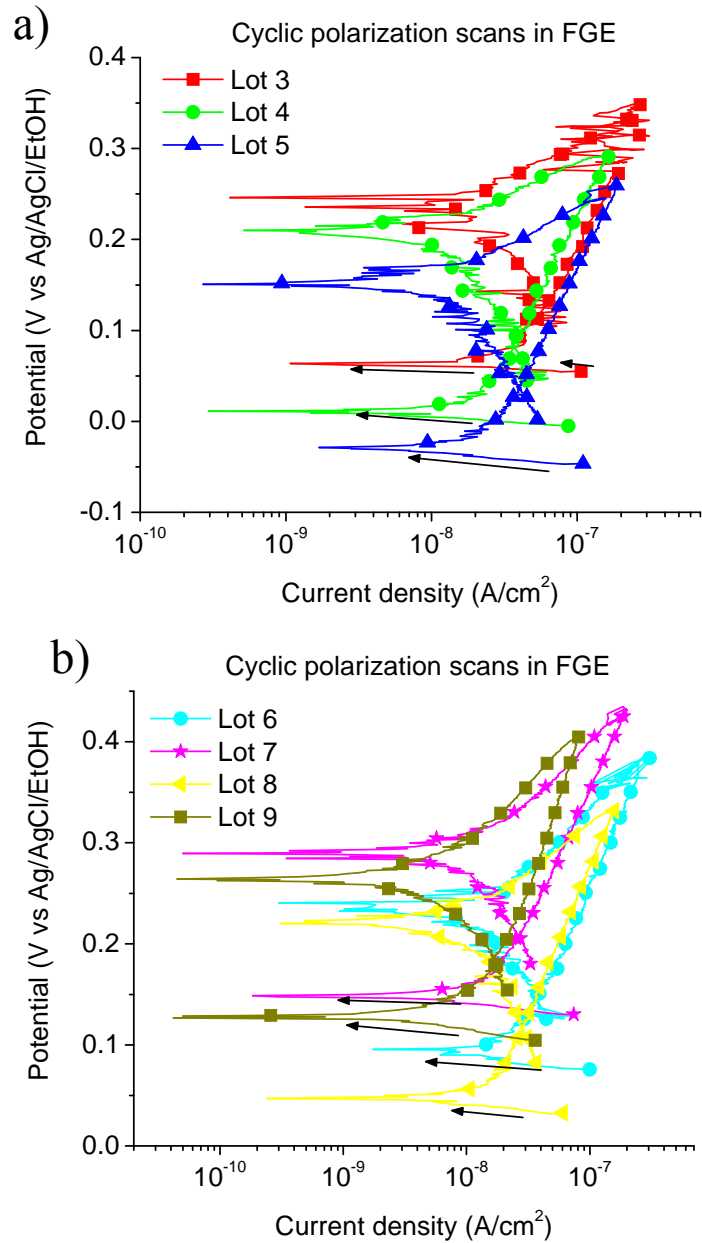


**Figure 4-3 (a) Potentiodynamic polarization of FGE lot 3 through 5, (b) Cyclic polarization of FGE lots 6 through 8**

Small changes in water content of organic solvents have been shown to affect passivation behavior in numerous studies of iron and steel in organic solvents [47, 52, 63, 98, 99]. OCP of X65 in Lot 7 FGE was more than 100mV higher than in any other FGE lot tested. High OCP values usually indicate the presence of an oxidizer which will raise

the mixed potential of the system. However, no constituents were detected in Lot 7 that were not also present in other FGE lots. In all FGEs tested, the rate of increase in current density decreases as potential is raised, but a clear active/passive transition typically represented by a marked decrease in current density is not exhibited. It is possible, however, that this decrease is masked by the cathodic reactions in the system [100], similarly to Cr and high-Cr stainless steels in aqueous environments [101]. Lot 2 and 3 both exhibited transpassive behavior within the potential ranges tested. Aside from differences in OCP, no marked differences in corrosion behavior were observed in the potentiodynamic data among all FGE lots.

The reverse hysteresis seen in the curves is not typically seen in aqueous environments, and is thought to be attributed to the oxidation of the water in the FGE at high anodic potentials [19]. Oxidation of alcohol molecules at the electrode surface may also contribute to measured current density during polarization measurements [51]. On the other hand, positive hysteresis is often exhibited when localized corrosion and pitting are present. Neither positive hysteresis nor pitting was observed on the steel samples in any as-received FGE environment within the applied potential range.

Based on the electrochemical and chemical data, SCC susceptibility was not expected to differ significantly among commercial FGE samples. Lot 7 did, however, exhibit a higher open circuit potential than others, indicating that Lot 7 might contain an oxidizer, though none was identified via chemical analysis. Changes in water content or pHe of the environment can also alter the OCP, but Lot 7 FGE did not differ from other lots with respect to these two parameters.

#### 4.4 SCC in FGE in Notched SSRT

Duplicate SSRT were performed on notched samples of X60 steel in each commercial FGE sample. After testing, failed specimens were rinsed with ethanol and stored under vacuum until visual analysis was performed. Fracture surfaces were examined optically and with SEM. EDS analysis was performed as needed. Stress corrosion cracking can be identified by thumbnail-shaped regions of brittle failure at the edge of the fracture surface (at the notch root), as shown in Figure 4-4 a). In severe cases, a region of brittle failure will encircle the entire fracture surface, as shown in Figure 4-4 b). No such brittle morphology was seen on notched samples strained in Lot 2, Lot 3, Lot 4, Lot 5, Lot 6, Lot 7, and Lot 9, indicating that samples strained in these environments did not undergo SCC. Their fracture surfaces were instead characterized by a dimpled morphology as a result of microvoid coalescence that is typical in the ductile failure of steels. An example of this dimpled morphology is shown in Figure 4-5 which displays the fracture surface of a notched X60 sample strained in Lot 2 FGE. Microvoids could be seen all the way to the edges of the specimen. Figure 4-6 shows the similar ductile fracture surface morphology of samples strained in Lot 6 and lot 9 FGE.

One sample strained in FGE from dry-milled corn (Lot 8) did display one small area of brittle failure. The morphology of this brittle region (Figure 4-7) contained faceted areas resembling that of intergranular or mixed mode (intergranular-transgranular) SCC. No SCC was observed in the duplicate test. It is possible that a microstructural anomaly, such as an inclusion or area of grain boundary segregation of alloying elements, existed at the notch surface and facilitated an SCC-like fracture behavior. This morphology did not recur in any of the previous or following experiments.

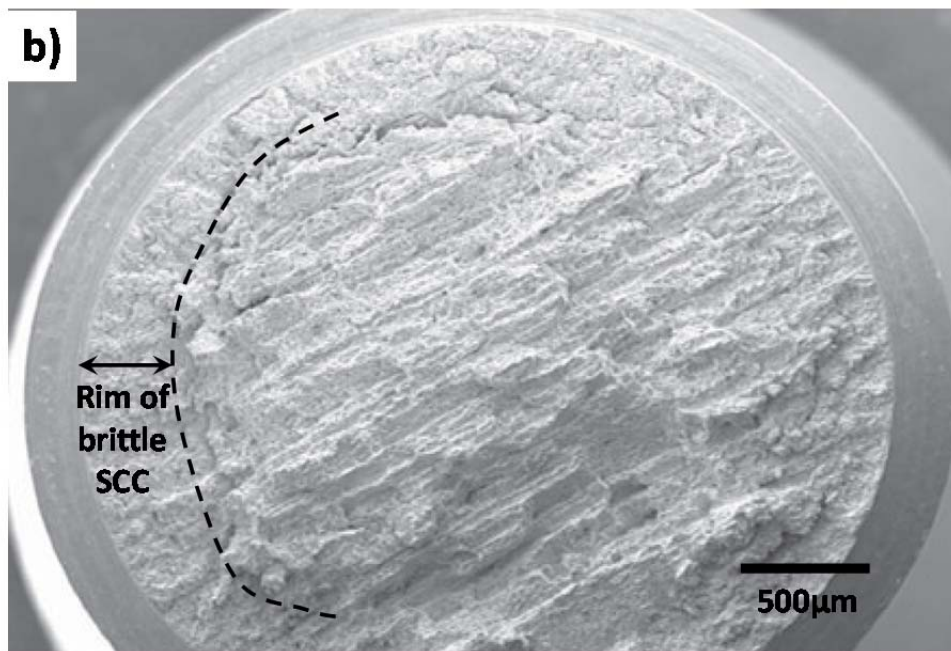
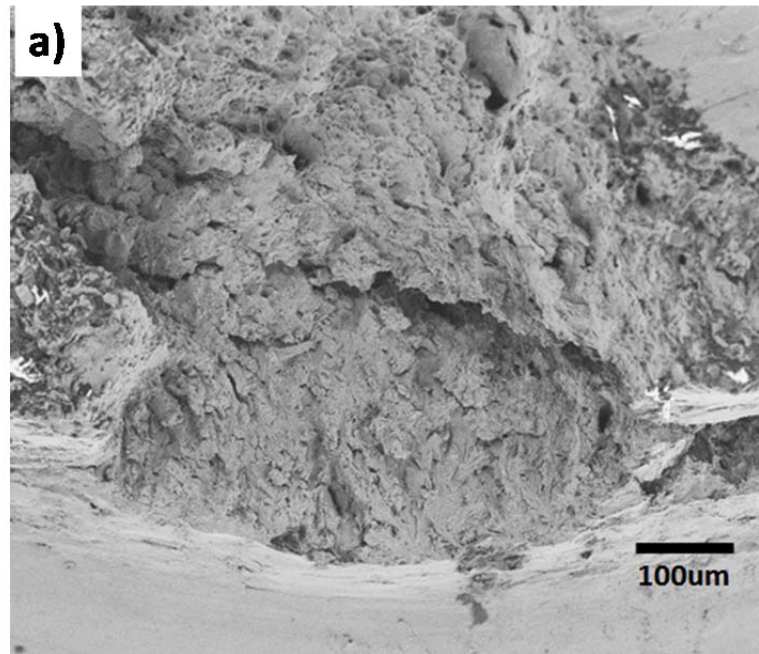
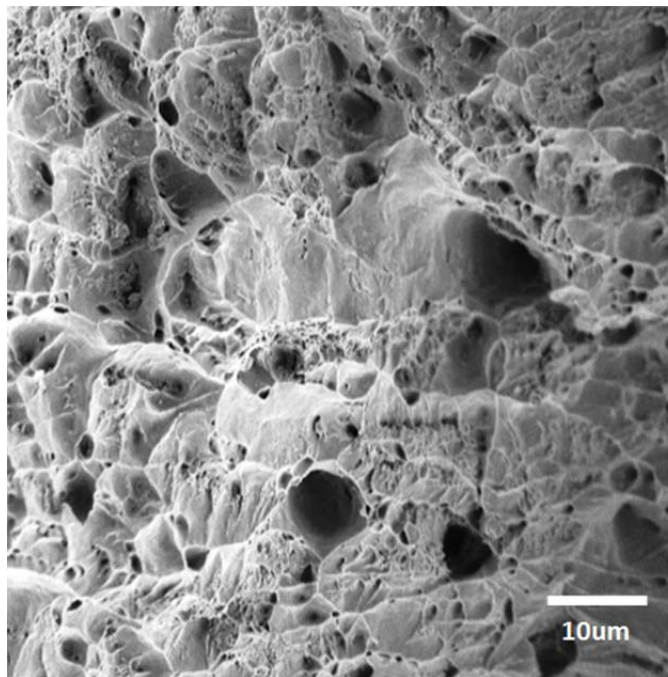
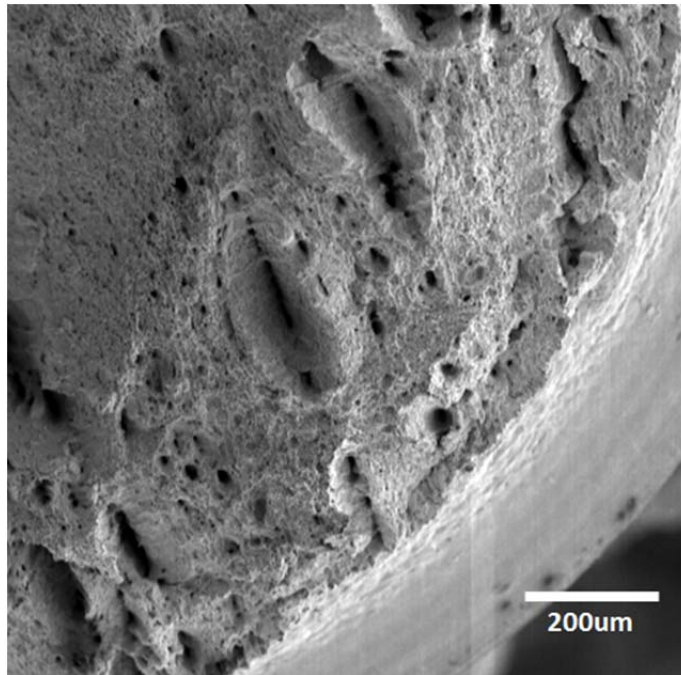
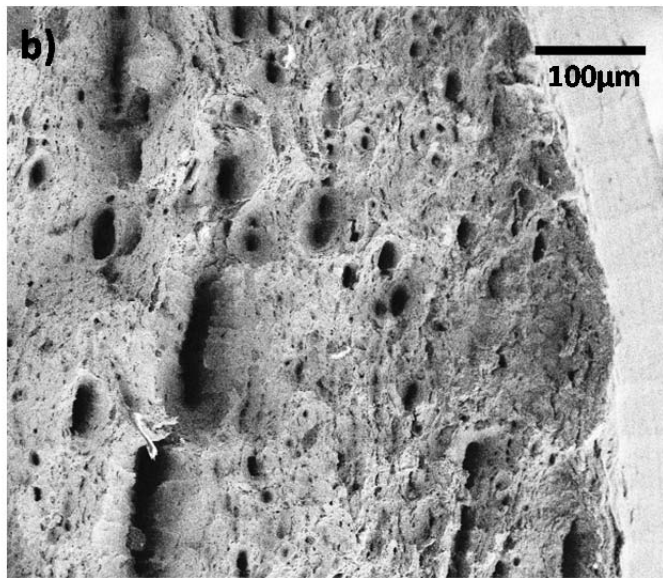
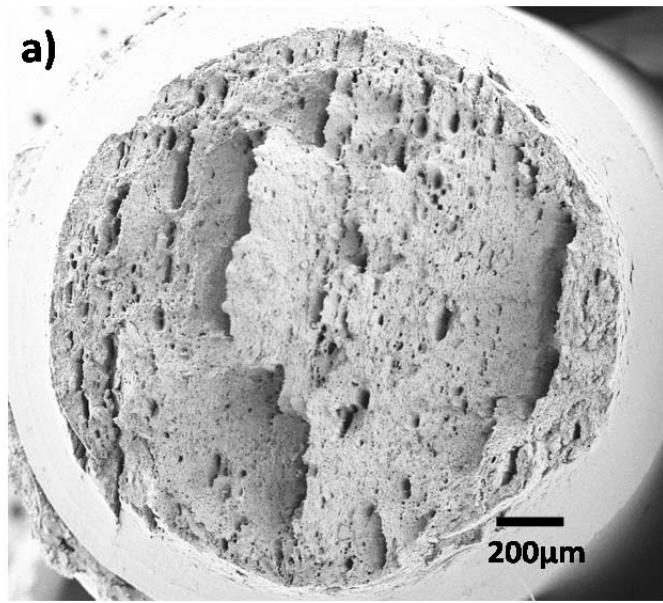


Figure 4-4 a) SSRT fracture surface exhibiting thumbnail-shaped area of brittle fracture. b) Notched SSRT specimen exhibiting a circumferential ring of brittle fracture [19].



**Figure 4-5 SEM images of fracture surfaces of notched samples strained in Lot 2 FGE which exhibit ductile failure characterized by microvoid coalescence. No brittle failure was detected; typical dimpled morphology of ductile failure surface is seen all the way to the outer edge of the sample.**



**Figure 4-6 Fracture surface of notched samples strained in a) Lot 6 FGE and b) Lot 9 FGE. No evidence of brittle fracture was observed around the circumference of either of the fracture areas.**

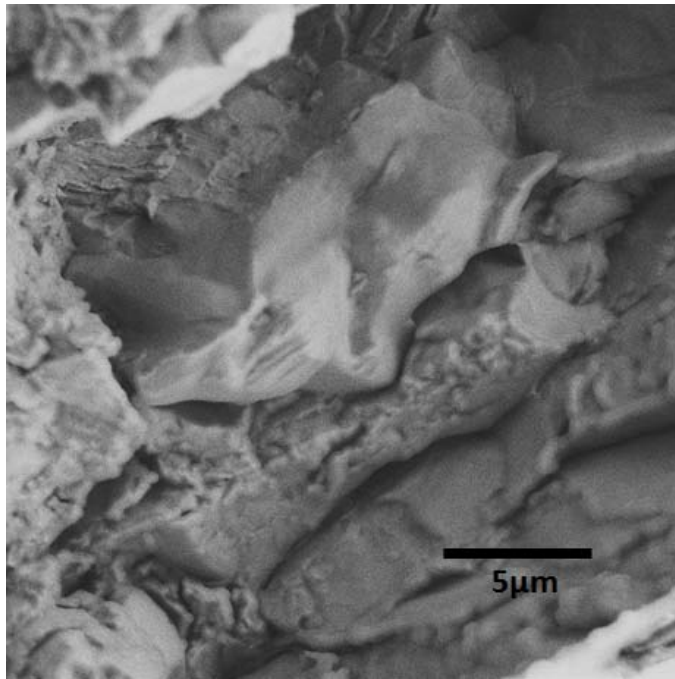
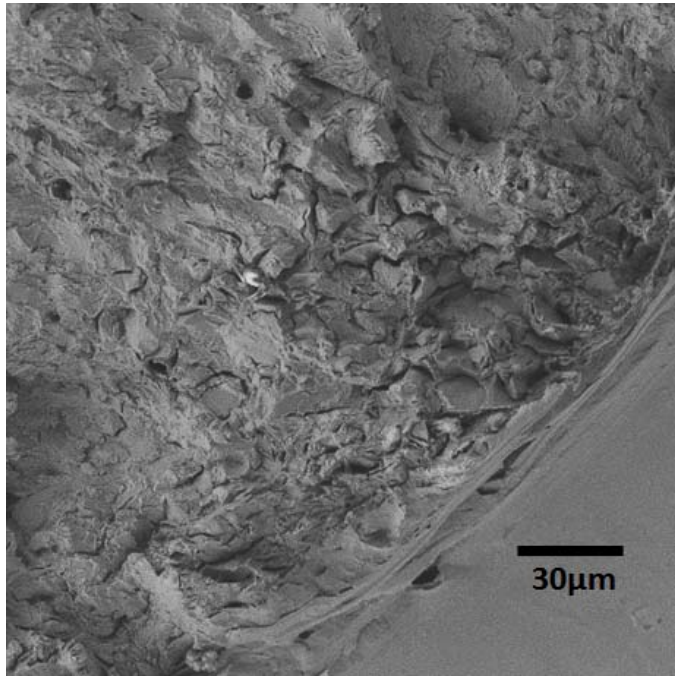
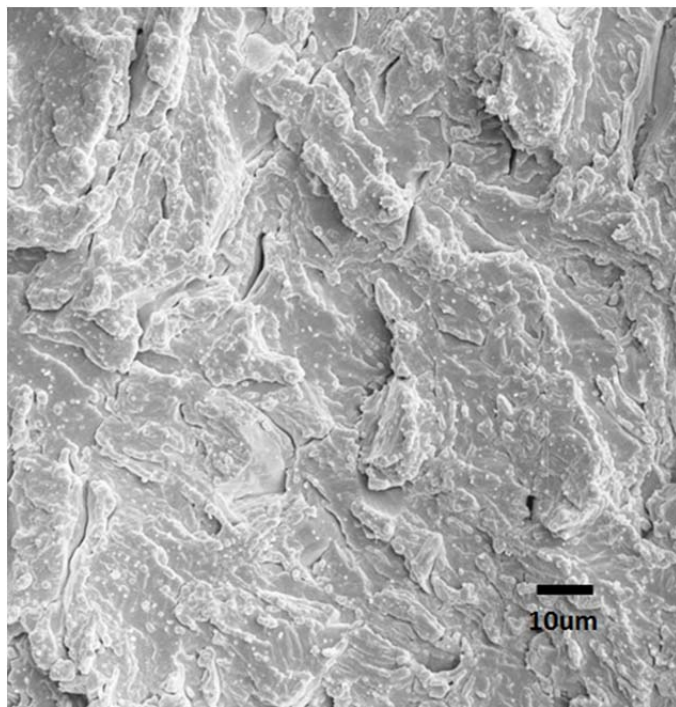
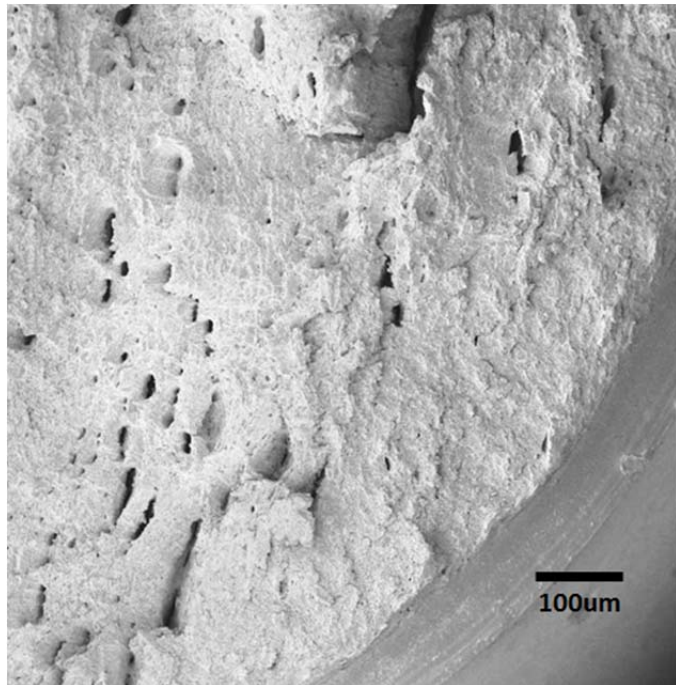


Figure 4-7 Thumbnail region of mixed-mode SCC of notched sample strained in Lot 8 FGE

#### 4.5 SSRT *In-situ* Electrochemistry

In a separate set of notched SSRT tests, in-situ open circuit potential measurements were performed in Lot 2 and Lot 3 FGE. In these tests, the Ag/AgCl/EtOH reference electrode and platinum counter electrode were inserted into the SSRT cell, as is shown in Figure 3-6. The Vycor salt bridge tip was placed approximately 1cm from the notch to reduce IR drop due to low solution conductivity. Fracture surfaces from these tests exhibited brittle transgranular fracture morphologies that formed nearly continuous rings around the outer rim of the surface (Figure 4-8). The duplicate test (Figure 4-10) showed identical signs of SCC fracture morphology.

A plot of stress and potential during straining is shown in Figure 4-9 (a). While in the elastic stress regime, OCP increased and leveled out at a stable value. Near the onset of plastic deformation however, overall OCP began to drop. Spikes appeared on the OCP curve, which corresponded to fluctuations in the stress-strain curve (Figure 4-9 (b)), seemingly caused by intermittent slip in the SSRT rig at high stresses. Slip in the machine caused slight relaxations of stress in the sample, during which times OCP increased until strain accumulated once again and OCP again began to decrease. Lou et al showed via impedance spectroscopy that in SFGE, this increase in potential signifies a growth of a dissolution-inhibiting film on the sample surface, whereas a potential drop denotes breakdown of the film [83]. This type of behavior during straining and strain relaxation conforms to the behavior expected from a film-rupture-induced anodic dissolution cracking mechanism.



**Figure 4-8 Fracture surface of a sample strained in Lot 2 FGE while OCP was measured. Transgranular SCC was exhibited, identifiable by the brittle fracture morphology near the outer edge of the sample.**

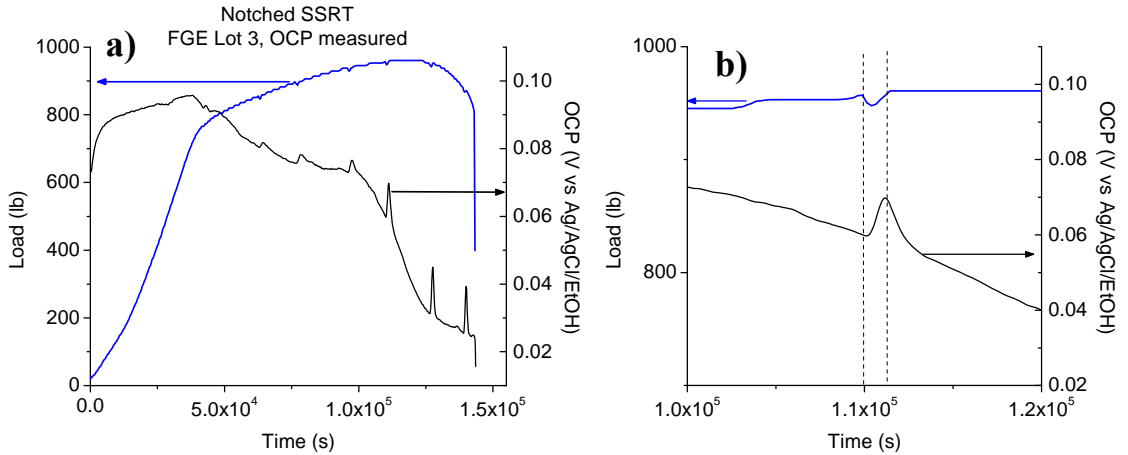


**Figure 4-9 Simultaneous loading and OCP measurement. (a) shows the OCP trend for the entire test duration. (b) depicts the rise and subsequent decrease in OCP corresponding to a stress relaxation event.**

In systems in which SCC follows the anodic-dissolution mechanism, holding the specimen at a potential anodic to its OCP can accelerate cracking because the potential-stabilized filmed surface will act as a large cathodic area, while the unfilmed crack tip becomes a small anode [17, 102]. However, since no potential was applied and OCP was allowed to vary freely as in all other SSRT where no electrochemical measurements were done, it was suspected that chloride contamination of the cell occurred from the reference electrode salt bridge, and that this affected the SCC behavior. To confirm this, post-SSRT FGE from the test cell was analyzed for  $\text{Cl}^-$  content from tests both with and without electrochemical measurements. Results of CIE analysis (Table 4-4) did confirm that minor  $\text{Cl}^-$  leakage did take place, resulting in a final bulk solution chloride content of 6ppm when the salt bridge was present in the test cell, and no chloride increase in the absence of electrochemical measurements. Leakage of chloride ions from the salt bridge was unexpected, as porous frits are commonly used without significant leakage issues in

aqueous test environments. In the case of ethanolic environments, leakage is thought to have occurred due to ethanol's superior wetting properties and lower surface tension as compared with water [18].

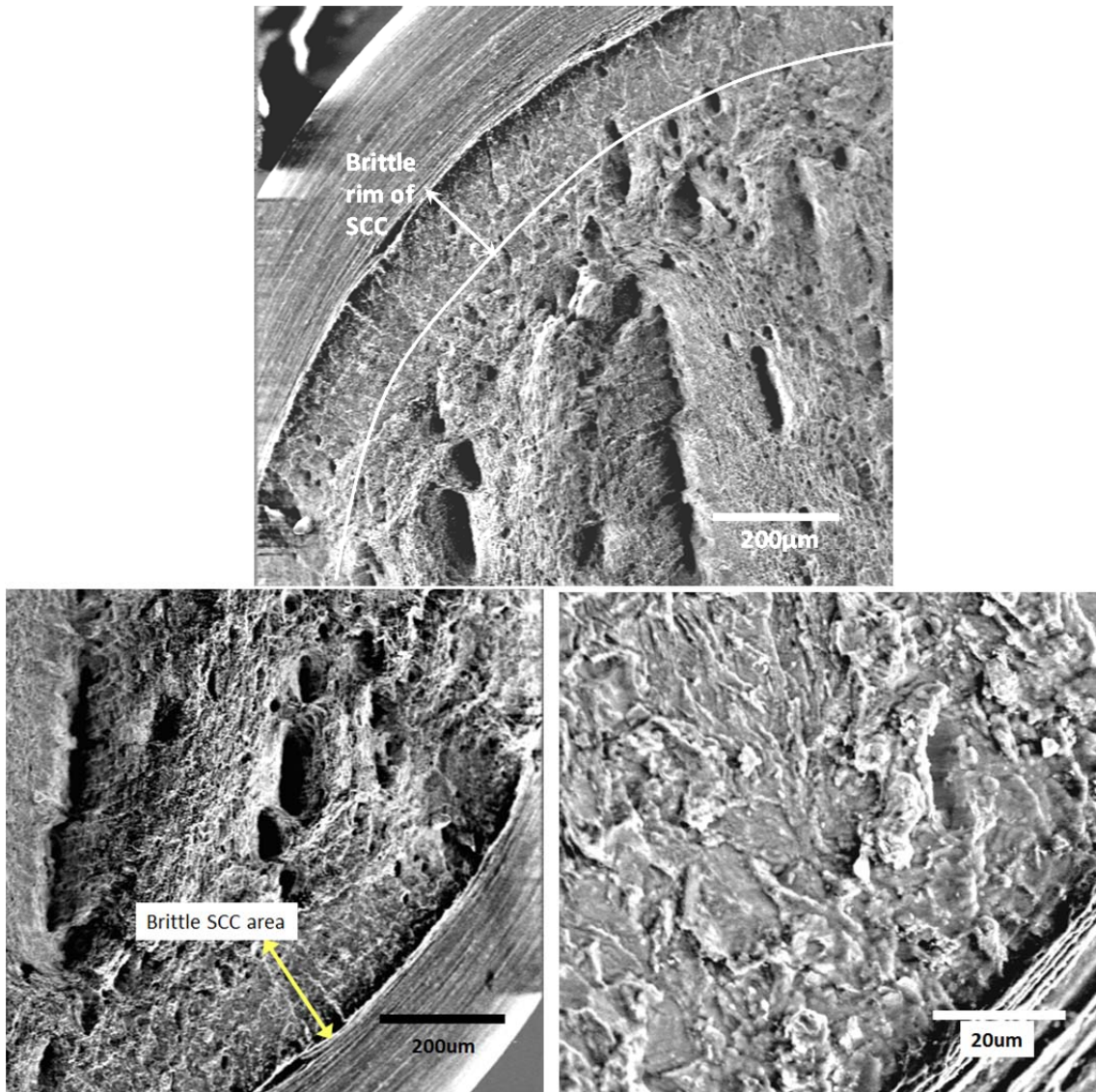


**Figure 4-10** Fracture surface of a sample from a repeated test, strained in Lot 2 FGE while OCP was measured. SCC results were nearly identical to the sample in Figure 4-8 Fracture surface of a sample strained in Lot 2 FGE while OCP was measured. Transgranular SCC was exhibited, identifiable by the brittle fracture morphology near the outer edge of the sample. Figure 4-8 above, with a ring of brittle transgranular SCC morphology.

**Table 4-4 Results of post-SSRT FGE chloride content analysis**

<b>Lot 2 FGE, post SSRT</b>		
	<b>No salt bridge</b>	<b>Salt bridge</b>
<b>Chloride (ppm)</b>	0.089	6.6

To confirm the result and eliminate the possibility that the SCC was promoted by other contamination or effects of OCP measurement, notched SSRT were performed in FGE environments containing into which several ppm of chloride were deliberately dissolved. No salt bridge was present in these tests. In these cases where Cl<sup>-</sup> was deliberately added, notched specimens did exhibit cracking, but in smaller areas. Brittle fracture regions took on thumbnail-shaped morphologies (Figure 4-11) instead of continuous rims around the sample perimeter. Continuous SCC rings morphology was readily apparent even in optical stereomicrographs, as can be seen in Figure 4-12 a).

Because cracking was found in small areas and had not coalesced into a continuous rim, cracking was defined as less severe in environments containing dissolved chloride than in those where chloride leaked from a salt bridge in close proximity to the sample notch. Chloride ions released near the notch may have concentrated at the steel/FGE interface, making Cl<sup>-</sup> much more highly concentrated in the solution at the steel surface than in the bulk solution.

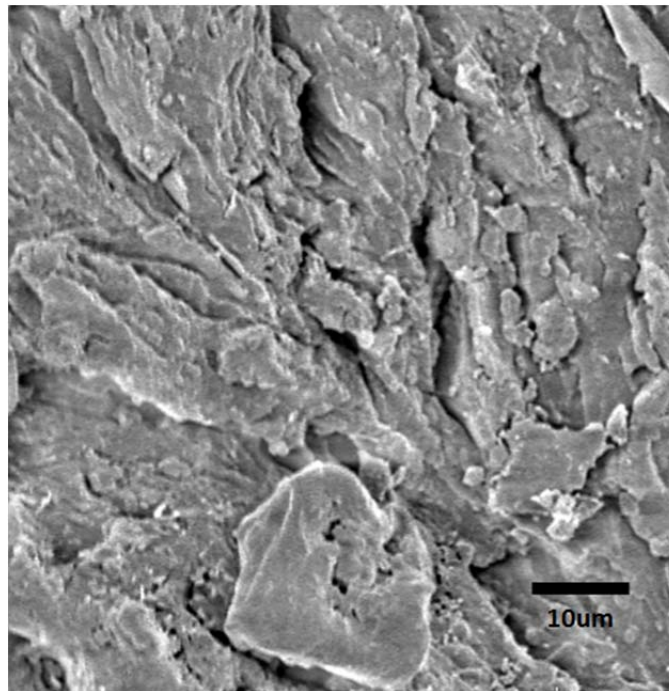
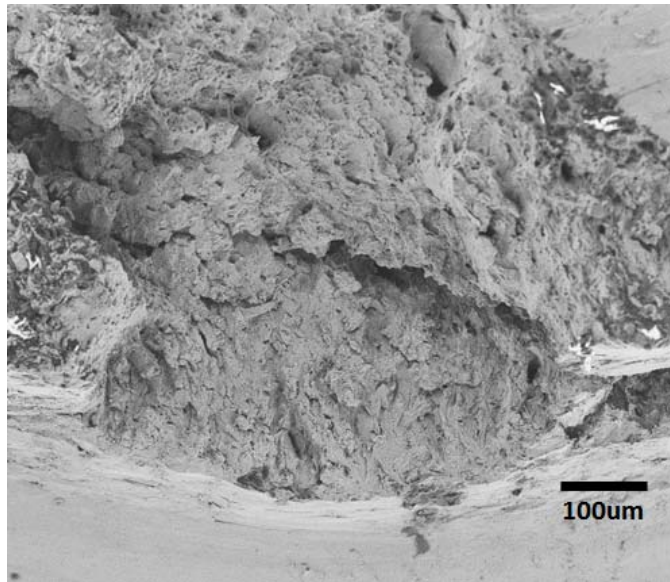


**Figure 4-11 Top: A thumbnail-shaped crack in a notched sample strained in Lot 2 FGE containing 6ppm Cl. Bottom: The brittle area showed a transgranular crack morphology.**

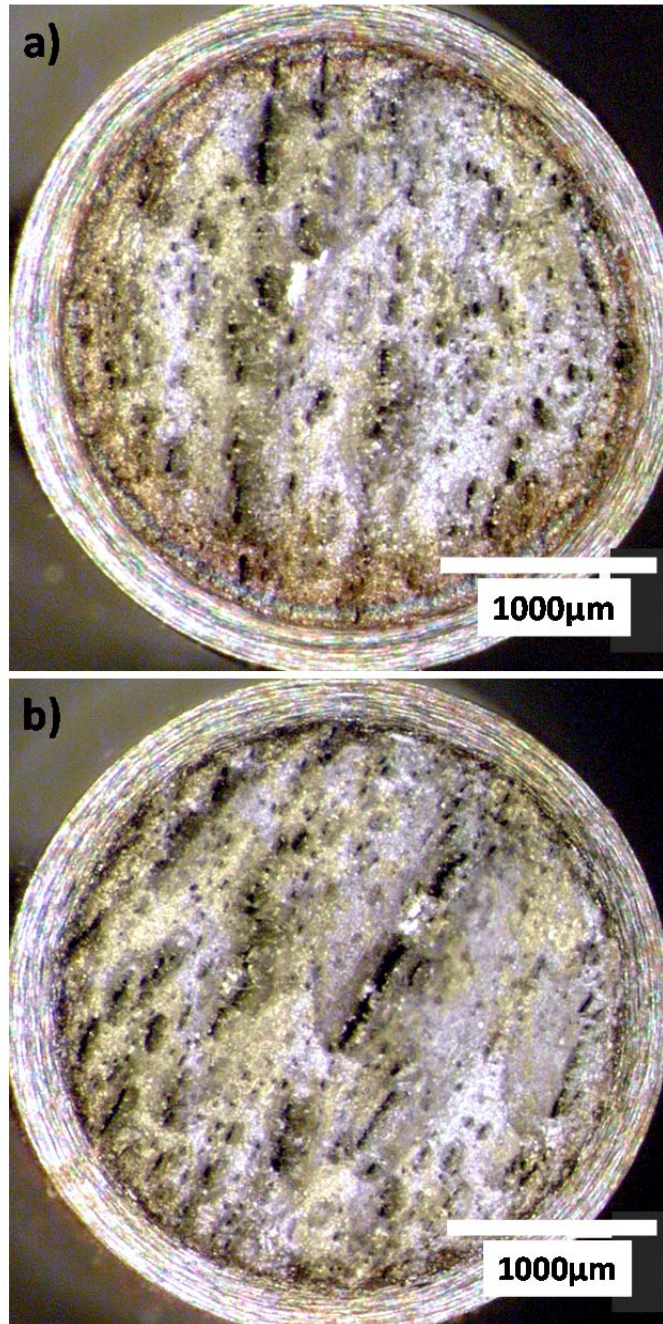


**Figure 4-12 Optical stereo micrographs of samples strained in lot 2 FGE. OCP was measured (salt bridge was present) during straining of the sample in a). This sample exhibited a continuous ring of transgranular SCC. No electrochemistry was performed during straining of the sample in b).**

Evidence exists in many instances [64 , 65, 103] that in mixed alcohol/water environments, water molecules form clusters or chains, making these solutions inhomogeneous on the microscale. In early research on corrosion of iron and steel in

organic solvents, de Anna proposed that any water in the solvent is present in higher concentrations at the metal/solution interface, forming a chemisorbed monolayer on the electrode surface [52]. Sodium chloride is highly soluble (26.5 mass fraction) in water and very sparingly soluble in ethanol (0.055 mass fraction) (see Table 2-1). It is possible then, in this steel/FGE system, that LiCl or NaCl is preferentially solvated by water, which concentrates at the electrode surface, producing a concentrated water/Cl<sup>-</sup> environment which differs from the bulk. If we approximate 10ppm Cl<sup>-</sup> to 10mg/L and assume that 95% of the Cl<sup>-</sup> ions travel with water molecules to the electrode surface, the near-surface concentration of Cl<sup>-</sup> ions (assuming 0.8 vol% water) is approximately 1200ppm, more than two orders of magnitude higher than in the bulk solution.

#### **4.6 Discussion of Results and Comparison to Similar Studies**

Similar studies on effects of ethanol composition on SCC of carbon steels showed that in SSRT with smooth specimens, specimens consistently exhibited intergranular SCC when chloride content was low, which transitioned to transgranular SCC when dissolved Cl<sup>-</sup> was added [19]. In the same study, it was noted that no SCC occurred in FGE obtained from a producer, whereas moderate to severe SCC occurred in user FGE samples. However, electrochemical measurements were performed during all SSRT in the study using a similar reference electrode and salt bridge filled with a 1M LiCl-Ethanol electrolyte. In light of the results presented in this chapter, the presence of the electrode may have contributed to SCC susceptibility in these prior studies.

## 4.7 Chapter Summary and Conclusions

SSRT were conducted on notched X60 samples in eight different commercial FGE environments. Test environments included FGE from three different feedstocks (corn, sugarcane, and cellulose), as well as corn ethanol from both user and producer conditions. Based on GC-MS, ICP, CIE, Karl Fischer, and pHe analysis, no significant compositional differences were detected between the commercial FGE samples prior to testing. In SSRT conducted in as-received FGE (no possible Cl<sup>-</sup> contamination), fracture surfaces of all but one X60 sample exhibited ductile fracture evidenced by a dimpled microvoid coalescence morphology to the edges of the fracture area. One specimen strained in a producer ethanol distilled from corn (Lot 8) exhibited a small region of mixed mode intergranular-transgranular fracture, but this result appeared to be anomalous, as it was not repeatable. No evidence of SCC was found in all other SSRT conducted on notched X60 tensile samples in as-received commercial FGE environments, regardless of ethanol feedstock or producer/user condition.

Moderate SCC, in the form of a partial rim of brittle failure on the fracture surface, was found in SSRT in which *in-situ* open-circuit electrochemical potential was measured. Analysis of FGE environment post-SSRT revealed that chloride contamination of less than 10ppm had occurred during SSRT. In SSRT where small quantities of Cl<sup>-</sup> were deliberately dissolved into the environment in amounts equivalent to that leaked from the reference electrode, only mild SCC was exhibited. The distribution of Cl<sup>-</sup> and water may differ greatly at the steel/FGE interface from that within the bulk FGE solution; however, X60 steel is susceptible to SCC when Cl<sup>-</sup> concentration of less than 10ppm is present in the bulk commercial FGE environment.

## **EFFECTS OF COMMON CONSTITUENTS AND CONTAMINANTS ON SCC AND CORROSION OF X65 IN FGE AND SFGE**

### **5.1 Introduction**

It was demonstrated and discussed in the previous chapter that feedstock-based and processing-based differences in the chemical composition of commercial FGE do not have a significant effect on the SCC susceptibility of pipeline steels in SSRT. In this chapter, effects of other contaminants or additives present in FGE which are not inherent from distillation, specifically water, chloride, acetic acid, inhibitor, denaturant, and dissolved oxygen, on pipeline steel SCC susceptibility are investigated. To control variations due to different processing source and standard additives (inhibitor, denaturant) in FGE, a simulated fuel grade ethanol (SFGE) of composition shown in Table 3-3 Composition of baseline simulated fuel grade ethanol used in this study was used for testing in cases where isolation of individual effects of water content, chloride content, and pHe was desired. This simulated environment has been used for this purpose in several prior studies [18, 19, 78, 83, 104]. Comparisons are made between commercial FGE environments and simulated FGE environments used in these and prior studies of SCC of carbon steel.

## 5.2 Denaturant and Inhibitor Effects

To investigate effects of denaturant and inhibitor on SCC in FGE, three additional FGE samples were obtained from the producer of Lot 5 FGE. Lot 5 contains inhibitor and denaturant, and for the purposes of this study is referred to as standard FGE (FGE-S). A virgin FGE sample containing no inhibitor or denaturant (Virgin FGE), a sample containing inhibitor but no denaturant (FGE-WOD), and a denatured sample containing no inhibitor (FGE-WOI) were obtained. The commercial inhibitor, Innospec DCI-11, is widely used as a corrosion inhibitor in gasoline and FGE. A sample of the denaturant had been previously characterized by GC-MS and its main contents were identified as 2-butenal, toluene, cyclohexane, octane, and xylene. Denatured FGE samples contained approximately 2 vol% of the denaturant, in accordance with ASTM 4806 [55]. For proprietary reasons, inhibitor samples could not be obtained for direct chemical analysis. Water content, pHe, and conductivity of the as-received samples are summarized in Table 5-1. Samples containing denaturant were slightly more conductive than samples without denaturant. Cyclic polarization tests performed on X65 in each of the four types of FGE showed that denaturant lowered the corrosion potential ( $E_{\text{corr}}$ ) of the steel, and presence of inhibitor lowered  $E_{\text{corr}}$  further (Figure 5-1).

**Table 5-1 Water content, pHe, and conductivity of FGE samples**

<b>FGE type</b>	<b>pHe</b>	<b>Water content (vol%)</b>	<b>Resistivity (k<math>\Omega</math>-cm)</b>	<b><math>E_{\text{corr}}</math> (V vs Ag/AgCl/EtOH)</b>
FGE-S	7.6	1.1	40	-0.029
FGE WOI	7.9	1.1	100	0.039
FGE WOD	7.8	1.1	40	-0.028
Virgin FGE	6.5	1.1	100	0.144

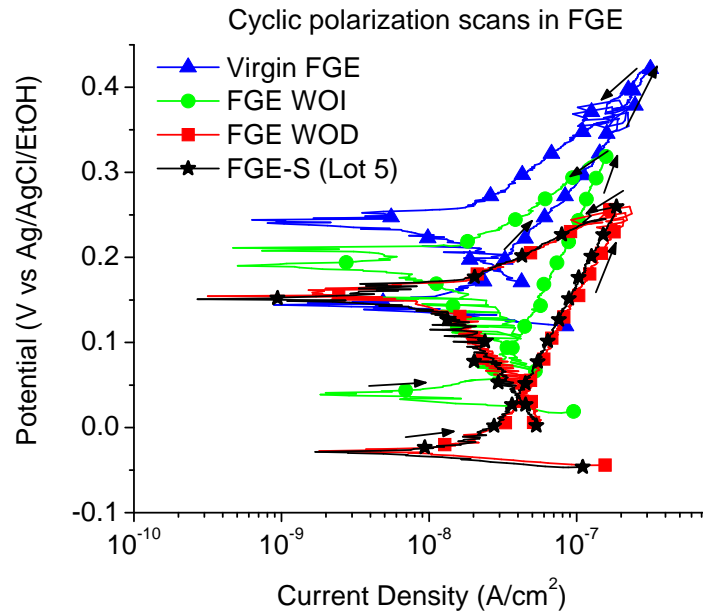


**Figure 5-1 Cyclic polarization scans in commercial virgin FGE (no added inhibitor or denaturant), FGE containing denaturant only (FGE WOI), inhibitor only (FGE WOD) and both inhibitor and denaturant (FGE-S).**

Slow strain rate tests on smooth specimens were conducted in the environmental conditions listed in Table 5-2. Two tests were done in each environment: one in the as-received FGE and one in which 150ppm Cl<sup>-</sup> was dissolved.

**Table 5-2 Summary table of SSRT for inhibitor/denaturant effects on SCC**

FGE sample name	Denaturant	Inhibitor	Dissolved Cl <sup>-</sup> added (ppm)	
			Test 1	Test 2
FGE-S	Y	Y	None	150
FGE WOI	Y	N	None	150
FGE WOD	N	Y	None	150
Virgin FGE	N	N	None	150

No cracking was observed in any of the as-received FGE. Upon adding 150ppm  $\text{Cl}^-$  to each test environment, SCC became apparent. Percent reduction in area (%RA) was calculated (Figure 5-2) and crack density evaluated for each sample (Figure 5-3). Maximum tensile stress ( $\sigma_{\text{max}}$ ) values were tabulated as well. SSRT maximum stress is a criterion that has been used in literature to discern SCC susceptibility in aqueous environments [105] as well as in FGE environments [19, 70]. When  $\sigma_{\text{max}}$  was plotted versus FGE environment and compared to that in an inert environment (air) (Figure 5-4), no trend was seen relating maximum stress to visual evidence of SCC. However, %RA results for the tested tensile samples were as expected; %RA for specimens strained in as-received FGE environments was comparable to that in air, where no cracking was observed on polished cross sections. %RA decreased significantly in environments with 150ppm dissolved  $\text{Cl}^-$  where visible cracking did occur. In these cases, crack density was greater in both of the FGE samples without inhibitor (Virgin FGE and FGE WOI). %RA was comparable for Virgin FGE, FGE WOI, and FGE-S. These results indicate that presence of inhibitor may slow crack initiation, but does not affect crack propagation once initiation has occurred. The fact that maximum stress did not correlate with SCC susceptibility indicates that the majority of crack propagation occurs at stresses near or beyond  $\sigma_{\text{max}}$  and plastic deformation plays a significant role in SCC in FGE in SSRT.

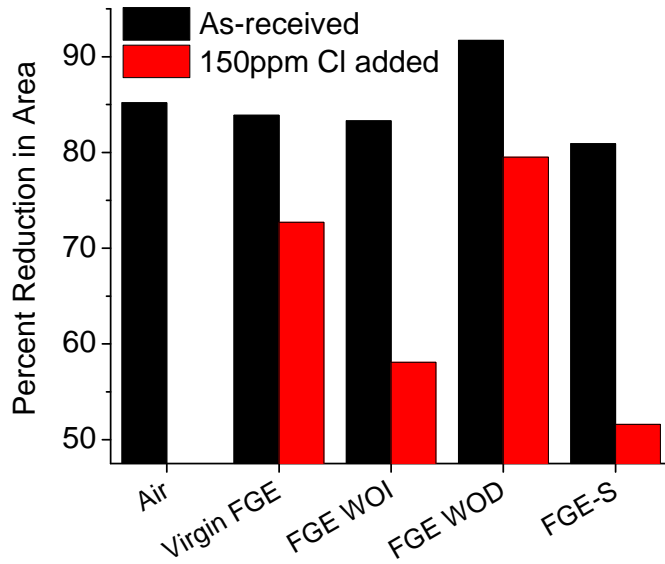


Figure 5-2 Percent reduction in area of specimens before and after cracking.

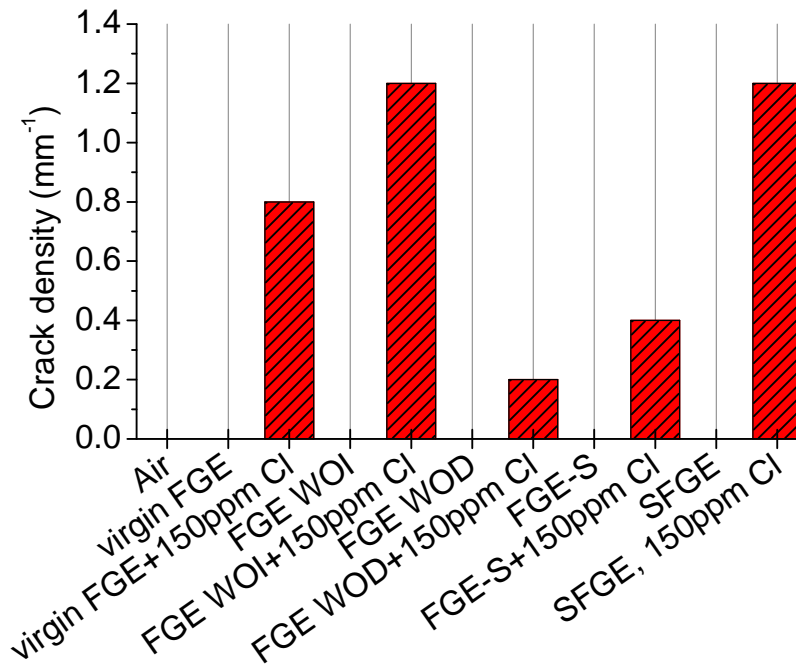
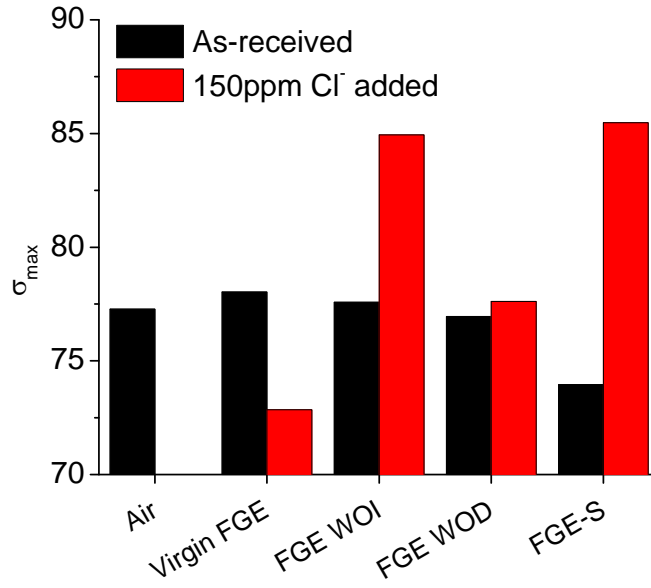
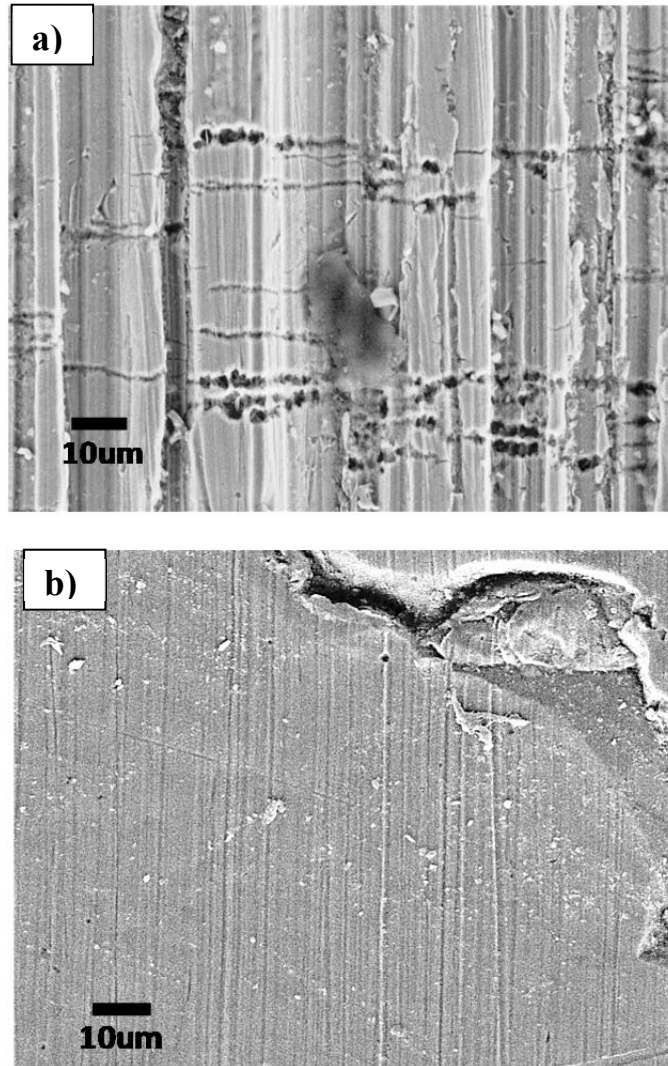


Figure 5-3 Number of cracks per millimeter on specimens strained in FGE in presence and absence of denaturant and inhibitor. Data for SFGE has been added for comparison.



**Figure 5-4 Maximum stress ( $\sigma_{\max}$ ) sustained by SSRT specimens in the FGE environments was not affected in a predictable manner by presence of SCC.**

To confirm the effects of inhibitor on crack initiation, tensile tests were done in which a carbon steel specimen was statically loaded at 110% of yield stress in the desired aerated FGE environment for 15 days, then visually evaluated for evidence of crack initiation sites. Static loading eliminated the factor of crack growth so crack initiation could be isolated. Samples loaded in FGE-WOI displayed localized attack at areas of high strain accumulation (Lüder's bands) (Figure 5-5a), perpendicular to the loading direction, whereas samples strained in FGE-S did not exhibit similar attack (Figure 5-5b). This result supports the conclusion that the presence of inhibitor may slow the crack initiation process.



**Figure 5-5 Surface of tensile samples statically strained in a) FGE-WOI and b) FGE-S. The sample strained in FGE-WOI exhibits localized dissolution at Lüder's bands, areas of high strain accumulation at the surface.**

### **5.3 Chloride Thresholds for SCC in FGE**

To evaluate the threshold  $\text{Cl}^-$  concentration necessary to enable SCC of pipeline steel in FGEs, NaCl was dissolved into samples of FGE WOI in quantities equating to 0.5, 1, 3, 5, 10, 32 and 150ppm of dissolved  $\text{Cl}^-$  ion. Smooth X65 samples strained to failure at a rate of  $1 \times 10^{-6}$  in/s at each  $\text{Cl}^-$  level were cross sectioned and evaluated optically and in

an SEM for the existence of stress corrosion cracks. No cracking was found below 5ppm  $\text{Cl}^-$ , while one very small (approximately  $25\mu\text{m}$  deep) crack was found in FGE containing 5ppm  $\text{Cl}^-$  (Figure 5-6 (a)). Above this threshold, crack density increased as chloride content increased. All cracks were transgranular. In Figure 5-6(b), crack yawning and material flow are indicative of the extensive plastic deformation occurring within the material before and during cracking. Presence of SCC did not affect  $\sigma_{\text{max}}$  (Figure 5-7), but did affect %RA (Figure 5-8).

In order to compare SCC susceptibility of carbon steel in SFGE and commercial FGE, SSRT were done in FGE-S and SFGE with 0, 10, and 150PPM dissolved  $\text{Cl}^-$ . Based on measured crack densities and %RA (Figure 5-8), SCC in SFGE appeared to be more severe than that in either of the commercial FGE environments. A similar study done on X65 steel in SFGE solutions yielded comparable results [18]; In the absence of chloride in SFGE, no cracking was seen, but transgranular cracking occurred with additions of as few as 1ppm  $\text{Cl}^-$ . In FGE-S, no cracking was found when  $\text{Cl}^-$  was at the 10ppm level, indicating that along with decreasing the number of cracks (demonstrated above in 0), presence of the corrosion inhibitor may raise the  $\text{Cl}^-$  threshold for SCC initiation.

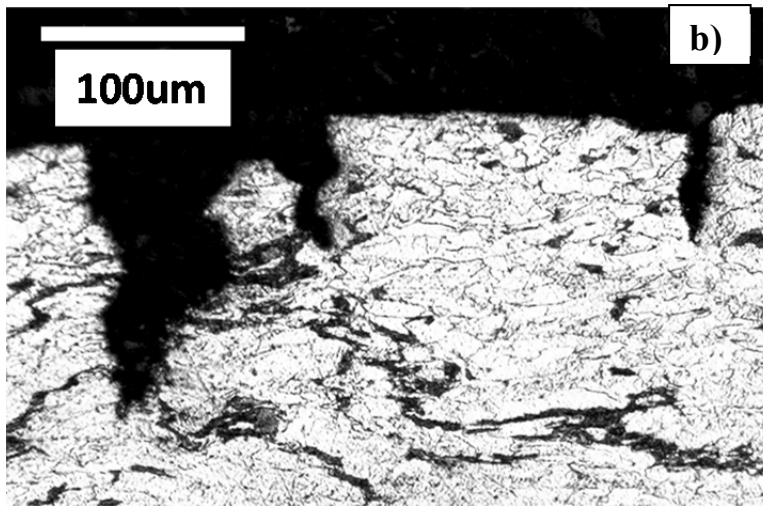
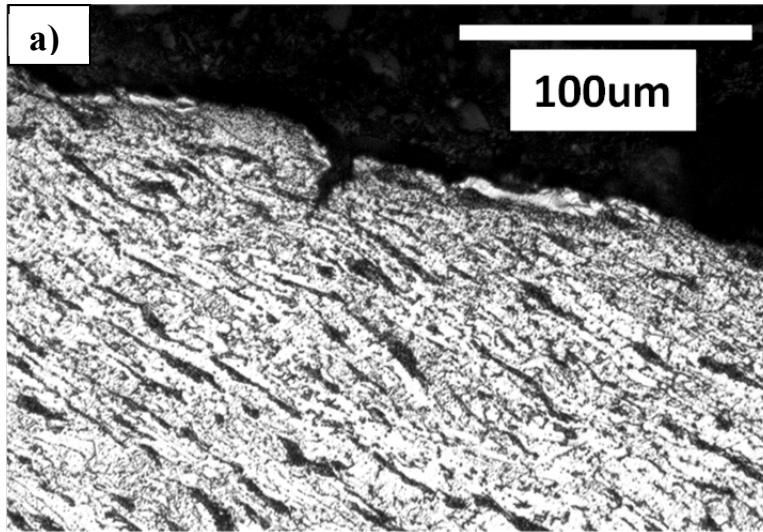


**Figure 5-6 Transgranular SCC seen on polished cross sections of SSRT specimens strained in FGE WOI with (a) 5ppm Cl and (b) 150ppm Cl. Light-colored grains are ferrite, and darker areas are pearlite.**

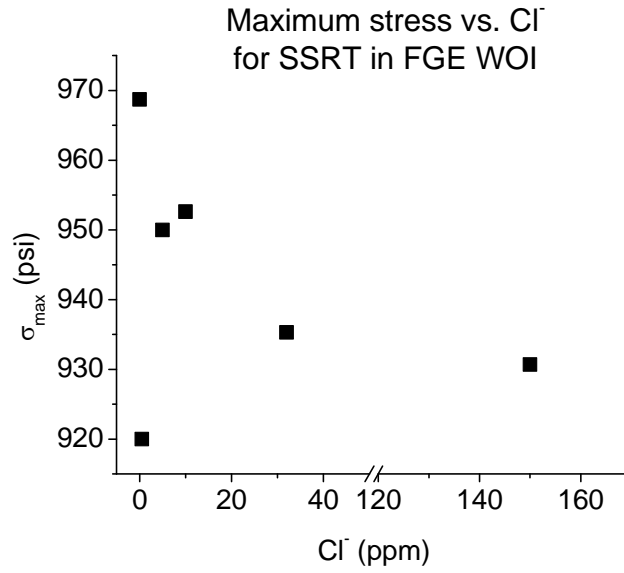


**Figure 5-7 Maximum stress vs.  $\text{Cl}^-$  content for SSRT done in FGE WOI with varied levels of dissolved  $\text{Cl}^-$ .**

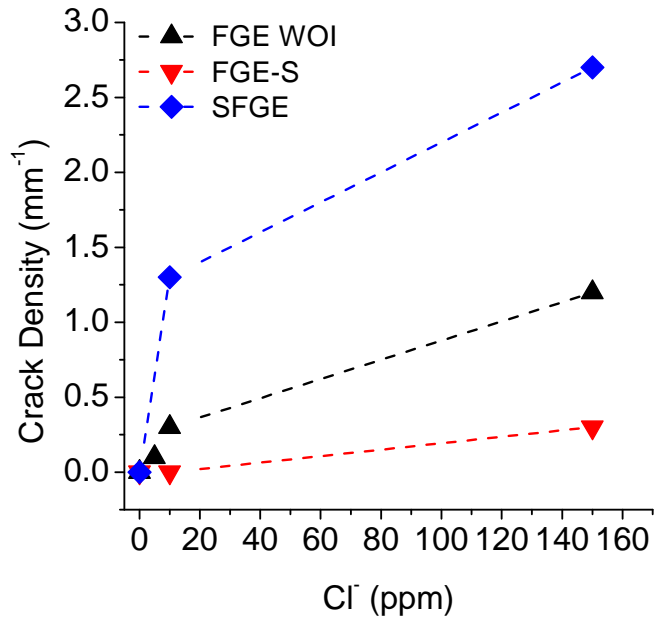
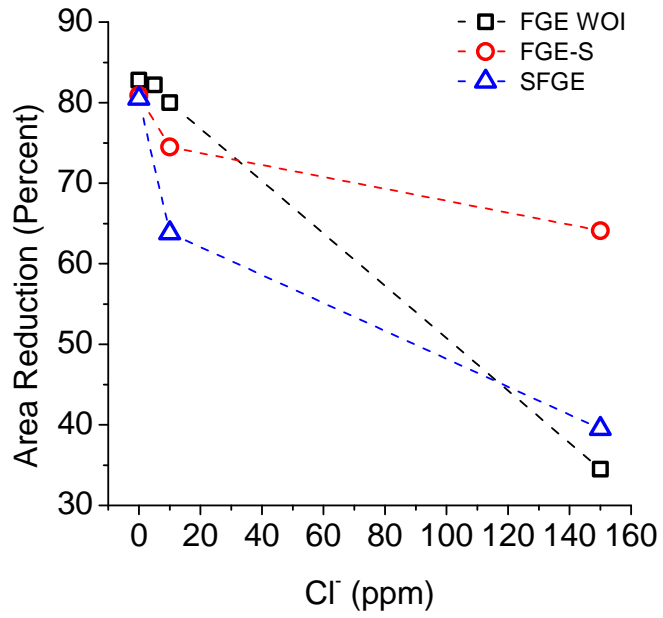


Figure 5-8 A comparison of SCC severity based on %RA and crack densities vs Cl<sup>-</sup> in FGE, FGE WOI, and SFGE

### 5.3.1 Electrochemical measurements

Cyclic polarizations in the tested FGE WOI solutions (Figure 5-9) revealed that increasing chloride did cause passivity to break down more readily as potential was increased, indicated by the decrease in slope of the  $i$  vs  $E$  curves. Increasing  $\text{Cl}^-$  also led to increase in the hysteresis loop size upon reverse potential scan for cyclic polarization curves and a decrease in  $E_{\text{prot}}$  as potential was stepped downward, indicating an increase in potential range for which pitting can occur. Polarization samples were pitted after undergoing cyclic polarization in  $\text{Cl}^-$ -containing FGE. The fact that OCP of a statically immersed coupon does not change appreciably upon chloride addition may indicate that  $\text{Cl}^-$  does not affect the nature of the passive film in the un-polarized static condition.  $\text{Cl}^-$  effects are seen in the form of pits when the coupon's surface film is broken down at high anodic overpotentials.

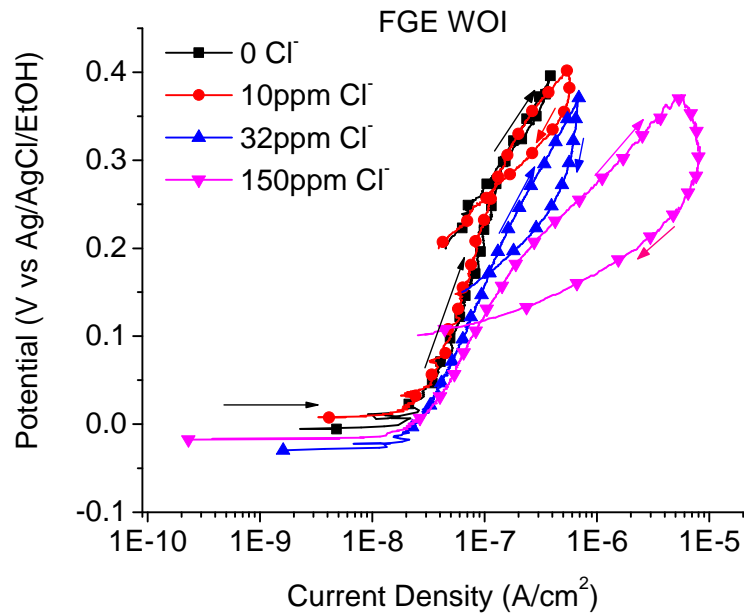


Figure 5-9 Cyclic polarization in FGE WOI with varied  $\text{Cl}^-$  levels

In prior work on SFGE [77, 104], it was shown that  $E_{\text{prot}}$  occurred below the original OCP in  $\text{Cl}^-$  containing SFGE, contrarily to the results shown here in commercial FGE without inhibitor. The added acetic acid in SFGE produces a significantly lower pHe than that in FGE, which likely creates a more aggressive environment within the occluded pit areas, hindering the repassivation process.

#### **5.4 Water Effects on SCC and Corrosion Behavior**

Small changes in the water concentration of alcohol environments can significantly affect the passivation behavior of iron and steel [60, 67]. In anodic dissolution SCC mechanisms, the nature of the passive film can determine SCC susceptibility. To investigate changes in SCC behavior with varying presence of water, SFGE was utilized instead of commercial FGE so that environments with water levels as low as 500ppm could be achieved without subjecting FGE to a chemical drying process, which can alter the pHe [67]. Baseline SFGE containing 10ppm  $\text{Cl}^-$  to ensure SCC occurrence (composition in Table 3-3) and varied amounts of water (0.05 vol%, 0.5 vol%, 1 vol%, 2.5 vol%, and 5 vol% water) was used for comparing SCC severity on smooth SSRT specimens. Further, to obtain electrochemical current data during SSRT, these tests were performed with counter and reference electrodes present in the cell, and open circuit potential was held throughout straining so that current could be measured. OCP measurements performed before straining indicate that OCP increases as water content decreases (Figure 5-10). In light of this, the slight variations in OCP among the different FGE lots may perhaps be attributed to the variations of water content within the FGE. Differences in OCP generally imply that cathodic surface reactions and the

thermodynamic stability of surface products differ among the given environmental conditions. The nature of passive film formed depends on the cathodic reaction and the stability of specific compounds, and thus depends on the potential of the electrode surface [28].

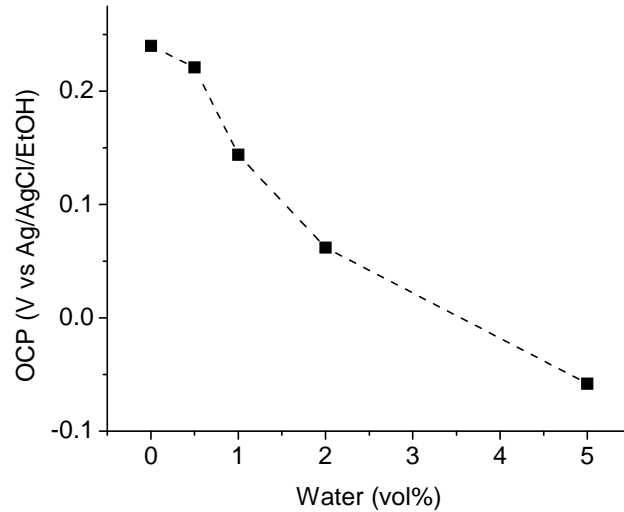


**Figure 5-10 Changes in open circuit potential (OCP) of X65 carbon steel with SFGE water content variations**

Images of fractured samples can be seen in Figure 5-11. Samples strained in 0.05, 0.5, 1, and 2 vol% water content exhibited SCC. In SSRT where water content was increased to 5 vol%, pitting and general corrosion were the dominant forms of degradation throughout the entire gauge region of the sample, and SCC was eliminated. SFGE with low water content did not produce any visible corrosion products on the sample surface. Tarnishing became more visible, particularly in the necked portions of the sample, as water content increased to 1 vol%, 2 vol%, and 5 vol%. A good indicator for SCC was %RA (Figure 5-12), which remained close to that in air (given above in

Figure 5-2) for higher water content SFGE where no cracking was observed, and low in the low water content SFGE where significant cracking was seen.

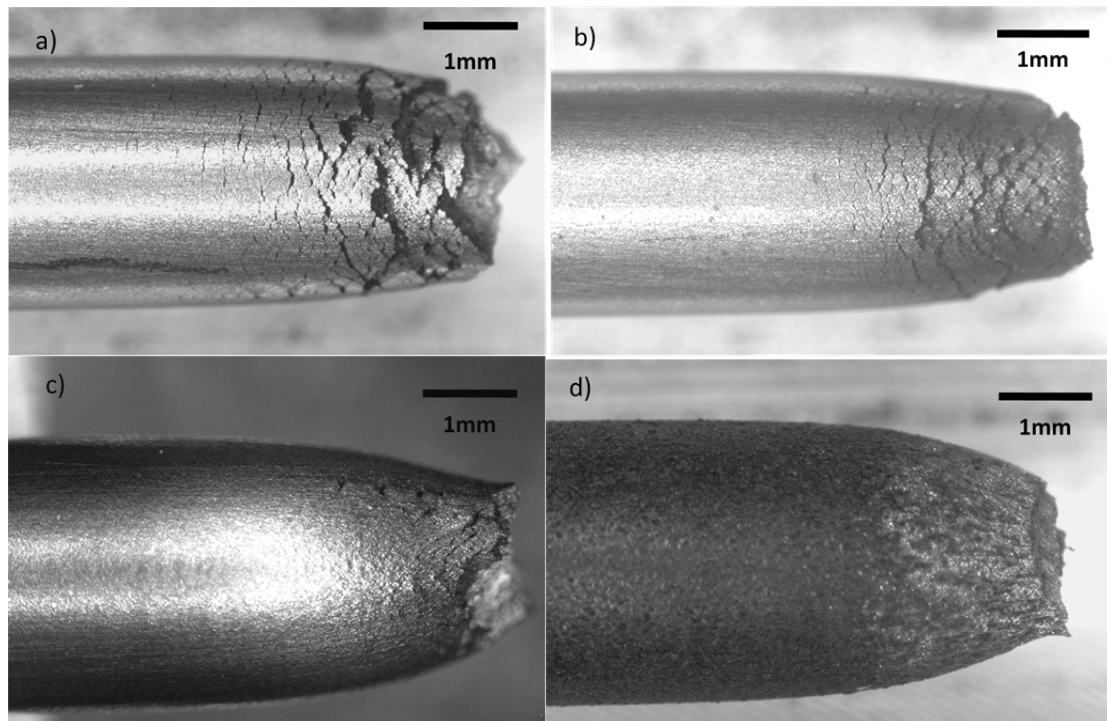


**Figure 5-11 smooth tensile samples strained to failure in SFGE with a) no added water, b) 1 vol % water, c) 2 vol % water, d) 5 vol% water**

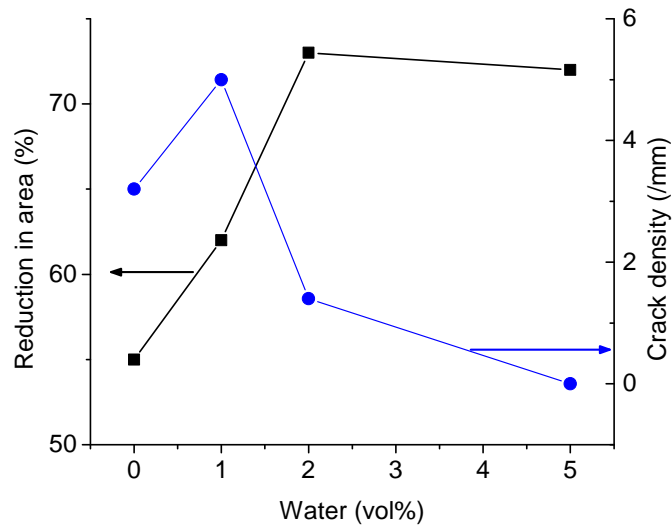


**Figure 5-12 %RA and crack density versus water content. At 2% water content, SCC was markedly less severe than in lower water content SFGE, and thus necked to a greater extent before failure**

In SFGE with 0.05 to 1 vol% water, global current measured on the sample gauge during straining (Figure 5-13 a, b) remains constant through the elastic strain regime. It appears that the rapid current increase occurs very close to the upper yield point in both cases. A test was done in the anhydrous SFGE in which the load was cycled once during current measurement to ascertain the repeatability of the stress value at the onset of anodic activity (Figure 5-14 a)). Stress level for anodic activity onset was repeatable, and occurred at 66.5 ksi (455 MPa) in the anhydrous and 61 ksi (420.6 MPa) in the 1 vol% water environment (Figure 5-14 b)). Anodic current activity decays until lower yield stress is reached, and a second, higher current activity increase is evident. During plastic straining, overall current decreases but small current spikes and subsequent decay continue to occur, indicating some interplay between passivation and anodic dissolution. In SFGE containing 5 vol% water (Figure 5-12 c), however, no sharp current spike occurs at yield, and current vacillates between anodic (positive) and cathodic (negative)

values, indicating local anodic and cathodic activities on the working electrode surface. The current was anodic on average, with a mean value of 11.8mA. In comparison, average measured current values for steel samples exposed to 0.05% and 1 vol% water content SFGE were 18 $\mu$ A and 6.4 $\mu$ A respectively, signifying a 3 orders of magnitude greater oxidation current occurring in high water content SFGE. Post-test solution color change indicated that as water content increased, quantity of dissolved Fe increased, which was confirmed by solution analysis via inductively coupled plasma spectroscopy. ICP results are given in Table 5-3.

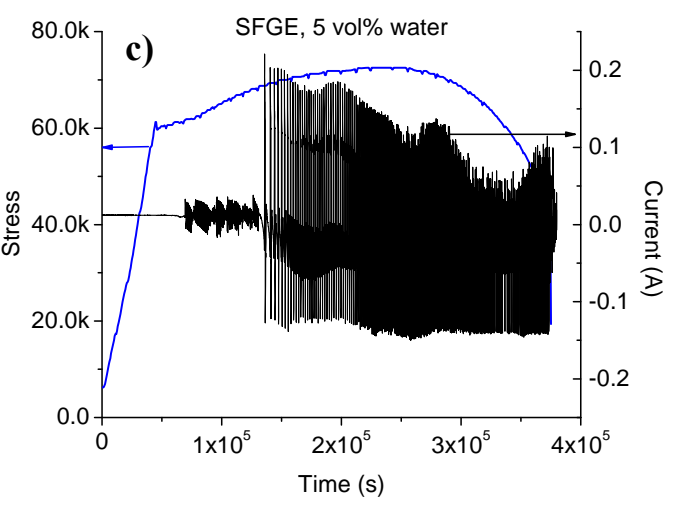
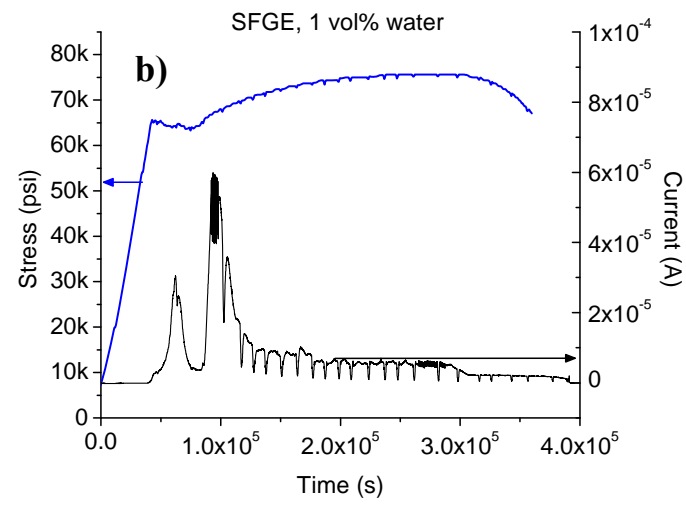
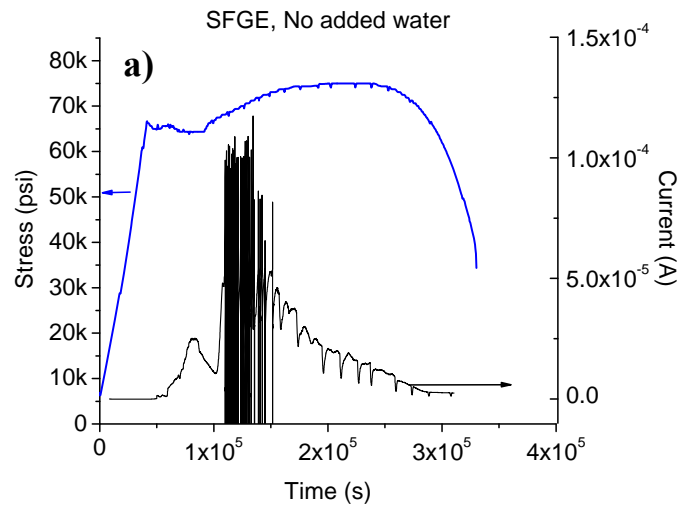


**Figure 5-13 Current measurement during straining in SFGE containing (a) 0.05 vol%, (b) 1 vol%, and (c) 5 vol% water**

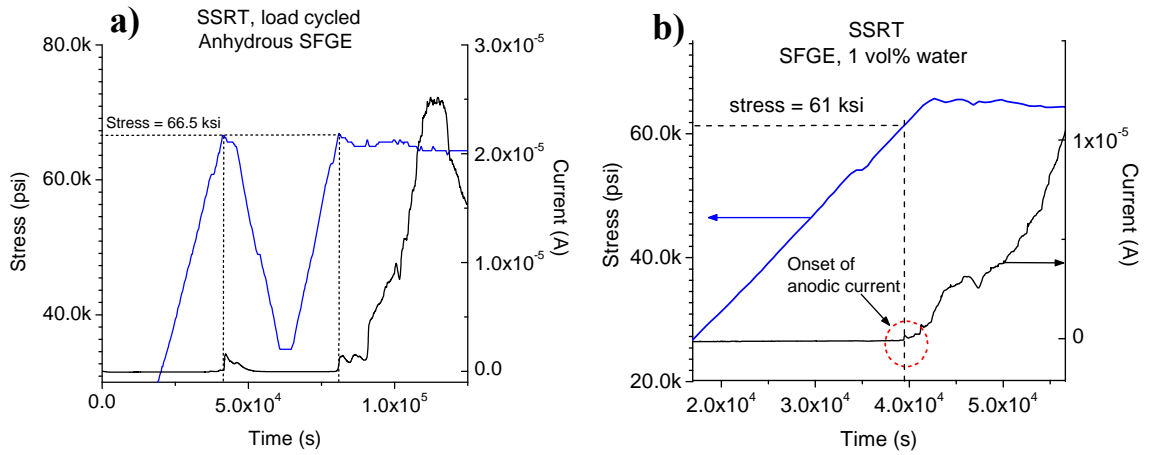


Figure 5-14 Enlarged stress vs time plot showing stress at the onset of anodic current for a) anhydrous SFGE, and b) baseline SFGE

Table 5-3 Post-test solution color change indicating increase in dissolved Fe at 5 vol% water content

SFGE water content	OCP value potentiostatically held (mV vs Ag/AgCl/EtOH)	Dissolved Fe ( $\mu\text{g/g}$ )	Image of post-test solution color
0.06	240	3.2	
1	132	1.8	
5	11	65	

In the set of tests described above, the steel specimen surfaces were held at constant potential for the duration of testing, and SCC density was significantly higher than in prior tests in SFGE and FGE which had the same Cl<sup>-</sup> content but in which no electrochemical measurements were conducted. This may have been partially due to the leakage of Cl<sup>-</sup> from the salt bridge, but may also have been affected by a potential gradient formed between the polarized surface and the active crack tip areas. Holding the steel potential stable by coupling to a scaled steel specimen did significantly affect the SCC susceptibility of carbon steel in FGE in previous studies [19].

Two additional SSRTs were done in the anhydrous SFGE (water content = 0.05 vol%) (environment composition shown in Table 5-4) with salt bridge present in both test cells: In one test, no electrochemical measurements were made, and in the other, OCP was measured (not applied). Crack density and %RA from these two tests were compared with the test in which OCP was applied (Table 5-5). The data clearly indicate that SCC was less severe when no potential was applied, despite Cl<sup>-</sup> leakage from the reference electrode. Holding the sample at its OCP measured prior to straining did lead to an increase in crack density and decrease in %RA. The un-stressed steel's relatively high OCP in the anhydrous or 1%-water-content SFGE leads to a greater potential difference between active (crack tip) and passive (filmed surface) areas during straining than in 2% or 5% water content SFGE, likely providing a greater driving force for anodic dissolution from areas where film breakdown has occurred.

**Table 5-4 Composition of anhydrous SFGE**

<b>Methanol (vol%)</b>	<b>NaCl (mg/L)</b>	<b>Acetic Acid (mg/L)</b>	<b>Ethanol (vol%)</b>	<b>Measured water content (ppm)</b>
0.5	10	56	Rem.	550

**Table 5-5 Changes in SCC severity when SSRT is potentiostatically held at its original OCP, based on crack density and percent reduction in area of failed specimen.**

<b>Electrochemistry performed</b>	<b>Maximum load (ksi)</b>	<b>%RA</b>	<b>Crack density (mm<sup>-1</sup>)</b>
None	75	64	1.3
OCP measured	74	61	1.1
OCP applied	75	55	3.7

Two possible explanations exist for this phenomenon: 1) By forcibly holding the filmed pipeline steel surface at a steady potential, we have forced a site which becomes active, i.e. acquires a more negative potential, as a result of strain. Thus the driving force for anodic activity is increased, increasing the kinetics of dissolution from the active site; 2) The forced potential gradient has caused evolution of reaction products along the length of the crack, altering the passivation kinetics of the crack tip because of chemistry changes. To verify these proposed processes, more studies are needed to determine the solution composition within the crack. However, in both cases, anodic activity appears to play the most important role in crack initiation and propagation.

### **5.5 Effects of Strain on SCC Initiation and Propagation**

Interrupted slow strain rate tests (I-SSRT) are useful in verifying threshold stress of SCC initiation as well as identifying microstructural features where SCC initiation occurs. In an interrupted SSRT, the sample is strained at a constant rate to a predetermined position on its stress-strain curve, and then removed and examined for signs of crack initiation using an optical microscope or SEM. Interrupting the test to look

for cracks at their initiation stage gives information about global stress conditions that must be met for SCC to begin and a means for identifying cracks at their initiation sites. In recent research in SFGE solutions, it was determined by interrupted SSRT that cracking initiated in crevices/pits formed by dissolution of aluminosilicate inclusions [18]. In NNpH environments, interrupted SSRT showed that MnS inclusions and scratches on the pipeline steel surface were preferential sites for SCC initiation [14].

I-SSRT were performed in the environments listed in Table 5-6. Cl<sup>-</sup> and acid were added to ensure cracking to occur. A test in air was done as a control in which no SCC was expected. For each test, a sample was strained in environment until just below yield (point 1 in Figure 5-15), then removed and examined in SEM. The sample was then re-inserted into the SSRT cell and strained again to point 2, 3, and 4, with removal and examination at each point. The same solution was re-used for all portions of the test. Any solution lost on loading and unloading the samples from the cell was replenished with fresh solution.

**Table 5-6 Environment compositions used in interrupted SSRT**

<b>Base Environment</b>	<b>Cl<sup>-</sup> (ppm)</b>	<b>Acetic acid (mg/L)</b>	<b>Initial solution pHe</b>
Air	--	--	--
FGE WOI	100	56	6.0
FGE-S	100	56	6.2

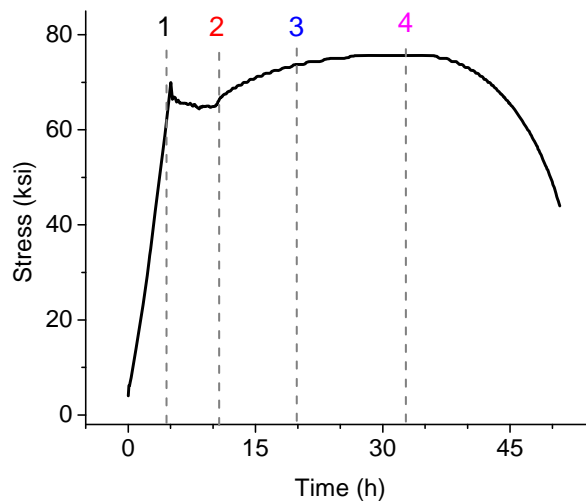


**Figure 5-15 Schematic of loading schedule for interrupted SSRT. Samples were loaded to point 1, then unloaded and examined in SEM. The process was repeated on the same sample for points 2, 3, and 4.**

Images of the I-SSRT samples at each point in air, FGE-WOI and FGE-S are shown in Figure 5-16, Figure 5-17 and Figure 5-18, respectively. As expected, the sample in air showed no signs of stress corrosion cracking at any point. In FGE-WOI, no crack initiation was seen before the yield point. At point 2, some localized dissolution at regions of strain accumulation became apparent. At point 3, localized dissolution at strain accumulated areas was more noticeable, and small cracks that appeared to initiate at areas of steel separation from surface intermetallic particles began to propagate into the steel matrix. After reaching UTS (point 4), cracks and fissures at regions of cross-slip had widened and begun to propagate. Localized dissolution and cracks/fissures were seen within the necked region only. Similarly, in FGE-S the sample did not show signs of crack initiation prior to yield. Straining to above yield (point 2) produced small initiating cracks. At point 3, cracks were seen emanating from intermetallic particles, and in the

necked region after the final strain increment (point 4), fissures and cracks were present as in the previous sample. Any cracking seen was confined solely to the necked region. These observations from I-SSRT tests help to confirm the conclusions made from electrochemical measurements above, i.e. that crack initiation in SSRT requires stresses beyond yield.

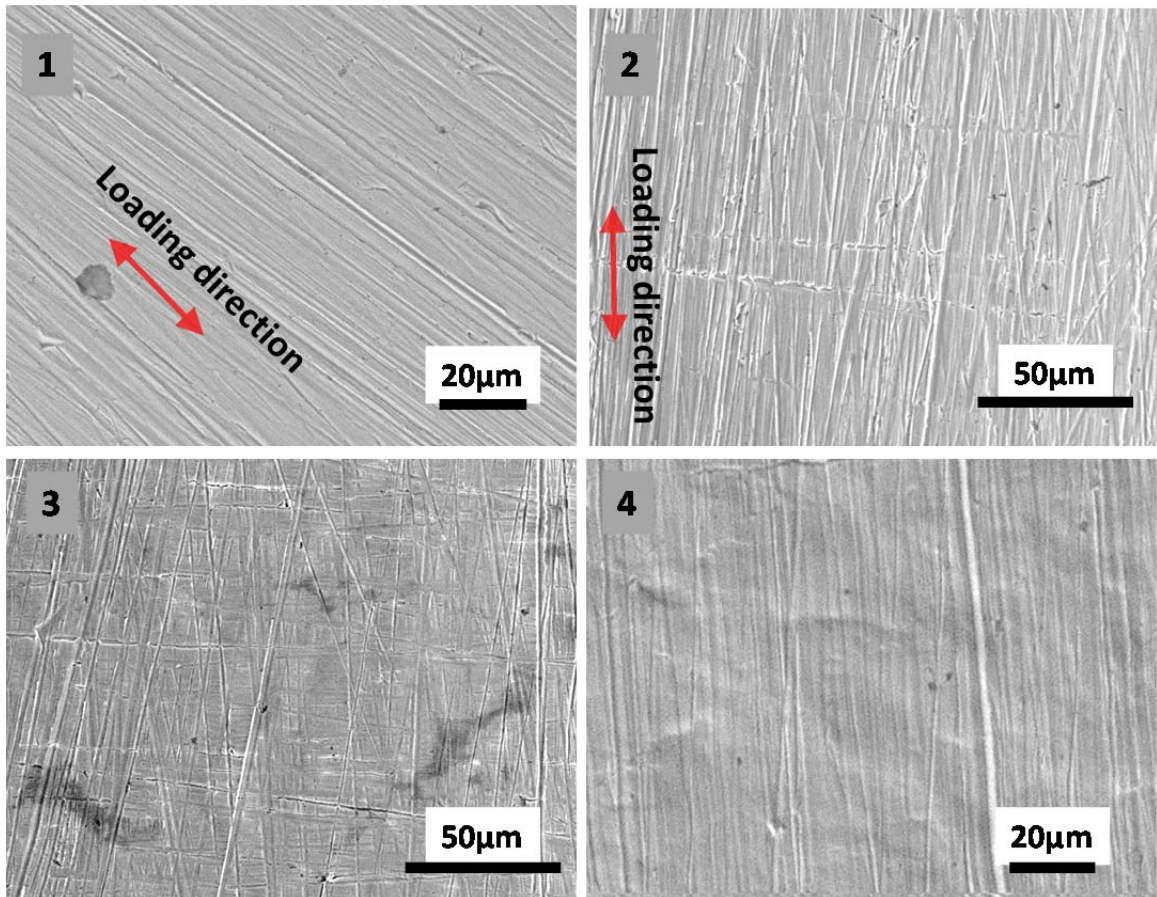


**Figure 5-16 SEM images of the I-SSRT sample strained in air. The straining direction was parallel to polishing lines. The numbering corresponds to the specific stress values shown in Figure 5-15. See text for description of images.**

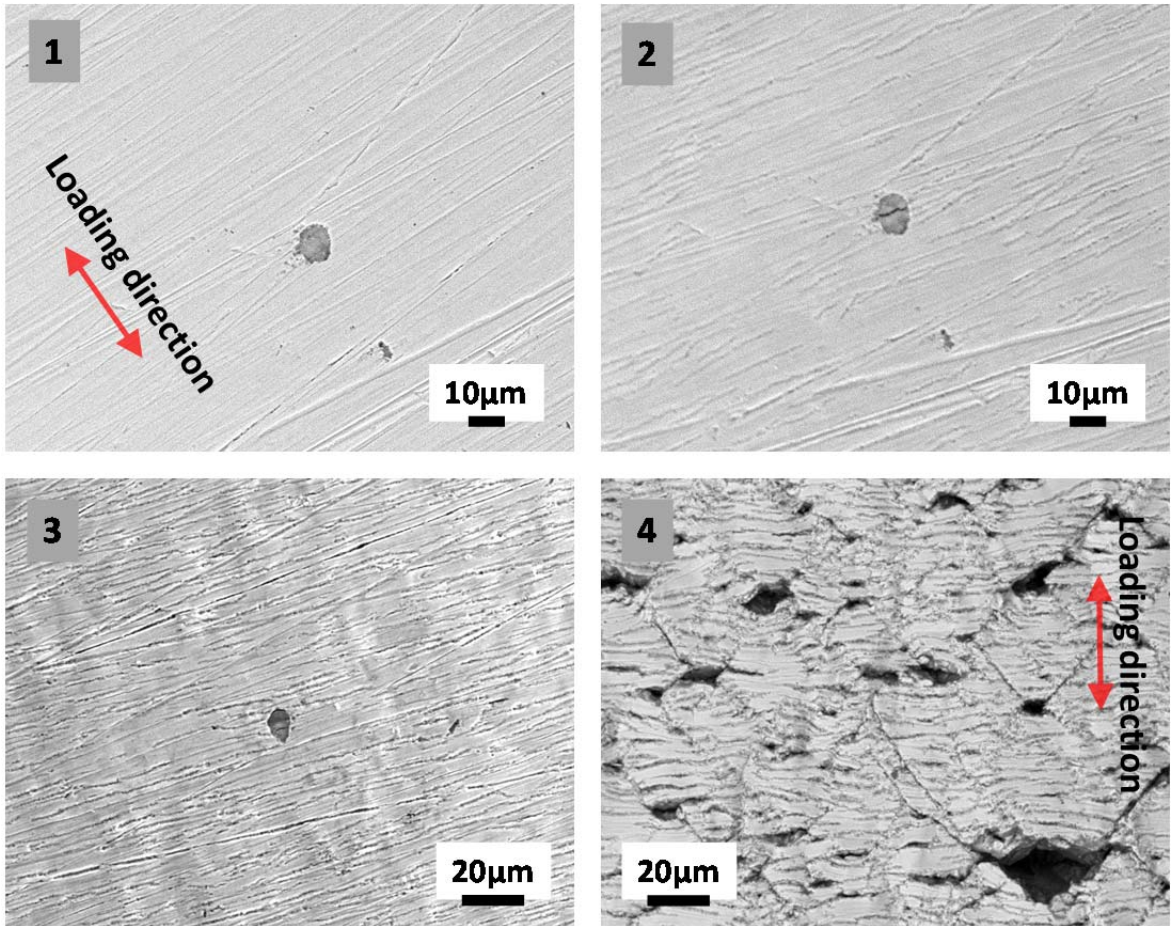


**Figure 5-17 SEM images of the I-SSRT sample strained in FGE-WOI (100ppm Cl<sup>-</sup> and 56ppm acetic acid). The straining direction was perpendicular to polishing lines. The numbering corresponds to the specific stress values shown in Figure 5-15. See text for description of images.**

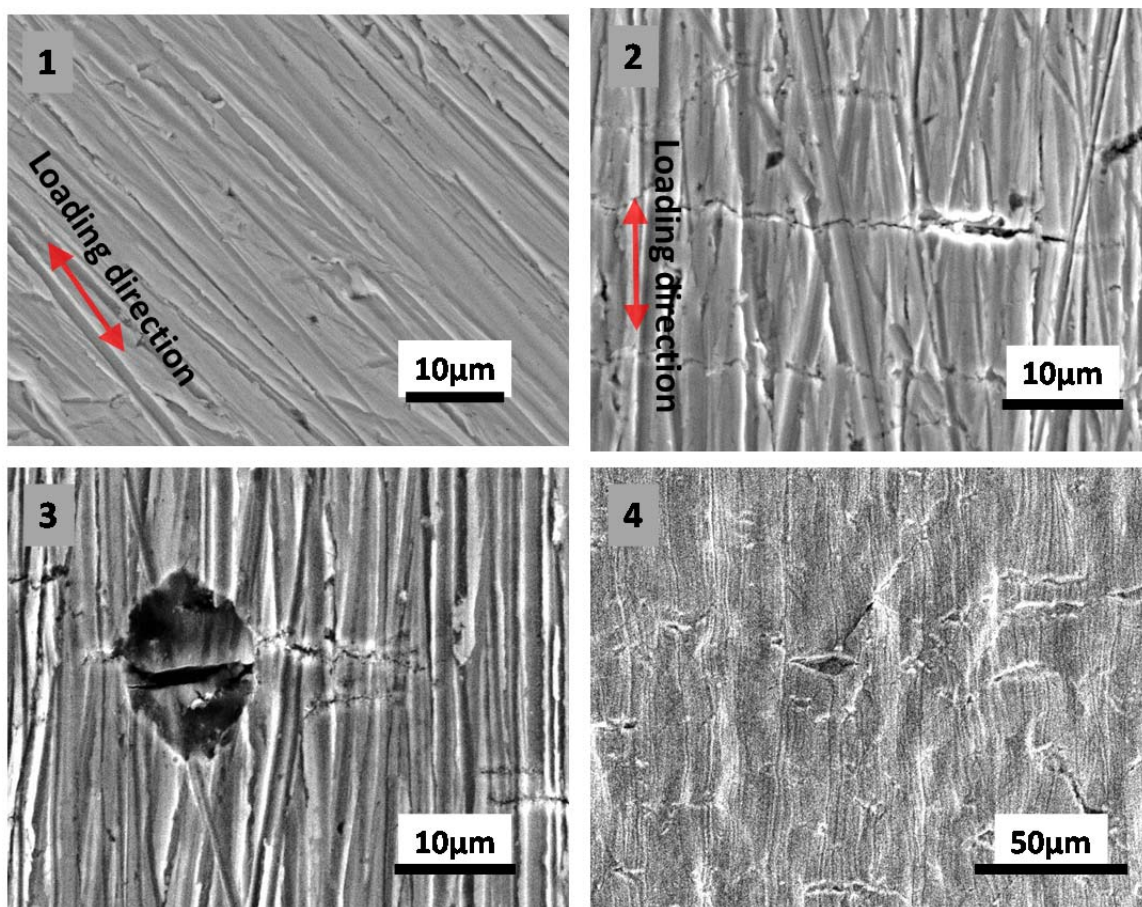


**Figure 5-18 SEM images of the I-SSRT sample strained in FGE-S (100ppm Cl<sup>-</sup> and 56ppm acetic acid). The straining direction was parallel to polishing lines. The numbering corresponds to the specific stress values shown in Figure 5-15. See text for description of images.**

## 5.5 Effects of pHe and Oxygen

To increase the pHe of SFGE, the usual 56ppm acetic acid in the baseline SFGE solution was replaced by 56 ppm of NaOH. Test solution with decreased pHe was formulated by including 10 times the allowable amount of acetic acid (560ppm) to the baseline SFGE. Two SSRT were performed in the alkaline as well as in the acidic SFGE solution. SSRT were also performed in SFGE that was deaerated, i.e. purged with N<sub>2</sub> gas for 90 minutes before as well as during the test. Cl<sup>-</sup> content was varied for the deaerated

tests. Solution compositions and open circuit potentials on static X65 coupons are shown in Table 5-7. Crack density and %RA are summarized for these conditions in Table 5-8.

**Table 5-7 Solution compositions for pHe and oxygen variations**

<b>Environment</b>	<b>Ethanol (vol%)</b>	<b>Methanol (vol%)</b>	<b>Water (vol%)</b>	<b>NaCl (mg/L)</b>	<b>Acetic Acid (mg/L)</b>	<b>pHe</b>	<b>OCP (V vs Ag/AgCl/EtOH)</b>
<b>Alkaline SFGE</b>	98.5	0.5	1.0	10	-- (56mg/L NaOH)	12.4	-0.120
<b>Acidic SFGE, No Cl<sup>-</sup></b>	98.5	0.5	1.0	0	560	4.2	0.155
<b>Acidic SFGE, with Cl<sup>-</sup></b>	98.5	0.5	1.0	150	560	4.2	0.160
<b>Deaerated SFGE</b>	98.5	0.5	1.0	0, 10, 51, 150	56	5.4	-0.220

**Table 5-8 Summary of results of tests with pHe variations and deaeration**

<b>Environment</b>	<b>SCC?</b>	<b>Crack Density (/mm)</b>	<b>%RA</b>
Alkaline SFGE	N	0	80.1
Acidic SFGE, No Cl <sup>-</sup>	N	0	73.8
Acidic SFGE, with Cl <sup>-</sup>	Y	3	51.5
Deaerated SFGE (all Cl <sup>-</sup> levels)	N	0	74.0 (average)

Addition of NaOH caused OCP to decrease to -200mV vs Ag/AgCl/EtOH, as did removal of oxygen (deaeration). SCC did not occur in the alkaline SFGE or in any of the deaerated SFGE, regardless of Cl<sup>-</sup> content, and thus %RA was constant in all deaerated tests (Figure 5-19). Increasing the acidity by adding up to 560ppm acetic acid, or 10 times the maximum allowable quantity [55], without the presence of chloride did not

produce cracking. When  $\text{Cl}^-$  was added to the acidic SFGE, cracking was present and severe, at a crack density of 3cracks/mm.

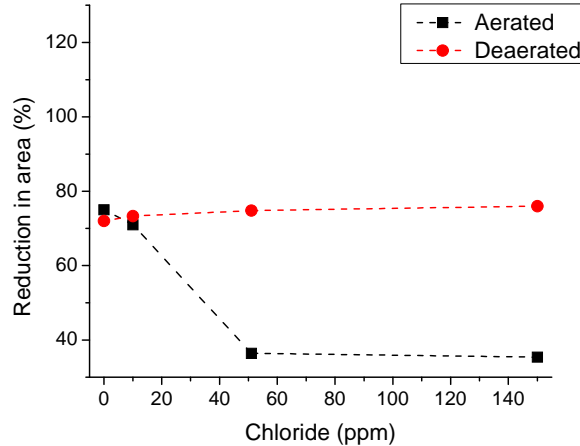


**Figure 5-19 Reduction in area vs. chloride content for SSRT in aerated and deaerated SFGE**

Similar results were found in prior studies [18 , 19, 106]. Specifically, Lou et al. [18] showed that high pH prevented SCC in SSRT, but no mechanism was discussed.  $\text{NH}_4\text{OH}$  was found to prevent SCC as well [106], but the mechanism of this SCC inhibition has not yet been elucidated. Both Lou et al. and Sridhar et al. [19] remarked on the importance of the presence of oxygen to SCC, and noted that SCC was prevented in deaerated SFGE and FGE test environments. Gui et al [75] proposed that the crack tip becomes deaerated, and thus oxygen is participating in two ways: 1) aiding in the passivation of crack walls, and 2) creating a potential gradient between the steel surface and crack entrance where oxygen is available and the deaerated crack tip, which in turn drives  $\text{Cl}^-$  to migrate into the crack. However, deaeration was linked to larger quantities of Fe dissolution during SSRT [18], implying that removal of oxygen may not only prevent a potential gradient, but may also contribute to crack blunting by active

dissolution. In light of this, complete deaeration of the crack tip might lead to crack blunting because of continued dissolution from crack walls. To confirm the effects of water content and oxygen-removal on iron dissolution, one SSRT was performed under potentiostatically held conditions in de-aerated SFGE containing 10ppm Cl<sup>-</sup> so that results of ICP analysis could be compared to analysis of potentiostatic SSRT discussed in 5.4. Dissolved Fe in the deaerated potentiostatic SSRT was indeed greater than that in the aerated test with identical water content (Table 5-9).

**Table 5-9 Dissolved Fe and solution color of deaerated SFGE after potentiostatic SSRT at X65 OCP (-0.111V vs. Ag/AgCl/EtOH).**

Environment	Dissolved Fe (µg/g)	Image of post-test solution color
Deaerated baseline SFGE (1 vol% water, 10ppm Cl <sup>-</sup> , 56ppm acetic acid, 0.5 vol% methanol, balance 200 proof ethanol)	225	

Though SCC is mitigated in all low-OCP environments (5 vol% water, deaerated, alkaline), based on SSRT specimen appearance and color and dissolved Fe content of the post-test solution, the passivation mechanism of the steel in high water-content SFGE differs from that in alkaline or deaerated SFGE. Additionally, even though OCP of the X65 steel in acidic SFGE is high, this environment did not cause SCC in the absence of Cl<sup>-</sup>, indicating that relatively high OCP is a necessary but not sufficient condition for SCC to occur. Based on the results of SSRT described in this chapter, it is unlikely that a potential gradient between the crack mouth and tip is the only contributor to SCC, as

crack blunting due to greater dissolution and slow repassivation of crack walls seems to contribute to SCC prevention. The mechanisms of SCC inhibition by deaeration and  $\text{NH}_4\text{OH}$  or  $\text{NaOH}$  addition will be clarified further in the upcoming chapters.

## 5.6 Chapter Summary and Conclusions

SCC susceptibility of smooth-sided X65 pipeline steel tensile samples was evaluated by performing SSRT in varied FGE and SFGE environments. Effects of inhibitor and denaturant content of commercial FGE were tested. SFGE was utilized to test effects of varied chloride content, water content, pHe and dissolved oxygen.

SSRT demonstrated a clear correlation between chloride content and SCC severity of X65 pipeline grade steel in a commercial FGE environment. SCC of X65 pipeline steel was not observed in SSRT performed in FGE in the absence of chloride.

When no corrosion inhibitor was present, SCC was observed in aerated FGE containing 5ppm or more of dissolved  $\text{Cl}^-$ . When inhibitor was present, no cracks were observed even with 10ppm dissolved  $\text{Cl}^-$ . Crack densities and reduction in ductility were lower in inhibitor-containing FGE-S than in FGE WOI. Samples strained in SFGE exhibited greater crack density and greater reduction in area than samples in commercial FGE-S and FGE WOI. All SCC in SSRT on smooth samples was transgranular. Cracks propagated mainly due to high stress and plastic deformation within the steel matrix around the crack.

Water content, oxygen availability, and pHe variations influence the open circuit potential of pipeline steel in FGE environments. Increasing pHe by  $\text{NaOH}$  addition decreased OCP by approximately 300mV. Addition of acid raised OCP value. Removal

of oxygen reduced OCP of the steel. These relatively low OCP values were linked to SCC mitigation. Cracking was prevented in deaerated solutions of FGE, alkaline FGE, and FGE containing >5 vol% water. Though cracking was mitigated in high water content SFGE, noticeable general corrosion occurred, indicated by the scaled appearance of the failed sample and a 65 ppm dissolved Fe content of the post-test solution. 225 ppm of dissolved Fe in the post-test solution from the sample strained in deaerated SFGE under potentiostatic control also indicated general dissolution, though there was no noticeable scaling.

X65 steel did undergo SCC in 10ppm chloride-containing SFGE containing 1 vol % water. X65 also underwent SCC in 10ppm chloride-containing SFGE when water content was very low (0.05 vol%). When samples in 0.05 vol% water-content SFGE were held potentiostatically at their OCP during straining, crack density increased significantly relative to samples that were not potentiostatically controlled, and based on %RA, failure was induced by brittle fracture to a greater extent in the sample held potentiostatically than samples that were not potentiostatically controlled.

## INVESTIGATION OF THE REPASSIVATION KINETICS OF X65 STEEL IN FGE AND SFGE ENVIRONMENTS

### 6.1 Introduction

In the experiments explained thus far, it has become apparent that SCC of X65 pipeline steel is affected by constituents within the FGE environment, and occurs when global stresses exceed yield stress in SSRT. Measurements of open circuit potential during straining of notched samples in FGE (Figure 4-9) show that OCP rises steadily until yield, at which point it drops, indicating that the surface has become more anodically active upon reaching yield stress. Measurements of current during straining in SCC-inducing FGE environments support this conclusion, showing large increases in anodic current from the global sample during yielding in Figure 5-13 and in previous work by Lou et al. [83].

The experiments within this chapter investigate the effects of environmental constituents on repassivation behavior of X65 carbon steel in FGE, as measured by the anodic current transient evolution. Specifically of interest are the quantity of current density and rate of current decay (repassivation rate) after a film rupture event. A significant body of past theoretical [107-109] and experimental [110-113] work has shown that repassivation rate is a significant factor in the SCC of metals and alloys. This concept relates to the anodic dissolution-controlled SCC mechanisms where crack propagation results from dissolution of the metal at the crack tip which perpetuates a localized mechanical stress concentration. It is proposed by the work mentioned above

that if a material repassivates very slowly or very rapidly it will not be susceptible to SCC, but will be susceptible if repassivation occurs at an intermediate rate.

Techniques used to assess repassivation generally involve measuring current from a potentiostatically controlled electrode while straining [110, 114], scraping [115] or scratching [116-120] to remove filmed material. In this work, mechanical scratch testing was used as the technique for plastically deforming the steel surface and removing any pre-existing film. For the reasons stated in Chapter 5, SFGE was used in place of commercial FGE to study effects of chloride concentration, oxygen removal, water content and pHe on repassivation of bared X65 pipeline steel. Repassivation in the SFGE is compared with that in commercial FGE.

Many studies on repassivation have been performed on stainless steels in aqueous environments, where it has been found that the slope determined from a plot of  $\log(t)$  versus  $\log(i)$ , where  $t$  and  $i$  are time and current density, respectively, represents repassivation rate and can be correlated to SCC susceptibility of Fe-Cr stainless steels [119]. Repassivation kinetics of stainless steels in aqueous environments has been extensively characterized and models have been proposed for repassivation in these systems, including the high-field ion conduction model [116], inverse-logarithmic film growth model [121], and the place-exchange model [122]. Studies have also been done on film formation on iron in aqueous environments [115, 123, 124]. Characterization of passive film formation kinetics on iron and low-carbon steels in organic solvents, however, has been the subject of only a few studies [61, 85, 99]. An attempt is made to analyze current vs time data using the existing repassivation models developed for stainless steels.

## 6.2 Repassivation Time Scale

The current decay behavior of carbon steel in SFGE environments was not known, so initial tests were conducted where data was sampled at a high rate, every millisecond, without automatic IR compensation. It was apparent from the initial tests that current decay due to repassivation of the scratch was slow and occurred on the order of minutes. Raw data recorded at two different sampling rates (Figure 6-1) shows that current decays slowly in this system. Note that this data has not been normalized for scratch area, so current magnitudes for these two tests are not comparable, but the repassivation kinetics information is similar. Sampling rate for subsequent tests was reduced in order to collect data over a longer time period, and enable the use of automatic IR compensation that could not be accurately employed when sampling period was less than 0.01s. In studies employing the same or similar current transient measurements on scratched stainless steels in environments in which passivity is well-defined in polarization data, current decay occurs very rapidly, usually within a few milliseconds [112, 115]. However, current decay from scratched carbon steel and iron in aqueous environments [124] and anhydrous non-protic solvents [61], and potential-step tests in anhydrous methanol [85] can take several minutes to reach a steady state value.

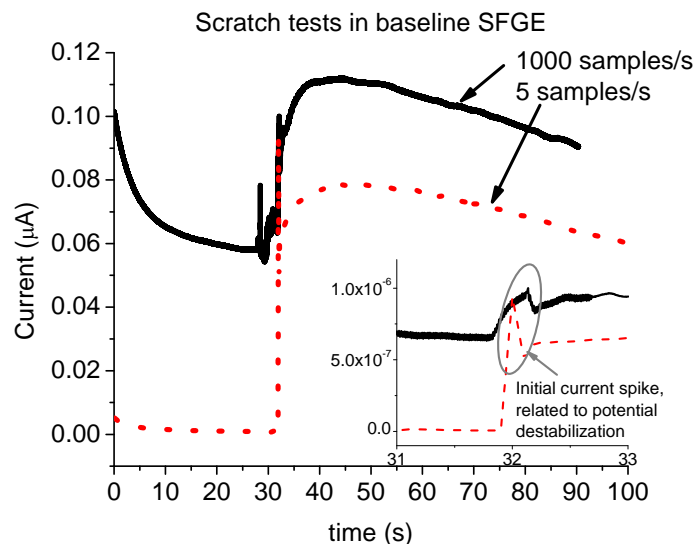


**Figure 6-1** Current transients measured at two different sampling rates to investigate decay on short and long time scales

### 6.3 Electrochemical Challenges When Measuring High Currents

One factor that can contribute significantly to the accuracy of electrochemical data recorded in a highly resistive electrolyte is the ohmic drop (IR drop) in solution between the working electrode surface and reference electrode probe, as described in Chapter 3.4.1. The magnitude of IR drop depends on the electrolyte resistance between the working electrode surface and the reference probe ( $R_u$ ), and the current ( $I$ ) flowing to or from the electrode. When electrode positions are fixed relative to one another, the  $R_u$  value should not change appreciably, however in highly resistive electrolytes when there is a sudden surge of current (as a result of a scratch, for example), IR drop can affect the system in two ways [114, 117, 125], which are discussed below.

The first possible effect of IR drop is that, when currents are high, the potentiostat compensates by supplying an erroneously low current to re-stabilize the potential, which

results in an erroneously low applied overpotential and artificially decreases the driving force for dissolution. The measured current will be a lower value than the actual current flow. Then, as current decays, the applied potential will increase incrementally as a function of time. These changes in applied potential can skew the shape of current transient decay if the changes in overpotential are significant. Additionally, if the scratch is large or counter electrode geometry is non-uniform with respect to the shape of the scratch, IR drop (and thus potential applied) between the scratch and reference electrode will be non-uniform as well. Work by Burstein et al. [126] and Pearson et al. [127] demonstrates that if scratch area is minimized (thus minimizing amount of current flow), IR drop becomes negligible and IR drop effects are confined within the scratched region. The ohmic resistance due to current flowing from the scratch,  $R_{scratch}$  can be calculated using the following formula [127]:

$$R_{scratch} = \frac{\rho}{\pi l_s} \ln\left(\frac{4l_s}{w_s}\right) \quad (6-1)$$

and thus IR drop can be quantified by:

$$V_{scratch} = il_s w_s R_{scratch} \quad (6-2)$$

where  $\rho$  is the solution resistivity ( $\Omega\text{-cm}$ ),  $w_s$  is the scratch width (cm),  $l_s$  is scratch length (cm), and  $i$  is peak current density ( $\text{A}/\text{cm}^2$ ). IR drop calculations for scratches in SFGE and FGE presented in Table 6-1 indicate that due to the low absolute current flow, potential drop within the scratch would produce negligible effects on the controlled value of potential by the potentiostat during the potentiostatic polarization tests used in this study. It is noted that because of ohmic resistance to current flow, the recorded peak current values may be slightly lower than actual peak currents [117, 126], but this should

not significantly affect the qualitative and semi-quantitative conclusions from the scratch test data, especially the effect of constituents on repassivation behavior.

**Table 6-1 Calculated scratch resistances ( $R_s$ ) and corresponding IR drops, assuming typical scratch lengths  $l_s = 5\text{mm}$  and widths  $w_s = 40\mu\text{m}$ .**

<b>Environment</b>	<b><math>\rho</math> (<math>\text{k}\Omega\text{-cm}</math>)</b>	<b><math>R_{\text{scratch}}</math> (<math>\Omega</math>)</b>	<b><math>\text{IR}_{\text{scratch}}</math> (mV) (from (6-2))</b>
SFGE, 10ppm Cl	9	35.6	0.048
FGE-S, 10ppm Cl	40	19.8	0.038
Alkaline SFGE	0.5	1.98	0.00074

The second possible effect of IR drop during scratch tests is to induce local currents between bare and filmed areas of the working electrode due to capacitive charging. Scratching or removing a film on a metal surface generally causes the un-filmed surface to become more “active,” or reside at a lower potential with respect to the nearby filmed area. Because a filmed surface is capacitive in nature, as it is proposed by some [114, 128] that the local potential gradient caused by removal of the film (scratching) causes the nearby filmed surface to discharge or accumulate charge depending on the direction of the local potential change. Because the initial large current leads to a decrease in applied overpotential, charge will flow from the filmed area to the bare area, and the potentiostat is not able to measure this local current activity, resulting in a measured current value that is lower than the actual dissolution current. When current from the bare surface begins to decay, charge supplied by the potentiostat will instead recharge the film capacitance. The double-layer discharging effect can become an issue in the event of a very large ohmic drop between filmed surface and bare steel [114, 117].

In light of these two factors, precautions were taken to reduce or eliminate the effects of ohmic drop on current transient response from the bared steel. As mentioned above, automatic IR compensation was employed, and distances between working, counter, and

reference electrodes were held close together at constant distances for all tests. Area of the scratch was kept minimal with respect to the filmed area of the specimen, thus minimizing the quantity of absolute current flow. Additionally, EIS scans were performed in several environments prior to scratching to obtain a surface capacitance value so that double layer charging effects could be quantified. Capacitance values for a similar SFGE-X65 system in literature [96] were reported as 20 to 200 $\mu\text{F}/\text{cm}^2$  using a constant phase element model [129], and were in agreement with the value of 125 $\mu\text{F}/\text{cm}^2$  calculated from the pre-scratch EIS data using an identical model.

For some tests, there was a large-magnitude current spike (Figure 6-1, inset) that occurred at the instant the scratch was initiated, which decayed in very short time, on the order of approximately 150ms. This initial current spike was stochastic however, and did not occur in a repeatable or predictable fashion. There was concern that double-layer charging from the surrounding sample surface may have been the contributing factor to this initial spike. Thus, assuming an atypically large potential difference of  $\Delta E=1\text{V}$  between bare and filmed steel and a typical scratch area of  $0.006\text{cm}^2$ , using the capacitance of 125 $\mu\text{F}/\text{cm}^2$  calculated above the maximum charge  $Q$  necessary to completely charge the double layer in the scratched area within the duration of the current spike was  $Q = 1.2\mu\text{C}$  ( $200\mu\text{C}/\text{cm}^2$ ). Integration of current density vs time data from the moment of scratch to 120s post-scratch for all scratch tests on carbon steel in SFGE in this study yields  $Q$  values of one to two orders of magnitude greater. Thus double layer charging effects were assumed to be negligible for carbon steels in ethanol environments. Instead, it was discovered that when spikes were present, a simultaneous shift in the controlled potential of about 5-6mV was observed over a range of 150-300ms (Figure

6-2), or approximately the amount of time it took to make the scratch, indicating that the act of applying the scribe to the steel surface caused a slight disturbance in the measured electrochemical data. The initial current spike and potential shift died simultaneously once the scratching process was complete, thus it was concluded that the spike was an artifact due to disturbance of electrode positions during scratching process in combination with the increase in IR drop at high currents due to the low conductivity of the test environment. Therefore, all analysis on scratch test data was performed on data beginning after the point of potential re-stabilization, i.e. peak current density is taken as the maximum value of current density after potential stabilization.

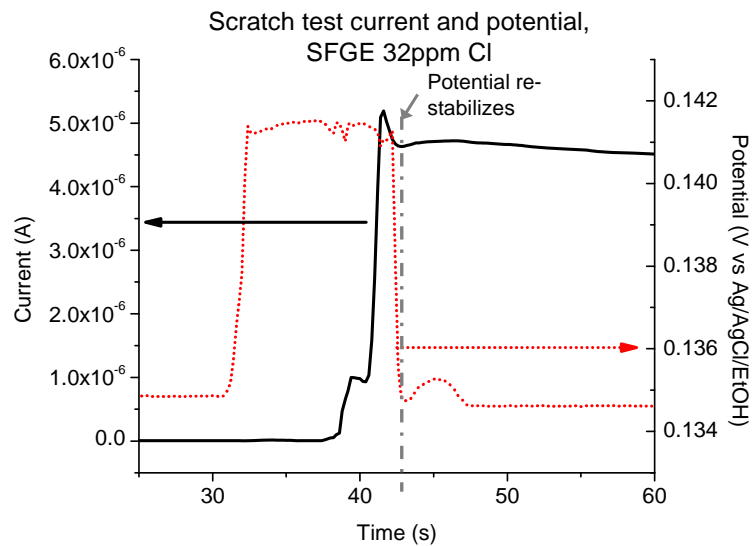


**Figure 6-2 Simultaneous potential and current measurements showing a potential drift during introduction of the scratch**

## 6.4 Effects of Environment on Current Decay and Localized Corrosion Within the Scratch

Open circuit potential (OCP) values, initial current density prior to scratching ( $i_{ps}$ ), peak current density ( $i_{bare}$ ), total charge passed within the first 120s after scratching ( $q_{t=120s}$ ), and current density at the 120s time point ( $i_{t=120s}$ ) are all given in Table 6-2 for SFGE environments in which chloride content and aeration condition were varied. Similar data for experiments in which water content and pHe of SFGE were varied is shown in Table 6-3 and Table 6-4, respectively. Values of  $i_{ps}$  were calculated by dividing the average current for 15s prior to scratching by the total sample area, which was approximately  $3.5\text{cm}^2$ . Peak current density was assumed to represent the magnitude of current density from a bare surface ( $i_{bare}$ ) which was likewise assumed in scratch tests by Lillard et al [120]. The purge gas was air unless noted otherwise.

**Table 6-2 Characteristic data from SFGE environments with varied chloride content. Two of the environments were also under deaeration via nitrogen purge (highlighted in gray).**

Environment	Added Cl <sup>-</sup> (ppm)	Vol % water	pHe	Purge gas	$i_{ps}$ (nA/cm <sup>2</sup> )	OCP (V vs Ag/AgCl/EtOH)	$i_{bare}$ (uA/cm <sup>2</sup> )	$i_{t=120}$ (uA/cm <sup>2</sup> )	$q_{t=120}$ (mC/cm <sup>2</sup> )
Baseline SFGE	0	1	5.1	Air	2.9	0.044	470	1.01	0.172
SFGE	0	1	5.1	N <sub>2</sub>	81	-0.06	539	221	26.9
SFGE	10	1	5.1	Air	7.7	0.076	672	63.8	21.37
SFGE	32	1	5.1	Air	1.7	0.065	858	36.6	24.8
SFGE	32	1	5.1	N <sub>2</sub>	310	-0.181	1490	506	71.2
SFGE	150	1	5.1	Air	0.86	0.056	2790	115	58.7

**Table 6-3 Characteristic scratch test data from aerated SFGE environments with varied water content**

Environment	Added Cl <sup>-</sup> (ppm)	Vol % water	pHe	$i_{ps}$ (nA/cm <sup>2</sup> )	OCP (V vs Ag/AgCl/EtOH)	$i_{bare}$ (uA/cm <sup>2</sup> )	$i_{t=120}$ (uA/cm <sup>2</sup> )	$q_{t=120}$ (mC/cm <sup>2</sup> )
Baseline SFGE	0	1	5.1	2.9	0.044	470	1.01	0.172
SFGE, no added water	0	0.06	5.3	5.1	0.145	97	52	9.75
SFGE, 0.5% water	0	0.5	5.3	2.6	0.221	77	33	6.28
SFGE, 5% water	0	5	5.2	16	0.058	53	45	5.81

**Table 6-4 Scratch data for SFGE environments with varying pHe, altered by additions of acetic acid or sodium hydroxide.**

Environment	Added Cl <sup>-</sup> (ppm)	Vol % water	pHe	$i_{ps}$ (nA/cm <sup>2</sup> )	OCP (V vs Ag/AgCl/EtOH)	$i_{bare}$ (uA/cm <sup>2</sup> )	$i_{t=120}$ (uA/cm <sup>2</sup> )	$q_{t=120}$ (mC/cm <sup>2</sup> )
Baseline SFGE	0	1	5.1	2.9	0.044	470	1.01	0.172
SFGE, 560ppm acid	0	1	4.3	13	0.145	n/a	185	19
SFGE, no acid	0	1	5.4	4.9	-0.008	22	2.17	0.47
SFGE, 56ppm NaOH	0	1	13	2.3	-0.079	187	3.4	1.07

Scratch data for aerated and deaerated chloride-containing SFGE are shown in Figure 6-3. In chloride-containing aerated SFGE, the  $i(t)$  vs time curve shows different rates and extents of current decay for all of the tested environments. Table 6-2 shows OCP,  $i_{ps}$ ,  $i_{bare}$ , and  $i_{t=120s}$  and  $q_{t=120s}$  for SFGE environments with varied chloride content and aeration condition. For both aerated and deaerated SFGE,  $i_{bare}$  increases as chloride content increases. The time necessary for the transient to return to a near steady-state

current density increases with  $\text{Cl}^-$  concentration in aerated SFGE, but does not increase appreciably with  $\text{Cl}^-$  increase in the absence of oxygen. Pre-scratch current is approximately an order of magnitude greater in the deaerated environment, and remains an order of magnitude greater at  $t=120\text{s}$ . Increasing chloride concentration in SFGE did not have any significant effects on the open circuit potential of the steel. SEM images within the scratched regions in SFGE containing greater than 10ppm  $\text{Cl}^-$  revealed pits surrounded by corrosion products (Figure 6-4). No pitting was seen outside of the areas where film had been damaged by scratching. No pitting was observed on the surface within scratches on samples tested in SFGE with chlorides below 10ppm. Pitting within the scratched region when  $\text{Cl}^-$  is present may be significant in relation to SCC initiation, as pit geometry can become an area of stress concentration and facilitate crack initiation [130-132].

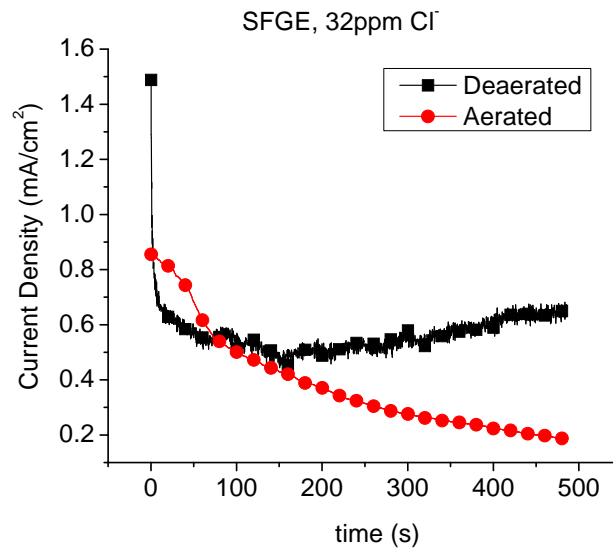


**Figure 6-3 Graph of current density vs. time for mechanically scratched X65 steel in SFGE containing 32ppm  $\text{Cl}^-$**

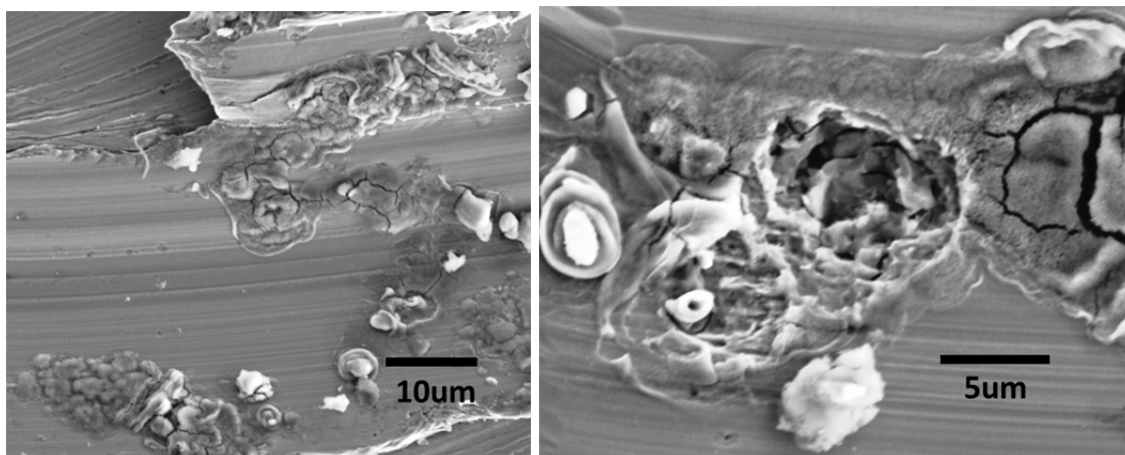


**Figure 6-4 Pitting and surrounding corrosion product within scratched region in SFGE containing 32ppm  $\text{Cl}^-$**

Open circuit potential of the sample decreased significantly when oxygen was removed from the solution. In deaerated SFGE,  $i_{ps}$  recorded prior to scratching and current density 120 seconds after scratching were both significantly higher than in aerated SFGE. The initial current transient quickly died and transitioned to a steady state value, and it was clear that even after reaching a steady state value, the current did not decay to the extent that it did in aerated SFGE (Figure 6-3). Addition of 32ppm  $\text{Cl}^-$  caused both peak current and final near-steady-state current to increase, but did not affect the time period of current decay to a nearly steady value. In deaerated environments, localized corrosion was noticeable within the scratch regardless of chloride content (Figure 6-5 and Figure 6-6). Unlike in the aerated environment, there were no noticeable corrosion products surrounding the pits. The effects of chloride on  $i_{ps}$  and  $i_{bare}$  in SFGE seem to indicate that the roles of chloride are to: 1) de-stabilize the film growth on the X65 surface and 2) increase current density by increased localized corrosion activity at the bared steel surface.

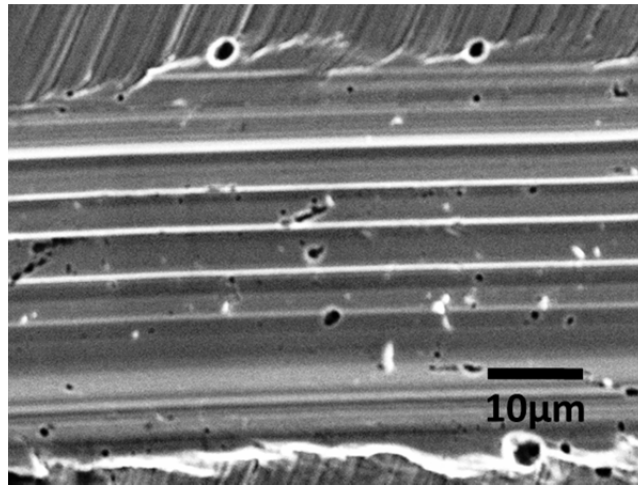


Figure 6-5 Pitting within the scratch in deaerated SFGE, 10ppm Cl<sup>-</sup>

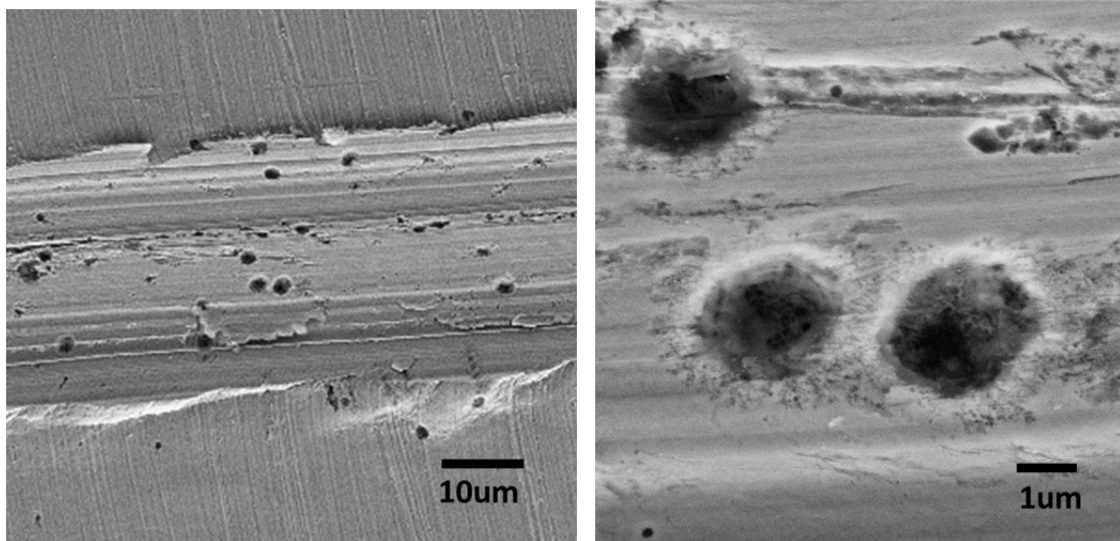


Figure 6-6 Pitting within the scratch in deaerated SFGE, no chloride

Open circuit potential of the carbon steel coupons decreased appreciably as water concentration increased, as shown by data in Table 6-3. Peak current density did not change significantly with change in water concentration, however pre-scratch  $i_{ps}$  decreased as water content increased from 0.06 to 1 vol%, then increased at 5 vol%

water. Similarly, total charge density after 120s ( $q_{t=120s}$ ) decreased as water content increased from 0.06 to 1 vol%, then increased at 5% water.  $q_{t=120}$  in the 1% water environment was significantly less than that in higher or lower water content SFGE tested. No visible corrosion was observed in or near scratched areas when water content was 1 vol% or less. At 5% water content, current decay was minimal, and localized corrosion was observed in the scratched region (Figure 6-7). A 50/50 water/SFGE mixture produced pitting throughout the sample, not just in the scratched region. Similar localized corrosion and scale formation in SFGE containing  $> 2.5$  vol% water has been reported earlier [59, 78].

Current density vs. time curves in SFGE with varied pHe are shown in Figure 6-8. Increasing the alkalinity of SFGE from pHe of 5.1 to a pHe of 13 by adding 56 ppm NaOH to the test environment produced significantly more rapid current decay from the scratch. The current decay in this alkaline SFGE resembled the typical scratch transient decay of iron in an aqueous environment, such on iron in alkaline water [124]. In the acidic SFGE (pHe 4.3) where 560ppm acetic acid was added to the baseline SFGE solution, no current decay is observed; current density increases continuously, as shown in Figure 6-8. Measured open circuit potential decreased as pHe increased in the range tested.

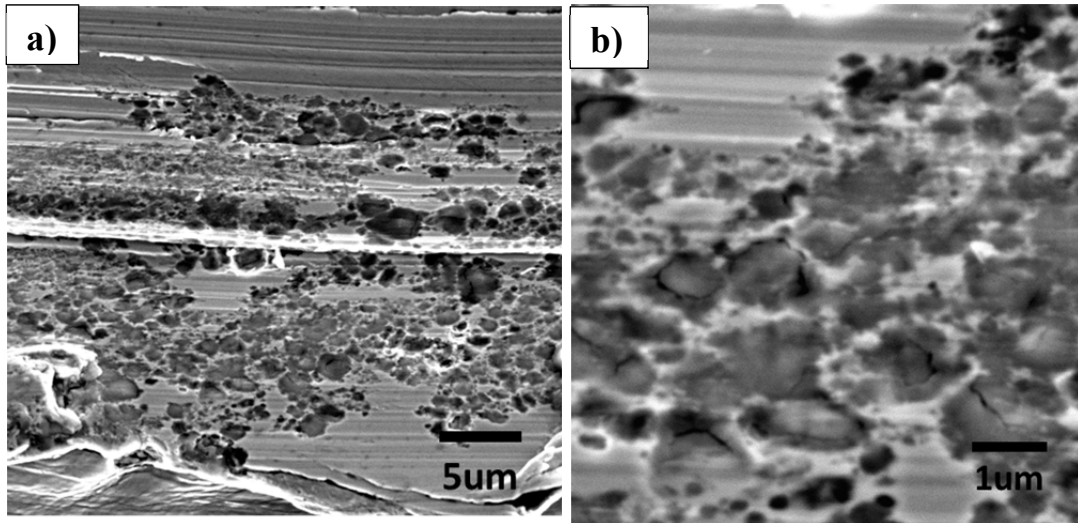


Figure 6-7 Localized corrosion within the scratched region in SFGE containing 5 vol% water

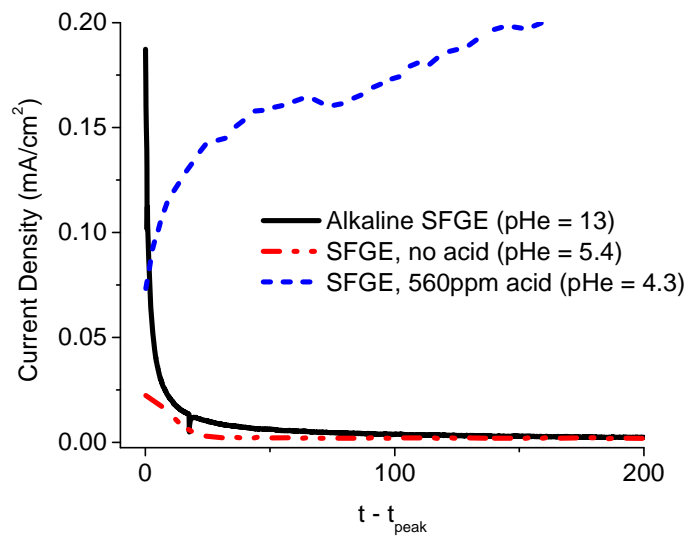


Figure 6-8 Current transients in alkaline (pHe = 13), neutral (pHe = 5.4), and highly acidic SFGE (pHe = 4.3)

## 6.5 Comparison of repassivation kinetics in commercial FGE and SFGE

Baseline SFGE solution used by many researchers contains the maximum allowable 56ppm concentration of acetic acid as described in ASTM D4806. However, as shown in Table 6-4 and Table 6-5,  $i_{bare}$ , current decay rate, and current decay extent for carbon steel in neutral (non-acid-containing) SFGE resemble more closely the equivalent data from a commercial FGE rather than the acid-containing SFGE. As demonstrated in the scratch test data for low pH SFGE, raising the acid content promotes dissolution from un-filmed areas, thus it seems that the baseline SFGE with acid is more aggressive than the commercial FGE. Presence of a commercial corrosion inhibitor in the FGE environment seemed to have the effect of lowering the  $i_{ps}$ , but in turn raising values of  $i_{bare}$  with respect to the FGE WOI environment.

**Table 6-5 Baseline current, OCP,  $i_{bare}$ , current density and total charge density 120s after introduction of a scratch in commercial FGE with and without inhibitor**

Base Environment	Added Cl- (ppm)	$i_{ps}$ (nA/cm <sup>2</sup> )	OCP (V vs Ag/AgCl/EtOH)	$i_{bare}$ (uA/cm <sup>2</sup> )	$i_{t=120}$ (uA/cm <sup>2</sup> )	$q_{t=120}$ (mC/cm <sup>2</sup> )
FGE-S	0	1.13	0.109	66	16.5	4.25
	10	0.56	0.135	963	356	69.15
	32	0.54	0.122	952	357	68.44
	150	5.6	0.084	3690	712	186
FGE WOI	0	2.06	0.005	6.3	1.01	0.172
	10	1.64	0.101	384	63.8	21.37
	32	4.78	0.047	626	36.6	24.83
	150	43.2	0.022	1640	115	58.74

## 6.6 Current transient analysis and modeling

An approximation of high field ion conduction model for oxide growth proposed by Cabrera and Mott [121] was demonstrated to accurately describe growth of passive films on stainless steels after film breakdown in neutral aqueous solutions [116, 133]. In this model, current decay from a bared surface approximately follows an inverse logarithmic relationship, where the  $\log(i)$  versus  $\log(t)$  curve follows a slope of approximately -1. Burstein and Marshall [116] determined that current decay of bared stainless steel is described by

$$\log(i) \propto \frac{BV}{x(t)} \quad (6-3)$$

where B is a constant, V is the potential drop across the film, and x is the film thickness. Film thickness can be calculated from charge density q that flows from a scratched surface by calculation of

$$q = \frac{zF\rho x}{M} \quad (6-4)$$

where z is the oxidation state of metal in the film, M is the molecular weight of the film,  $\rho$  is the density of the film, and F is Faraday's constant. Thus the relationship between  $\log(i)$  and  $1/q$  is linear with slope  $BVzF\rho/M$ , and was demonstrated to give a reliable measurement of the repassivation rate and protectiveness (film thickness) of the formed passive film [116, 119]. Kwon et al were able to correlate the value of the slopes to SCC susceptibility of stainless steel in chloride solution under different environmental conditions [112].

$\log(i)$ - $\log(t)$  and  $\log(i)$  vs  $q^{-1}$  plots were generated from the repassivation data from this study, and typical plots are shown in Figure 6-9 a) and Figure 6-9 b),

respectively. According to the high field ion conduction model for stainless steels,  $\log(i)$ - $\log(t)$  plots will approach a slope close to -1, and  $\log(i)$  vs  $q^{-1}$  will have a linear relationship. The only environment tested in this study in which the  $\log(i)$ - $\log(t)$  slope approached a value of -1 was the alkaline SFGE.  $\log(i)$  vs  $q^{-1}$  curves also did not behave as expected by the model, and curves in aerated SFGE environments approached a linear region only at very large values of  $q$ .

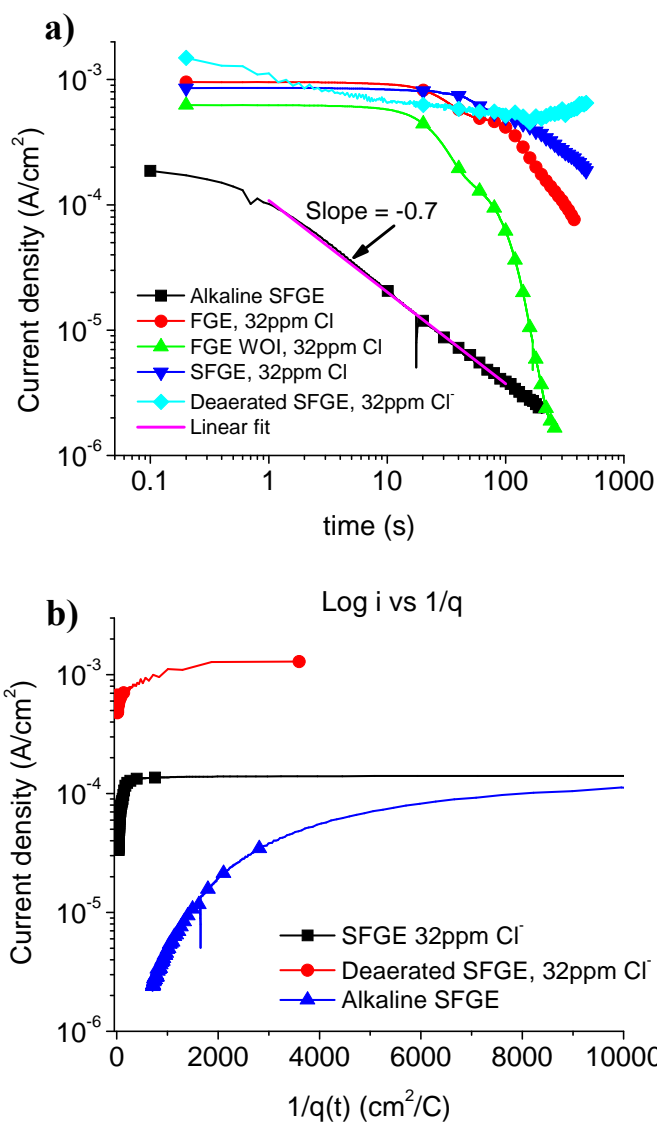


**Figure 6-9 (a) Log-log plots of current transients in selected environments. Linear fitting was performed on the curve in alkaline SFGE (b) Plots of Log(i) vs q-1**

Two main issues with this model are: 1) It is assumed that all initial current passing from the scratch participates in film formation, and dissolution contributions to early current transients are ignored; 2) At early times (large  $i$  and small  $q$ ) and later times (larger  $q$ ), the model breaks down, and little explanation is given for the deviation of early current transients. Burstein & Marshall explain that, first, a monolayer of film is

formed, and there will be a large barrier to further dissolution from the metal underneath the film due to the high electric field across the film [116]. Dissolution of the film itself can potentially occur at a steady rate at later times, causing deviation of  $\log(i)$  vs  $q^{-1}$  from linearity as  $t$  increases, but dissolution of the underlying metal will be negligible. Cho et al [119] address the issue of early transients for stainless steels in aqueous  $MgCl_2$  solutions, explaining that initially, film formation is accomplished by a place-exchange mechanism, which transitions to the high-field mechanism after a monolayer of film has formed. In the place exchange mechanism,  $\log(i)$  vs  $q$  should be linear for small  $q$  values, which was not the case in the carbon steel-fuel ethanol system. Thus, to explore the possibility that the charge from the scratched surface in the initial stages is partially be a result of dissolution and not simply from film formation alone, it was necessary to investigate an alternative model to fit our data at early times. In a study of 304L stainless steel repassivation in nitrate-containing acidic waste tank stimulant solutions, Lillard et al. [120] address early current transients by using contributions from both metal dissolution and film nucleation and growth to model early current transients. The model used aims to fit the current transient ( $I_{tot}$ ) using the following mathematical expression:

$$I_{tot} = I_{diss} + I_{film} = (1 - \theta) * I_{bare} + \theta A t^{-b} \quad (6-5)$$

where  $A$  is a characteristic charge density coefficient, and  $b$  is a constant.  $\theta$  is an expression that describes the fraction of the bare surface that is covered by the growing passive film, derived from Avrami kinetics [134], and described by

$$\theta = 1 - \exp(-kt^n) \quad (6-6)$$

where  $k$  is a rate constant for growth of the film and  $n$  is an exponent related to the geometry of the film growth.

Current transient curves in SFGE were fitted to this Avrami kinetics-based model in an attempt to deconvolve the current decay process at early times after the scratch into dissolution and film formation components. The geometrical parameter  $n$  was held constant at 1. Current density was used instead of current. Scratch data from the tested deaerated environments as well as the low pH SFGE where repassivation currents were significantly higher than the pre-scratch currents did not fit this model. This is because the model is based on an assumption that the surface film will repair itself with time, and thus the dissolution component will cease to dominate after a relatively short time period. Decent fits ( $R^2 > 0.98$ ) were obtained in some of the  $\text{Cl}^-$  containing SFGE solutions as well as the alkaline SFGE, which are shown in Figure 6-10. At higher chloride content, goodness of fit decreased as the abrupt slope change in the data became more apparent. This slope change due to the onset of localized corrosion processes in the scratch caused a slowing of current decay, or possibly fluctuations between current decay due to film formation and dissolution.

The deconvoluted current components,  $i_{\text{diss}}$  and  $i_{\text{film}}$  as well as the fraction of surface coverage,  $\theta$ , are plotted along with the fitted data in Figure 6-10. It is clear that in SFGE containing chloride, the dissolution component of current decays significantly more slowly and thus the time necessary to form one monolayer of coverage on the bare surface in chloride-containing SFGE is considerably longer than that in alkaline SFGE.

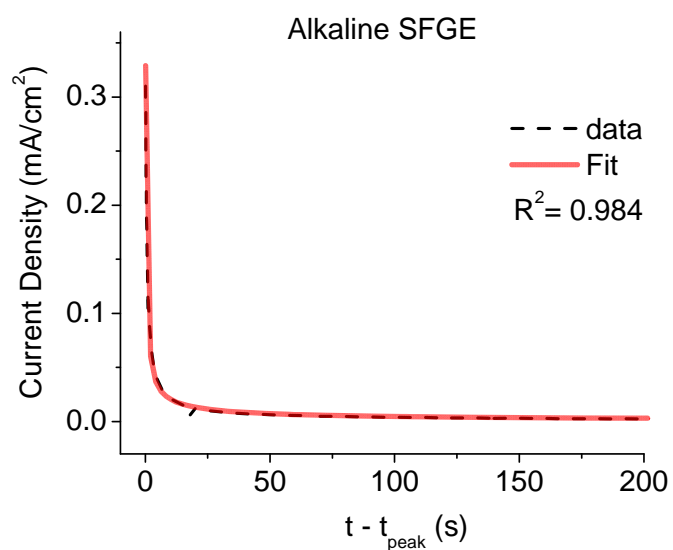
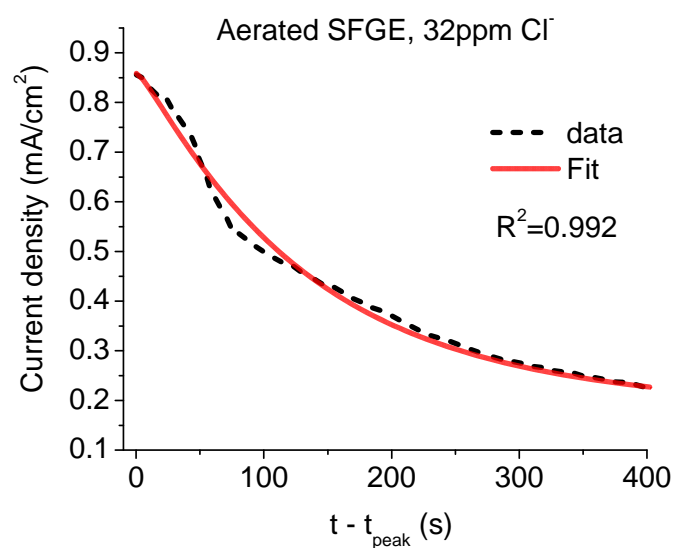


**Figure 6-10 Current transients fitted with equation ( 6-5)**

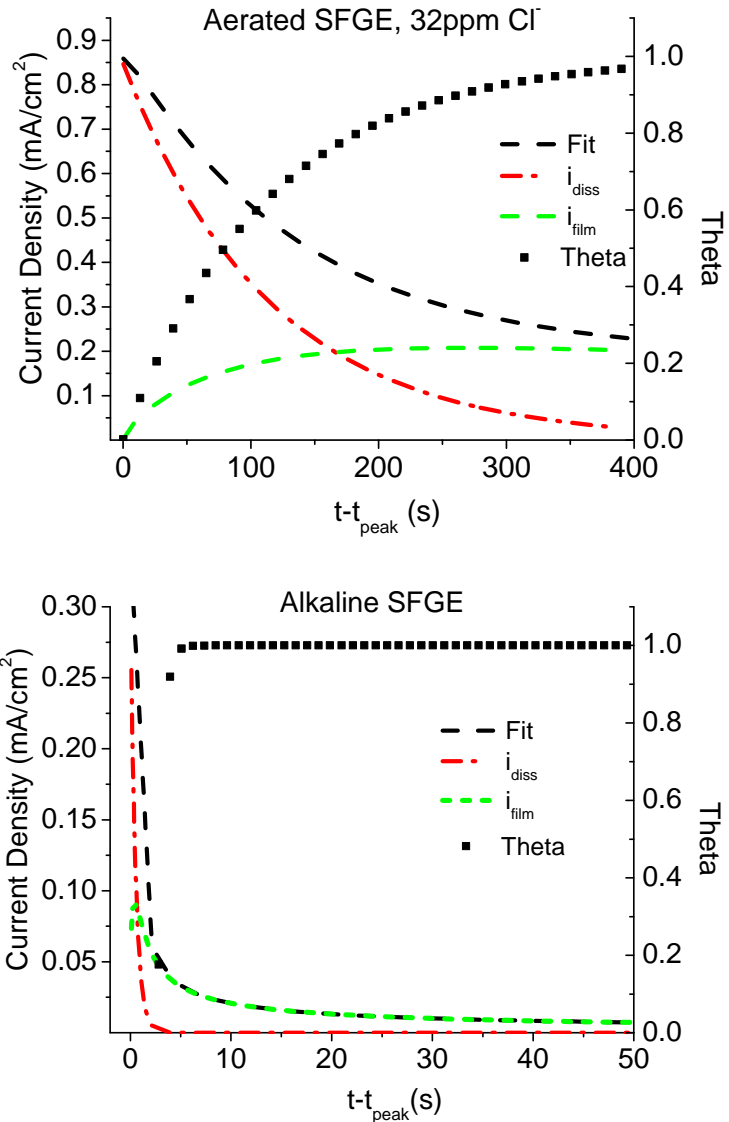


Figure 6-11 Fitted scratch transient data, deconvoluted into dissolution current and film current components. Fraction of surface coverage,  $\theta$ , is also displayed.

## 6.7 Summary and Relationship of Current Decay to SCC Behavior

From scratch test data, it is clear that common constituents of ethanol fuels have a significant effect on the overall mechanism and kinetics of passive film formation of pipeline steel. The presence of chloride in quantities lower than  $10^{-3}\text{M}$  leads to pitting and

increased anodic current density in scratch areas. The fitted data suggest that if chloride concentration were to increase within the crack, by the dissolution model, crack advance would progress more rapidly because a greater initial amount of dissolution would occur from the bared steel and dissolution would be sustained for a longer period of time than in the absence of chloride. This result is in agreement with past research that has found crack velocity to increase with increasing  $\text{Cl}^-$  [18].

Low (<0.1%) and high (5%) water concentrations in SFGE prevent SCC susceptibility for carbon steel in tested environments. With high water content, high dissolution of iron and unstable film formation lead to general corrosion and thus crack geometry may not be maintained. It was indeed shown [18] that after slow strain rate testing of X65, the quantity of dissolved Fe ions in solution significantly increased with an increase in the water content of SFGE, however crack density and velocity were greatest in SFGE with 1% water. Around 2% water, pitting corrosion was reported which changed to general corrosion at 5% or higher water content.

Decreasing the pHe in the system from 5.4 to 4.3 prevents repassivation and promotes active dissolution. Additionally, since  $i_{ps}$  of the steel in acidic SFGE was four times higher than in baseline SFGE, it can be concluded that decreasing the pHe of the SFGE promotes dissolution of the air-formed film as well. If conditions within a crack become highly acidic, it is possible that dissolution of the film on the crack walls and tip will occur, leading to general attack and crack blunting. On the other hand, increasing the pHe of SFGE by addition of NaOH decreased both  $i_{ps}$  and total charge passed from the scratch while significantly increasing repassivation rate. Thus, one reason for

prevention of SCC in alkaline solutions likely involves the increased stability and formation rate of the passive film.

A similar crack blunting mechanism seems to operate in deaerated SFGE. In deaerated SFGE,  $i_{ps}$  is high and current density remains high after a scratch event, rapidly settling at a near-steady value that is greater than that in aerated SFGE. Oxygen removal from the overall environment has indeed been shown to prevent SCC in SSRT [18, 20, 135]. However, Lou et al also showed selective dissolution of ferrite phase in pearlite areas, leaving cementite at the surface [18].

In Chapter 4, current and potential monitoring during SSRT tests of notched tensile samples was used to show that the crack initiation and propagation is related to an increase in the anodic activity, which indicates that SCC propagation involves dissolution at the crack tip [83]. Comparison of published SCC data and SSRT results from Chapters 4 and 5 with the present scratch test study on repassivation behavior of carbon steel in different SFGE environments indicates that carbon steel is susceptible to SCC in SFGE environments where the repassivation of bare metal occurs at an intermediate rate, neither very slow nor very fast. Dissolution current appears to play a large role in the current decay process in the typical SCC-causing SFGE solutions. This data indicates that SCC propagation likely occurs by a dissolution mechanism, wherein dissolution of the steel at the bare crack tip, advances the crack into the bulk material. When  $Cl^-$  is present in aerated SFGE and FGE, areas where film is damaged due to high stress or strain accumulation are susceptible to localized corrosion or pitting, which can produce stress-concentrations and lead to crack initiation.

## 6.8 Conclusions

Mechanical scratch testing on X65 carbon steel was performed in simulated and commercial fuel grade ethanol environments. Assessment of electrochemical current transients and surface morphology within scratched areas led to the following conclusions:

1. Repassivation in SFGE and FGE occurs slowly compared to aqueous environments, on a time scale on the order of minutes
2. In deaerated SFGE, or aerated SFGE containing  $> 10\text{ppm}$  chloride or 5% water, pitting and localized corrosion occurred preferentially in the region where film had been removed by scratching
3. Current density from both filmed (unscratched) steel and bare steel increased as environment  $\text{Cl}^-$  concentration increased in the SFGE environment
4. Removing oxygen from the environment caused significant increases in current density from filmed steel and bare steel and makes repassivation difficult.
5. Carbon steel exposed to low pHe (pHe = 4.3) SFGE did not show repassivation or post-scratch decay in current
6. Current from the bare carbon steel surface ( $i_{\text{bare}}$ ) in baseline SFGE was greater than that in either of the as-received commercial FGE samples tested

Repassivation models developed for stainless steels in aqueous solutions involving ion conduction through a passive film due to a high electric field were generally not applicable to the carbon steel repassivation in SFGE and commercial FGE environments.

# **EFFECTS OF SFGE AND FGE ENVIRONMENT ON THE COMPOSITION AND MORPHOLOGY OF THE X65 SURFACE FILM**

## **7.1 Introduction**

It has been shown thus far that in the FGE-carbon steel system, SCC susceptibility can vary widely with small changes in chemical composition of the bulk environment. By understanding the nature of passivity in non-aqueous solvents and factors leading to its breakdown, improvements in corrosive behavior of alloys can be made [61].

Identification of the mechanism of corrosion reactions of pipeline steel in FGE can be achieved through studies of passive film composition in this system, which can lead to progress in SCC and corrosion mitigation.

Four types of general passivation mechanisms exist for metals [61, 136]: 1) protection from an air-formed film; 2) precipitation of a salt film; 3) dissolution-inhibiting layer formed by solvent chemisorption; 4) direct oxide/oxy-hydroxide formation. Studies on the composition of passive films formed on iron and carbon steels have been performed in anhydrous propylene carbonate (PC) [61, 99], and anhydrous methanol [137, 138] and hydrated methanol [60], but the composition of films formed on carbon steel in FGE environments has not been directly investigated. Neither the passivation mechanism of carbon steel in FGE nor the effects of common FGE constituents on passivity have been determined. Up to this point, compositional

information on film formation in FGE has only been discussed based on inferences from theoretical calculations [19] and electrochemical data [79] and has not been directly verified. The experiments described in this chapter are geared toward characterizing the composition of the X65 steel passive film formed under static immersion conditions in SFGE and FGE, and the effects of chloride, water, pHe and aeration on film composition, stability and thickness.

## **7.2 Effects of SFGE and FGE on X65 Surface Film Composition and Morphology**

To study effects of pHe, water, oxygen, and chloride on passive layer composition, polished X65 coupons were statically immersed in varied SFGE environments for a five to seven day duration, then analyzed using XPS. XPS is a surface-sensitive technique that is capable of obtaining information on elemental composition and oxidation states of elements on a sample surface. Researchers have utilized x-ray photoelectron spectroscopy (XPS) in corrosion to gain information about the characteristics of passive films on metals in corrosion studies in aqueous solutions [88, 93, 139, 140] and organic solvents [137, 138] to help identify mechanistic interactions between metal and environment. Sampling depth for XPS is generally less than 10nm. It was shown in previous chapters and prior work [83, 96] that measurements of OCP of X65 steel in FGE and SFGE environments show a slow rise in the OCP value over time for relatively long (10-12h) time periods, indicating consistent changes in or growth of a surface film, or restructuring of ions or molecules at the environment/steel interface. Scratch tests in SFGE and FGE also indicate that a dissolution-inhibiting film exists on the X65 surface that can be ruptured by mechanical deformation and can re-form under specific conditions. However, in SSRT and electrochemical tests, X65 surfaces do not visually appear to have

grown a thick oxide layer in most cases, as surfaces often appeared shiny and polishing lines can still be distinguished, thus it was necessary to employ a highly surface sensitive technique for film analysis.

In characterizing the film composition, it was desirable to eliminate effects of denaturants, inhibitors, and other impurities, so SFGE was used in most tests. One sample was exposed only to air, to serve as a control sample on which the composition of the air-formed film could be identified. One test was performed in commercial FGE to compare SFGE and FGE film composition. Detailed experimental procedures of the static immersion tests and exposure times are described in Chapter 3. Details of environment compositions used in XPS exposure tests are given in Table 7-1. It is known that some oxides formed *in-situ* may be unstable and can decompose or oxidize to other, more stable compounds on exposure to air [137-139]. In light of this fact, steps were taken to avoid exposing the X65 coupons to air between immersion and insertion into the XPS chamber. After exposure to the solutions, each coupon was removed from solution and dried under N<sub>2</sub> to avoid oxidation or decomposition of any surface products that had formed. Coupons were stored in sealed vials under vacuum until XPS analysis was performed. Fe2p, C1s, and O1s photoemission spectra were obtained from each sample surface and fitted to gather compositional information about the films formed on X65 steel exposed within the listed environments.

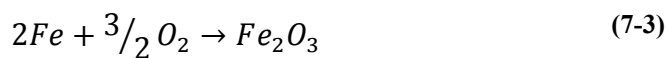
Topography of the exposed surfaces was obtained using AFM. AFM is a powerful technique for investigating the morphology of surface microstructure. Often, films formed in corrosion experiments will be visible in optical or SE microscope, but there were no easily discernible changes to the surface features on X65 in most SFGE

solutions, so the AFM method allowed characterization of surface topography on the micro-scale. After exposure to solution, changes in surface roughness of a sample can be measured by AFM, and can indicate differences in corrosion rate. Preferential dissolution of a particular phase or feature can also be clarified by AFM. It was suggested in prior work by Lou et al. that preferential dissolution of cementite in pearlite grains occurs in deaerated SFGE, and that SCC of X65 steel in SFGE initiates due to preferential dissolution near inclusions [18], so surface roughness changes, and existence of preferential dissolution of inclusions or cementite lamella were of interest in the AFM analysis of X65 coupons after exposure to FGE and SFGE environments. AFM scans of 20x20  $\mu\text{m}^2$ , 10x10  $\mu\text{m}^2$ , 5x5  $\mu\text{m}^2$ , and 2x2  $\mu\text{m}^2$  were obtained on each sample surface after XPS analysis was complete to minimize the samples' exposure to air prior to XPS analysis. Details of the AFM procedure are given in Chapter 3.

**Table 7-1 Coupons of X65 were exposed to the environments listed, prior to XPS analysis**

Sample	Environment	Solution Composition (Bal. 200 proof Ethanol)				
		Water (vol%)	Chloride (ppm)	Methanol (vol%)	Acetic acid (mg/L)	pHe
A	Air	--	--	--	--	--
B	Baseline SFGE	1	0	0.5	56	5.4
C	Low pHe SFGE	1	0	0.5	560	4.3
D	High pHe SFGE	1	0	0.5	56 (NaOH)	13
E	Anhydrous SFGE	0.06	0	0.5	56	5.4
F	High water content SFGE	5	0	0.5	56	5.2
G	FGE-S (as-received)	1	<1 ppm	--	--	7.8
H	SFGE, Cl <sup>-</sup>	1	10	0.5	56	5.4

Metallic surfaces are inherently unstable in their pure form and thus react quickly in the presence of oxygen, forming passive oxide films. Thermodynamically, it takes approximately 1ns for a monolayer of oxygen to adsorb onto a metal surface at atmospheric pressure [141], which can lead to formation of one of the following iron oxides at room temperature and  $pO_2$  of 1atm:



which have free energies of oxide formation ( $\Delta G^0$ ) of -117.5, -242.6 and -177.1 kcal/mol, respectively, so it was assumed that despite careful sample preparation, an air-formed film or “native film” existed on all samples prior to SFGE exposure. The atmospheric oxidation under these conditions will generally produce an oxide layer which provides a barrier to further reaction, and so will cease to thicken after a few monolayers have formed. It was thus necessary to identify the composition and thickness of the native film so a baseline could be established. This was also done to find out the nature of contamination from ambient conditions. Since the samples were exposed to ambient conditions briefly before evacuation in the XPS chamber, minor amounts of atmospheric contamination were a concern. As the control, a polished X65 coupon was placed in a glass flask purged with high purity dry air for the same 5-day exposure period as SFGE-exposed samples.

AFM images of the air-exposed steel sample are shown in Figure 7-1. The darker spots indicate that small particles became embedded into the surface and shaken loose,

likely during the final Al<sub>2</sub>O<sub>3</sub> polishing step and subsequent ultrasonic cleaning. Since the particles were shaken loose and the remaining indentations are small and scattered, it is not likely that this change in surface morphology interfered with XPS characterization.

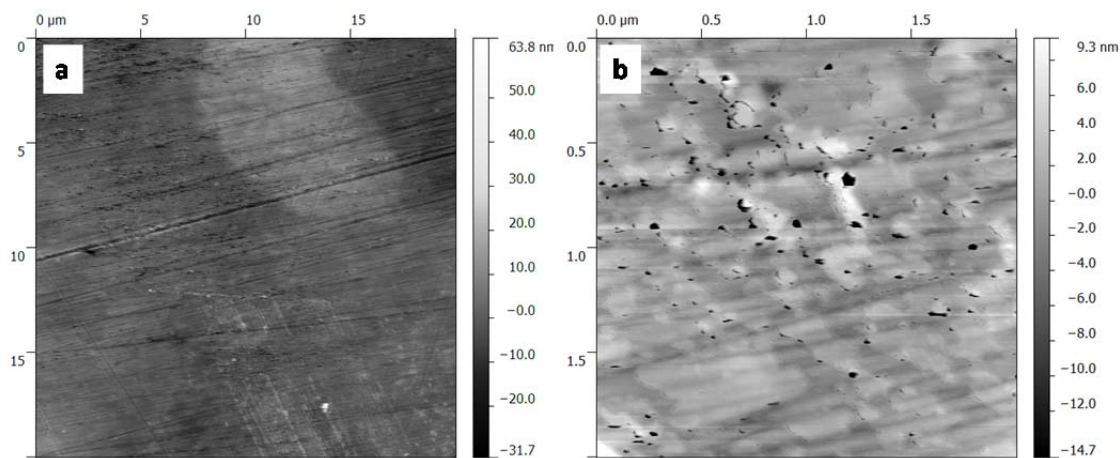


**Figure 7-1 Topographical AFM scans of the air-exposed coupon surface. The color gradients on the right side of each image correspond to topographical differences in nm.**

Surface spectra were obtained on the air-exposed sample surface and then the sample was sputtered with Ar<sup>+</sup> for a total of 90 seconds at 3000eV energy and 10uA current to remove any oxide (Figure 7-2). It was assumed that spectra obtained from the sputtered surface represented the “bare” steel, and could be used as a reference spectrum for the unoxidized steel matrix. Peaks were fitted, and the fitting parameters found were used to fit the pure iron peaks in all subsequent spectral analyses. Detailed XPS peak fitting procedures are explained in Chapter 3. From fitting with the XPS software, FWHM for the metallic Fe was determined to be 1.2eV, and the peak binding energies for Fe2p<sub>3/2</sub> and Fe2p<sub>1/2</sub> were 706.68 and 719.57eV, respectively. These peak positions agreed well with values found in literature for XPS on pure iron and steel. Once peak positions for bare steel were determined, the values were fixed and the peak shape parameters were

varied due to the noticeable asymmetry of the peaks. Asymmetry of the metallic iron ( $\text{Fe}^0$ ) peaks was expected to be more noticeable than asymmetry of cationic iron ( $\text{Fe}^{2+,3+}$ ) peaks because of the increased possibility for shake-up type effects due to the greater number of conduction-band electrons present. Shake-up effects from  $\text{Fe}^{2+/3+}$  components result in discrete satellite peaks instead of peak asymmetry. The optimal fit for  $\text{Fe}^0$  peaks was obtained with a 60% Lorentzian/Gaussian (L/G) mix with a tail exponent (asymmetry parameter) of 0.06. These fitting parameters were subsequently utilized to fit the metallic iron components of the Fe2p spectra from all sample surfaces. To reduce the number of variable parameters, it was assumed that asymmetry of other components of the Fe2p spectrum were reasonably symmetric, so all other peaks in the Fe2p spectra, as well as all peaks in the O1s and C1s spectra, were fitted with a 30% L/G and asymmetry of 0.

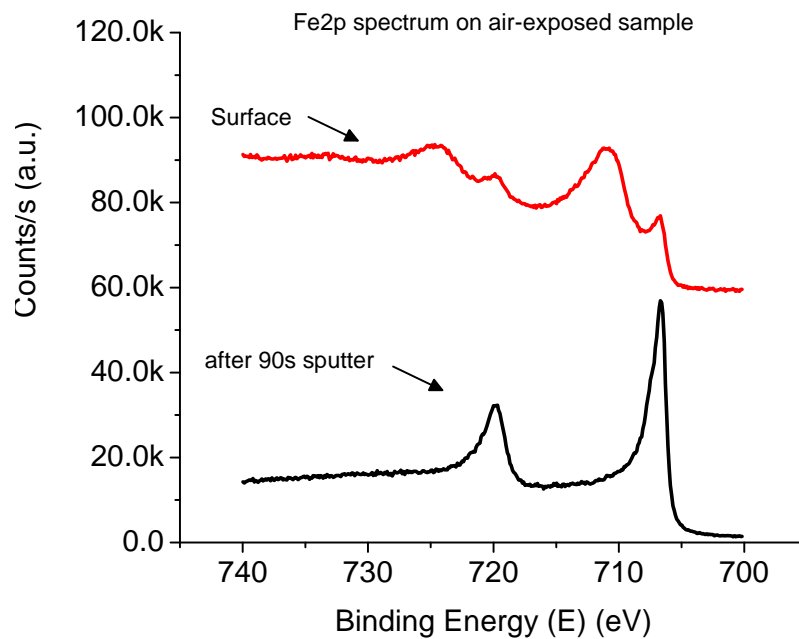


**Figure 7-2 XPS Fe2p data on surface and after removal of surface layers by  $\text{Ar}^+$  sputtering.**

Deconvolution and fitting of the peaks in the Fe2p spectrum of the air-exposed sample surface (Figure 7-3) as well as all solution-exposed sample surfaces revealed four distinct sets of doublet peaks. When fitting with the Thermo Avantage software, all peak BE were allowed to vary by  $\pm 0.3$  eV from the literature averages to achieve the best fit possible. Fe2p peak binding energy values were consistent among all sample surfaces whether SFGE-exposed or air-exposed. Compounds represented by the remaining peaks were identified using binding energy values found in literature and from the NIST database [88, 93, 142-145] (Figure 7-4). Some of the peak binding energies were verified by obtaining spectra of Fe<sub>2</sub>O<sub>3</sub> and Fe<sub>3</sub>O<sub>4</sub> powder standards with the Thermo K-alpha . Fe2p peak binding energies from the standards are listed in Table 7-2.

**Table 7-2 Fe2p peak binding energies found from powder standards**

Compound	B.E. (eV) of main peak	
	Fe2p <sub>3/2</sub>	Fe2p <sub>1/2</sub>
Fe <sub>2</sub> O <sub>3</sub>	711.0	724.4
Fe <sub>3</sub> O <sub>4</sub>	710.3	723.0

Average Fe2p peak binding energies and FWHM from all X65 sample surfaces and their corresponding ions are listed in Table 7-3. The lowest binding energy peak at 706.8 eV represents metallic iron (Fe<sup>0</sup>), and has a doublet peak at 719.8 eV due to spin-orbit splitting. The peaks at 709.6 and 723.2eV, and 711.2 and 724.1eV represent iron in the Fe<sup>+2</sup> and Fe<sup>+3</sup> states respectively, either as Fe<sub>2</sub>O<sub>3</sub>, Fe<sub>3</sub>O<sub>4</sub>, FeO, or FeOOH. Oxidized iron peaks are accompanied by shake-up satellite peaks near 713.8 and 726.0eV [90, 93, 142]. A peak representing Fe bonded with C (Fe<sub>3</sub>C) which is contained in pearlite lamella, usually lies at approximately 709.2eV, but this peak was not included in the analysis

because of the low (below accurate detection limits) quantities of cementite expected. In pearlite colonies, cementite will comprise approximately 0.77 wt%, and with a bulk steel composition of 0.08 wt% C (Table 3-1), the analyzed surface would be expected, based on the standard iron-carbon phase diagram, to contain 0.059 percent cementite, of which carbon comprises 25 at%. Thus, only 0.015 at% carbon would be expected from cementite.

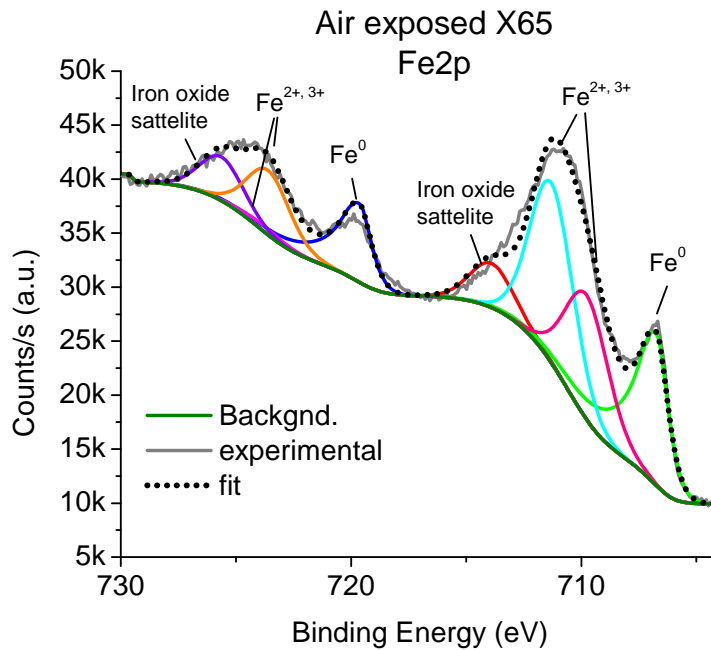


**Figure 7-3 XPS data of Fe2p on the surface of an X65 "control" sample, polished and exposed only to dry air. Eight peaks are present, representing iron in its un-oxidized state, 2+ and 3+ oxidized states, and oxide satellite peaks**

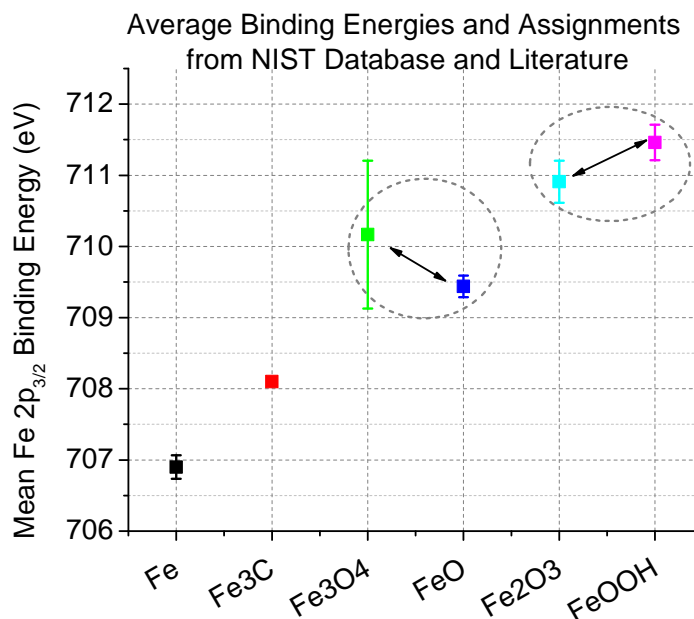


Figure 7-4 Average binding energy values and assignments as determined from standard reference compounds in literature and the NIST database [88, 93, 144, 146] B.E. values that were very close together were grouped as “mixed iron oxides” in the analysis of X65 surfaces.

Table 7-3 Average peak binding energies and assignments for the peaks found in the Fe2p spectra of X65 sample surfaces after environmental exposures

Element (photo- electron core level)	Fe2p <sub>3/2</sub>		Fe2p <sub>1/2</sub>		Assignment	Reference
	Average Peak B.E. (eV) (±0.3)	Average FWHM (eV) (±0.3)	Average Peak B.E. (eV) (±0.3)	Average FWHM (eV) (±0.3)		
Fe2p	706.74	1.69	719.67	1.64	Fe <sup>0</sup> (metallic iron)	[92, 143]
	709.6, 711.2	2.11, 2.3	723.2, 724.6	2.20, 2.21	Fe <sup>2+</sup> /Fe <sup>3+</sup> (mixed iron oxides)	[139]
	713.8	2.30	726.0	2.21	Iron oxide satellite	[88]

Sampling depth ( $d$ ) was calculated for the iron oxide surface layer using a similar procedure to Ghods et al. [93, 147]:

$$d = 3\lambda \cos(\theta) \quad (7-1)$$

where  $\theta$  is the takeoff angle to the surface normal ( $0^\circ$  for the XPS system used) and  $\lambda$  is the attenuation length of the ejected photoelectron for the specific surface material. For iron oxides,  $\lambda$  is estimated as [148]

$$\lambda \approx 0.096\sqrt{E_k} \quad (7-2)$$

where  $E_k$  is the kinetic energy of the ejected photoelectron, which can be calculated using the following formula if the characteristic binding energy of the individual element ( $E_b$ ) is known:

$$E_k = h\nu - E_b - \phi_s \quad (7-3)$$

where  $\phi_s$  is the work function of the spectrometer, which was 4.2eV for this system. So, using an average of sampling depth values listed in Table 7-4 for both Fe2p and O1s, sampling depth for the film on the steel surface was approximately 8.4nm.

**Table 7-4 Sampling depth of XPS data from steel surface,  $h\nu = 1486.7\text{eV}$ ,  $\phi_s = 4.2\text{eV}$ ,  $\theta = 0^\circ$ .**

	<b><math>E_b</math> (eV)</b>	<b><math>E_k</math> (eV)</b>	<b><math>\lambda</math> (nm)</b>	<b><math>d</math> (nm)</b>
<b>Fe2p</b>	707	775.5	2.7	8.0
<b>O1s</b>	532	950.5	3.0	8.9
<b>Average</b>				8.4

Some adventitious carbon contamination was expected on the sample surface from exposure to atmosphere before entering the XPS analysis chamber. Three distinct carbon peaks were resolved (Table 7-5 a), the main being a hydrocarbon peak at a B.E. of 285.0 eV, which is almost always present in XPS experiments due to atmospheric carbon contamination. Fitting the C1s spectrum on the air-exposed sample helped to establish a baseline for expected levels and peaks due to atmospheric carbon so they could be distinguished from peaks from organic species incorporated into the film or chemisorbed in the SFGE-exposed samples. The peak that would normally represent cementite in the C1s spectrum (B.E.  $\approx$  283.5 eV) was ignored because of the very small volume of cementite ( $< 0.1$  at%) expected in this low carbon steel. The strong carbon signal attenuated significantly after merely 8s sputtering, leaving a small C=C peak, and remained constant for subsequent sputtering (Figure 7-6), indicating that a small amount of hydrocarbon contamination may have been present in the chamber. The other small surface carbon peaks present prior to etching may have been residual from cleaning with acetone after sample preparation.

Oxygen present on the sample surface was also deconvoluted into three main peaks: one was attributed to iron oxide (B.E.  $\approx$ 530 eV), one to iron hydroxide (B.E.  $\approx$  531.5eV) and the last to a C=O bond (Figure 7-5 b). The C1s and O1s peak values of importance and their corresponding assignments are listed in Table 7-5.

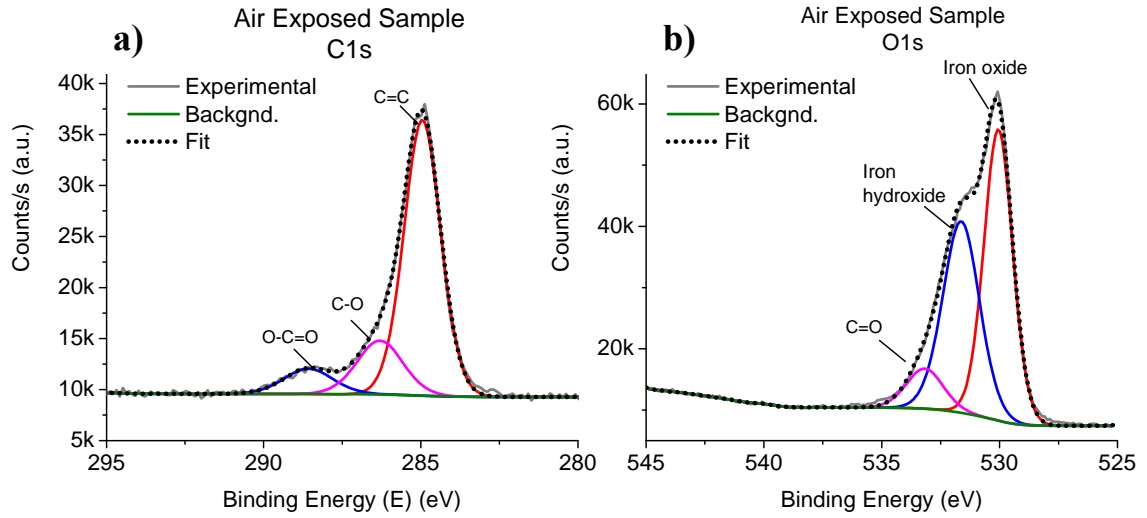


**Figure 7-5 High-resolution (a) carbon and (b) oxygen spectra from air-exposed X65 surface**

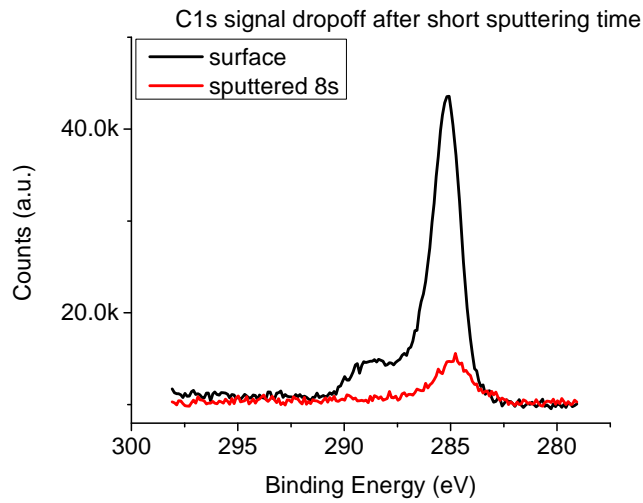


**Figure 7-6 C1s signal from air-exposed X65 coupon after brief sputtering time showed rapid attenuation of C1s signal just below surface**

**Table 7-5 Average peak B.E. for O1s and C1s XPS spectral data of X65 surfaces after peak fitting**

Element (photoelectron core level)	Average Peak B.E. (eV) ( $\pm 0.3$ )	Average FWHM (eV) ( $\pm 0.3$ )	Assignment	Reference
O1s	530.1	1.45	Iron oxide	[139]
	531.7	1.61	Fe-OH (FeO(OH), Fe(OH) <sub>3</sub> )	[149]
	532.1	1.85	OCH	[137, 138]
	533.5	1.93	C=O	[93]
C1s	285.0	1.57	C-C	[144]
	286.7	1.49	C=O	[144]
	288.8	1.75	O-C=O, CO <sub>2</sub>	[144]

Thickness of the air-formed oxide film was clearly less than the sampling depth since peaks from the steel substrate (metallic iron) were detected. The thickness of the oxidized layer was calculated for all exposed samples from peak area ratios of oxidized ( $I_{ox}$ ) and metallic iron ( $I_m$ ) peaks, using the equation [90, 146]:

$$d_{ox} = \lambda_{ox} \cos(\theta) \ln\left(1 + \frac{I_{ox} N_m \lambda_m}{I_m N_{ox} \lambda_{ox}}\right) \quad (7-4)$$

where  $\theta$  is the takeoff angle of photoelectrons ( $90^\circ$  in this case),  $\lambda_{Fe}$  and  $\lambda_{ox}$  are the inelastic mean free paths of metallic iron and oxidized iron (taken as 1.57nm and 1.65nm respectively) [146],  $I_{Fe}$  and  $I_{ox}$  are the calculated peak areas of metallic iron and oxidized iron peaks, and  $N_m$  and  $N_{ox}$  represent the atomic densities of iron (84 atoms/nm<sup>3</sup>) and iron oxide (38 atoms/nm<sup>3</sup>). This calculation assumed a homogenous bi-layer model, i.e. a uniformly thick oxidized layer on the steel substrate [93, 150]. Results from this calculation are shown in Table 7-6. As a check, these calculated depths were compared with instrument sputter rates, calibrated using the same sputter settings on a Ta<sub>2</sub>O<sub>5</sub>

substrate. Sputter rates on Ta<sub>2</sub>O<sub>5</sub> was found to be 0.2nm/s. Since complete removal of the oxide on the air-exposed X65 sample took approximately 95s, corresponding to a thickness of 2nm using the instrument value, it was concluded that the calculated thicknesses in Table 7-6 are reasonably accurate.

**Table 7-6 Oxide thickness in each environment, calculated using equation (7-4)**

Sample	Environment	I <sub>Fe</sub> (At% Fe <sup>0</sup> /Total At% Fe)	I <sub>ox</sub> (At% Fe <sub>ox</sub> /Total At% Fe)	d <sub>ox</sub> (nm)
A	Air	40.1	59.9	2.3
B	SFGE	32.4	67.6	2.8
C	Acidic SFGE	55.8	44.2	1.6
D	Alkaline SFGE	42.2	57.8	2.2
E	Anhydrous SFGE	37	63	2.5
F	Hydrated SFGE	42.1	57.9	2.2
G	FGE-S	33	67	2.7
H	SFGE+ 10ppm Cl <sup>-</sup>	34.7	65.3	2.6
I	Deaerated SFGE	23.6	76.3	3.4

### 7.2.1 Film behavior in baseline SFGE and comparison to commercial FGE

XPS spectra from the X65 surface exposed to baseline SFGE are shown in Figure 7-7. Based on thickness calculations, film thickness in baseline SFGE is 0.5 nm thicker than that formed in air, but does not exhibit significant differences in the analyzed composition. Analysis of spectra of the film formed in commercial FGE (Figure 7-8) yields very similar data and nearly identical film thickness. No significant differences were posed between the effects of SFGE and commercial FGE on the air-formed film on X65 pipeline steel in static immersion experiments.

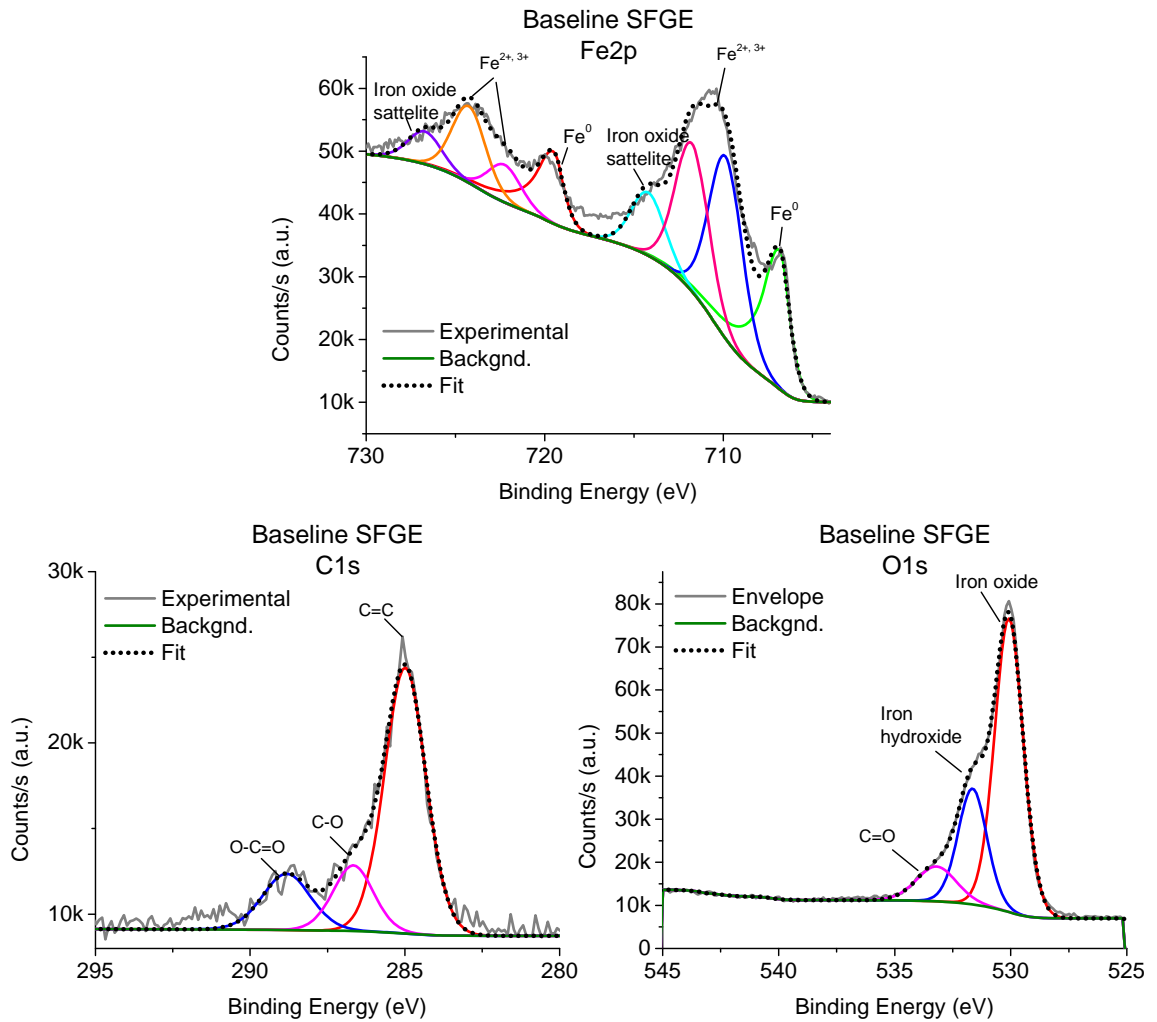


Figure 7-7 Fe2p, C1s, and O1s XPS data from X65 surface after 5-day exposure in baseline SFGE

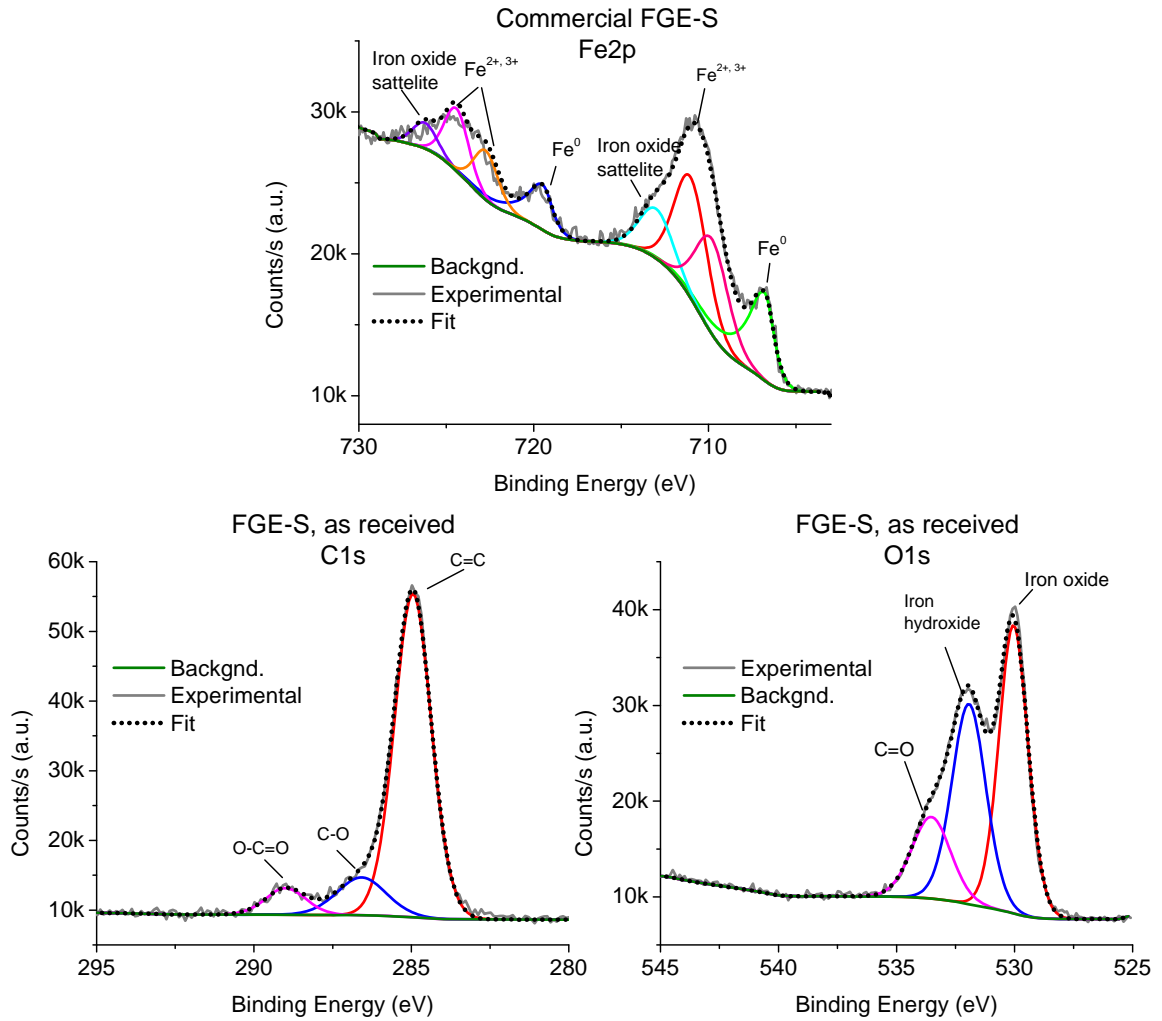
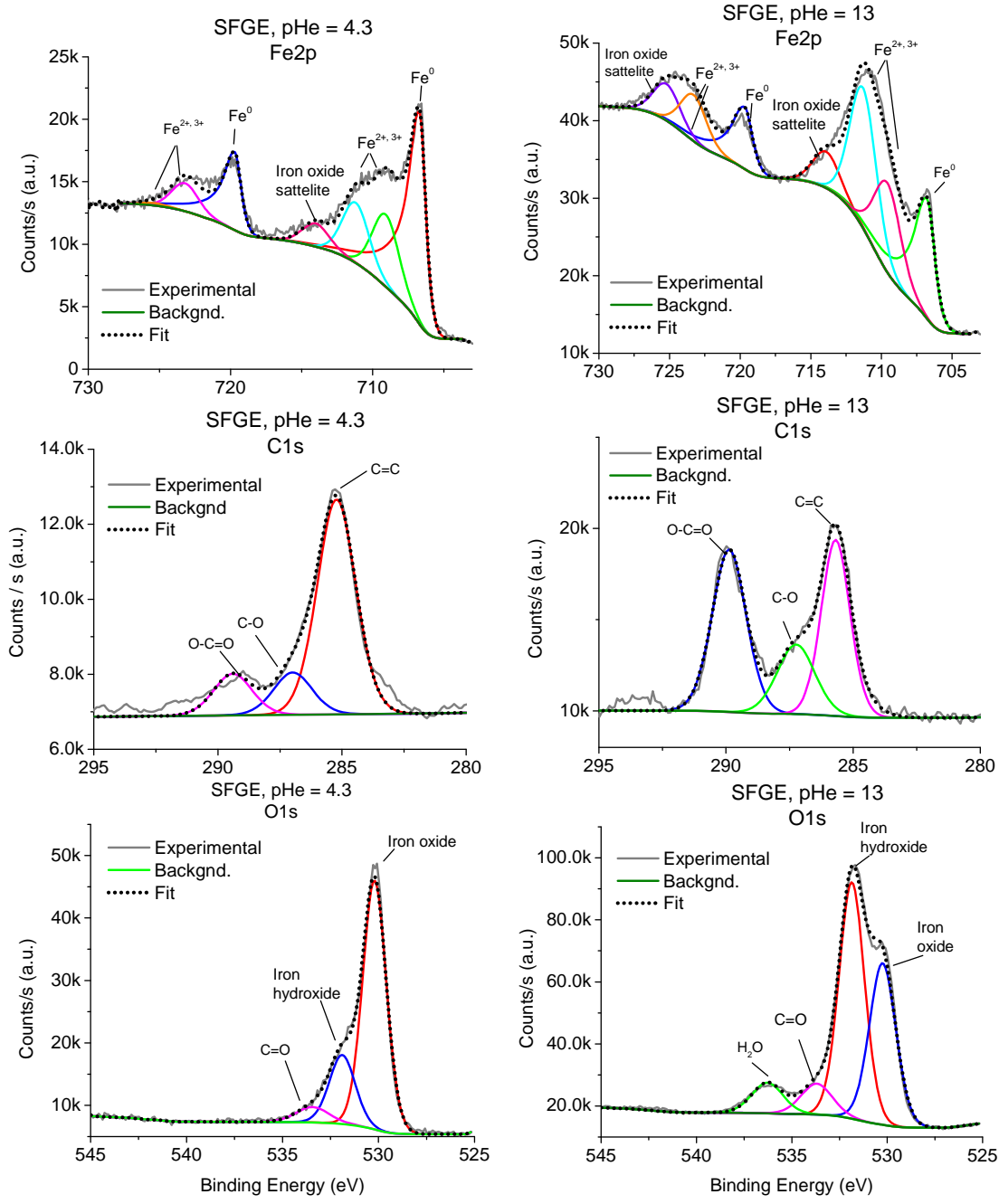


Figure 7-8 Fe<sub>2p</sub>, C<sub>1s</sub>, and O<sub>1s</sub> XPS data from X65 surface after 5-day exposure in standard commercial FGE

## 7.2.2 Effects of pH variations on film composition

Spectra from high pH SFGE (containing 56ppm NaOH) and low pH SFGE (with 560ppm acetic acid) are shown in Figure 7-9. According to oxide thickness calculations, in the acidic environment the oxide thickness decreases by about 55% from baseline SFGE, indicating dissolution of the air-formed film induced by the presence of acidic species. This is evident from the prominent metallic iron peak in the acidified SFGE Fe<sub>2p</sub>

spectrum. Film thickness in alkaline SFGE is comparable to that of the air-formed film. However, the oxygen spectra reveal that composition of the surface oxide on the sample surface exposed to high pH SFGE has changed- the iron hydroxide peak area increased, while the non-hydrated oxide peak area decreased. Moreover, a new peak appears at approximately 536eV, confirming the increased presence of water in the surface oxide film [151]. No such peak was seen in other samples' O1s spectrum. The O-C=O peak is more prominent as well, which could denote the presence of an organo-metallic constituent incorporated into or chemisorbed onto the hydroxide film. The oxide film on the alkaline sample was thinner than on most other samples, with the exception of the air-exposed and high-water-content samples. Thinner films often indicate a greater level of protectiveness, as they are generally more compact and hinder access of the oxidizing species to the bulk metal. AFM images of the alkaline sample (Figure 7-10) shows large raised bumps, which appear to be hydroxide crystals that have formed on the surface during exposure or after sample drying. Underneath the large crystals, polishing lines are still visible on the surface signifying that a tightly adherent, protective and uniform film has formed. The film may be a salt-like  $\text{Fe}(\text{OH})_3$  film which precipitates onto the surface when its solubility is exceeded near the metal/SFGE interface. Observations of repassivation kinetics in Chapter 6 indicate that if it is indeed a salt film, the solubility limit is exceeded relatively quickly, leading to the rapid current decay from the surface.



**Figure 7-9 High resolution iron, carbon, and oxygen spectra from the surface of X65 exposed to acidic SFGE, pHe = 4.2 (left column) and alkaline SFGE, pHe = 13 (right column)**

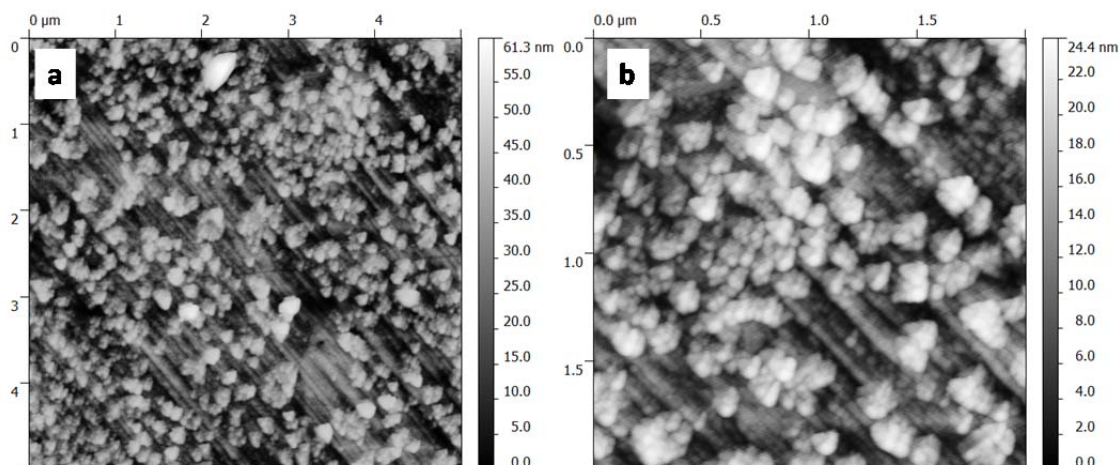


**Figure 7-10 AFM images of the X65 coupon surface after exposure in alkaline SFGE.**

### 7.2.3 Water effects

Samples exposed to SFGE with no added water (water content 0.06 vol%) and 5 vol% water differed in composition, based on high resolution Fe2p, O1s and C1s scans. In order to fit the Fe2p scan of the anhydrous sample, it was necessary to insert a single extra peak at a B.E. of 718.6eV. According to Lin et al [88] this is a satellite peak for Fe<sup>3+</sup> and is a singlet peak (i.e. does not have a matching doublet). This particular peak was not found in Fe2p spectra of any other surface. Both the O1s and C1s scans showed that the sample exposed in anhydrous conditions contained a greater volume of C=O bonded carbon than that in the 5 vol% water SFGE, indicating that in the absence of water, chemisorption of the organic solvent is more likely to occur. Moreover, the anhydrous sample displayed a peak with a relatively large area at 532.1eV, a slightly higher B.E. value than the peak attributed to iron hydroxide at 531.6eV. According to comparison of XPS analysis of iron in anhydrous methanol and a ferrous methoxide

(Fe(OCH)<sub>3</sub>) reference compound [137, 138], the 532 eV B.E. peak in the O1s spectrum is an indication of a methoxy compound. In the ethanolic environments studied in this dissertation, this peak may instead represent the ethoxy-iron compound, in which iron will be in its 3+ state, and thus the presence of an iron ethoxide does indeed help explain the auxiliary satellite peak in the Fe2p spectrum. To verify the peak B.E. of oxygen in iron ethoxide, an Fe (III) ethoxide (C<sub>6</sub>H<sub>15</sub>FeO<sub>3</sub>) powder standard (Alfa Aesar) was obtained for XPS analysis. Fitting of the spectra yielded the expected O1s peak at 532.1eV (Figure 7-12). Because ferrous methoxide [137] and ethoxide are very unstable at elevated temperatures or in the presence of air, so decomposition of the ferrous ethoxide or evaporation of the solvent may have changed some of the X65 film to a traditional oxide like FeO or Fe<sub>2</sub>O<sub>3</sub>.

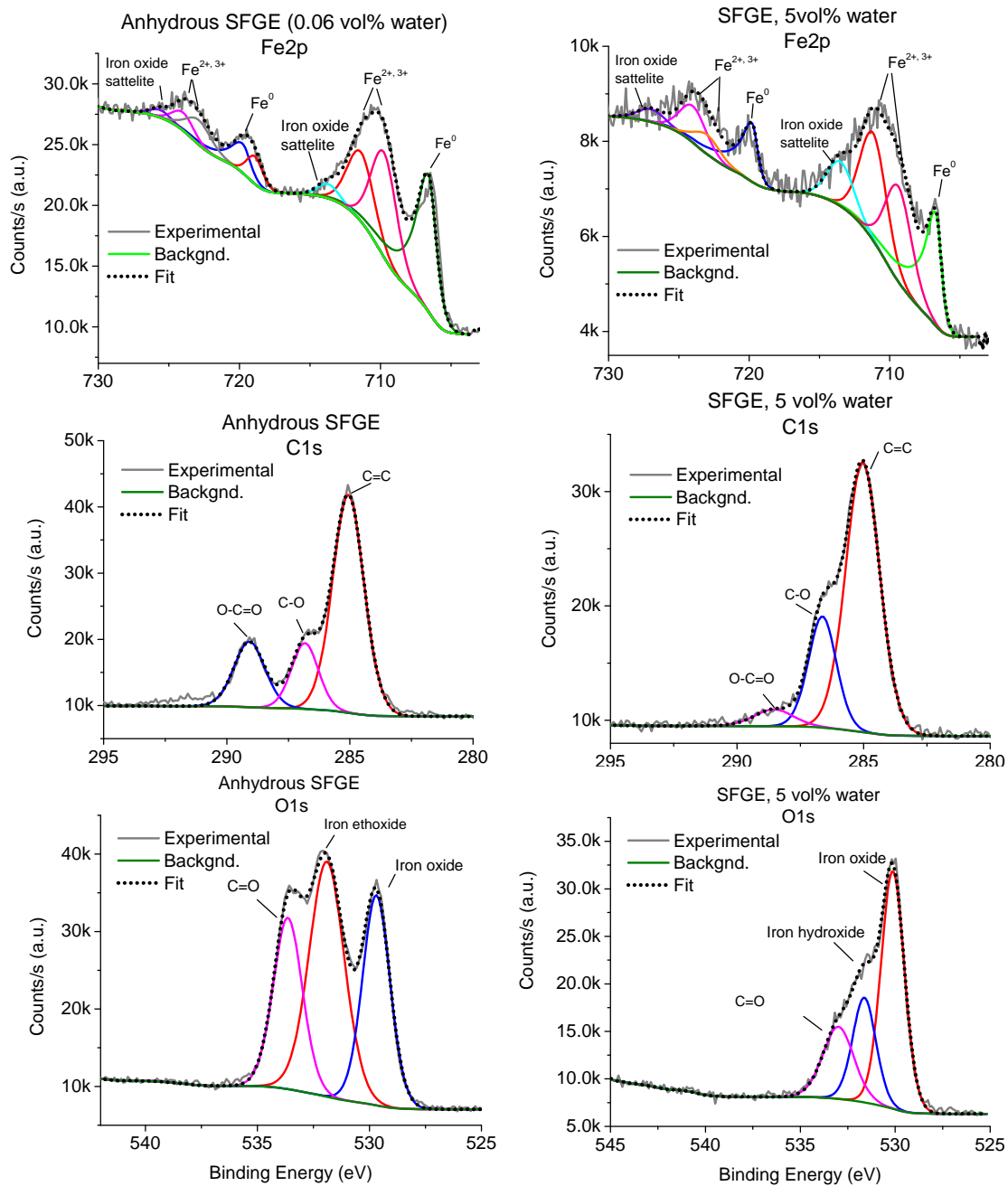
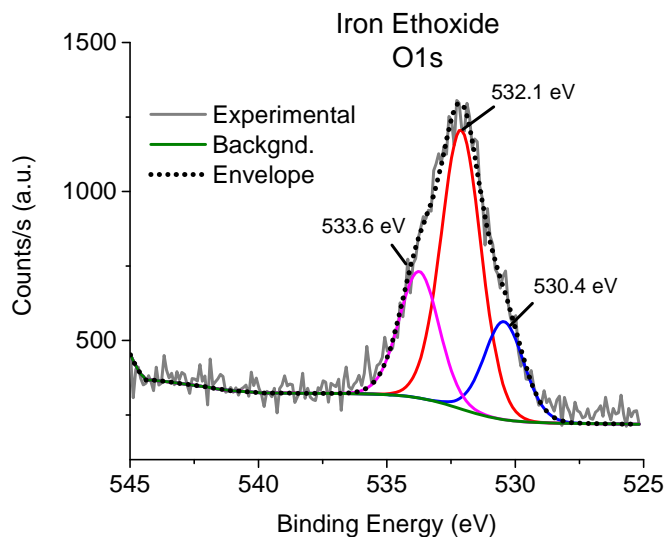


Figure 7-11 High resolution Fe2p, O1s, and C1s spectra from the anhydrous sample (left) and the high water-content sample (right)



**Figure 7-12 O1s spectrum of iron ethoxide powder**

#### 7.2.4 Effects of chloride and deaeration

In aqueous environments, chloride often has the effect of destabilizing the carbon steel passive film and initiating spontaneous film breakdown, [121, 122, 152]. Under static immersion conditions, this spontaneous film breakdown would be expected to manifest itself as a reduction in average thickness of the oxide layer, similarly to the behavior seen above in acidic SFGE. XPS spectra of the X65 surface exposed to Cl<sup>-</sup> containing SFGE (Figure 7-13) show no such features. Oxide thickness calculations in Table 7-6 also do not indicate significant thinning of the oxide layer in presence of Cl<sup>-</sup>. Depth profiles of Cl2s do show an existing small Cl<sup>-</sup> peak that diminishes after approximately 15s of etching (Figure 7-14), which can indicate Cl<sup>-</sup> incorporation into the film. However, small crystals were evident in AFM scans (Figure 7-13) and SEM images, and EDS analysis confirmed that these crystals contained Cl<sup>-</sup>, (Figure 7-15) signifying Cl<sup>-</sup>

residue was left on the surface after solution drying. On coupons exposed to 150ppm  $\text{Cl}^-$  containing SFGE, EDS analysis showed that a  $\text{Cl}^-$  containing residue was left on the coupon surface after the coupon was removed from the solution and dried (Figure 7-16). It can be concluded that instead of participating in spontaneous destabilization by incorporation into or breakdown of the “native film ” (passive film), it is more likely that  $\text{Cl}^-$  in SFGE and FGE environments interacts detrimentally with the base metal in areas of the steel surface where the film has been damaged or removed due to mechanical factors. This conclusion is supported by scratch test data in Chapter 6 where  $\text{Cl}^-$  does not lead to localized corrosion or increased current density on the un-stressed areas of the X65 steel, but slows repassivation, leads to pit initiation, and increases current density in areas where the film has ruptured due to mechanical deformation.

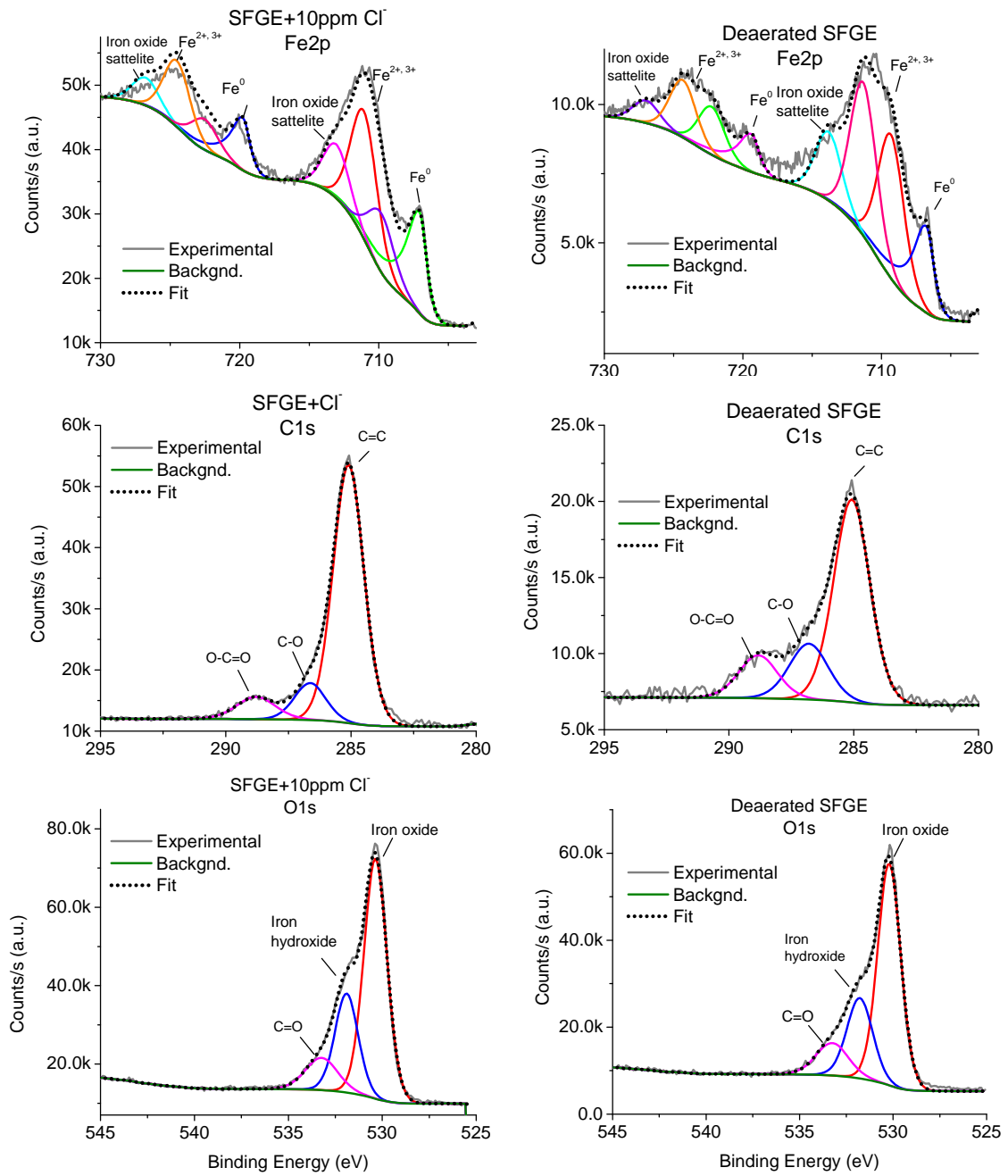


**Figure 7-13 High resolution Fe2p, O1s, and C1s spectra from the samples exposed to SFGE containing 10ppm Cl<sup>-</sup> (left) and deaerated SFGE (right)**

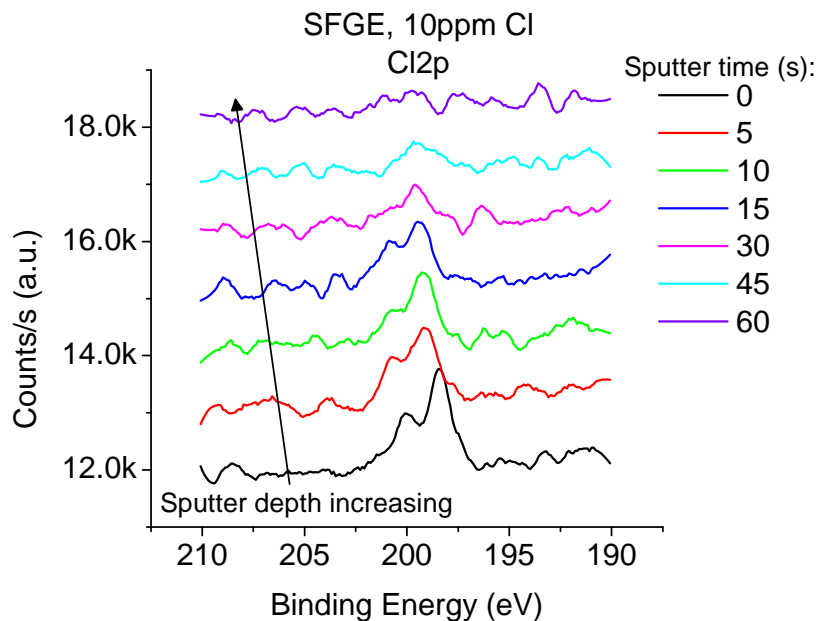


Figure 7-14 XPS Cl<sub>2</sub>p depth profile from X65 coupon surface after 5-day static exposure in SFGE containing 10ppm Cl<sup>-</sup>.

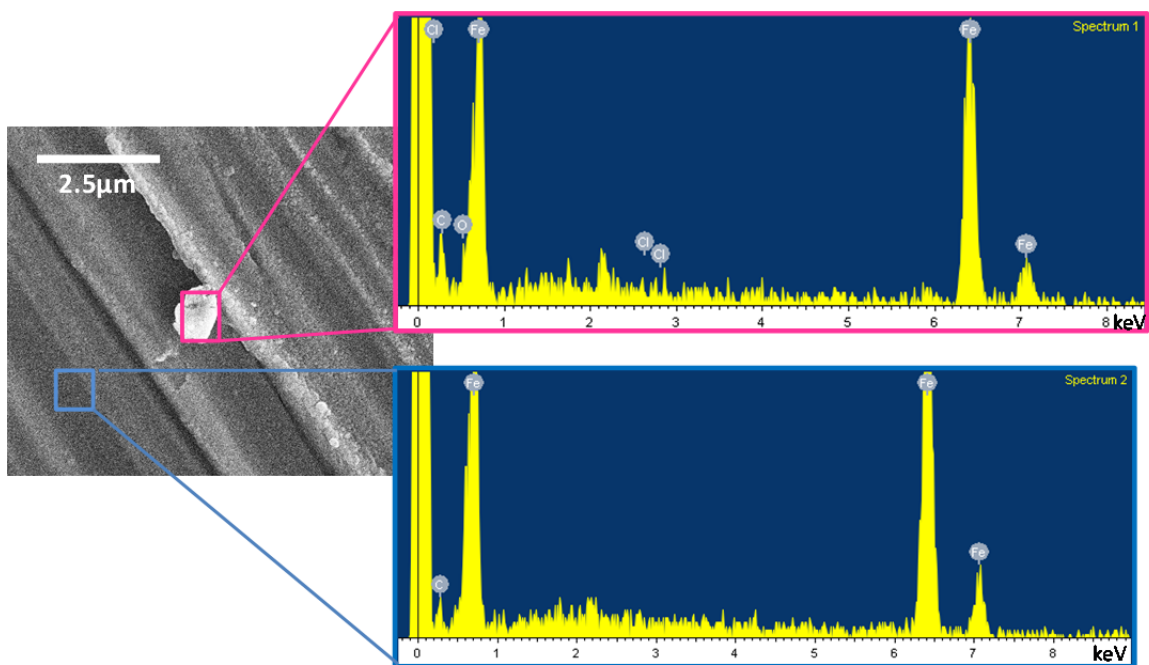
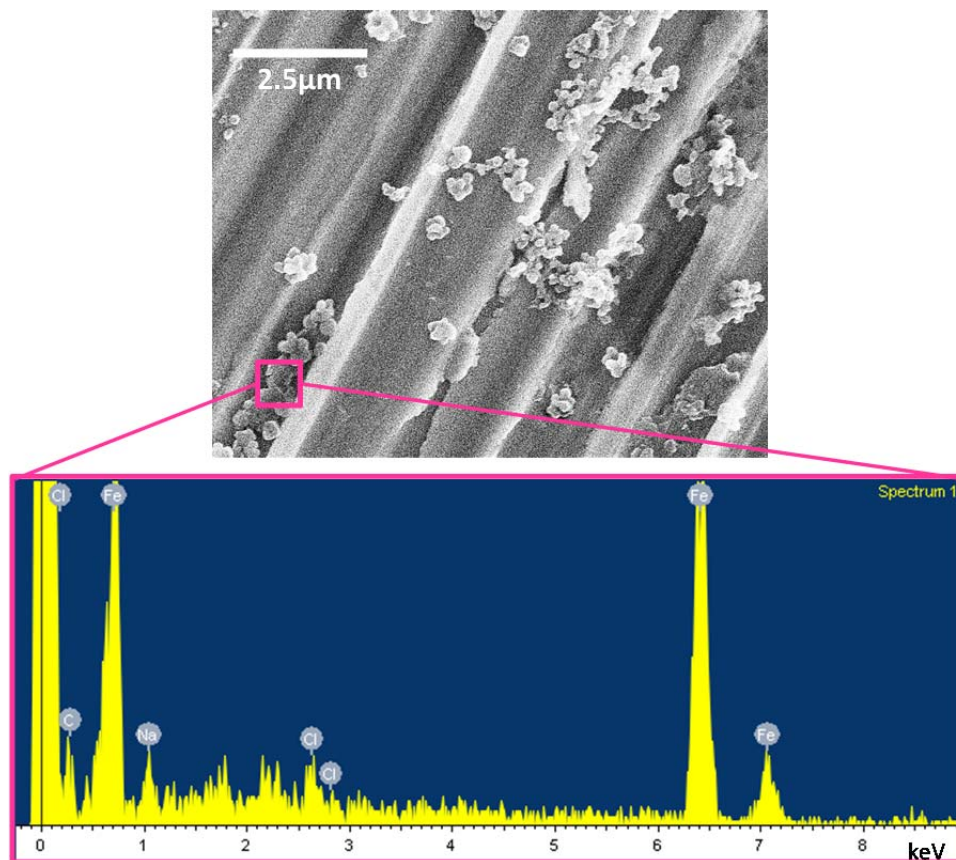


Figure 7-15 SEM of X65 sample after exposure to SFGE containing Cl. The top EDS spectrum, taken in the area on a white particle, shows peaks for Cl. The bottom EDS spectrum, taken on the base metal away from the particle, does not show Na or Cl peaks.



**Figure 7-16 Top: SEM image of an X65 coupon after removal from FGE containing 150ppm Cl. Patches of dried crystalline-looking residue are present on the coupon. Bottom: EDS of the boxed area, indicating presence of Na and Cl in the dried residue.**

AFM images of the as-polished X65, as well as X65 after exposure to deaerated SFGE, alkaline SFGE, and Cl<sup>-</sup>-containing SFGE are shown in Figure 7-17 a), b), c) and d) respectively. Calculated surface roughness values for a selected 5um x 5um region of the 10 x 10um AFM image are shown in Figure 7-18. Selected regions, indicated by light-colored boxes in Figure 7-17, were chosen to eliminate anomalous roughness effects from any large dust particles or contaminants present on the surfaces. Surface roughness calculations were performed using Gwyddion image analysis software.

AFM images of the surface after exposure in deaerated SFGE also show rougher surface features than AFM images obtained of sample surfaces in aerated environments, indicating that some dissolution did occur. This was not surprising, given the greater pre-scratch current density in deaerated SFGE discussed in Chapter 6. Further, Deaeration during static immersion testing caused film thickness to increase by nearly 1nm (23%) relative to the film in aerated SFGE (Table 7-6). Thicker films are often assumed to be less protective, so a greater extent of dissolution (higher surface roughness) should be associated with a thicker film. In the deaerated SFGE solution, it is therefore likely that the oxide thickened, on average, due to dissolution and re-deposition of oxidized iron in selected areas as a porous, non-protective oxide.

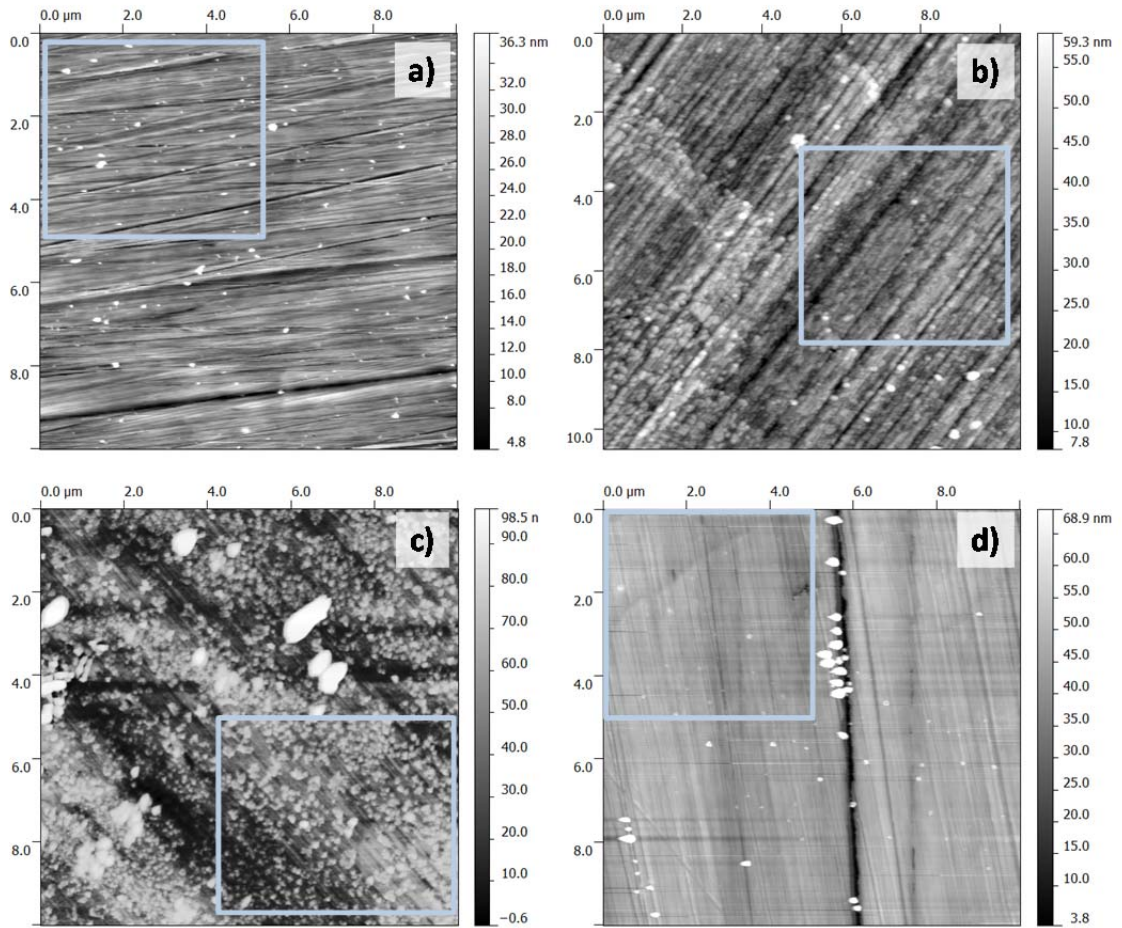


**Figure 7-17 AFM images of X65 surfaces a) as-polished, b) after 5-day exposure to deaerated SFGE, c) after 5-day exposure to alkaline SFGE, d) after 5-day exposure to SFGE containing 10ppm Cl<sup>-</sup>. Bounded regions are 5μm x 5μm areas selected for surface roughness analysis.**

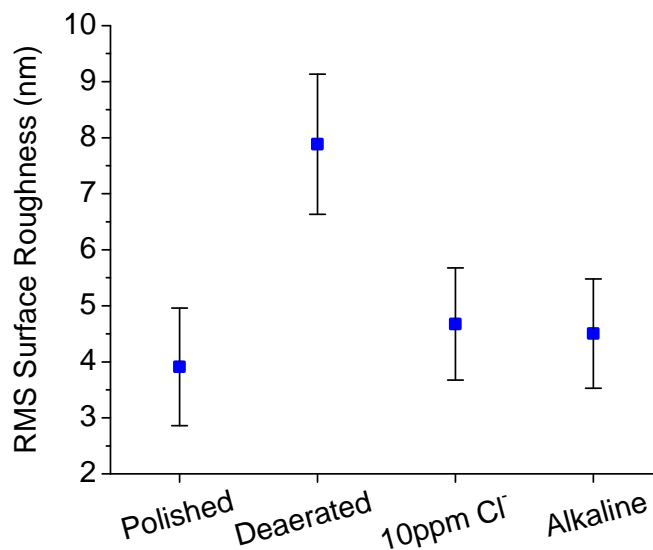


**Figure 7-18** Calculated RMS surface roughness for X65 surfaces after exposure to the given SFGE environment.

### 7.3 Chapter Summary and Conclusions

The composition of films formed on polished X65 coupons in various SFGE environments under static immersion conditions was characterized using X-ray photoelectron spectroscopy. Film morphologies were obtained using atomic force microscopy. Based on the data, the following conclusions can be drawn:

1. The air-formed film is stable in all neutral pH<sub>e</sub> SFGE and FGE (pH<sub>e</sub> 5.4 to 7.8) environments under static immersion conditions.
2. Dissolution of the air-formed oxide occurs in acidic SFGE (pH<sub>e</sub> =4.2) containing acetic acid concentration of 7mM.
3. Cl<sup>-</sup> does not lead to spontaneous breakdown of the X65 passive film in static immersion tests within the tested time frame of 5 days. Sputter depth profiles of

Cl<sup>-</sup> indicate that Cl<sup>-</sup> may become incorporated into the outer film layers or may be simply present as a result of solution drying at the surface.

4. In anhydrous SFGE, a peak in the O1s spectrum at 532.1 eV, attributed to an iron-alkoxide compound, replaces the typical hydroxide component peak at 531.6eV seen in the O1s spectra from baseline SFGE and SFGE containing 1% or more of water.
5. A protective Fe(OH)<sub>3</sub> forms under alkaline conditions, indicated by the presence of a H<sub>2</sub>O peak and a strong iron hydroxide peak in the XPS O1s surface spectrum. Molecules of ethanol may also be incorporated into this film, signified by the relatively large O-C=O peak at a B.E. of 288.8eV. Alternately, this may indicate some formation of iron ethoxide (Fe(C<sub>2</sub>H<sub>5</sub>O<sub>2</sub>)) under alkaline conditions.

# **OVERALL CONCLUSIONS, PROPOSAL OF SCC MECHANISMS IN FGE, IMPLICATIONS FOR THE FUEL INDUSTRY, AND RECOMMENDATIONS FOR FUTURE WORK**

## **8.1 Introduction**

The objectives of this work were to expand the mechanistic understanding of SCC of X65 pipeline steel in commercial and simulated FGE environments. Specifically, the goals were to determine the effects of feedstock or processing-based FGE compositional differences, as well as water, chloride, oxygen and pHe effects on the SCC of X65 in ethanol fuel environments using SSRT. In this chapter, the results of SSRT, repassivation kinetics tests, and film compositional analysis will be used to explain SCC behavior and propose a mechanism of SCC of X65 in steel in FGE and SFGE.

## **8.2 Summary of Constituent Effects on SCC behavior**

The results shown in Chapter 4 show that the differences in FGE feedstock did not affect the SCC susceptibility of X65 pipeline steel in SSRT. When Cl<sup>-</sup> is present, stress corrosion cracking of X65 pipeline steel does occur in SFGE environments as well as in commercial FGE environments in SSRT, regardless of feedstock. Even bulk chloride levels below 10ppm, which are in compliance with the ASTM specification for Fuel Grade Ethanol [55], can lead to SCC of the X65 base metal in both FGE and SFGE. Based on SCC susceptibility testing of X65 in FGE and SFGE via slow strain rate tests,

analysis of SFGE and FGE environments after SSRT, characterization of films formed on X65 steel exposed to FGE and SFGE, and analysis of the repassivation kinetics of strained areas of X65 in FGE and SFGE environments, clear evidence of the film rupture-anodic dissolution mechanism was discovered, which is discussed in more detail in the next section. Chloride was found to play a major role in increasing SCC susceptibility, while oxygen removal and increase in the pHe were found to mitigate SCC. Explanations for increased SCC susceptibility with increase in  $\text{Cl}^-$ , and prevention of SCC with oxygen removal and high pHe were found to be related to the environmental effects on repassivation kinetics, composition, and morphology of films formed on the x65 steel in the ethanol fuel environment.

### **8.3 Evidence of Film Rupture-Anodic Dissolution Mechanism**

For a film-rupture anodic dissolution mechanism to be descriptive of an SCC process, certain general conditions must be met: (1) Dissolution of the material must be thermodynamically possible in the environmental conditions; (2) A passive film must be stable and the material must repassivate to some extent after film rupture, slowing dissolution of crack walls and maintaining crack geometry (i.e. dissolution must be localized); (3) Repassivation kinetics after film rupture must be optimal to ensure crack extension before dissolution transients die out . XPS analysis discussed in section 7.2.4 indicated that in environments where X65 was susceptible to SCC in SSRT, i.e. chloride-containing SFGE, an air-formed film was stable under static immersion conditions. Scratch testing was used to show that X65 does repassivate in  $\text{Cl}^-$  containing SFGE. Results in Chapter 6.4 show that presence of  $\text{Cl}^-$  increased the initial dissolution currents. In light of these experimental results, it can be concluded that X65 steel in SFGE

containing  $\text{Cl}^-$  meets the conditions for an anodic dissolution SCC mechanism. However, in SFGE and FGE without  $\text{Cl}^-$  present, the first two conditions are met, but the lower quantity of dissolution prior to repassivation, as presented in scratch experiments, likely was not enough to cause crack extension. Repassivation test results in the alkaline environment show a quick repassivation, which may prevent crack initiation as well as extension. Under acidic SFGE conditions, in which no SCC was observed in SSRT, the passive film was not stable and dissolved under static immersion conditions, as indicated by a thinning of the oxide layer shown in XPS spectra in Section 7.2.2, and a continual rise in current density from the scratched surface described in Chapter 6.4. In deaerated SFGE, scratch tests revealed that repassivation does not occur after the air-formed film is ruptured, and SCC gives way to general dissolution under these environmental conditions due to the inability of crack walls to repassivate. The pattern of film and repassivation behavior of X65 in ethanolic environments adheres well to the conditions of the film rupture-anodic dissolution mechanism.

#### **8.4 Film Formation of X65 Surface in FGE and SFGE**

Steel passivation can be characterized by the following four types of phenomena: (1) air-formed film; (2) salt film; (3) solvent chemisorption; (4) oxide/oxy-hydroxide formation [153, 154]. One or more than one of the listed film formation mechanisms may act in passivation of a steel surface. As described in Chapter 7, XPS analysis of film composition on X65 coupon surfaces before and after SFGE exposure indicates that the air-formed oxide film remains stable during exposure to neutral (pHe 7.8) FGE and slightly acidic (pHe 5.4) SFGE containing 1% water. Observed changes in the surface carbon content and shifts in binding energy of oxygen peaks imply that chemisorption of

ethanol may also contribute to dissolution inhibition, specifically in SFGE environments with very low (<600 ppm) water content. Lowering of pHe to around 4.3 by acetic acid addition leads to breakdown of the air-formed film, as is shown by the results discussed in section 7.2.2. Whereas, increasing pHe to 13 by addition of small quantities of a hydroxide salt like NaOH alters film composition from air-formed  $\text{Fe}_2\text{O}_3$  or  $\text{Fe}(\text{OH})_2$  to the more stable and protective  $\text{Fe}(\text{OH})_3$ . These conclusions from XPS data analysis are direct verifications of the theoretically calculated film stability fields in Pourbaix diagrams of pure iron in ethanol-water from [19] which predicted stability of an ethoxy-iron salt compound in ethanol/400ppm water below pHe of 6, and conversion of ferrous oxide to ferric hydroxide under alkaline conditions.

It is likely, however, that the composition of the film formed on bare steel after film rupture (without pre-existing air-formed film), i.e. film formed at a crack tip, differs from the investigated films on portions of steel with pre-existing films and should be investigated in the future.

Analysis of XPS peak areas suggests that the oxide film thickness is on the order of a few nanometers, and does not vary appreciably between air-exposed steel and SFGE or FGE-exposed steel. However, OCP of X65 measured during exposure to these environments over long periods of time does signify that film growth indeed occurs when X65 is immersed in SFGE. It has been suggested that the film growth phenomena evident in electrochemical measurements is a result of chemisorption of solvent molecules, forming a dissolution-inhibiting solution layer on top of the air-formed film that raises the activation energy for charge transfer from Fe to solution [53, 59, 91, 137, 147]. Rearrangement of the solvent molecules near the X65 surface is also a possible

explanation for the changing OCP. Additions of water, especially, can lead to significant changes in solvent structure [64, 65, 103] and properties like oxygen solubility[48], acidity[18], and dielectric constant. It is also proposed that in methanol, the cathodic reaction occurring closest to OCP is the reduction of the pre-existing oxide film [155] [79], thus reactions fluctuating between anodic dissolution of Fe and cathodic reduction of the air-formed oxide may result in slight film thickening and the observed continual OCP changes. Characterization of surface electrochemical reactions between steel and ethanol may be important in the SCC mechanism because reaction intermediates or products, such as acetaldehyde or organic acids, can accumulate within a crack and alter the crack tip chemistry. However, evidence of acid production or alcohol intermediates was not seen in surface compositional analysis of X65 by XPS after static immersion, but in-situ analysis may prove more sensitive. In-situ investigation of the FGE/X65 interface is necessary to confirm the near-surface environmental composition since the film may change or evaporate when removed from environment for ex-situ analyses.

### **8.5 Proposed Mechanism of SCC of X65 Steel in FGE and SFGE: Role of Chloride, Oxygen, and Water**

The presence of  $Cl^-$  in the SFGE or FGE environment causes an increase in initial dissolution current after film rupture, as observed in scratch tests. Presence of chloride did not, however, affect the magnitude of dissolution current from X65 steel measured prior to scratching, and also did not affect the oxide thickness on static immersion samples calculated from XPS analysis. The role of chloride in SCC is therefore to increase current density locally from areas of film rupture when the steel is strained. Each burst of this local dissolution serves to extend the crack into the material. More

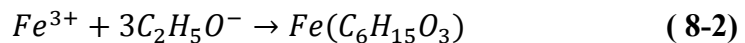
importantly, based on scratch test results, repassivation is able to occur even at relatively large (150ppm) concentrations of  $\text{Cl}^-$ , signifying that even as  $\text{Cl}^-$  migrates into and concentrates within the crack, crack morphology can still be preserved, as crack walls and tip can repassivate. In addition to the large burst of current followed by a current decay within a reasonably short time period in high  $\text{Cl}^-$  SFGE, it was found in chapter 6 that unfilmed steel is susceptible to pitting when  $\text{Cl}^-$  is present. No localized corrosion was observed within scratched areas of X65 in SFGE or FGE when  $\text{Cl}^-$  was not present. Small pits can sometimes lead to stress concentrations sufficient to initiate a crack; however microstructural incongruities like intermetallic inclusions and bands of strain accumulation at a material surface can similarly act as stress raisers. Though, the environment within a pit can contain higher chloride concentrations and be more highly acidic than the bulk environment, creating SCC-favorable conditions in a localized area of the steel.

Oxygen appears to have a dual role in the SCC of X65 pipeline steel. First, the availability of oxygen in SFGE and FGE environments raises the X65 surface potential, creating a potential gradient between filmed steel and bare crack tip. Researchers have proposed that OCP is significant in exacerbating SCC because when OCP is high, potential difference between bare (active) steel and filmed steel is high, thereby increasing the driving force for anodic dissolution [74, 78, 156]. This potential gradient can also be responsible for driving  $\text{Cl}^-$  into the occluded crack area, where it concentrates and creates a potent SCC environment locally [18, 74, 78]. Second, oxygen contributes to re-formation of a stable dissolution-inhibiting film as demonstrated in this and other work [74, 78, Lou,]. The steps in this proposed mechanism are depicted in Figure 8-1.

SSRT in anhydrous Cl-containing SFGE in Chapter 5 confirm that SCC of X65 can occur at very low water content of SFGE. Based on film composition data obtained by XPS in chapter 7, it is evident that water (or lack of water) can change the composition of the passive film on the X65 surface. When 1 vol% water is present in SFGE, peaks in the O1s photoelectron spectrum occur at 531.7 eV, indicating presence of iron oxide or hydroxide. When water content is reduced to 0.05 vol%, the hydroxide peak is replaced by a peak at a slightly higher binding energy (532.1), denoting a possible shift to organometallic film composition. In several past corrosion studies in anhydrous organic solvents, it is postulated that when water is absent from solution, the air-formed film is stable but can be further bolstered by a chemisorbed layer of solvent molecules [61, 67, 99, 137, 157]. Moreover, some of these studies also show that after rupture of the air-formed film, iron and carbon steel repassivate by forming a chemisorbed layer of solvent molecules, because the absence of water precludes formation of an oxy-hydroxide film, and no salt films were observed [61, 67, 99]. In SFGE in the presence of oxygen, Lou et al. found that a possible cathodic reaction on X65 steel at potentials close to OCP is [79]:

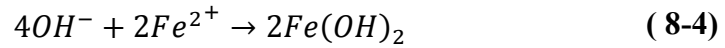
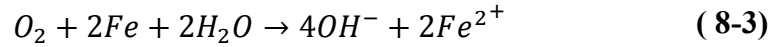


so in ethanol-based solutions, this chemisorbed layer may convert to form iron ethoxide in the presence of oxygen by



Therefore, the only difference in SCC mechanism between the water-containing (1 vol% water) and anhydrous (0.05 vol% water) SFGE should be the repassivation mechanism of the crack walls, and SCC in anhydrous Cl-containing SFGE would follow that depicted in

Figure 8-1. When sufficient water is available in the environment, which can be as little as 1000 ppm in neutral organic solvents, film formation on the crack walls when oxygen is present will proceed according to



as is the general case in aqueous environments. The kinetics of film formation by chemisorption may differ from oxy-hydroxide formation, but this would only effect a change in the crack propagation rate from anhydrous to water-containing SFGE and FGE environments. The potential of the X65 surface is also slightly higher in anhydrous SFGE, which could provide a greater driving force to  $Cl^-$  ions to enter a crack, which would also alter crack propagation rate.

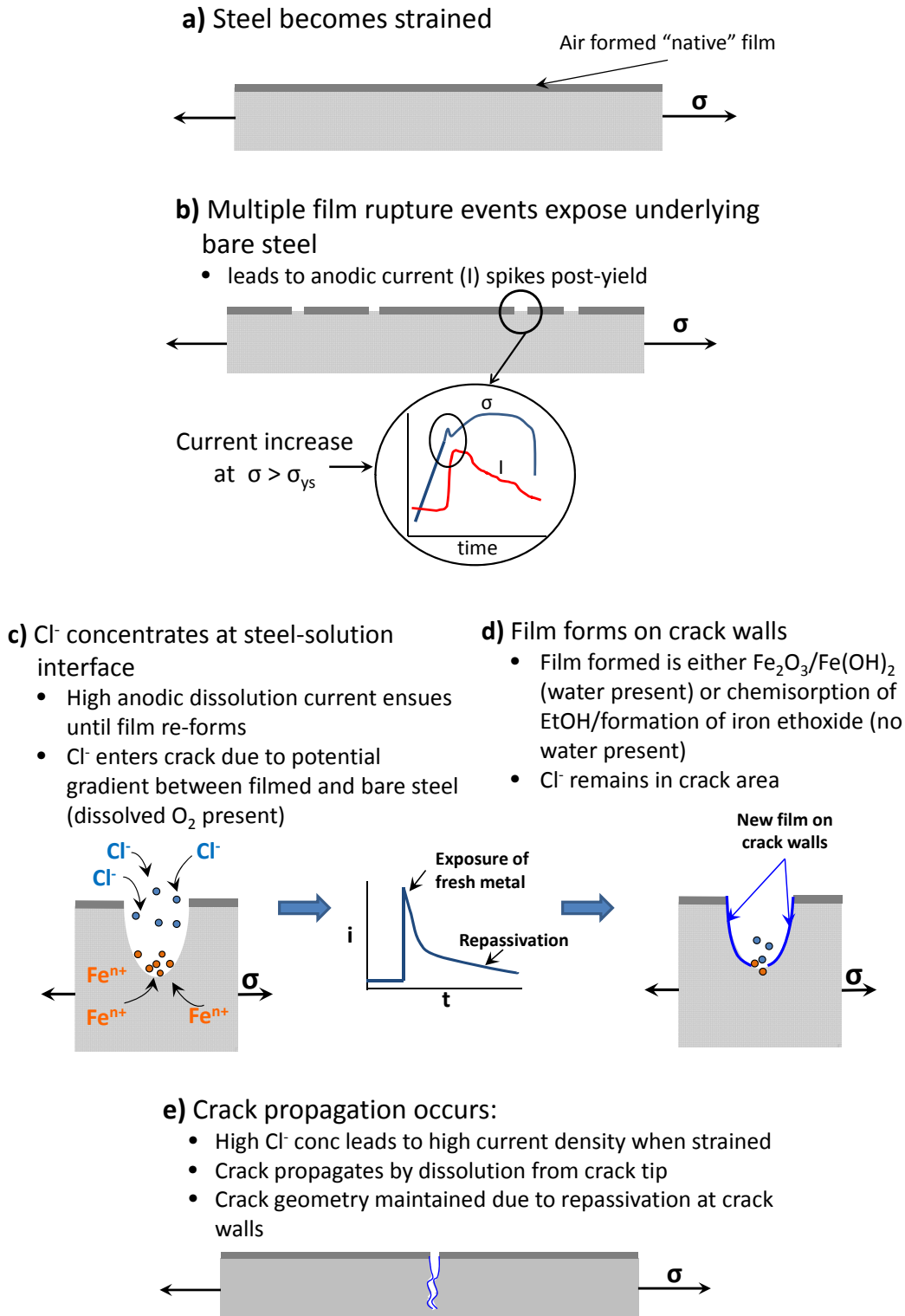


**Figure 8-1 Schematic of proposed SCC mechanism. a) straining of the steel leads to b) multiple film rupture events as stress ( $\sigma$ ) exceeds yield. c) Chloride increases anodic dissolution current from film-ruptured sites. Crack extends, which increase stress concentration locally. d) further straining causes exposure of bare steel, which dissolves anodically. Crack walls are able to passivate, maintaining crack geometry. e) Process repeats.**

## 8.6 Mechanisms of SCC Mitigation in De-oxygenated and Alkaline SFGE and FGE

In this work, SCC mitigation was achieved under three tested environmental conditions: (1) removal of oxygen by deaeration; (2) pH of 12-13; (3) 5 vol% water. Electrochemically, these three conditions have one effect in common: they all cause the OCP of the x65 steel to decrease from the baseline SFGE by 60 to 200mV, which reduces the driving force for Cl<sup>-</sup> migration into a crack, as well as reducing driving force for anodic dissolution. However, scratch test results imply that there are other mechanisms which account for SCC mitigation when open circuit potential is low. In general, low OCP indicates a more highly active surface condition where general dissolution is occurring. In both deaerated and high water content SFGE, current decay after mechanical film rupture only occurred to a small extent, and a low, steady active dissolution current continued from the site of film rupture. Moreover, in the absence of oxygen, dissolution even occurred in un-stressed conditions, as evidenced by the increase in surface roughness in immersion tests and higher pre-scratch current in potentiostatic scratch tests. These behaviors indicate that SCC propagation does not occur in these environments because crack geometry cannot be maintained. When dissolution current remains relatively high after rupture, and repassivation cannot occur on film-ruptured sites, localized stress concentrations leading to crack growth will not be sustained and general dissolution will dominate.

In alkaline SFGE, repassivation is rapid relative to neutral or low pH FGE environments; thus SCC mitigation in the alkaline environment is achieved by an altogether different mechanism. Crack mitigation in alkaline SFGE was observed in

previous research [78, 96] but no mechanism was suggested. It is now clear that because film re-formation is accelerated in alkaline SFGE, therefore anodic dissolution required to propagate a crack does not occur at the crack tip under these conditions.

Characterization of film morphology and chemical composition indicate that the nature of the film formed in the alkaline ethanol differs from those formed in neutral and acidic ethanol; presence of an alkaline constituent leads to formation of a more-protective hydroxide salt film ( $\text{Fe}(\text{OH})_3$ ) that rapidly precipitates onto the steel surface due to its low solubility in ethanol and slows or prevents further dissolution of the steel.

### **8.7 Implications for Safe Transport of FGE in X65 Steel Pipelines**

Stress corrosion cracking of X65 pipeline steel did occur within a small range of FGE environment composition. Presence of dissolved oxygen was necessary for SCC occurrence. Low levels of  $\text{Cl}^-$  (approximately 5ppm for FGE WOI, 10ppm for FGE-S, and 1ppm in SFGE ()) also had to be present for the X65 to undergo SCC. SCC was only observed in FGE and SFGE with water content of less than 5 vol% in this work and other studies[18]. To avoid SCC during pipeline transport of FGE, it is imperative to keep chloride content as low as possible. Plastic stress is necessary for crack propagation, thus relieving stresses in welds may help mitigate SCC. Removal of oxygen will lower the potential of the steel surface, helping to prevent crack propagation; however, oxygen removal may be an impractical solution to the SCC issue. Oxygen removal to prevent SCC would require the addition of chemical oxygen scavengers to FGE, such as hydrazine or diethanolamine, which were each found to mitigate SCC in FGE at concentrations of 1000ppm [20]. These chemicals can be costly to obtain in the quantities necessary, and may also potentially have adverse environmental effects or on ethanol fuel

combustion and other materials with which FGE comes into contact. Moreover, as shown in the scratch tests in Chapter 6, dissolved oxygen is necessary for repassivation to occur, thus oxygen removal may lead to issues with general dissolution.

A more practical approach to SCC mitigation would be to develop an alkaline inhibitor to not only lower the steel's OCP, but also to ensure rapid repassivation and strengthening of the passive film, creating a barrier to dissolution and ceasing crack propagation. Experiments within this dissertation have shown that raising pHe to 12 or 13 using small quantities of an alkaline substance such as NaOH leads to SCC mitigation by rapid formation of a stable passive film. Other recent studies have shown that SCC is also mitigated when pHe is raised by NH<sub>4</sub>OH addition [78, 106].

## **8.8 Recommendations for Future Work**

To further the phenomenological understanding of the interactions of FGE with carbon steel beyond the research presented, several options may be explored:

### **1. In-situ film characterization.**

In this dissertation, film characterization was performed on dry X65 surfaces after exposure to simulated FGE environments. It is known that during sample transport and loading into the UHV environment, atmospheric oxygen and carbon can cause minor surface contamination, thus partially obstructing the true composition of the films.

Additionally, film composition may become altered as a result of drying, particularly since the films formed in this are mostly hydrated oxides. In-situ characterization of the film composition will eliminate some of the above limitations, and will facilitate verification of the film-growth processes over time.

## **2. Characterization of solution within crack.**

Evidence is presented in this research, as well as in other studies [19, 74, 78, 106] of the effects of a potential gradient on the cracking process. These potential effects may simply be the result of active dissolution occurring at the crack tip while a passive film is intact outside the crack. It is also very plausible, however, that the solution within the occluded crack area changes in composition (water content, chloride content, acidity) along the length of the crack as suggested by Beavers et al. [74] and Gui et al. [78].

## **3. Computational simulations of the interactions of ethanol, water, and contaminants (Cl<sup>-</sup>, OH<sup>-</sup>) near the steel surface.**

Molecular dynamics simulations may be able to verify the theory of a concentrated water and chloride environment at the ethanol/steel interface

## **4. Investigation of reason for change in crack path in bulk material (transgranular) and in field (intergranular, in HAZ).**

Different testing methods, such as four-point bend tests and pre-cracked compact tension specimens may be better alternatives to SSRT for studying crack path.

## **5. Cyclic tests and realistic cyclic stress parameters**

SSRT are very severe tests, geared toward accelerating the cracking process to facilitate analysis of SCC under laboratory conditions. However, stress conditions in SSRT do not accurately represent conditions seen in actual service. To properly evaluate conditions leading to SCC of FGE-carrying pipelines, cyclic tests should be carried out in a four-point bend configuration to represent typical stress conditions on pipelines in liquid fuel service.

## APPENDIX

Tables of GC-MS analysis for commercial FGE lots, FGE WOI, and a commercial denaturant:

Sample Name	retention time (min)	Lot 2	Lot 3	Lot 4	Lot 5	Lot 6	Lot 7	Lot 8
		1524407	1526470	1527139	1531177	1602554	1602533	1641499
		mg/mL						
<b>Alcohol</b>								
2-butenal	7.15	0.00	0.00	0.00	0.00	0.00	0.00	389.355
3-methyl butanol	7.57	433.66	372.73	617.55	0.00	0.00	0.00	0.00
Subtotal, mg		433.66	372.73	617.55	0.00	0.00	0.00	389.355
<b>Fatty acid esters</b>								
C10:COOH, ethyl ester	32.57	1.52	0.00	0.00	0.00	0.00	0.00	0.00
C12:COOH, ethyl ester	44.307	1.16	0.00	0.00	0.00	0.00	0.00	0.00
C14:COOH, ethyl ester	48.46	0.00	0.00	0.00	0.00	0.00	0.00	0.00
C16:COOH		0.00	0.00	0.00	0.06	0.00	0.67	0.00
C16:COOH, ethyl ester	51.152	2.49	0.00	0.13	1.57	0.00	1.78	0.00
C18:COOH, methyl ester	52.353	0.00	0.00	1.03	0.00	0.00	0.00	0.00
9,12-octadecadienoic acid, ethyl ester	53.046	0.86	0.00	0.00	0.18	0.00	0.00	0.00
9-octadecenoic acid, ethyl ester	53.127	0.16	0.00	0.00	0.13	2.29	2.95	0.00
Subtotal, mg		6.18	0.00	1.16	1.94	2.29	5.39	0.00
C18:COOH	53.556	1.45	7.45	0.17	0.00	0.00	0.00	1.21
Subtotal, mg		1.45	7.45	0.17	0.00	0.00	0.00	1.21
2,2-bis(4-hydroxy)phenylpropane	53.729	3.16	7.73	0.00	0.00	0.00	0.00	0.00
Subtotal, mg		3.16	7.73	0.00	0.00	0.00	0.00	0.00
<b>Hydrocarbons</b>								
C22H46	53.36	0.00	0.00	0.00	0.00	0.00	0.00	0.00
C23H48	54.301	0.00	0.00	0.00	0.00	0.00	0.00	0.00
C24H50	55.256	0.00	0.00	0.00	0.00	0.00	0.00	0.00
C25H52	56.237	0.00	0.00	0.00	0.00	0.00	0.00	0.00
C26H54	57.244	0.00	0.00	0.00	0.00	0.00	0.00	0.00

C27H56	58.336	0.00	0.00	0.00	0.00	0.00	0.00	0.00
C28H58	59.58	0.00	0.00	0.00	0.00	0.00	0.00	0.00
C29H60	61	0.00	0.00	0.00	0.00	0.00	0.00	0.00
<b>Subtotal, mg</b>		<b>0.00</b>	<b>0.00</b>	<b>0.00</b>	<b>0.00</b>	<b>0.00</b>	<b>0.00</b>	<b>0.00</b>
<b>Rosin Acids</b>								
Pimaric acid	54.385	0.86	5.30	0.07	0.06	0.69	1.05	0.53
Sandaracopimaric acid	54.617	0.61	2.99	0.10	0.04	0.56	0.98	0.39
Isopimaric acid	54.937	0.75	3.40	0.07	0.07	0.64	1.07	0.42
Palustric acid	55.206	1.15	5.92	0.08	0.07	0.29	0.34	0.27
DHA	55.617	0.99	4.79	0.08	0.07	0.53	1.22	0.62
Abietic acid	55.966	1.31	6.92	0.14	0.08	0.67	1.41	0.68
<b>Subtotal, mg</b>		<b>5.66</b>	<b>29.31</b>	<b>0.54</b>	<b>0.39</b>	<b>3.38</b>	<b>6.07</b>	<b>2.91</b>
<b>Terpenes</b>								
2,2-bis[4-hydroxyphenyl]propane								2.13
unidentified terpene								0.465
unidentified terpene								0.896
unidentified terpene								0.198
<b>Subtotal, mg</b>								<b>3.689</b>
<b>Paraffin wax components</b>								
2,2-bis[4'-hydroxyphenyl]propane		0.00	0.00	0.00	0.25	0.49	2.92	0.00
Plasticizer		0.00	0.00	0.00	0.04	10.30	0.97	0.00
Plasticizer		0.00	0.00	0.00	0.04	0.00	0.47	0.00
<b>Subtotal, mg/ml</b>		<b>0.00</b>	<b>0.00</b>	<b>0.00</b>	<b>0.33</b>	<b>10.79</b>	<b>4.36</b>	<b>0.00</b>
<b>Total <sup>c</sup> mg</b>		<b>450.12</b>	<b>417.22</b>	<b>619.43</b>	<b>2.66</b>	<b>16.46</b>	<b>15.82</b>	<b>397.17</b>

Sample name	Denaturant	FGE WOI
	mg/mL	mg/mL
<b>Volatile</b>		
2-butenal	31609.37878	8.57
Toluene	76179.70663	0
cyclohexane	27516.49522	0
3-methyl octane	30025.65343	0
m-Xylene	12188.19704	0
<b>Subtotal, mg</b>	<b>177519.43</b>	<b>8.57</b>
<b>Fatty acid esters</b>		
C10:COOH, ethyl ester	0.00	0.00
C12:COOH, ethyl ester	0.00	0.00
C14:COOH, ethyl ester	0.00	0.00
C16:COOH, ethyl ester	0.00	0.00
C18:COOH, methyl ester	0.00	0.00
9,12-octadecadienoic acid, ethyl ester	0.00	0.00
9-octadecenoic acid, ethyl ester	0.00	0.00
<b>Subtotal, mg</b>	<b>0.00</b>	<b>0.00</b>
C16COOH	0.00	0.00
C18:COOH	0.00	0.00
<b>Subtotal, mg</b>	<b>0.00</b>	<b>0.00</b>
<b>Hydrocarbon</b>		
Hydrocarbon	1.64	0.00
Hydrocarbon	0.68	0.00
Hydrocarbon	0.70	0.00
Hydrocarbon	1.40	0.00
Hydrocarbon	0.00	0.00
Hydrocarbon	0.58	0.00
Phthalate	0.00	0.00
C29H60	0.00	0.00
<b>Subtotal, mg</b>	<b>4.99</b>	<b>0.00</b>
<b>Rosin Acids</b>		
Pimaric acid	0.00	0.00
Sandaracopimaric acid	0.00	0.00
Isopimaric acid	0.00	0.00
Palustric acid	0.00	0.00
DHA	0.00	0.00
Abietic acid	0.00	0.00
<b>Subtotal, mg</b>	<b>0.00</b>	<b>0.00</b>
<b>Total <sup>c</sup> mg</b>	<b>177524.43</b>	<b>8.57</b>

Compositional Data for X65 Pipeline Steel:

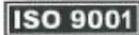


*COLONIAL PIPE  
USED BY LINDSEY & (DO)*  
**APPLIED TECHNICAL SERVICES, INCORPORATED**

1049 Triad Court, Marietta, Georgia 30062 • (770) 423-1400 Fax (770) 424-6415

CHEMICAL TEST REPORT										
Ref. C169114	Date	June 29, 2011				Page	1	of	1	
Customer: Georgia Tech Research Institute, 500 10 <sup>th</sup> Street NW, Atlanta, GA 30308										
Attention: Jamshad Mahmood/ Lindsey Goodman										
Purchase Order #:	Credit Card	Part #/Name:		1.5" x 0.5" x 0.35" chunk of X65 Carbon Steel						
Material Designation: Carbon Steel										
Special Requirement: N/A										
Lab Comment: Analyzed by optical emission, ICP atomic emission and combustion techniques.										
Test Results										
Composition: Weight %										
Identification	C	Mn	P	S	Si	Al	V	Ti	Mg	
Alloy or Spec. Req. <sup>(1)</sup>	—	—	—	—	—	—	—	—	—	
Sample	0.08	1.30	0.012	0.004	0.25	0.04	0.05	0.01	<0.01	

(1) None supplied



Prepared by: *T. Gholar* T. Gholar  
Senior Chemist

Approved by: *W. M. Katter* W. M. Katter  
Senior Chemist

This report may not be reproduced except in full without the written approval of ATS. This report represents interpretation of the results obtained from the test specimen and is not to be construed as a guarantee or warranty of the condition of the entire material lot. If the method used is a customer provided, non-standard test method, ATS does not assume responsibility for validation of the method. Measurement uncertainty available upon request where applicable.

ATS300, 05/2010

## REFERENCES

- [1] Ethanol Expansion in the United States; How Will the Agricultural Sector Adjust?, USDA, Washington, D.C., 2007
  
- [2] M. Iooty, et al., Automotive Fuel Consumption in Brazil: Applying Static and Dynamic Systems of Demand Equations, in: M. Chiaberge (Ed.) New Trends and Developments in Automotive System Engineering, InTech, Online: <http://www.intechopen.com/books/new-trends-and-developments-in-automotive-system-engineering/automotive-fuel-consumption-in-brazil-applying-static-and-dynamic-systems-of-demand-equations>, 2011, pp. 29-44.
  
- [3] HR6: Energy Independence and Security Act of 2007, 110th US Congress, 2007
  
- [4] Y. Pu, et al., The New Forestry Biofuels Sector, Biofuels, Bioproducts and Biorefining, 2 (2008) 58-73.
  
- [5] L.R. Lynd, et al., Fuel Ethanol from Cellulosic Biomass, Science, 251 (1991) 1318-1323.
  
- [6] API, Stress Corrosion Cracking of Carbon Steel in Fuel-grade Ethanol: Review, Experience Survey, Field Monitoring, and Laboratory Testing Washington, D.C., 2007,
  
- [7] NACE International, et al., Corrosion Costs and Preventative Strategies in the United States, in, 2002.
  
- [8] Pipeline Accident Brief DCA00-MP-005, N.T.S. Board, Washington, D.C., 2001
  
- [9] Pipeline Accident Brief DCA-99-MP-005, N.T.S. Board, Washington D.C., 2001
  
- [10] Notes from PHMSA Trip to Brazil, PHMSA, 2007
  
- [11] C.A. Farina, U. Grassini, Stress Corrosion Cracking in Non-Aqueous Media, Electrochim. Acta, 32 (1987) 977-980.

- [12] B.N. Leis, R.J. Eiber, Stress-Corrosion Cracking on Gas-Transmission Pipelines: History, Causes, and Mitigation, in: First International Business Conference on Onshore Pipelines, Berlin, 1997
- [13] R.N. Parkins, A Review of Stress Corrosion Cracking of High Pressure Gas Pipelines, in: NACE Corrosion Conference and Expo, NACE International, Orlando, FL, 2000.
- [14] S.L. Asher, Investigating the Mechanism of Transgranular Stress Corrosion Cracking in Near-Neutral pH Environments on Buried Fuel Transmission Pipelines, Georgia Institute of Technology School of Materials Science and Engineering PhD dissertation, 2007
- [15] S.L. Asher, et al., Investigating a Mechanism for Transgranular Stress Corrosion Cracking on Buried Pipelines in Near-neutral pH Environments, *Corrosion*, 63 (2007) 932-939.
- [16] R.N. Parkins, et al., Transgranular Stress Corrosion Cracking of High-Pressure Pipelines in Contact with Solutions of Near Neutral pH, *Corrosion*, 50 (1994) 394-408.
- [17] R.N. Parkins, Mechanistic Aspects of Intergranular Stress Corrosion Cracking of Ferritic Steels, *Corrosion*, 52 (1996) 363-374.
- [18] X. Lou, et al., Effect of Ethanol Chemistry on Stress Corrosion Cracking of Carbon Steel in Fuel-grade Ethanol, *Corrosion*, 65 (2009) 785-797.
- [19] N. Sridhar, et al., Stress Corrosion Cracking of Carbon Steel in Ethanol, *Corrosion*, 62 (2006) 687-702.
- [20] J.A. Beavers, et al., Prevention of Internal SCC in Ethanol Pipelines, in: *Corrosion 2008*, NACE International, New Orleans, LA, 2008.
- [21] *Stress Corrosion Cracking: Materials Performance and Evaluation*, ASM International, Materials Park, 1999
- [22] J.E. Truman, Influence of Chloride Content, pH and Temperature of Test Solution on the Occurrence of Stress Corrosion Cracking with Austenitic Stainless Steel, *Corros. Sci.*, 17 (1977) 737-746.

- [23] B.F. Brown, Stress-Corrosion Cracking in High Strength Steels and in Titanium and Aluminum Alloys, Naval Research Laboratory, Washington, 1972.
- [24] R. Chu, et al., Microstructure Dependence of Stress Corrosion Cracking Initiation in X-65 Pipeline Steel Exposed to a Near-Neutral pH Soil Environment, *Corrosion*, 60 (2004) 275-283.
- [25] B.E. Wilde, Failure Analysis and Prevention, in: *Metals handbook*, The Society, Cleveland, Ohio, 1990, pp. 203.
- [26] *Principles and Prevention of Corrosion*, Prentice Hall, Upper Saddle River, NJ, 1996
- [27] M.G. Fontana, *Corrosion Engineering*, 3rd ed. ed., McGraw-Hill, New York :, 1986.
- [28] M. Pourbaix, *Atlas of Electrochemical Equilibria in Aqueous Solutions*, Oxford, New York, Pergamon Press, 1966.
- [29] M. Pourbaix, *Atlas of Electrochemical Equilibria in Aqueous Solutions*, [1st English ed.]. ed., National Association of Corrosion Engineers, Houston, TX, 1974.
- [30] J. Küpper, et al., Intergranular Corrosion of Iron-Phosphorus Alloys in Nitrate Solutions, *Corros. Sci.*, 21 (1981) 227-238.
- [31] R.N. Parkins, S. Zhou, The Stress Corrosion Cracking of C-Mn Steel in CO<sub>2</sub>-HCO<sub>3</sub><sup>-</sup>-CO<sub>3</sub><sup>2-</sup> Solutions. I: Stress Corrosion Data, *Corros. Sci.*, 39 (1997) 159-173.
- [32] S. Rashkov, et al., Stressed Electrolytically Deposited Bright Nickel Coatings Obtained During the Cathodic Formation and Decomposition of Nickel Hydride in Acidic Media, *Surface Technology*, 17 (1982) 309-314.
- [33] J.-B. Vogt, Hydrogen-Induced Phase Transformation in a High Nitrogen Austenitic Stainless Steel, *Corros. Sci.*, 41 (1998) 519-528.
- [34] T.L. Anderson, *Fracture Mechanics : Fundamentals and Applications*, 3rd ed. ed., Taylor & Francis, Boca Raton, FL :, 2005.

- [35] J.S.L. Leach, The Possible Role of Surface Films in Stress Corrosion Cracking, in: Stress Corrosion Cracking and Hydrogen Embrittlement of Iron Base Alloys, R.W. Stahele (Ed.), NACE International, Houston, Tx, 1977, pp. 16-20.
- [36] A. Turnbull, Modeling of the Chemistry and Electrochemistry in Cracks- A Review, Corrosion, 57 (2001) 175-189.
- [37] A. Turnbull, The Solution Composition and Electrode Potential in Pits, Crevices and Cracks, Corros. Sci., 23 (1983) 833-870.
- [38] Parkins Symposium on Fundamental Aspects of Stress Corrosion Cracking, in: TMS/ASM-MSD Corrosion & Environmental Effects Committee, TMS, Cincinnati, OH, 1991
- [39] P.L. Andresen, L.M. Young, Crack Tip Microsampling and Growth Rate Measurements in Low-Alloy Steel in High-Temperature Water, Corrosion, 51 (1995) 223-233.
- [40] H.W. Pickering, Role of Gas Bubbles and Cavity Dimensions on the E-pH Ion Concentrations Inside Cavities, in: Equilibrium Diagrams, Localized Corrosion. Proceedings of an International Symposium Honoring Professor Marcel Pourbaix on his Eightieth Birthday., Electrochemical Soc Inc, New Orleans, LA, USA, 1984
- [41] ASTM International, G39-99 Standard Practice for Preparation and Use of Bent-Beam Stress-Corrosion Test Specimens, West Conshohocken, PA, 1999,
- [42] ASTM International, G39-97 Standard Practice for Making and Using U-Bend Stress-Corrosion Test Specimens, West Conshohocken, PA, 1997,
- [43] B. Moniz, W. Pollock (Eds.), Process Industries Corrosion: The Theory and Practice, NACE International, Houston, TX, 1986
- [44] ASTM International, G129-00 Standard Practice for Slow Strain Rate Testing to Evaluate the Susceptibility of Metallic Materials to Environmentally Assisted Cracking, West Conshohocken, PA, USA, 2000,
- [45] Metals Handbook, 9th edition ed., ASM, Cleveland, Ohio, 1990.

- [46] R.N. Parkins, Strain Rate Effects in Stress Corrosion Cracking, *Corrosion*, 46 (1990) 178-189.
- [47] E. Heitz, Corrosion of Metals in Organic Solvents, in: *Advances in Corrosion Science and Technology*, Plenum Press, New York, 1974, pp. 149-243.
- [48] R. Battino, et al., The Solubility of Oxygen and Ozone in Liquids, *J. Phys. Chem. Ref. Data*, 12 (1983) 163-178.
- [49] S.P. Pinho, E.A. Macedo, Representation of Salt Solubility in Mixed Solvents: A Comparison of Thermodynamic Models, *Fluid Phase Equilib.*, 116 (1996) 209-216.
- [50] S.P. Pinho, E.A. Macedo, Solubility of NaCl, NaBr, and KCl in Water, Methanol, Ethanol, and their Mixed Solvents, *Journal of Chemical Engineering Data*, 50 (2005) 29-32.
- [51] R.C. Newman, Review and Hypothesis for the Stress Corrosion Mechanism of Carbon Steel in Alcohols, *Corrosion*, 64 (2008) 819-823.
- [52] P.L. de Anna, The effects of Water and Chloride Ions on the Electrochemical Behaviour of Iron and 304L Stainless Steel in Alcohols, *Corros. Sci.*, 25 (1985) 43-53.
- [53] J.T. Demo, Effect of low concentrations of acid and water on the corrosion of metals in organic solvents, *Chemical Engineering World*, VII (1972).
- [54] R. Vilar, R. da Silva, Preliminary characterization of anhydrous ethanol used in Brazil as automotive fuel, *J. Chromatogr. A*, 985 (2003) 367-373.
- [55] ASTM International, ASTM 4806-10 Standard Specification for Denatured Fuel Ethanol for Blending with Gasolines for Use as Automotive Spark-Ignition Engine Fuel, West Conshohocken, PA, USA, 2010,
- [56] API, 5L Specification for Line Pipe, 2004,
- [57] C. Kalwa, et al., High Strength Steel Pipes: New Developments and Applications, in: *Europipe Onshore Pipeline Conference* Europipe, Houston, TX, 2002.

- [58] E. Cavalcanti, et al., The Effect of Water, Sulphate and pH on the Corrosion Behaviour of Carbon Steel in Ethanolic Solutions, *Electrochim. Acta*, 32 (1987) 935-937.
- [59] X. Lou, L.R. Goodman, Pitting Corrosion of Carbon Steel in Fuel Grade Ethanolic Environment, in: *Corrosion 2009*, NACE International, Atlanta, GA, 2009.
- [60] C.S. Brossia, et al., The Electrochemistry of Iron in Methanolic Solutions and its Relation to Corrosion, *Corros. Sci.*, 37 (1995) 1455-1471.
- [61] D.A. Shifler, et al., The Passivity of Iron and Carbon Steel in Anhydrous Propylene Carbonate Solvents, *Corros. Sci.*, 32 (1991) 475-496.
- [62] D.A. Shifler, et al., Passivity and Breakdown of Carbon Steel in Organic Solvent Mixtures of Propylene Carbonate and Dimethoxyethane, *J. Electrochem. Soc.*, 145 (1998) 2396-2404.
- [63] J. Banas, Passivity of Iron and Nickel in a  $\text{CH}_3\text{OH-H}_2\text{O-H}_2\text{SO}_4$  System, *Electrochim. Acta*, 32 (1987) 871-875.
- [64] S. Dixit, et al., Molecular Segregation Observed in a Concentrated Alcohol-Water Solution, *Nature*, 416 (2002) 829-832.
- [65] K. Egashira, N. Nishi, Low-Frequency Raman Spectroscopy of Ethanol-Water Binary Solution: Evidence for Self-Association of Solute and Solvent Molecules, *J. Phys. Chem. B*, 102 (1998) 4054-4057.
- [66] A. Wakisaka, et al., Solute-Solvent and Solvent-Solvent Interactions Evaluated through Clusters Isolated from Solutions: Preferential Solvation in Water-Alcohol Mixtures, *J. Mol. Liq.*, 90 (2001) 175-184.
- [67] R.G. Kelly, P.J. Moran, The Passivity of Metals in Organic Solutions, *Corros. Sci.*, 30 (1990) 495-509.
- [68] S.L. Asher, P.M. Singh, Role of stress in transgranular stress corrosion cracking of transmission pipelines in near-neutral pH environments, *Corrosion*, 65 (2009) 79-87.

- [69] J.A. Beavers, C.E. Jaske, Near-neutral pH SCC in pipelines: effects of pressure fluctuations on crack propagation, in: Corrosion 98, NACE International, Houston, TX, 1998.
- [70] J.G. Maldonado, N. Sridhar, SCC of Carbon Steel in Fuel Ethanol Service: Effect of Corrosion Potential and Ethanol Processing Source, in: Corrosion 2007 Conference and Expo, NACE international, 2007
- [71] J.A. Beavers, et al., Effects of Steel Microstructure and Ethanol-Gasonline Blend Ratio on SCC of Ethanol Pipelines, in: Corrosion 2009 Conference and Expo, NACE International, Atlanta, GA, 2009
- [72] X. Lou, et al., Understanding the Stress Corrosion Cracking of X-65 Pipeline Steel in Fuel Grade Ethanol, in: Corrosion 2010 Conference and Expo, NACE International, San Antonio, Tx, 2010.
- [73] L. Goodman, et al., Investigation of the Stress Corrosion Cracking of Carbon Steel in Fuel Grade Ethanol Environments, in: TMS 2010 139th Annual Meeting and Exhibition, TMS, Seattle, WA, 2010.
- [74] J.A. Beavers, et al., Effects of Environmental and Metallurgical Factors on the Stress Corrosion Cracking of Carbon Steel in Fuel Grade Ethanol, Corrosion, 67 (2011) 025005-025001-025005-025015.
- [75] F. Gui, et al., Effect of Ethanol Composition on the SCC Susceptibility of Carbon Steel, in: Corrosion 2010 Conference and Expo, NACE International, San Antonio, TX, 2010
- [76] G. Cragolino, et al., The critical potential for the stress corrosion cracking of Fe-Ni-Cr alloys and its mechanistic implications, in: Chemistry and electrochemistry of corrosion and stress corrosion cracking: A symposium honoring the contributions of R.W. Staehle, R.H. Jones (Ed.), TMS, San Antonio, TX, 2001.
- [77] X. Lou, P.M. Singh, Role of Water, Acetic Acid, and Chloride on Corrosion and Pitting Behaviour of Carbon Steel in Fuel Grade Ethanol, Corros. Sci., 52 (2010) 2303-2315.
- [78] F. Gui, et al., Localized Corrosion of Carbon Steel and its Implications on the Mechanism and Inhibition of Stress Corrosion Cracking in Fuel-grade Ethanol, Corrosion, 66 (2010) 125001-125001-125001-125012.

- [79] X. Lou, P.M. Singh, Cathodic Activities of Oxygen and Hydrogen on Carbon Steel in Simulated Fuel-grade Ethanol, *Electrochim. Acta*, 56 (2011) 2312-2320.
- [80] ASTM International, D 6423 Standard Test Method for Determination of pH<sub>e</sub> of Ethanol, Denatured Fuel Ethanol, and Fuel Ethanol (Ed75-Ed85), West Conshohocken, PA, USA, 2008,
- [81] ASTM International, E8/E8M-08 Standard Test Methods for Tension Testing of Metallic Materials, West Conshohocken, PA, USA, 2008,
- [82] W.C. Young, Roark's Formulas for Stress and Strain, 7th ed. ed., McGraw-Hill, New York :, 2002.
- [83] X. Lou, et al., Film Breakdown and Anodic Dissolution During Stress Corrosion Cracking of Carbon Steel in Bioethanol, *J. Electrochem. Soc.*, 157 (2010) C86-C94.
- [84] C.A. Farina, et al., Electrochemical Behavior of Iron in Methanol and Dimethylformamide Solutions, *Corros. Sci.*, 18 (1978) 465-479.
- [85] F. Bellucci, et al., The Behaviour of Iron and Low Alloy Steels in Anhydrous Organic Solvents-Methanolic Solutions, *Corros. Sci.*, 28 (1988) 371-384.
- [86] M.G. Athayde, et al., The Anodic Behaviour of Iron in Ethanol-Water Solutions in the Presence and Absence of NaClO<sub>4</sub> as the Supporting Electrolyte, *Electrochim. Acta*, 32 (1987) 909-913.
- [87] L. Cao, et al., Corrosion and Cracking of Carbon Steel in Fuel Grade Ethanol-Supporting Electrolyte and Susceptible Potential Regime, in: *Corrosion 2011 Conference and Expo*, NACE International, Houston, TX, 2011.
- [88] T.C. Lin, et al., A Consistent Method for Quantitative XPS Peak Analysis of Thin Oxide Films in Polycrystalline Iron Surfaces, *Appl. Surf. Sci.*, 119 (1997) 83-92.
- [89] C. Battistoni, et al., Quantitative Surface Analysis by XPS: A Comparison among Different Quantitative Approaches, *Surf. Interface Anal.*, 7 (1985) 177.

- [90] A.P. Grosvenor, et al., Use of QUASES™/XPS Measurements to Determine the Oxide Composition and Thickness on an Iron Substrate, *Surf. Interface Anal.*, 36 (2004) 632-639.
- [91] E. Paparazzo, XPS Analysis of Iron Aluminum Oxide Systems, *Appl. Surf. Sci.*, 25 (1986) 1-12.
- [92] P. Mills, J.L. Sullivan, Study of the Core Level Electrons in Iron and its Three Oxides by Means of X-Ray Photoelectron Spectroscopy, *J. Phys. D: Appl. Phys.*, 16 (1983) 723-732.
- [93] P. Ghods, et al., XPS depth profiling study on the passive oxide film of carbon steel in saturated calcium hydroxide solution and the effect of chloride on the film properties, *Appl. Surf. Sci.*, 257 (2011) 4669-4677.
- [94] N.S. McIntyre, D.G. Zetaruk, X-ray photoelectron spectroscopic studies of iron oxides, *Anal. Chem.*, 49 (1977) 1521-1529.
- [95] J.G. Maldonado, N. Sridhar, SCC of Carbon Steel in Fuel Ethanol Service: Effect of Corrosion Potential and Ethanol Processing Source, in: *Corrosion 2007*, NACE international, Nashville, TN, 2007.
- [96] X. Lou, P.M. Singh, Phase Angle Analysis for Stress Corrosion Cracking of Carbon Steel in Fuel-grade Ethanol: Experiments and Simulation, *Electrochim. Acta*, 56 (2011) 1835-1847.
- [97] F.L. LaQue, *Marine Corrosion Causes and Prevention*, John Wiley and Sons, New York, 1975.
- [98] R.G. Kelly, et al., The Passivity of Iron in Mixtures of Propylene Carbonate and Water, *Electrochim. Acta*, 34 (1989) 823-830.
- [99] R.G. Kelly, et al., Passivity of Fe in Anhydrous Propylene Carbonate, *J. Electrochem. Soc.*, 136 (1989) 3262-3269.
- [100] R.G. Kelly, R.C. Newman, Confirmation of the Applicability of Scratched Electrode Techniques for the Determination of Bare Surface Current Densities, *J. Electrochem. Soc.*, 137 (1990) 357-358.

- [101] H. Kaesche, *Metallic Corrosion : Principles of Physical Chemistry and Current Problems*, NACE, Houston, Tex. :, 1985.
- [102] D.A. Jones, *Localized Surface Plasticity During Stress Corrosion Cracking*, *Corrosion*, 52 (1996) 356-362.
- [103] A. Wakisaka, et al., *Solute-Solvent and Solvent-Solvent Interactions Evaluated through Clusters Isolated from Solutions: Preferential Solvation in Water-Alcohol Mixtures*, *J. Mol. Liq.*, 90 (2001) 175-184.
- [104] F. Gui, N. Sridhar, *Conducting Electrochemical Measurements in Fuel-Grade Ethanol Using Microelectrodes*, *Corrosion*, 66 (2010) 045005-045001-045005-045008.
- [105] R. Nishimura, Y. Maeda, *Metal Dissolution and Maximum Stress During SCC Process of Ferritic (type 430) and Austenitic (type 304 and type 316) Stainless Steels in Acidic Chloride Solutions under Constant Applied Stress*, *Corros. Sci.*, 46 (2004) 755-768.
- [106] J.A. Beavers, F. Gui, *Recent Progress in Understanding and Mitigating SCC of Ethanol Pipelines*, in: *Corrosion 2010 NACE International*, San Antonio, TX, 2010.
- [107] J.C. Scully, *Kinetic Features of Stress Corrosion Cracking*, *Corros. Sci.*, 7 (1967) 197-207.
- [108] G.J. Bignold, *Electrochemical Aspects of Stress Corrosion of Steels in Alkaline Solutions*, *Corrosion*, 28 (1972) 307-312.
- [109] *Stress Corrosion Cracking and Hydrogen Embrittlement of Iron Base Alloys*, NACE International, Houston, Tx, 1977.
- [110] R.M. Carranza, J.R. Galvele, *Repassivation Kinetics in Stress Corrosion Cracking-I. Type AISI 304 Stainless Steel in Chloride Solutions*, *Corros. Sci.*, 28 (1988) 233-249.
- [111] K.A. Yeom, et al., *Predicting SCC susceptibility of austenitic stainless steels by rapid scratching electrode technique*, *Mater. Sci. Forum*, 289-292 (1998) 969-978.

- [112] H.S. Kwon, et al., Prediction of Stress Corrosion Cracking Susceptibility of Stainless Steels Based on Repassivation Kinetics, *Corrosion*, 56 (2000) 32-41.
- [113] P.H. Chou, et al., Repassivation Behavior and Stress Corrosion Cracking Susceptibility of Stainless Steels Containing Silicon, in: *NACE Corrosion Conference and Expo*, NACE International, San Antonio, TX, 2010.
- [114] R.P. Wei, et al., Peak Bare-Surface Current Densities Overestimated in Straining and Scratching Electrode Experiments, *J. Electrochem. Soc.*, 136 (1989) 1835-1836.
- [115] D. Boomer, et al., Refilming Kinetics of Scraped Steel Electrodes in Simulated Corrosion Fatigue Crack-Tip Environments, *Corros. Sci.*, 29 (1989) 1087-1101.
- [116] G.T. Burstein, P.I. Marshall, Growth of Passivating Films on Scratched 304L Stainless Steel in Alkaline Solution, *Corros. Sci.*, 23 (1983) 125-137.
- [117] P.D. Bastek, et al., Measurement of Passive Film Effects on Scratched Electrode Behavior, *J. Electrochem. Soc.*, 140 (1993) 1884-1889.
- [118] H.J. Raetzer-Scheibe, H. Buhl, Repassivation Behavior of Metallic Materials Using a Titanium Alloy as an Example, *Werkst. Korros.*, 30 (1979) 846-853.
- [119] E.A. Cho, et al., Quantitative Analysis of Repassivation Kinetics of Ferritic Stainless Steels Based on the High Field Conduction Model, *Electrochim. Acta*, 45 (2000) 1933-1942.
- [120] R.S. Lillard, et al., The Kinetics of Anodic Dissolution and Repassivation on Stainless Steel 304L in Solutions Containing Nitrate, *J. Electrochem. Soc.*, 158 (2011) C194-C201.
- [121] N. Cabrera, N.F. Mott, Theory of the Oxidation of Metals, *Reports on the Progress in Physics*, 12 (1949) 163-184.
- [122] N. Sato, M. Cohen, Kinetics of Anodic Oxidation of Iron in Neutral Solution. I. Steady Growth Region, *J. Electrochem. Soc.*, 111 (1964) 512-519.
- [123] D.D. Macdonald, Passivity- the Key to our Metals-Based Civilization, *Pure Applied Chemistry*, 71 (1999) 951-978.

- [124] S. Ahn, et al., Role of Chloride Ion in Passivity and Breakdown on Iron and Nickel, *J. Electrochem. Soc.*, 152 (2005) B482-B490.
- [125] G.T. Burstein, A.J. Davenport, The Current-Time Relationship during Anodic Oxide Film Growth under High Electric Field, *J. Electrochem. Soc.*, 136 (1989) 936-941.
- [126] G.T. Burstein, G. Gao, Verification of the Validity of Peak Bare Surface Current Densities Obtained from the Scratched Electrode, *J. Electrochem. Soc.*, 138 (1991) 2627-2630.
- [127] H.J. Pearson, et al., Resistance to Flow of Current to Scratched Electrodes, *J. Electrochem. Soc.*, 128 (1981) 2297-2303.
- [128] R.P. Wei, M. Gao, Further Observations on the Validity of Bare Surface Current Densities Determined by the Scratched Electrode Technique, *J. Electrochem. Soc.*, 138 (1991) 2601-2606.
- [129] G.J. Brug, et al., The Analysis of Electrode Impedances Complicated by the Presence of a Constant Phase Element, *Journal of Electroanalytical Chemistry and Interfacial Electrochemistry*, 176 (1984) 275-295.
- [130] R.N. Parkins, Localized Corrosion and Crack Initiation, *Materials Science and Engineering: A*, 103 (1988) 143-156.
- [131] R.N. Parkins, et al., Transgranular Stress Corrosion Cracking of High-Pressure Pipelines in Contact with Solutions of Near Neutral pH, *Corrosion*, 50 (1994) 394-408.
- [132] P.M. Singh, et al., Stress Corrosion Cracking and Corrosion Fatigue Cracking of a Duplex Stainless Steel in White Water Environments, *Corrosion*, 60 (2004) 852-861.
- [133] M. Stern, Evidence for a Logarithmic Oxidation Process for Stainless Steel in Aqueous Systems, *J. Electrochem. Soc.*, 106 (1959) 376-381.
- [134] M. Avrami, Kinetics of Phase Change. I. General Theory, *J. Chem. Phys.*, 7 (1939) 1103-1112.

- [135] L.R. Goodman, et al., Formation and Breakdown of Passive Film on X65 Pipeline Steel in Fuel Grade Ethanol Environments and its Implications for Stress Corrosion Cracking, in: Corrosion 2012, NACE International, Salt Lake City, UT, 2012.
- [136] U.R. Evans, Inhibition, Passivity and Resistance: A Review of Acceptable Mechanisms, *Electrochim. Acta*, 16 (1971) 1825-1840.
- [137] J. Banas, et al., Corrosion and Passivity of Metals in Methanol Solutions of Electrolytes, *J. Solid State Electrochem.*, 13 (2009) 1669-1679.
- [138] M. Sakakibara, et al., Corrosion of Iron in Anhydrous Methanol, *Corros. Sci.*, 34 (1993) 391-402.
- [139] G. Seshadri, et al., Combined UHV-Electrochemical Study of Polycrystalline Iron Electrodes in Borate and Sulfate Media, *Langmuir*, 13 (1997) 3219-3225.
- [140] P. Ghods, et al., Angle-Resolved XPS Study of Carbon Steel Passivity and Chloride-Induced Depassivation in Simulated Concrete Pore Solution, *Corros. Sci.*, 58 (2012) 159-167.
- [141] D. Landolt, *Corrosion and Surface Chemistry of Metals*, CRC Press, Boca Raton, FL, USA, 2003.
- [142] C.R. Brundle, et al., Core and Valence Level Photoemission Studies of Iron Oxide Surfaces and the Oxidation of Iron, *Surf. Sci.*, 68 (1977) 459-468.
- [143] P.C.J. Graat, M.A.J. Somers, Simultaneous Determination of Composition and Thickness of Thin Iron-Oxide Films from XPS Fe2p Spectra, *Appl. Surf. Sci.*, 100/101 (1996) 36-40.
- [144] NIST, NIST x-ray photoelectron spectroscopy database, in, National Institute of Standards and Technology, Gaithersburg, MD, 2011.
- [145] A.P. Grosvenor, et al., Activation Energies for the Oxidation of Iron by Oxygen Gas and Water Vapour, *Surf. Sci.*, 574 (2005) 317-321.
- [146] A.P. Grosvenor, et al., Examination of the Oxidation of Iron by Oxygen Using X-Ray Photoelectron Spectroscopy and QUASES<sup>TM</sup>, *Surf. Sci.*, 565 (2004) 151-162.

- [147] D. Briggs, M.P. Seah, Auger and X-ray Photoelectron Spectroscopy, Wiley, Chichester, 1990.
- [148] M.P. Seah, W.A. Dench, Quantitative Electron Spectroscopy of Surfaces: A Standard Database for Electron Inelastic Mean Free Paths in Solids, Surf. Interface Anal., 1 (1979) 2-11.
- [149] E. De Vito, P. Marcus, XPS Study of Passive Films Formed on Molybdenum-implanted Austenitic Stainless Steels, Surf. Interface Anal., 19 (1992) 403-408.
- [150] X. Zhang, et al., Estimation of Kinetic Parameters of the Passive State of Carbon Steel in Mildly Alkaline Solutions from Electrochemical Impedance Spectroscopic and X-Ray Photoelectron Spectroscopic Data, Electrochim. Acta, 56 (2011) 5010-5918.
- [151] B.E. Koel, et al., X-Ray photoelectron study of the reaction of water with cerium, J. Electron. Spectrosc. Relat. Phenom., 21 (1980) 31-46.
- [152] D.D. Macdonald, The Point Defect Model for the Passive State, J. Electrochem. Soc., 139 (1992) 3434-3449.
- [153] U.R. Evans, Inhibition, Passivity and Resistance: a Review of Acceptable Mechanisms, Electrochim. Acta, 16 (1971) 1825-1840.
- [154] T.P. Hoar, et al., The Relationships Between Anodic Passivity, Brightening and Pitting, Corros. Sci., 5 (1965) 279-289.
- [155] F. Bellucci, et al., The Passivity of Ferritic (Fe-18% Cr) Stainless Steel in Methanolic Solutions, J. Appl. Electrochem., 11 (1981) 781-785.
- [156] H.L. Logan, Film-Rupture Mechanism of Stress Corrosion, Journal of Research of the National Bureau of Standards, 48 (1952) 99-105.
- [157] V.A. Safonov, et al., Specific Features of the Metal Passivation in Organic and Water-Organic Media, Mater. Sci. Forum, 185-188 (1995) 853-860.

## VITA

Lindsey Roberta Goodman was born in Seattle, WA on November 18<sup>th</sup>, 1983. She was raised by her parents, Elaine F. Goodman and Mark R. Goodman with her sister Hallie F. Goodman on the Upper West Side of Manhattan, NY, which remains Lindsey's favorite city in the world. Lindsey graduated from Bronx High School of Science (Bronx Science) in 2001 and went on to earn her B.S. in Applied Physics and a minor in French in May of 2006 from Binghamton University in Binghamton, NY. She became interested in engineering during the last two years of her undergraduate career and proceeded to Argonne National Laboratory where she participated in the Student Undergraduate Learning Internship program where she worked in the Energy Systems Division where she performed tribological testing of Ultrananocrystalline Diamond® thin films and participated in startup and operation of a pilot plant for electrolytic production of chemical fertilizers. In August 2007, she moved to Atlanta, GA and commenced her doctoral studies under the guidance of Dr. Preet M. Singh in the school of Materials Science and Engineering at Georgia Tech. Upon completing of her graduation requirements, Lindsey will begin work as an engineering consultant at Gibson Applied Technology and Engineering, Inc. in Houston, TX.